Øyvind Johansen

# Antiferromagnetic Insulator Spintronics

Doctoral thesis

Øyvind Johansen

**NTNU**
Norwegian University of
Science and Technology

**NTNU**
Norwegian University of
Science and Technology

NTNU

Øyvind Johansen

# Antiferromagnetic Insulator Spintronics

Thesis for the Degree of Philosophiae Doctor

Trondheim, December 2019

Norwegian University of Science and Technology
Faculty of Natural Sciences
Department of Physics

**NTNU**

Norwegian University of
Science and Technology

# Abstract

The emerging field of spintronics utilizes the spin degree of freedom of the electron in information storage and processing instead of the electron charge as in conventional electronics. Spintronics research has already led to a revolution in magnetic storage technology and has the potential for considerable improvements in future technologies.

A recent new avenue for research in spintronics is spin dynamics in magnetic insulators. In these materials, the electric charge cannot move, but information can still be transported through fluctuations in the electron spin because the spins strongly interact in magnetic materials. Eliminating the motion of the electric charges reduces Joule heating, a central limitation for the performance of nanoelectronics. Consequently, insulator spintronics is a good candidate for energy-efficient technologies.

A particular type of magnetic insulator that has gained significant interest over the past few years is the antiferromagnetically ordered insulator. Antiferromagnetic materials have several promising qualities, the most prominent of which is a vanishing net magnetic moment, which renders them insensitive to magnetic noise and allows for a denser stacking of components; another key ingredient is the ultrafast dynamics on the THz scale. Moreover, antiferromagnets are abundant in nature, making them easily accessible. Very recently, several remarkable experimental results have been obtained when using antiferromagnets as the main active component. These results include a long-distance transport of a spin current through an antiferromagnetic insulator and the demonstration of an antiferromagnetic memory operating at a THz frequency.

The research presented herein aims to improve our fundamental understanding of antiferromagnetic insulator spintronics. To this end, we study key aspects at the microscopic and quantum levels. This thesis starts by providing an overview of the historical background and the main motivation for antiferromagnetic insulator spintronics. Microscopic descriptions of antiferromagnetic ordering and magnetization dynamics are then given before these concepts are applied to the transport

i

of spin in heterostructures. Moving to a quantum mechanical description, we analyze quantized spin excitations in antiferromagnetic insulators and study how these excitations interact with both microwave photons and fermions such as electrons. We then move beyond antiferromagnetic insulators to study magnetic phases in two-dimensional ferromagnets. Finally, we present the main results of this doctoral work in five research papers.

The main research topics can be divided into (i) the electrical generation and detection of spin currents in heterostructures consisting of antiferromagnetic insulators and normal metals and how these are significantly enhanced at the spin-flop transition [1, 2]; (ii) the interaction between spin fluctuations in ferromagnets and antiferromagnets over macroscopic distances, mediated by independent coupling to microwave photons [3]; and (iii) the formation of exotic states of matter, such as indirect exciton condensates, caused by an interaction between the electron spin and magnetic fluctuations in an antiferromagnetic insulator at magnetic interfaces [4]. In addition, we also explore current-induced spin dynamics in selected two-dimensional ferromagnetic conductors and how this can be used to control magnetic phases, including a potential means for observing the topological Berezinskiǐ–Kosterlitz–Thouless phase transition in the two-dimensional $XY$ model in magnetic systems [5].

# List of publications

## Paper [1]

*"Spin pumping and inverse spin Hall voltages from dynamical antiferromagnets"*
Øyvind Johansen and Arne Brataas
Physical Review B **95**, 220408(R) (2017)　[Editor's Suggestion]

## Paper [2]

*"Spin-transfer antiferromagnetic resonance"*
Øyvind Johansen, Hans Skarsvåg, and Arne Brataas
Physical Review B **97**, 054423 (2018)

## Paper [3]

*"Nonlocal Coupling between Antiferromagnets and Ferromagnets in Cavities"*
Øyvind Johansen and Arne Brataas
Physical Review Letters **121**, 087204 (2018)

## Paper [4]

*"Magnon-Mediated Indirect Exciton Condensation
through Antiferromagnetic Insulators"*
Øyvind Johansen, Akashdeep Kamra, Camilo Ulloa,
Arne Brataas, and Rembert A. Duine
Preprint arXiv:1904.12699 (2019)　[Submitted to Physical Review Letters]

## Paper [5]

*"Current Control of Magnetism in Two-Dimensional $Fe_3GeTe_2$"*
Øyvind Johansen, Vetle Risinggård, Asle Sudbø, Jacob Linder, and Arne Brataas
Physical Review Letters **122**, 217203 (2019)

# My contributions to the publications

I have made substantial contributions to all the publications in this thesis. In Papers [1–4], I carried out the analytical calculations, and I am the main author of these manuscripts. I also created all the figures in these papers. In Paper [4], the initial part of the calculations was a generalization to two-sublattice magnetic systems based on a calculation for single-sublattice magnetic systems performed by the third author.

In Paper [5], the second author and I are both main authors, and we both made substantial contributions to the calculations and writing of the manuscript. My main individual contributions to this publication are primarily found in the sections labeled *"Micromagnetics"*, *"Magnon gap"*, and *"Curie temperature"*. I participated in writing and discussions pertinent to all aspects of the manuscript.

# Preface

This thesis is submitted to the Norwegian University of Science and Technology (NTNU) as a partial fulfillment of the requirements for the degree of Philosophiae Doctor. The work was performed at the Department of Physics under the supervision of Professor Arne Brataas, with Professor Jacob Linder as a cosupervisor, from August 2016 until the fall of 2019. During the course of this doctoral work, I also had a research stay for three months at Utrecht University in the Netherlands under the guidance of Professor Rembert A. Duine, from the beginning of April until the end of June 2018. This doctoral work resulted in five research papers, all of which are presented at the end of this thesis. In addition to research, the doctoral program also included coursework amounting to 30 ECTS, corresponding to a workload of one semester, as well as teaching undergraduate physics laboratory exercises for three semesters, also corresponding to a workload of one semester. The PhD was funded by the Research Council of Norway, under Grant No. 239926 "Super Insulator Spintronics" and through its Centres of Excellence funding scheme Project No. 262633 "QuSpin", as well as by the European Research Council via Advanced Grant No. 669442 "Insulatronics".

The first part of this thesis provides an introduction to the fields of spintronics and magnetization dynamics on semiclassical and quantum levels to readers unfamiliar with these fields. As these are quite broad fields, the focus is on the most important concepts that are discussed and utilized in the research papers at the end of this thesis. The purpose is to provide an intuitive understanding of the physics and methods utilized in the research papers, without extensive rigorous mathematical derivations, which are left to the research papers and other literature. The aim of this first part is not to simply reformulate the contents of the research papers, but there are several parts where I have found it useful to spend more time examining the research results in more detail or through an alternative way of seeing things. Because some journals have a length restriction on their manuscripts, one is often forced to condense the discussion in the research papers themselves, occasionally making it more demanding for the reader to grasp certain ideas. Moreover, in my

experience, one may often consider some of the research results in a new light post-publication. With these aspects in mind, I have attempted to write this thesis in a way such that it complements the research papers presented at the end.

The structure of this thesis is designed in an order that I personally find to be the most intuitive to read up on the research fields. To make the topics easier for readers who do not read this thesis from cover to cover or who occasionally need a reminder of different definitions, I have created an index with a list of terms and definitions at the end of this thesis. I hope that this thesis will serve as a useful source of information to readers interested in antiferromagnetic insulator spintronics.

Øyvind Johansen
Trondheim, Norway
September 2019

# Acknowledgments

First and foremost, I would like to express my profound gratitude to my advisor, Professor Arne Brataas. Your physical insights and overview of the field of spintronics have been invaluable to this PhD. I also highly value having the opportunity to partake in your network and the ability to take advantage of this network to have a research stay abroad. Thank you for your confidence in me and for your patience; I could not have asked for an advisor more suited to my needs.

I would also like to extend my sincere appreciation to Professor Rembert A. Duine for hosting and supervising me during my visit to Utrecht University and thank his group for making me feel welcome. My time in Utrecht was very educational and definitely one of the highlights during my PhD.

I have had the fortune of having several wonderful and talented collaborators. A big thank you to Akashdeep Kamra, Hans Skarsvåg, Vetle Risinggård, Camilo Ulloa, Jacob Linder, and Asle Sudbø is therefore in order. I have learned much from the discussions with you, and I am very grateful to have had the benefits of your support and insights during my PhD.

I would also like to thank Martin, Haakon, Even, and Håvard for giving me helpful comments and valued feedback regarding this thesis.

Although the PhD itself might be an individual commitment, I do not think it would have been possible without all the other great people around me. I would have liked to thank all of you by name, but I'm afraid this would quickly fill up the page. To my seniors from the former section of theoretical physics, thank you all for making me feel part of the group and for showing me the ropes. To my colleagues at QuSpin, thank you for continuing to make it an awesome place to be. To my fellow PhD students from the other sections of the Department of Physics and other departments, your camaraderie has been highly appreciated. I have really enjoyed my time during this PhD and had much fun with all of you at conferences, workshops, LAN parties, D&D campaigns (extra shout out to our outstanding Dungeon Master Trygve for taking the initiative and bringing us on an epic adventure), cinema visits, cabin trips, and late evenings with both scientific and hilariously unscientific

discussions. I will always remember this time of my life fondly.

In addition to having great people around me at work, I also had the luck of having some of the same great people as my neighbors as well. Thank you Trygve, Jonas and Tina for an amazing time in Nardosletta borettslag. I will sincerely miss our weekly dinner dates, board game/movie nights, and barbecues.

I would like to thank my parents, Harry and Ingeborg, and my sisters, Marit and Kristin, for your support and for always believing in me. My interest in the natural sciences and logical problem solving is in no small part thanks to you. To all of my friends and family outside of Trondheim, thank you for being there for me and for many memorable gatherings, of which there will hopefully be many more in the future.

Last, but not least, thank you my dear Andrea for all your love, support, and patience. You are by far the best thing that happened to me during my time as a PhD student. I look forward to having many new adventures with you, but most of all, finally removing the 'distance' from our long-distance relationship.

# Contents

# 1

# Introduction

## 1.1 Electronics and information technology

Information and communication technology has experienced an explosive development over the past century. A nice illustration of this trend is *Moore's law*. This law is based on Moore's prediction that there will be an exponential growth in the number of components (transistors) on integrated circuits [6]. Initially predicted to be a doubling in the number of components every year, it was later updated to a doubling every two years from 1975 [7]. Quite surprisingly, this prediction has thus far proven to be quite accurate for half a century. This trend in technological development has had an immense impact on the community as a whole. Where computers were enormous and extremely expensive half a century ago, the significant reduction in both size and price has led to computers becoming an essential commodity for a major part of society.

When most people think about technological devices in today's society, they think about devices based on *electronics*. Electronics is a technology that relies on information processing through the controlled transport of the fundamental electrical charge of electrons. Although the technological development of electronic devices has thus far been marvelous, electronics has certain fundamental limitations at its core
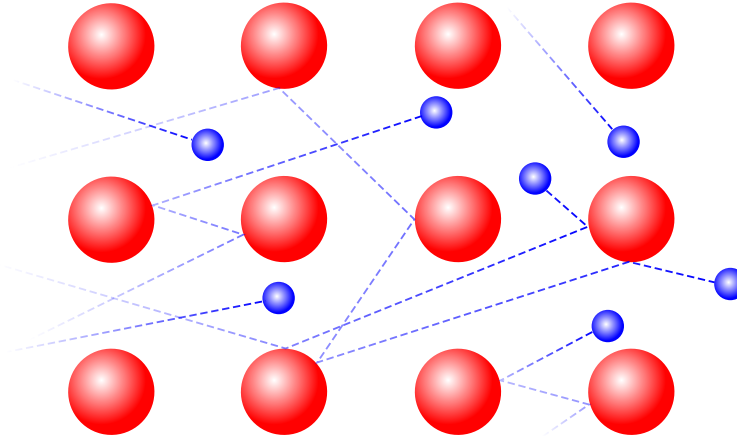
**Figure 1.1.** An electric current is carried by negatively charged electrons, illustrated here as small blue spheres, moving from the left to the right. In a classical picture, when the electrons move, they collide with the positively charged crystal lattice, illustrated as large red spheres, or with each other. These collisions transfer energy in the form of heat to the crystal lattice and cause an unwanted Brownian motion of the electrons around the desired current direction. This results in a significant decrease in the energy efficiency of the charge current when the overall purpose is to transfer information in the form of an electron flow from left to right.

that will eventually cause further development to come to a standstill. An example of such a limitation is *Joule heating*. Electric currents consist of moving particles, and these particles can collide with each other and generate heat, as illustrated in Fig. 1.1. The power of the heating in the material where the current passes through is proportional to the square of the current and therefore increases quite rapidly with increasing current. This heating is occasionally beneficial, as this effect is utilized in e.g. incandescent light bulbs and electrical ovens or heaters; however, it is an unwanted effect for information and communication technology for two main reasons. First, as devices become increasingly smaller, the electric circuits where the current passes through become narrower, leading to a significant increase in the current density needed to pass a certain amount of current through the wires. The increased current density in these wires leads to a drastic increase in the local heating, causing the wires to easily burn up if one passes a current that is too large through the wire. This places a significant restraint on how small one can make these electric circuits. Second, the heating from the electric currents results in a substantial energy loss for applications where this heating is unwanted, such as in computers. This point is of particular interest today, where the importance of creating an energy-efficient and

sustainable society using clean energy is becoming central. Although information and communication technology is perhaps not the first thing that comes to mind when people think of a green society, the explosive growth of its use in today's society makes it increasingly important to take into consideration. A study from 2015 estimated that a worst case scenario in 2030 could be that communication technology will account for as much as 51% of the global electricity usage and could be responsible for up to 23% of the greenhouse gas emissions worldwide [8]. While one can argue that it can be extremely difficult to make realistic predictions about something so complex, the development of energy usage in information and communication technology should be a reason for concern. With these drawbacks of electronics in mind, if the current progress is to be continued for the better, we need to change something fundamental about what we base our technology on. Here, the emerging field of *spintronics* shows some promising features that might help us address some of these issues.

## 1.2 Spintronics

### 1.2.1 Conventional spintronics

In addition to having a negative charge, the electron has an internal degree of freedom in the form of an intrinsic angular momentum, which is called the *spin* of the electron. A simple analogy of the electron spin is that the electron spins around its own axis, much like the Earth, as illustrated in Fig. 1.2. Note, however, that this picture is just a naive attempt to obtain a physical intuition of the electron spin. The behavior of the electron is inherently quantum mechanical. And if there is one thing we have learned about quantum mechanics thus far, it is that it can be extremely difficult, and often impossible, to align our intuitive understanding of classical physics on a macroscopic scale with quantum physics. An example of this mismatch is that the electron spin can *only be in one of two possible states*, often referred to as *spin up* and *spin down*, as can be understood from Fig. 1.2 (a). The electron spin and its orbital motion around the atomic nucleus are the fundamental building blocks for magnetic materials. This is because the combination of the spin and the electric charge results in an intrinsic magnetic moment and a corresponding magnetic field, as illustrated in Fig. 1.2 (b). The atomic nucleus can also possess a magnetic moment, but it is much smaller than that of the electron due to its comparatively heavy mass and can therefore often be neglected [9].
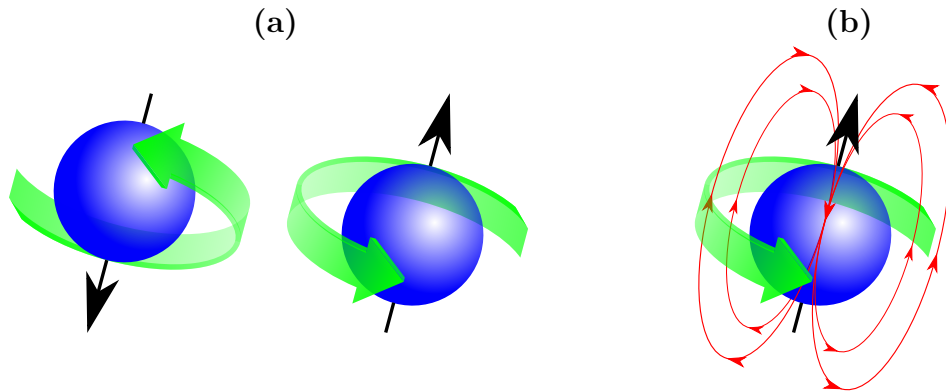
**Figure 1.2.** (a) An illustration of two electrons with spin down and spin up. The spin of the electron is often just illustrated by vectors, as in this figure. (b) The electron spin results in a magnetic moment and thereby a magnetic field, as illustrated by the red field lines.

In magnetic materials, the direction of the electron spins will follow certain types of ordering. As an example, in *ferromagnetic* materials, commonly referred to simply as "magnets" in layman terms (this is the material that will stick to your fridge door), the electron spins tend to align in the same direction. This causes the individual magnetic moments to interfere constructively, thereby creating an external magnetic field. The tendency for spins to order means that neighboring spins communicate with each other in magnetic materials (the mechanism of which will be discussed in the next chapter). This is the basis for the field of *spintronics*. The name spintronics is short for *"spin transport electronics"* [10, 11], and in this field, we are interested in information processing, storage, and control using the spin of the electron instead of its charge as in conventional electronics.

The concept of spintronics might be unfamiliar to many readers, but much of the technology used today already relies on some of its applications. The first major applications of spintronics began after the discovery of the *giant magnetoresistance* (GMR) effect in 1988 by the experimental groups of Fert and of Grünberg [12, 13]. These two groups independently studied the electrical resistance in heterostructures consisting of ferromagnetic layers separated by nonmagnetic/*normal metal* (N) spacers. It was discovered that when an electric current passes through a $| \uparrow |N| \downarrow |$ structure, where the arrows indicate the average spin direction in two separate ferromagnetic layers, the electric resistance was significantly higher than that in $| \uparrow |N| \uparrow |$ or $| \downarrow |N| \downarrow |$ structures. This property allowed for reading
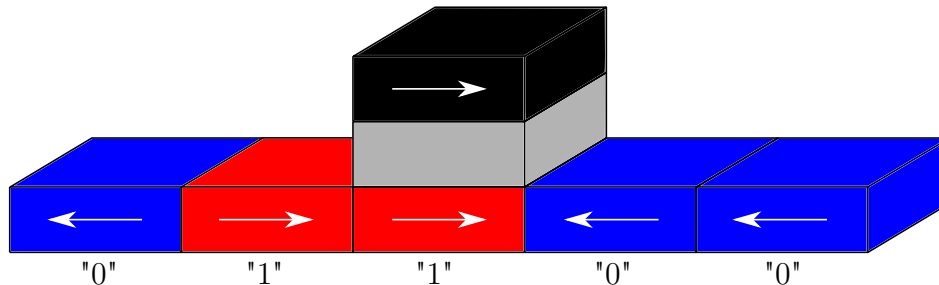
**Figure 1.3.** Basic illustration of the read-out concept used in magnetic memories. A fixed ferromagnetic layer (black) in the read head is placed over a location in the magnetic memory. The local magnetization direction in the magnetic memory can then be read by measuring the electrical resistance by passing a current through the nonmagnetic spacer (gray). The spacer layer is a conductor for the giant magnetoresistance (GMR) effect and an insulator for the tunnel magnetoresistance (TMR) effect. For instance, one can assign the bit value "1" to the parallel magnetization configuration and the bit value "0" to the antiparallel configuration with respect to the fixed layer.

out the local magnetization in a material along a given axis through electric measurements. This discovery was very beneficial for magnetic memories, such as hard disk drives (HDDs), which are now widely used in computers, and magnetoresistive random-access memory (MRAM). In these magnetic memories, one can store digital information in the form of local variations of the magnetization direction in magnetic materials, which can then be read via the GMR effect, as illustrated in Fig. 1.3. The discovery of the GMR effect was awarded the Nobel prize in physics in 2007, as *"It is thanks to this technology that it has been possible to miniaturize hard disks so radically in recent years"* [14]. The possibility of storing substantially more data on much smaller devices using the GMR effect, the commercialization of which was to a great extent because of Parkin at IBM, subsequently led to technological innovations such as the iPod [15]. Although it was the discovery of GMR that sparked the applications of spintronics in magnetic memories, another related effect has since replaced its role. This effect is called *tunnel magnetoresistance* (TMR) and functions quite similarly to GMR, but with the nonmagnetic conducting layer being replaced by a nonmagnetic electric insulator. When this insulating layer is sufficiently thin, the electric current can still pass through via quantum tunneling. While TMR was discovered over a decade prior to GMR [16], the initial discovery was achieved at very low temperatures and did not exhibit a very large change in

resistance; therefore, it did not attract much attention. However, more recent experiments of TMR have shown that this effect can also occur at room temperature with a tremendous change in the electrical resistance, which has increased significantly over the years. The initial resistance change of 14% in the 1975 discovery has since increased to $\sim$200% in 2004 [17, 18], $\sim$600% in 2008 [19], to the staggering values of $\sim$19000% [20] and even one million percent [21] in 2018. These values make TMR a more sensitive and favorable measuring technique than GMR.

In addition to using spintronics for storing and reading information, there is also ongoing research on how to use spintronics to effectively write information to memory. A decade before the discovery of the GMR effect, Berger predicted that spins in an electric current could move ferromagnetic domain walls [22–25], which are the borders between the different magnetic directions/domains in Fig. 1.3, via so-called *spin-transfer torques* (STTs) [26]. Later, Berger and Slonczewski independently predicted that these torques could transfer angular momentum in magnetic multilayers, and that the torques could be used to change the magnetization direction in one of the magnetic layers [27, 28]. STTs can be used for writing the memory and transferring the magnetic information in a bit line to the read head. This is greatly advantageous, as we can then avoid having any moving parts, which will cost less energy and be more durable [29]. The commercialization of MRAM utilizing STTs, known as STT-MRAM, is currently in progress. As an example, Everspin has manufactured 256 Mbit STT-MRAM chips [30].

Another promising application of spintronics that has attracted considerable attention is the spin field-effect transistor proposed by Datta and Das in 1990 [31]. The transistor is the invention that revolutionized modern electronics. It works as a switch and can therefore be used to represent a bit in memory applications or to carry out logical operations in processors. The spin field-effect transistor is a nonvolatile alternative to the current transistors, which causes lower energy consumption. Realizations of spin field-effect transistors have been reported over the past decade [32–34], but the development has not yet reached the stage of large-scale implementation in modern devices, to the best of my knowledge.

## 1.2.2   Insulator spintronics

### – Future technology for a more energy-efficient society?

The applications of spintronics discussed in the previous section are generally referred to as applications of *conventional spintronics*. While they utilize the spin
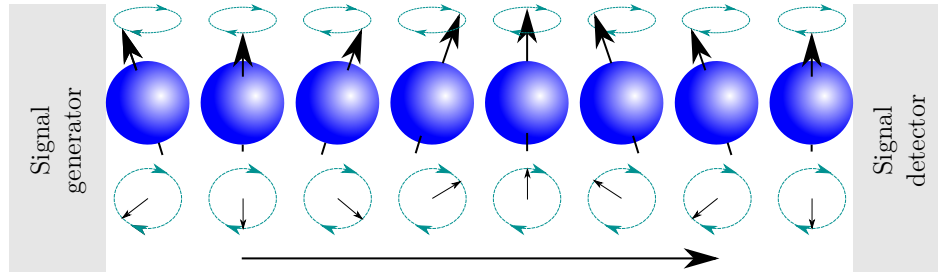
**Figure 1.4.** Instead of transferring information via moving electrons, one can transfer information via the electron spins in the form of spin waves, as illustrated here. The signal generator causes the electron spin on the left-hand side to precess, and as the electron spins are coupled in magnetic materials, this precession propagates to the neighbors to the right. The signal detector to the right can then detect the signal coming from the left once the spin(s) next to the detector start precessing. The in-plane precessions of the electron spins are illustrated by the rotating arrows beneath the electrons.

of the electron, the motion of the spin is interconnected with the motion of the electron itself. Consequently, even if conventional spintronics has greatly assisted in miniaturizing computers, it suffers the same drawback as conventional electronics in regard to effects such as Joule heating because we still rely on electric currents. It would therefore be more beneficial if we could transport spin without the accompanying transport of charge. This is where magnetic insulators and insulator spintronics become interesting. In electrically insulating materials, the electronic charge is no longer free to move as in conductors such as metals. However, if the insulator also exhibits a magnetic ordering, one can transport information via the spins instead, as these couple to their neighboring spins. An example of such spin transport is the propagation of a spin wave from a generator to a detector, as shown in Fig. 1.4. Experiments demonstrating the transport of spin in a magnetic insulator have already been realized [35–37]. The transport of information purely via the electron spins does not suffer the same disadvantages as electronics such as Joule heating. Insulator spintronics therefore shows great promise as a candidate to solve some of the fundamental problems of electronics in e.g. computers.

### 1.2.3   Antiferromagnetic spintronics

**– Smaller and faster components**

Another type of magnetic ordering that commonly occurs in nature is that of *antiferromagnetic ordering*. Ferromagnets prefer having all the spins aligned along one direction, whereas antiferromagnets would like to have each spin point in the opposite direction with respect to its neighboring spins. For a one-dimensional spin chain, we would then have a spin ordering such as ↑↓↑↓↑↓. This type of ordering was initially suggested by Louis Néel, who later won the Nobel prize in physics for his work on magnetic ordering in condensed matter physics. However, he was not very optimistic regarding the applications of this type of magnetic ordering:

> *"A large number of antiferromagnetic materials is now known; these are generally compounds of the transition metals containing oxygen or sulphur. They are extremely interesting from the theoretical viewpoint but do not seem to have any applications."*

> – Louis Néel, Nobel Lecture December 1970

Despite this outlook, antiferromagnets have found applications with the birth of spintronics. Initially, antiferromagnets had a passive role in spintronic devices. A prime example is the use of the exchange bias effect at interfaces between ferromagnets and antiferromagnets, which pins the magnetization in the ferromagnet in a specific direction [38]. This is utilized in the GMR and TMR effects to pin the magnetization direction in the fixed ferromagnetic layer in the read head (black layer in Fig. 1.3) by having an additional antiferromagnetic layer adjacent to the fixed ferromagnetic layer. Recently, however, interest in using antiferromagnets as the active component in spintronic devices has been surging [39, 40]. This interest is because antiferromagnets have several advantages over ferromagnets:

- Antiferromagnets produce no external/stray magnetic fields, which allows for a denser packing of antiferromagnetic components, as shown in Fig. 1.5.

- Antiferromagnets are insensitive to magnetic noise.

- Antiferromagnets have a very high resonance frequency compared to ferromagnets. While ferromagnets typically have a resonance frequency on the GHz scale, antiferromagnets have resonance frequencies in the range of hundreds of GHz to THz. This allows for much faster dynamics when e.g. switching the magnetization orientation.
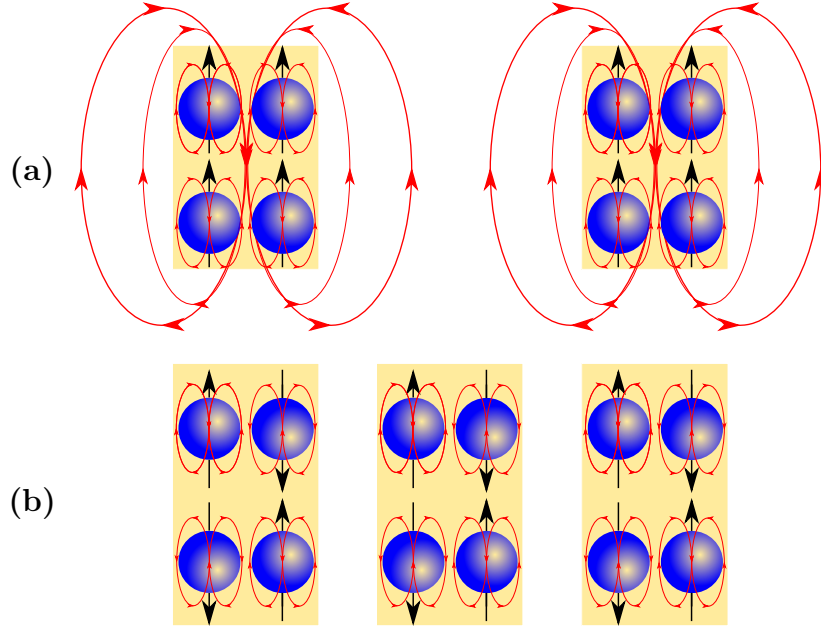
**Figure 1.5.** (a) Ferromagnetic components need to have a sufficient separation between themselves to avoid unwanted crosstalk via the external magnetic fields they produce (red field lines). (b) Antiferromagnetic components have a strong internal magnetic field, but the external magnetic field is canceled due to the antiparallel ordering. They can therefore be more densely packed than ferromagnetic components, without any crosstalk via self-produced magnetic fields.

One of the applications of antiferromagnets currently being investigated is an antiferromagnetic memory. While bits can be encoded in the two magnetization directions ↑ and ↓ in ferromagnets, the situation is a bit different in antiferromagnets. It is extremely challenging to distinguish a configuration such as ↑↓↑↓ from ↓↑↓↑ because they are almost the same - just shifted with an atomic distance with respect to one another. For antiferromagnets, one instead encodes the bits in the two configurations where the spins either point along ↕ or ⟷, which can be distinguished from one another. The electrical switching of the antiferromagnetic spin ordering has recently been theoretically predicted [41] and demonstrated experimentally [42–44], where it was also shown that one could obtain a THz writing speed of the antiferromagnetic memory [44]. In addition to applications of antiferromagnets in memory technologies, there has also been very recent progress in the transport of spin currents through antiferromagnetic insulators. In an experiment using the an-

tiferromagnetic insulator hematite ($Fe_2O_3$), a very common iron oxide and the main component of rust, the experimentalists were able to transport and detect an injected spin current over distances of $80\,\mu m$ [37]. Although this is not a large distance from a macroscopic perspective, it is very far in the context of nanotechnology.

The work in this thesis is, as the title suggests, primarily focused on insulator spintronics in antiferromagnetic materials. The aim of the presented work is to further improve the fundamental understanding of the field, which may hopefully also be of use in future applications of antiferromagnetic spintronics. This thesis covers a variety of topics. In Papers [1, 2], we study the generation and detection of a spin current in an antiferromagnetic insulator and how this depends on the parameters of the free energy of the antiferromagnet. In Paper [3], we present a possible way to bridge antiferromagnetic and ferromagnetic spintronics via interactions between the spins and photons. In Paper [4], we study how fluctuations in the antiferromagnetic spin structure can mediate an attractive interaction between fermionic particles to create exotic states of matter that can be used for dissipationless transport. An introduction to the terminology and formalism in the papers is given in the remaining chapters of this thesis. Chapters 2 and 3 provide an introduction to semiclassical magnetization dynamics in antiferromagnetic insulators, as well as spintronics in multilayer heterostructures, laying the groundwork for Papers [1, 2]. Chapter 4 presents a quick introduction to the quantum mechanical description of magnetization dynamics in antiferromagnets. Building upon this, Chapter 5 gives an introduction to interacting bosons, specifically between quantized spin fluctuations (known as magnons) and microwave photons, which is considered in Paper [3]. In Chapter 6, we consider interactions between magnons and fermionic particles and give an introduction to the formalism in Paper [4]. The last chapter and paper of this thesis, Chapter 7 and Paper [5], do not involve antiferromagnetic insulators. Instead, these consider the magnetic phases in recently experimentally detected two-dimensional ferromagnetic materials and how these magnetic phases can be controlled with an electric current in certain materials.

# 2

## Antiferromagnetic magnetization dynamics

Magnetic ordering has a quantum mechanical origin but still persists on a macroscopic level. When describing the overall system behavior, it is no longer necessary to provide a rigorous description of all the individual spins in the system. Thus, it can be beneficial to use a so-called semiclassical treatment of the electron spins rather than a quantum mechanical one. In this semiclassical treatment, we consider the expectation values of quantum mechanical operators, such as the electron spin, instead of describing a macroscopic ensemble of physical quantities in terms of operators. This semiclassical description is often referred to as *micromagnetics*, and it is capable of describing numerous magnetic phenomena on a microscopic level. This chapter will give an introduction to the micromagnetic description of antiferromagnets both in equilibrium and in response to a dynamical source.

## 2.1 Antiferromagnetic order

In antiferromagnetic materials, the neighboring spins prefer to point in opposite directions, unlike in ferromagnetic materials, where they prefer to point in the same
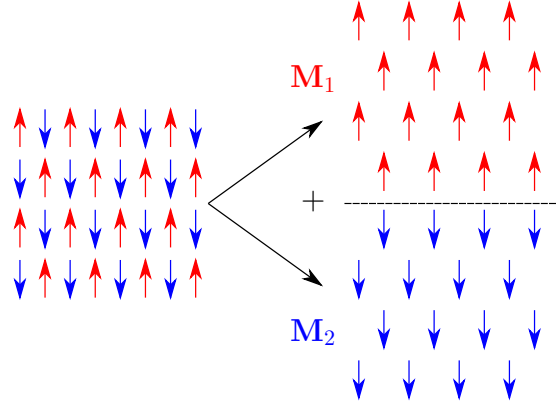
**Figure 2.1.** An antiferromagnet can be considered two (coupled) ferromagnets with opposite magnetizations if we split the sublattices.

direction. Antiferromagnetic ordering is illustrated for a two-dimensional square lattice to the left in Fig. 2.1. When describing antiferromagnetic materials, it is convenient to divide the material into two *sublattices*, as illustrated in Fig. 2.1. In each sublattice, all the spins point in the same direction for a spatially uniform antiferromagnet. To describe the magnetic order of an antiferromagnet, we can consider the average magnetization, which is the density of magnetic moments, within each of the two sublattices. Let us denote these as $\mathbf{M}_i$ ($i = 1, 2$). Note that for an antiferromagnetic material, $|\mathbf{M}_1| = |\mathbf{M}_2| \equiv M$. If these are not exactly equal but still point in opposite directions, the material is *ferrimagnetic*. Because the magnetization within the two sublattices is equal in magnitude for an antiferromagnet, it is common to only describe the direction of the magnetization in terms of the unit vectors $\mathbf{m}_i = \mathbf{M}_i/M$.

Although we can describe the antiferromagnetic order in terms of the sublattice magnetization unit vectors $\mathbf{m}_i$, it is often more convenient to work in a different basis where the antiferromagnetic order is more apparent. In this basis, we describe the antiferromagnetic order in terms of the average magnetization $\mathbf{m}$ and average *staggered magnetization* $\mathbf{n}$, defined as

$$\mathbf{m} = \frac{\mathbf{m}_1 + \mathbf{m}_2}{2}, \quad \mathbf{n} = \frac{\mathbf{m}_1 - \mathbf{m}_2}{2}. \tag{2.1}$$

The average staggered magnetization vector $\mathbf{n}$ is often referred to as the antiferromagnetic order parameter, or the *Néel order parameter*. This is because this parameter intuitively describes the degree of antiferromagnetic ordering. When $|\mathbf{n}| = 1$ (which also entails $|\mathbf{m}| = 0$), we have a perfect collinear antiferromagnetic ordering,

whereas if we have $|\mathbf{n}| = 0$ (and $|\mathbf{m}| = 1$), we no longer have antiferromagnetic ordering but rather a ferromagnetic ordering. From the definitions of $\mathbf{m}$ and $\mathbf{n}$ in Eq. (2.1), we note that they are not unit vectors as $\mathbf{m}_1$ and $\mathbf{m}_2$ but satisfy the following relations:

$$\mathbf{m}^2 + \mathbf{n}^2 = 1\,, \quad \mathbf{m} \cdot \mathbf{n} = 0\,. \tag{2.2}$$

Now that we have a description of antiferromagnetic ordering, we will discuss how this ordering occurs.

## 2.2 Micromagnetic energy

There are many different types of energy contributions in magnetic systems that affect the structure and dynamics of the magnetic moments. These are typically microscopic in origin but can have a macroscopic effect on the magnetic order. In this section, we will discuss three common contributions to the micromagnetic energy, namely, the exchange interaction, magnetocrystalline anisotropy, and the Zeeman interaction. While there are several other possible energy contributions, the work presented in this thesis primarily focuses on systems that can be described by a combination of these three effects. Notably, one magnetic interaction that is absent in this description of antiferromagnets is the dipole-dipole interaction. Although the dipole-dipole interaction is generally a significant contribution to the description of e.g. ferromagnets, its contribution in antiferromagnetic materials is relatively insignificant because there is no net magnetization that creates a dipole field worth considering.

### 2.2.1 Exchange interaction

The *exchange interaction* causes the magnetic ordering of spins. The exchange interaction can be considered as a balance between two principles: electrostatic Coulomb repulsion and the *Pauli principle*. The Pauli principle states that two identical fermionic particles (particles with half-integer spin), such as electrons, have to have an overall antisymmetric wave function, which means that two fermions cannot be in the same state. In other words, if two electrons are in the same spatial state, it requires them to have opposite spins in an antisymmetric singlet state, whereas if they have the same spin, it requires them to have an antisymmetric spatial wave function.

The form of the exchange interaction depends on the balance between the Coulomb repulsion and the Pauli principle. In materials with a strong Coulomb repulsion, it will be energetically favorable to have the electrons far from each other or electrons that have a small overlap in their wave functions and as a consequence are less visible to each other (e.g. by having spatially antisymmetric two-particle wave functions). Due to the Pauli principle, this is a natural state for electrons with aligned spins, and a ferromagnetic ordering is therefore favorable [45, 46].

Antiferromagnetic ordering occurs when the Coulomb interaction is short ranged due to a combination of quantum fluctuations and the Pauli principle. The mechanism for antiferromagnetic ordering is quite subtle and is best explained through the following example: consider a case where we have a square lattice of atoms, and each atom can host at most two electrons in the same spatial orbital. Let us further specify a scenario where we have a number of electrons equal to the number of atoms, and we have a short-ranged Coulomb repulsion between the electrons such that they only repel each other if they are at the same atom. Consequently, the ground state of the system must be the case where we have one electron at each atom because this does not cost energy due to Coulomb repulsion. In addition to a Coulomb repulsion between the electrons, the electrons also have a small contribution to the kinetic energy from processes where the electrons hop from atom to atom. We assume that the kinetic energy is much smaller than the Coulomb repulsion and treat this as a perturbation. If we start from the ground-state configuration with one electron at each atom, once an electron hops to the neighboring atom, it will hop to an atom that is already hosting another electron. For this to be allowed by the Pauli principle, the electron hopping to the neighboring atom must have the opposite spin of the electron already there because the two electrons are not allowed to have the same spatial and spin states. After the first hopping process, the electron will hop back to its original atom because it costs energy due to Coulomb repulsion for it to remain at the already-occupied atom. However, the ability of the electron to move back and forth between the neighboring atoms delocalizes its wave function and lowers its overall energy by a small amount. Delocalized particles generally having less energy (when disregarding contributions from other interactions) can be found in other systems, such as particles in a box and quantum wells, where the ground-state energy decreases with an increase in the box or well size. Because only the electron with a spin antiparallel to its neighbors can lower its energy via delocalization through hopping processes to neighboring atoms, the ground-state of this system has an antiferromagnetic ordering of the spins. The above model is a
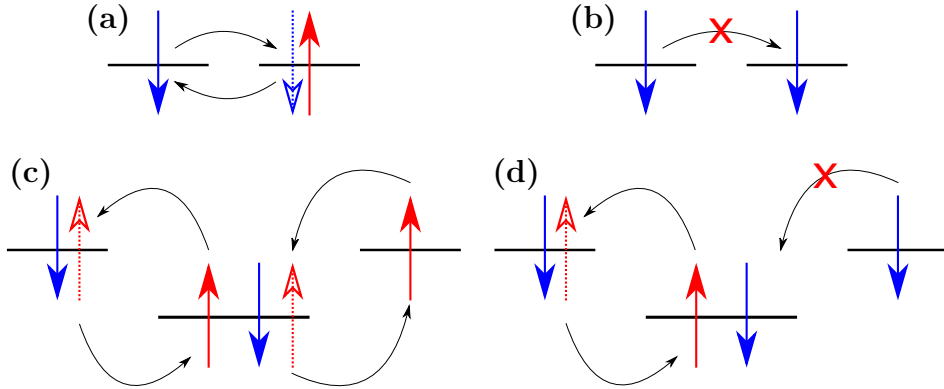
**Figure 2.2.** (a) When two neighboring spins are antiparallel, electrons are allowed to (virtually) hop back and forth between the atoms to lower its energy, unlike scenario (b), where the neighboring spins are parallel. In superexchange, an indirect magnetic interaction between two magnetic atoms is mediated by exchange interactions with a nonmagnetic atom. In (c), both of the higher-energy magnetic orbitals can undergo a simultaneous exchange interaction with the nonmagnetic orbital, whereas this is not possible with the parallel configuration in (d). This causes a preferred magnetic ordering of the magnetic atoms, which is often antiferromagnetic [9].

special case of the Hubbard model, and its ground state has indeed been shown to be an antiferromagnetic insulator in one dimension [47]. Often, these quantum fluctuations between two magnetic atoms (= atoms with a net spin) involve exchange interactions with an intermediary nonmagnetic atom. The magnetic interaction is then called a *superexchange* [48, 49], and it is illustrated in Fig. 2.2.

The exchange interaction between localized spins can be expressed by the Heisenberg Hamiltonian

$$\mathcal{H}_{\text{Heisenberg}} = J_{\text{ex}} \sum_{\langle i,j \rangle} \mathbf{S}_i \cdot \mathbf{S}_j \,, \tag{2.3}$$

where the sign of the exchange constant $J_{\text{ex}}$ indicates whether ferromagnetic ($J_{\text{ex}} < 0$) or antiferromagnetic ($J_{\text{ex}} > 0$) ordering of the spins is preferred. The above Heisenberg model only includes nearest-neighbor interactions, denoted by $\langle i,j \rangle$, but it can be extended to include interactions over several atomic distances. However, the exchange interaction is a short-ranged interaction, and a nearest-neighbor model often captures the essential physics. For a spatially uniform magnetization within each sublattice of the antiferromagnet, the contribution to the free energy from the

exchange interaction can be written as

$$F_{\text{Exch.}} = \int \mathrm{d}V \left|\tilde{J}_{\text{ex}}\right| \mathbf{M}_1 \cdot \mathbf{M}_2 = V \left|\tilde{J}_{\text{ex}}\right| M^2 \mathbf{m}_1 \cdot \mathbf{m}_2 = V \left|\tilde{J}_{\text{ex}}\right| M^2 \left(\mathbf{m}^2 - \mathbf{n}^2\right) . \quad (2.4)$$

Here, $\tilde{J}_{\text{ex}}$ is the exchange interaction strength between the two sublattice magnetizations, analogous to the single-spin exchange constant $J_{\text{ex}}$. If we also take spatially varying magnetization profiles into account, the exchange interaction also obtains a contribution from the spatial fluctuations [50]:

$$F_{\text{Exch.}} = \int \mathrm{d}V \left|\tilde{J}_{\text{ex}}\right| M^2 \left\{\mathbf{m}^2 - \mathbf{n}^2 + \frac{a^2}{4} \left[(\boldsymbol{\nabla}\mathbf{m})^2 + (\boldsymbol{\nabla}\mathbf{n})^2\right]\right\} . \quad (2.5)$$

Here, $a$ is the lattice constant of the antiferromagnet.

## 2.2.2   Magnetic anisotropy

If the magnetic interactions in a magnet are solely described by the Heisenberg model in Eq. (2.3), where the exchange interaction $J_{\text{ex}}$ is equal in all directions, then this is called an *isotropic* Heisenberg magnet. This is because there is then an isotropy in spin space, where the direction along which the spins order does not matter. This is not true for many magnetic materials, as they often exhibit a phenomenon known as a *magnetic anisotropy*, where the energy of the system depends on the direction along which the spins point. The magnetic anisotropy is often closely related to *spin-orbit coupling*, where there is, as the name implies, an interaction between the motion of the electron and its spin. The spin-orbit interaction is a relativistic effect. Its origin can be explained heuristically as follows: as seen from the reference frame of the electron, the positively charged nuclei of the crystal are moving, thereby creating a dynamical electric potential. This in turn leads to a magnetic field that interacts with the magnetic moment of the electron, i.e. its spin. This case is illustrated in Fig. 2.3. The magnetization of a material is caused by the electron spins of the outer orbitals, where the shells are unfilled and can carry a net spin. These orbitals are not spatially isotropic, unlike the lowest energy *s*-orbital, and there are therefore certain orbits that are more probable for the electrons to follow. Consequently, this also leads to an anisotropy in spin space due to the spin-orbit coupling, and certain directions are therefore easier to magnetize than others.

In micromagnetics, we often simplify the mathematical description of the magnetic anisotropy by a model such as

$$\mathcal{H}_{\text{Ani}} = \sum_\alpha \frac{k_\alpha}{2} \sum_i (\mathbf{S}_i \cdot \hat{\mathbf{e}}_\alpha)^2 . \quad (2.6)$$
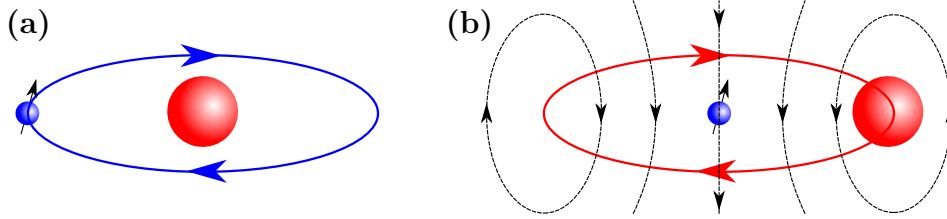
**Figure 2.3.** (a) The electron (blue sphere) orbits the positively charged atom core (red sphere). (b) From the reference frame of the electron, the atom core will instead orbit the electron. This leads to a charge current around the electron, which generates a magnetic field (dotted field lines) that interacts with the electron spin (black arrow).

Here, $k_\alpha$ is the strength of the magnetic anisotropy along the anisotropy axis $\hat{\mathbf{e}}_\alpha$. Note that this energy is even in the spin; therefore, both directions along the axis are equally (un)favorable. This is because the free energy has to be invariant under time-reversal symmetry in the absence of external influences, such as external magnetic fields. Higher-order even terms are often neglected because these terms are generally small compared to the term that is second order in the spin. The axis along $\hat{\mathbf{e}}_\alpha$ that corresponds to the lowest value of $k_\alpha$ is typically called the *easy axis* of the system, and similarly, the axis that corresponds to the highest value of $k_\alpha$ is called the *hard axis*. Any axes with nonextremal values of $k_\alpha$ are called *intermediate axes*. In the lowest-energy state, the spins align along the easy axis, and in the highest-energy state, they align along the hard axis if the contribution from other interactions is neglected. The anisotropy Hamiltonian for the spins can be generalized to macroscopic magnetic moments for an antiferromagnet:

$$F_{\text{Ani}} = \int \mathrm{d}V \sum_\alpha \frac{K_\alpha}{2} \left[ (\mathbf{M}_1 \cdot \hat{\mathbf{e}}_\alpha)^2 + (\mathbf{M}_2 \cdot \hat{\mathbf{e}}_\alpha)^2 \right] \tag{2.7a}$$

$$= \int \mathrm{d}V \sum_\alpha K_\alpha M^2 \left[ (\mathbf{m} \cdot \hat{\mathbf{e}}_\alpha)^2 + (\mathbf{n} \cdot \hat{\mathbf{e}}_\alpha)^2 \right] . \tag{2.7b}$$

The anisotropy constants $K_\alpha$ have a physical meaning equivalent to the anisotropy constants $k_\alpha$ but have different units due to the minor differences in the definitions of Eq. (2.6) and Eq. (2.7).

### 2.2.3  Zeeman interaction

The *Zeeman interaction* is the interaction between the magnetization of a material and a magnetic field (which is generally external). This interaction is the macroscopic version of the Zeeman effect, which is the spin-dependent energy level splitting

of electrons in a static magnetic field. The Zeeman interaction makes it energetically favorable for the magnetization of a material to point in the same direction as a magnetic field. This is the case regardless of the magnetic field being static or dynamic. The contribution of the Zeeman interaction to the free energy can be expressed as

$$F_{\mathrm{Z}} = - \int \mathrm{d}V \mathbf{H} \cdot \mathbf{M} \,, \tag{2.8}$$

where $\mathbf{H}$ is a magnetic field in units of Tesla and $\mathbf{M}$ is the net magnetization. For a spatially uniform antiferromagnet, this free energy becomes

$$F_{\mathrm{Z}} = -VM\mathbf{H} \cdot (\mathbf{m}_1 + \mathbf{m}_2) = -2VM\mathbf{H} \cdot \mathbf{m} \,. \tag{2.9}$$

While antiferromagnets are infamous for being highly insensitive to magnetic fields, there is nonetheless an interaction with external magnetic fields even if the material has a vanishing net magnetization. We will later see that an easy-axis antiferromagnet at resonance does have a small net magnetization that can interact with external magnetic fields. First, however, we will consider the case of a strong static magnetic field in equilibrium and what occurs when the strength of this field becomes comparable to other energy contributions in the system.

## 2.3   The spin-flop transition

Let us consider a system where we have a uniaxial easy-axis antiferromagnet in an external magnetic field along the easy axis. This system has three competing interactions, which we introduced in the previous section:

- Exchange interaction: wants the spins in the two sublattices to be antiparallel.

- Easy-axis anisotropy: wants the spins to be aligned with the easy axis.

- Zeeman interaction: wants a net magnetization along the magnetic field, i.e. parallel spins on both sublattices.

The easy-axis anisotropy can cooperate with both the exchange interaction and Zeeman interaction (as long as the magnetic field is along the easy axis), but there is an obvious conflict of interest for the exchange interaction and the Zeeman interaction. The exchange interaction is, in almost all cases, the dominating contribution to the effective interaction, with an interaction strength that can be comparable to external magnetic fields in the range of 50-1000 T [51–53]. Consequently, unless
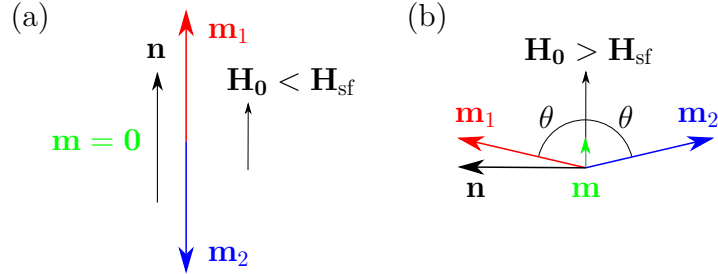
**Figure 2.4.** (a) Below the spin-flop transition, the magnetic moments are collinear and parallel to the easy axis. (b) If we apply an external magnetic field $\mathbf{H_0}$ along the easy axis, above some critical field strength $\mathbf{H}_{sf}$, the magnetic moments "flop" and are at an angle $\theta$ with respect to the easy axis, creating a net magnetization along the magnetic field. At $\mathbf{H}_{sf}$, the angle is $\theta \approx \pi/2$ due to the strength of the exchange interaction, and $\theta$ decreases for increasing $\mathbf{H_0}$.

the external magnetic field is very large, antiferromagnets will effectively remain in the antiparallel configuration. However, when the external magnetic field becomes sufficiently large compared to the exchange and anisotropy energy contributions, the lowest-energy state becomes one where the sublattice magnetizations are not completely antiparallel to one another. They are instead tilted in the direction of the magnetic field. This tilting leads to a net magnetic moment along the field direction, which we choose to be along the easy axis in this scenario. If the external magnetic field is small compared to the effective exchange field, which is the case for realistic scenarios, the magnetic moments will still be mostly antiparallel. To satisfy this, in addition to having a small net magnetic moment along the easy axis of the material, the spins need to "flop" to a state where they are almost perpendicular to the easy axis. This case is illustrated in Fig. 2.4.

The transition from the antiparallel state along the easy axis to the tilted state with a net magnetic moment is called the *spin-flop transition*. The critical field strength $\mathbf{H}_{sf}$ at which this transition occurs is $\mathbf{H}_{sf} \approx M\sqrt{2\left|\tilde{J}_{ex}K_{\parallel}\right|}$ [54], to the lowest order in $K_{\parallel}/\tilde{J}_{ex}$. Here, $K_{\parallel}$ is the strength of the easy-axis anisotropy. The ratio $K_{\parallel}/\tilde{J}_{ex}$ is typically quite small because the magnetic anisotropy is much weaker than the exchange interactions. The approximation when higher-order terms in this ratio are discarded is commonly referred to as the *exchange approximation*. The critical spin-flop field $\mathbf{H}_{sf}$ is always larger than the effective anisotropy field; thus, it is more energetically favorable to have a small component of the sublattice magnetizations along the easy axis. It is also dependent on the exchange interaction

strength since it costs exchange energy to tilt the sublattice magnetizations to obtain a net magnetization.

## 2.4   The Landau–Lifshitz–Gilbert equation

Now that we have considered the static configuration and energy contributions to antiferromagnets, we will focus on the dynamical behavior of the magnetic moments. Before considering the antiferromagnetic case, we will start with the simpler case of a ferromagnet to obtain a better intuition of the dynamical equations.

### 2.4.1   Ferromagnetic magnetization dynamics

Magnetic moments in an external magnetic field $\mathbf{H_0}$ perform something known as a *Larmor precession* around the magnetic field. These precessions can be described mathematically as

$$\dot{\mathbf{m}} = -\left|\gamma\right| \mathbf{m} \times \mathbf{H_0} = -\omega_H \mathbf{m} \times \hat{\mathbf{H}}_\mathbf{0}\,, \qquad (2.10)$$

where $\gamma$ is the *gyromagnetic ratio* ($\left|\gamma\right| \approx 1.76 \cdot 10^{11}$ s$^{-1}$T$^{-1}$) and $\omega_H = \left|\gamma \mathbf{H_0}\right|$ is the *Larmor frequency*. If the external magnetic field is the only component that interacts with the magnetic moment, the external field denotes the direction of minimal energy for the magnetic moment. If we now also account for other contributions to the free energy, such as the exchange energy and magnetic anisotropy discussed earlier, we can do this mathematically by treating their contribution as some *effective magnetic field* that denotes the direction of minimal total free energy for the magnetic moment:

$$\mathbf{H}_{\text{eff}} = -\frac{1}{M}\frac{\delta f}{\delta \mathbf{m}}\,, \qquad (2.11)$$

where $f = \delta F/\delta V$ is the total free energy density in a volume $V$ and $F$ is the total free energy. The contribution from the Zeeman interaction to the effective field $\mathbf{H}_{\text{eff}}$ will then simply be the external magnetic field $\mathbf{H}_0$, whereas the other interactions are written in a form such that they can effectively be treated as magnetic fields.

The Larmor precession of the magnetic moments described in Eq. (2.10) will lead to an endless rotation of the magnetization in a closed loop around the effective field. In real systems, however, dissipation will cause the magnetization to gradually relax to its equilibrium direction along the effective field unless the dynamics is sustained by some externally applied source. To take dissipation into account, one
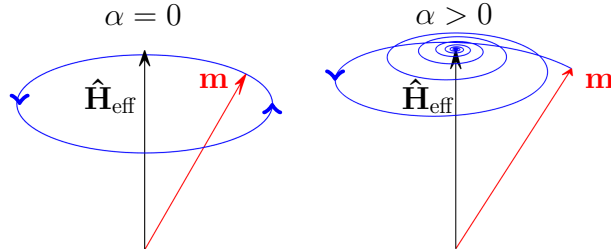
**Figure 2.5.** Without damping ($\alpha = 0$), the magnetization performs a right-handed Larmor precession around the effective field direction. When damping is present ($\alpha > 0$) in the absence of a source to sustain the dynamics, the Larmor precession amplitude spirals inwards as the magnetization relaxes to its equilibrium state along the effective field.

commonly describes the magnetization dynamics by the *Landau–Lifshitz–Gilbert* (LLG) equation

$$\dot{\mathbf{m}} = -|\gamma|\,\mathbf{m} \times \mathbf{H}_{\text{eff}} + \alpha\mathbf{m} \times \dot{\mathbf{m}}\,, \tag{2.12}$$

where $\dot{\mathbf{m}}$ is a short-hand notation for $\mathrm{d}\mathbf{m}/\mathrm{d}t$. Here, the phenomenological Gilbert damping term [55, 56], parameterized by the dimensionless damping factor $\alpha > 0$, has been added to the Larmor precession to account for dissipation. The effect of this term on the precession of the magnetization is shown in Fig. 2.5. Note that this differential equation only describes the dynamics of the direction of the magnetization and does not describe any change in the magnitude of the magnetization.

## 2.4.2 Generalization to antiferromagnets

To obtain dynamical equations for the sublattice magnetizations in antiferromagnets, one can describe each sublattice magnetization by its own LLG equation:

$$\begin{pmatrix} \dot{\mathbf{m}}_1 \\ \dot{\mathbf{m}}_2 \end{pmatrix} = \begin{pmatrix} -|\gamma|\,\mathbf{m}_1 \times \mathbf{H}_{\text{eff}}^{(1)} + \alpha_{11}\mathbf{m}_1 \times \dot{\mathbf{m}}_1 \\ -|\gamma|\,\mathbf{m}_2 \times \mathbf{H}_{\text{eff}}^{(2)} + \alpha_{22}\mathbf{m}_2 \times \dot{\mathbf{m}}_2 \end{pmatrix}\,. \tag{2.13}$$

The effective fields for each sublattice are defined as $\mathbf{H}_{\text{eff}}^{(i)} = -\delta f/\delta \mathbf{M}_i$. At first glance, these equations might appear to be uncoupled differential equations, but they are coupled through the effective fields as $\mathbf{H}_{\text{eff}}^{(1)}$ depends on $\mathbf{m}_2$, and similarly, $\mathbf{H}_{\text{eff}}^{(2)}$ depends on $\mathbf{m}_1$.

Recent works have suggested that the model in Eq. (2.13) does not provide a complete and accurate description of dissipation in two-sublattice systems [57–59],

and the damping in these systems needs to be treated more generally. Rather than having a Gilbert-damping torque $\boldsymbol{\tau}_{\mathrm{GD}}^{(i)}$ acting on sublattice $i$ that is given by

$$\boldsymbol{\tau}_{\mathrm{GD}}^{(i)} = \sum_{j=1,2} \alpha_{ij} \mathbf{m}_i \times \dot{\mathbf{m}}_j \tag{2.14}$$

where the tensor $\alpha_{ij}$ is diagonal ($\alpha_{ij} = \alpha_{ii}\delta_{ij}$), one should not inherently assume that any of the tensor elements vanish. This introduces new cross terms into the Gilbert damping for a two-sublattice LLG equation of the form $\boldsymbol{\tau}_{\mathrm{GD}}^{(1)} \sim \alpha_{12} \mathbf{m}_1 \times \dot{\mathbf{m}}_2$ and $\boldsymbol{\tau}_{\mathrm{GD}}^{(2)} \sim \alpha_{21} \mathbf{m}_2 \times \dot{\mathbf{m}}_1$ [59]. These cross terms are not accounted for in the works presented in this thesis. The model that we have used is based on the work by Cheng et al. [60], where $\alpha_{11} = \alpha_{22} \equiv \alpha$ and $\alpha_{12} = \alpha_{21} = 0$. We will return to this discussion in the next chapter, where we discuss the concept of spin pumping from antiferromagnets. We will argue that the difference between the models does not necessarily entail any significant changes in the main results and conclusions of the papers relying on the model by Cheng et al.

The antiferromagnetic LLG equation in Eq. (2.13) can be transformed into the $\mathbf{m}$, $\mathbf{n}$ basis through a substitution of variables. Using the definitions in Eq. (2.1), the LLG equation becomes

$$\begin{pmatrix} \dot{\mathbf{m}} \\ \dot{\mathbf{n}} \end{pmatrix} = \begin{pmatrix} \frac{1}{2}\boldsymbol{\omega}_m \times \mathbf{m} + \frac{1}{2}\boldsymbol{\omega}_n \times \mathbf{n} + \alpha\mathbf{m} \times \dot{\mathbf{m}} + \alpha\mathbf{n} \times \dot{\mathbf{n}} \\ \frac{1}{2}\boldsymbol{\omega}_m \times \mathbf{n} + \frac{1}{2}\boldsymbol{\omega}_n \times \mathbf{m} + \alpha\mathbf{m} \times \dot{\mathbf{n}} + \alpha\mathbf{n} \times \dot{\mathbf{m}} \end{pmatrix}, \tag{2.15}$$

where we have introduced the frequency vectors $\boldsymbol{\omega}_m = -\frac{|\gamma|}{M}\delta f/\delta\mathbf{m}$ and $\boldsymbol{\omega}_n = -\frac{|\gamma|}{M}\delta f/\delta\mathbf{n}$ that correspond to the effective fields.

## 2.5   Antiferromagnetic resonance

### 2.5.1   Linear response

Finding a general analytic solution of the antiferromagnetic LLG equation can be difficult because we have a system of 6 coupled nonlinear differential equations. However, as the differential equations are all first order in time, we are able to find a solution if we can linearize the equations. For instance, we can linearize the equations by assuming that the dynamical response of the system is a small offset from some equilibrium value. We use the ansatz that the average magnetization and Néel order parameter can be written as

$$\mathbf{m}(t) = \mathbf{m}_0 + \delta\mathbf{m}(t), \quad \mathbf{n}(t) = \mathbf{n}_0 + \delta\mathbf{n}(t). \tag{2.16}$$

If we consider the system below the spin-flop transition ($\mathbf{H_0} < \mathbf{H}_{\text{sf}}$) and assume that the $z$ axis is the easy axis, we have that the equilibrium values $\mathbf{m_0}$ and $\mathbf{n_0}$ are $\mathbf{m_0} = \mathbf{0}$ and $\mathbf{n_0} = \hat{\mathbf{z}}$. Furthermore, the linear response ansatz requires that $|\delta\mathbf{m}(t)|, |\delta\mathbf{n}(t)| \ll 1$. To linearize Eq. (2.15), we then only keep terms up to the first order in $\delta\mathbf{m}(t)$ and $\delta\mathbf{n}(t)$.

Let us now consider the response from a small oscillating magnetic field $\mathbf{h}(t)$ for an antiferromagnet with a uniaxial easy-axis anisotropy. If we consider a spatially uniform magnetization within each sublattice, which we will call the *sublattice macrospin mode*, the free energy density of the system under consideration can be written as

$$f = \left|\tilde{J}_{\text{ex}}\right| M^2 \left(\mathbf{m}^2 - \mathbf{n}^2\right) - \left|K_\alpha\right| M^2 \left(m_z^2 + n_z^2\right) - 2M\left[h_x m_x + h_y m_y + (H_0 + h_z)m_z\right]$$
$$\equiv \frac{M}{|\gamma|}\left\{\omega_E\left(\mathbf{m}^2 - \mathbf{n}^2\right) - \omega_\parallel\left(m_z^2 + n_z^2\right) - 2\left[\omega_x m_x + \omega_y m_y + (\omega_H + \omega_z)m_z\right]\right\}.$$
$$(2.17)$$

Here, we introduced the frequencies $\omega_E$, $\omega_\parallel$, and $\omega_H$, which describe the strengths of the exchange, easy-axis anisotropy, and Zeeman interactions, respectively. We have also introduced the frequencies $\omega_i$ ($i = x, y, z$), which describe the strength of the $i$-th component of the oscillating magnetic field, which is our dynamical source. Next, we perform a Fourier transform of the time-dependent parameters in our system ($\delta\mathbf{m}(t), \delta\mathbf{n}(t), \mathbf{h}(t)$), defined by

$$g(t) \equiv \frac{1}{2\pi}\int_{-\infty}^{\infty} \mathrm{d}\omega\, \hat{g}(\omega)e^{i\omega t}. \tag{2.18}$$

The antiferromagnetic LLG equation can then be reduced to a set of 4 nontrivial linear equations:

$$\frac{1}{2\pi}\int_{-\infty}^{\infty} \mathrm{d}\omega\, e^{i\omega t}\underline{\chi}^{-1}\begin{pmatrix}\hat{m}_x \\ \hat{m}_y \\ \hat{n}_x \\ \hat{n}_y\end{pmatrix} = \frac{1}{2\pi}\int_{-\infty}^{\infty} \mathrm{d}\omega\, e^{i\omega t}\begin{pmatrix}0 \\ 0 \\ \hat{\omega}_y \\ -\hat{\omega}_x\end{pmatrix}, \tag{2.19}$$

where $\underline{\chi}^{-1}$ is the inverse susceptibility given by

$$\underline{\chi}^{-1} = \begin{pmatrix} i\omega & \omega_H & 0 & i\alpha\omega + \omega_\parallel \\ -\omega_H & i\omega & -i\alpha\omega - \omega_\parallel & 0 \\ 0 & i\alpha\omega + 2\omega_E + \omega_\parallel & i\omega & \omega_H \\ -i\alpha\omega - 2\omega_E - \omega_\parallel & 0 & -\omega_H & i\omega \end{pmatrix}. \tag{2.20}$$

Let us consider a case where the applied magnetic field oscillates harmonically with a fixed frequency $\omega_{\mathrm{rf}}$ such that $\mathbf{h}(t) = \mathbf{h}e^{i\omega_{\mathrm{rf}}t}$. The time dependence of the magnetic moments will be that of the source, and the solution to the antiferromagnetic LLG equation is then

$$\begin{pmatrix} \hat{m}_x \\ \hat{m}_y \\ \hat{n}_x \\ \hat{n}_y \end{pmatrix} = \chi(\omega \to \omega_{\mathrm{rf}}) \begin{pmatrix} 0 \\ 0 \\ \hat{\omega}_y \\ -\hat{\omega}_x \end{pmatrix} . \qquad (2.21)$$

Note that in linear response, a dynamical source along the magnetic moments (i.e. an oscillating magnetic field $h_z$ along the easy axis) has no effect; this only contributes when one includes terms to the second order or higher. Similarly, the dynamical response in the antiferromagnet is just perpendicular to the easy axis in linear response because this is the direction in which it is easiest to create excitations.

### 2.5.2   Resonance modes of antiferromagnets

We have now seen that the susceptibility of the antiferromagnet, meaning how large the dynamical response is for a given source, depends on the frequency of the applied source. The frequencies at which this susceptibility obtains its maxima are called the *resonance frequencies* of the system. If we assume that the damping of the system is sufficiently small to not affect the resonance frequencies significantly, we can set $\alpha = 0$. Without dissipation, the susceptibility diverges at resonance in the linear response model. We can use this to determine the resonance frequencies through the condition $\det\left(\chi^{-1}\right) = 0$. The resonance frequencies of the uniaxial easy-axis antiferromagnet are then found to be

$$|\omega_{\mathrm{res}}| = \sqrt{\omega_\parallel(2\omega_E + \omega_\parallel)} \pm \omega_H . \qquad (2.22)$$

The eigenvectors of $\chi^{-1}$ describe how the magnetization and Néel order parameter will precess in the absence of dissipation and a dynamical source. By calculating these eigenvectors, one can find that the resonance modes are circularly polarized, where the mode corresponding to the high-resonance frequency in Eq. (2.22) has a right-handed circular polarization with respect to the external magnetic field $\mathbf{H}_0$, and the mode corresponding to the low-resonance frequency has a left-handed polarization. Moreover, from the eigenvectors, one can also find that the precession in the net magnetization is typically much smaller than that in the Néel order parameter:

$$|m_{x,y}| = \sqrt{\frac{\omega_\parallel}{2\omega_E + \omega_\parallel}} |n_{x,y}| . \qquad (2.23)$$
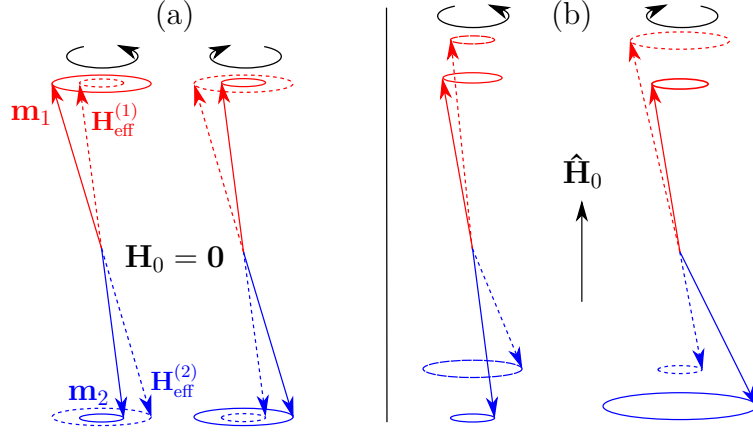
**Figure 2.6.** Antiferromagnetic resonance modes for different magnetic fields [61].
The red and blue solid arrows denote the directions of $\mathbf{m}_1$ and $\mathbf{m}_2$, respectively,
and the dashed arrows show the respective effective fields $\mathbf{H}_{\text{eff}}^{(1,2)}$. The black circular
arrows denote the precession direction of all the arrows below. (a) In the zero external
magnetic field, we have a symmetry along the easy axis, and the left- and right-
handed resonance modes have the same energy/resonance frequency. (b) By applying
a magnetic field along the easy axis, the symmetry along the easy axis is broken.

Because the magnetic anisotropy is typically much weaker than the exchange energy
($\omega_\parallel \ll \omega_E$), one can therefore disregard higher-order contributions in $m_{x,y}$ in the
exchange approximation.

The two antiferromagnetic resonance modes are illustrated for zero and finite
magnetic fields in Fig. 2.6. Under zero applied magnetic field, the resonance fre-
quencies of the two modes are degenerate. When there is no external magnetic field
to break the inversion symmetry along the easy axis, the two resonance modes are
mirror images of each other (with the mirror plane being perpendicular to the easy
axis): their resonance frequencies are the same, but they have opposite polariza-
tions/chiralities. Once the inversion symmetry along the easy axis is broken by the
application of a magnetic field, as shown in Fig. 2.6 (b), the resonance modes are also
no longer inversion symmetric and become nondegenerate. To understand the dis-
tinction of the two resonance modes, it can be beneficial to consider each resonance
mode to be "driven" by one of the magnetic sublattices [62]. This can be understood
as follows. In Fig. 2.6 (b), we apply a magnetic field along the equilibrium direction
of $\mathbf{m}_1$, which increases the magnitude of the effective field $\mathbf{H}_{\text{eff}}^{(1)}$. Because of this in-
crease in the effective field for the first sublattice, $\mathbf{m}_1$'s desired precession frequency
increases accordingly, as we recall that the Larmor frequency increases linearly with

the magnetic field strength. Conversely, for the second sublattice, the opposite is true. The external magnetic field counteracts the effective magnetic field at this sublattice, thereby reducing its magnitude and $\mathbf{m}_2$'s desired precession frequency. This explains the lifting of the degeneracy of the antiferromagnetic resonance frequencies in the presence of a magnetic field. In the high-frequency mode, $\mathbf{m}_1$ drives the resonance by oscillating at its preferred higher resonance. Since the effective field $\mathbf{H}_{\mathrm{eff}}^{(2)}$ strongly depends on the direction of $\mathbf{m}_1$ due to the exchange interaction, this also precesses with $\mathbf{m}_1$'s frequency, thereby forcing $\mathbf{m}_2$ to precess at the same rate as $\mathbf{m}_1$. However, since $\mathbf{m}_2$ prefers oscillating at a slower rate, the dynamical response (i.e. the precession angle away from its equilibrium direction) is smaller for $\mathbf{m}_2$ compared to that of $\mathbf{m}_1$ for the high-frequency mode. A similar picture can be made for the scenario when $\mathbf{m}_2$ drives the resonance, which corresponds to the low-frequency resonance mode.

### 2.5.3   The critical behavior at the spin-flop transition

In addition to the applied magnetic field splitting the resonance frequency degeneracy, it also affects the precession amplitudes of the sublattice magnetizations. It costs more energy for the magnetization to move away from the effective field direction when the effective field is stronger. Consequently, the high-resonance mode (where the resonance is driven by the sublattice magnetization with the strongest effective field) should have smaller precession amplitudes than the low-resonance mode for a fixed strength of the applied dynamical source. In fact, for uniaxial easy-axis antiferromagnets, the precession amplitudes in frequency space can be shown to be inversely proportional to the resonance frequency. If we consider the resonance frequencies in Eq. (2.22), as we approach the spin-flop field corresponding to $\omega_H = \sqrt{\omega_\parallel(2\omega_E + \omega_\parallel)}$, the low-frequency resonance mode goes to having zero frequency. In other words, fluctuations that drive the sublattice magnetizations away from the equilibrium position along the easy axis cost no energy at this field strength. At this point, the precession amplitudes of the magnetic moments become very large (in fact, they diverge, which is due to our linear response ansatz breaking down at this point). This explains the spin-flop phase transition, where the magnetic moments suddenly "flop" away from the easy axis, as shown in Fig. 2.4. Because of the low energy cost for creating fluctuations near the spin-flop transition, we expect the region just below it to be optimal for having large precession amplitudes of the magnetic moments. In the next chapter, we will consider some scenarios where this effect can be utilized in a beneficial manner.

# 3

# Spin dynamics in multilayer heterostructures

In the introduction, we discussed how information can be transported via spin waves in magnetic insulators. However, there are no good approaches for directly detecting these spin waves. At present, a common technique for measuring the spin signal is to convert it into an electrical signal, which is easier to measure experimentally. Because the magnetic insulator cannot carry an electrical current, we must therefore combine the magnetic insulator with a different material with other properties, forming a heterostructure. Now that we have studied the magnetization dynamics in an antiferromagnetic insulator in the previous chapter, we will examine what happens to the spin signal in these heterostructures. Specifically, we will study how these other materials can be used to both generate and detect spin signals in magnetic insulators.

## 3.1   Charge currents and spin currents

In spintronics, we consider the transport of both spin and charge degrees of freedom of the electron. It is beneficial to briefly consider what this means in a physical
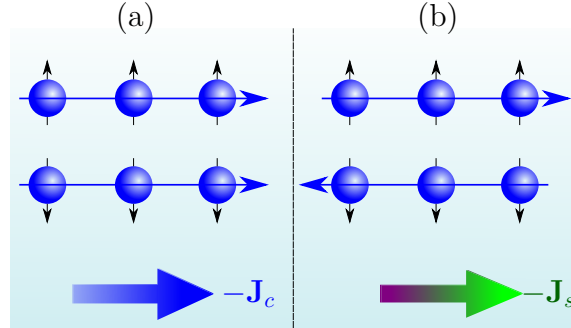
**Figure 3.1.** (a) An unpolarized (net spin equal to zero) charge current $-\mathbf{J}_c$ of electrons is moving to the right. (b) A pure spin current (net charge equal to zero) $-\mathbf{J}_s$ of electron spins is moving to the right. The negative signs on the currents are due to the particles being electrons that have a negative charge, whereas the common definition of currents is with positively charged particles. Note that a spin current is, strictly speaking, a tensor product between the current direction and the spin polarization direction, although we only illustrate the current direction here.

picture. In conventional electronics, the information is passed through *charge currents* $\mathbf{J}_c$, where a net amount of charge is transported in one direction, as illustrated in Fig. 3.1 (a). Normally, in charge currents, we only have electrons carrying their negative charge in one direction. However, if we also had positively charged particles in a charge current, these would be transported in the opposite direction compared to the electrons. In other words, a positive charge current to the right can either be caused by positively charged particles moving to the right or negatively charged particles moving to the left.

A spin current $\mathbf{J}_s$ is defined analogously to a charge current, but there is now a net transport of spin (or angular momentum) instead of charge. Whereas opposite charges move in opposite directions in the charge current, antiparallel spins move in opposite directions in the spin current, as illustrated in Fig. 3.1 (b). Mathematically, the spin current is slightly different from the charge current. As charge is a scalar, the charge current can effectively be described as a vector. However, spin and angular momentum have a direction in addition to a scalar magnitude, and a spin current must therefore be described by the tensor product between the spin polarization axis and the transport direction of the spins.

Spin and charge are two independent properties of an electron, and we can therefore have currents with varying degrees of overlap between charge and spin

currents. In Fig. 3.1 (a), we have a net transport of charge but a zero net transport of spin, which is called an *unpolarized charge current*. However, if we flip one of the electron spins in Fig. 3.1 (a), e.g. we flip one of the down spins to be spin up, we would then have four electrons with spin up and two electrons with spin down moving to the right. In this case, we also have a net transport of spin in addition to charge, which is then referred to as a *polarized charge current*. If all the electrons moving in one direction have parallel spin, it is often referred to as a fully polarized charge current. In Fig. 3.1 (b), we have no net transport of charge but a net transport of spin, which is called a *pure spin current*. Although the electrons in Fig. 3.1 (b) are moving, spin currents can also be carried by stationary electrons. The spins interact through the exchange interaction in magnetic materials. If we then perturb one of the electron spins, this perturbation will propagate to the neighboring spins, thereby carrying a spin current. In magnetic insulators where there are no free electrons moving, we can then suppress the motion of the electrons but still transport information through a pure spin current. This situation was illustrated in Fig. 1.4 in Section 1.2.2.

## 3.2   Spin Hall effect and inverse spin Hall effect

### – Conversion between charge and spin currents

Spin currents can be more energy efficient than charge currents, but they do have some disadvantages compared to charge currents. Charge currents are easy to generate and detect through either applying or detecting a voltage bias to a conductor. The same is not true for spin currents because there currently are no direct methods for generating or detecting a local spin bias that are as practical as the methods utilized in electronics. However, in some materials, it is possible to convert charge currents into spin currents and vice versa through the *spin Hall effect* and *inverse spin Hall effect*. We can then generate and detect spin currents by using charge currents as the "middle man" in an intermediary process.

The spin Hall effects occur in materials with strong spin-orbit coupling, such as the heavy metals platinum (Pt) [63, 64], tungsten (W) [65, 66], and tantalum (Ta) [67]. The spin Hall effects are typically divided into an extrinsic part and an intrinsic part. The extrinsic part is due to spin-dependent scattering with impurities in the material [68, 69], whereas the intrinsic part is due to an interaction between the momentum and spin of the conduction electrons [70] and does not require impurities
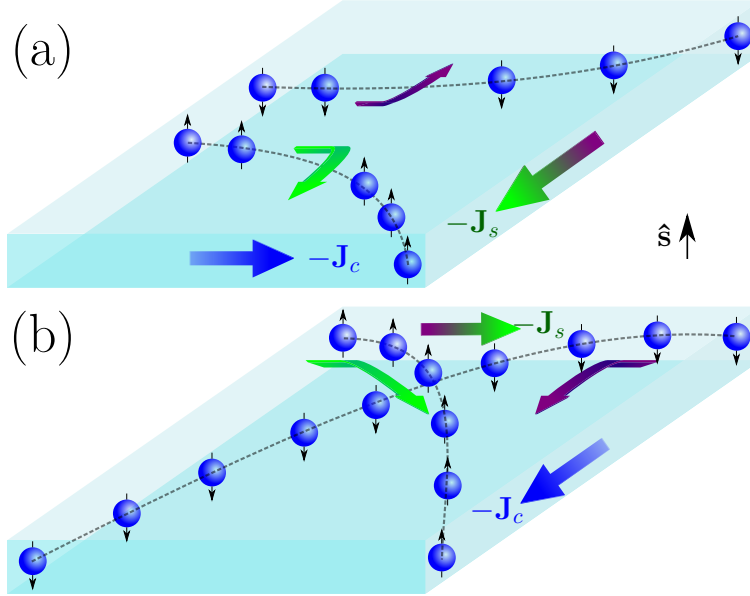
**Figure 3.2.** Illustration of the (a) spin Hall effect and (b) inverse spin Hall effect. In the spin Hall effect, a charge current $\mathbf{J}_c$ leads to a spin current $\mathbf{J}_s$ that is perpendicular to the charge current and the spin polarization axis $\hat{\mathbf{s}}$. The inverse spin Hall effect is the reciprocal effect that leads to a conversion of a spin current to a charge current. These effects can, for instance, be caused by spin-orbit coupling inside the material.

in the system. The intrinsic spin Hall effect originates from spin-orbit coupling, where electrons with antiparallel spins prefer to move in opposite directions, as can be understood from Fig. 2.3. In both the extrinsic and intrinsic parts of the spin Hall effects, opposite spins are, on average, scattered or deflected in opposite directions.

The spin Hall effect is illustrated in Fig. 3.2 (a), where the spins in an unpolarized charge current are deflected in opposite directions, giving rise to a spin current that is perpendicular to the charge current. The efficiency of this conversion is typically given in terms of the *spin Hall angle* $\theta_{\mathrm{SH}}$, which is defined through the relation

$$\frac{\mathbf{J}_s^{\mathrm{SHE}}}{\hbar/2} = \theta_{\mathrm{SH}} \frac{\mathbf{J}_c \times \hat{\mathbf{s}}}{e} \, , \tag{3.1}$$

where $\mathbf{J}_s^{\mathrm{SHE}}$ is the spin current with a spin polarization direction $\hat{\mathbf{s}}$ resulting from the spin Hall effect and $\mathbf{J}_c$ is the charge current. Each current is divided by its transport quantity, i.e. the charge current is divided by the electron charge $e$ and

the spin current by the electron spin $\hbar/2$ such that the currents are expressed as simple time rates. The spin Hall angle is then a dimensionless number that provides an indication about how large a percentage of the charge current is converted to a spin current.

The inverse spin Hall effect is, as its name suggests, the reciprocal effect to the spin Hall effect, where a charge current is induced perpendicularly to a spin current, as illustrated in Fig. 3.2 (b). The mechanism for the inverse spin Hall effect is exactly the same as that for the spin Hall effect. The conversion efficiency $\theta_{\mathrm{SH}}$ from the charge current to the spin current in the spin Hall effect is also identical to the conversion efficiency from spin current to charge current in the inverse spin Hall effect. Consequently, the charge current resulting from the inverse spin Hall effect is given by

$$\frac{\mathbf{J}_c^{\mathrm{ISHE}}}{e} = \theta_{\mathrm{SH}} \frac{\mathbf{J}_s \times \hat{\mathbf{s}}}{\hbar/2} \, . \tag{3.2}$$

Now that we have seen how spin and charge currents can be converted to one another through the spin Hall effects in heavy metals, we will begin to study heterostructures of heavy metals and magnetic insulators and show how the heavy metal layers can be used as detectors and generators of spin currents in magnetic insulators.

## 3.3   Spin pumping

In addition to the spin Hall effect, another way to generate a spin current is through *spin pumping.* In heterostructures that consist of a magnetic material and a nonmagnetic material, a precession of the magnetization in the magnetic layer can transfer nonequilibrium angular momentum from the electrons in the magnetic material to the electrons in the nonmagnetic material. This process is known as spin pumping [71] and leads to an injection of a spin current into the nonmagnetic material. This spin current can, for instance, be generated by driving the magnetization at resonance by an oscillating magnetic field, as we considered in Section 2.5. Spin pumping is illustrated in Fig. 3.3. If we inject this spin current into a conducting material with strong spin-orbit coupling, such as platinum, we can then detect the spin current through the inverse spin Hall effect. The heavy metal layer can then be used to detect the presence of a spin current in the magnetic insulator. Moreover, by detecting the pumped spin current, we can also obtain information such as the magnetic resonance frequency and the linewidth of the resonance peaks, thereby providing a means to probe the magnetization dynamics.
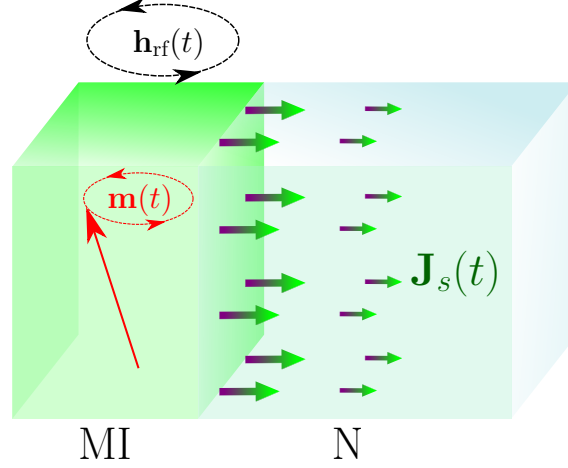
**Figure 3.3.** A precessing magnetic moment $\mathbf{m}(t)$ in a magnetic insulator (MI) can pump a spin current $\mathbf{J}_s$ into a normal metal (N), which acts as a spin sink. The spin pumping can be sustained by driving the magnetic moments at resonance by an oscillating magnetic field $\mathbf{h}_{\mathrm{rf}}(t)$. Without a dynamical source for the magnetization dynamics, the transfer of angular momentum to the spin sink causes the magnetic moment to relax towards equilibrium, thereby acting as an enhanced damping of the magnetization dynamics [71].

### 3.3.1   Spin pumping from ferromagnets

The pumped spin current from a ferromagnetic material is given by [71]

$$\mathbf{I}_s^{\mathrm{pump}}(t) = \frac{\hbar}{4\pi} \left[ \mathrm{Re}(g_\perp)\mathbf{m}(t) \times \dot{\mathbf{m}}(t) - \mathrm{Im}(g_\perp)\dot{\mathbf{m}}(t) \right] , \qquad (3.3)$$

where $g_\perp$ is the *transverse spin conductance* (also commonly referred to as the *spin-mixing conductance* $g^{\uparrow\downarrow}$) across the magnetic insulator/normal metal interface. The real part of transverse spin conductance is a measure of how many electron spins are pumped across the interface per precession cycle of the magnetization. Henceforth, we assume that $\mathrm{Im}(g_\perp) = 0$ because it is negligible in many materials [71]. The remaining term proportional to the real part of the transverse spin conductance is then of the same form as the Gilbert damping in the LLG equation in Eq. (2.12). Consequently, spin pumping leads to an enhanced damping of the magnetization dynamics at magnetic interfaces [71]. This can be understood quite intuitively: when the magnetic material pumps nonequilibrium spins into the adjacent material acting as a spin sink, conservation of angular momentum requires that the magnetization relaxes towards equilibrium. Note that the pumped spin current $\mathbf{I}_s^{\mathrm{pump}}$ is not defined

analogously to the spin current $\mathbf{J}_s$ in the previous section: whereas $\mathbf{J}_s$ is defined as the propagation direction of the spin current with polarization $\hat{\mathbf{s}}$, $\mathbf{I}_s^{\mathrm{pump}}$ is defined along the direction of the spin current polarization. The propagation direction of the pumped spin current is along the interface normal, in the direction pointing away from the magnetic material.

To obtain a better understanding of the contributions from the pumped spin current, we will consider a brief example. Let us assume the magnetization to be of the form $\mathbf{m}(t) \approx (\delta m_x(t), \delta m_y(t), 1)$, where $\delta m_x(t), \delta m_y(t) \ll 1$, and that $\delta m_x(t) = \delta m_x \cos(\omega t)$, $\delta m_y(t) = \delta m_y \sin(\omega t + \phi)$. We then have that the pumped spin current is

$$\mathbf{I}_s^{\mathrm{pump}}(t) \approx \frac{\hbar}{4\pi} \operatorname{Re}(g_\perp)\mathbf{m}(t) \times \dot{\mathbf{m}}(t) = \frac{\hbar\omega}{4\pi} \operatorname{Re}(g_\perp) \begin{pmatrix} -\delta m_y \cos(\omega t + \phi) \\ -\delta m_x \sin(\omega t) \\ \delta m_x \delta m_y \cos(\phi) \end{pmatrix}. \qquad (3.4)$$

We see that the pumped spin current has two different types of contributions. In the $x$ and $y$ components, we have a time-dependent contribution that is first order in $\delta m_x$, $\delta m_y$, which is denoted as the AC pumped spin current. The AC pumped spin current can be difficult to detect because its time average vanishes. It is, however, a means of generating an oscillating spin current in an adjacent spin sink. The $z$ component of the pumped spin current, on the other hand, is fully independent of time and is second order in $\delta m_x$, $\delta m_y$, which is denoted as the DC pumped spin current. Note that the area that the precessions enclosed in the $xy$ plane can be found to be $A = \pi \delta m_x \delta m_y |\cos(\phi)|$. From this and Eq. (3.4), one can find that the DC spin pumping is directly proportional to the area enclosed by the precessions and the frequency of the precessions. In other words, if we have a linear precession of the magnetization, where the magnetic moment precesses along a line and thereby does not enclose an area, the corresponding DC pumped spin current vanishes completely.

### 3.3.2 Spin pumping from antiferromagnets

Spin pumping is an interfacial effect and therefore highly depends on the magnetic structure at the interface. For antiferromagnets, there are two general types of interfaces that one typically considers, denoted as uncompensated and compensated interfaces. These interfaces are depicted in Fig. 3.4.

For the case of uncompensated interfaces, where only one magnetic sublattice is present at the interface, spin pumping in antiferromagnets becomes completely analogous to spin pumping in ferromagnets [60]. The magnetization $\mathbf{m}(t)$ in Eq.
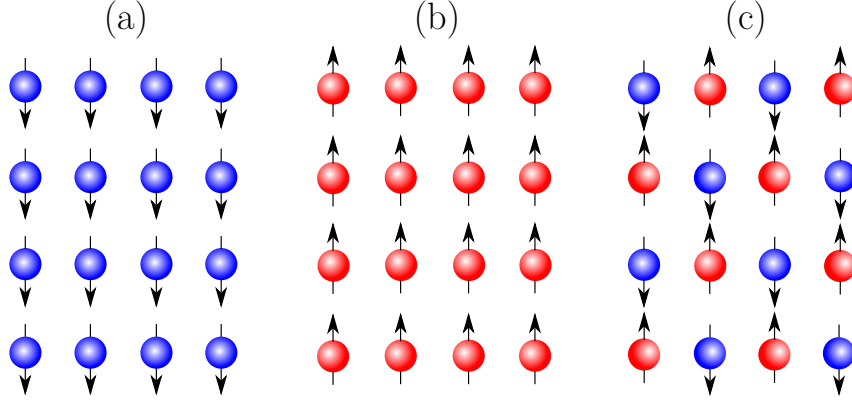
**Figure 3.4.** The figures show the spin structures of the atoms at the antiferromagnetic interface. (a) and (b) are interfaces with only one sublattice present. These are called *uncompensated interfaces*. (c) is an interface with both magnetic sublattices present in a chessboard pattern. This is called a *compensated interface*, as the magnetic moment at the interface is compensated. This figure is from the supplementary material to Paper [4].

(3.3) is then replaced by the sublattice magnetization $\mathbf{m}_{1/2}(t)$ that is present at the interface.

What is more unique to spin pumping from antiferromagnets is the case of spin pumping at compensated interfaces, such as in Fig. 3.4 (c). Both sublattice magnetizations will then contribute to the spin pumping, and the question is then whether the two magnetic sublattices pump spin constructively or destructively. As mentioned in the previous subsection for ferromagnetic spin pumping, when the imaginary part of the transverse spin conductance is negligible, spin pumping takes the form of enhanced Gilbert damping at magnetic interfaces. Following the discussion of Gilbert damping in antiferromagnets from Section 2.4.2, the general form of spin pumping from antiferromagnets can then be expressed as [57]

$$\mathbf{I}_s^{\text{pump}}(t) \approx \frac{\hbar}{4\pi} \sum_{i,j=1,2} \text{Re}(g_\perp^{ij}) \mathbf{m}_i(t) \times \dot{\mathbf{m}}_j(t) \equiv \frac{\hbar}{4\pi} \sum_{\boldsymbol{\mu},\boldsymbol{\nu}=\mathbf{m},\mathbf{n}} \text{Re}(g_\perp^{\mu\nu}) \boldsymbol{\mu}(t) \times \dot{\boldsymbol{\nu}}(t) . \quad (3.5)$$

Here, $g_\perp^{ij}$ $(i,j=1,2)$ is a generalized tensor of the transverse spin conductance, and the definition of $g_\perp^{\mu\nu}$ $(\mu,\nu=m,n)$ follows from the definitions of $\mathbf{m}$ and $\mathbf{n}$ in Eq. (2.1). The theory of spin pumping from antiferromagnets was initially studied by Cheng et al. in Ref. [60]. In this work, Cheng et al. derived spin pumping from antiferromagnets by considering scattering theory in a nearest-neighbor tight-binding model for a perfectly matched interface. In this model, the nondiagonal

terms (often referred to as cross terms) proportional to $g_\perp^{12}$ and $g_\perp^{21}$ vanish, and the spin pumping in the basis of $\mathbf{m}$ and $\mathbf{n}$ can be expressed via the relations $g_\perp^{mm} = g_\perp^{nn} = g_\perp^{11} + g_\perp^{22}$ and $g_\perp^{mn} = g_\perp^{nm} = 0$. Spin pumping from antiferromagnets and ferrimagnets was further studied by Kamra and Belzig in Ref. [57]. The results from the work of Kamra and Belzig differ quite significantly from those of Cheng et al. Notably, Kamra and Belzig found that the nondiagonal (cross) terms are finite: $g_\perp^{12} = g_\perp^{21} = \sqrt{g_\perp^{11} g_\perp^{22}}$. This finding has a noteworthy effect on the transverse spin conductance in the $\mathbf{m}$ and $\mathbf{n}$ basis. Kamra and Belzig showed that the transverse spin conductances are then given by $g_\perp^{mm} = (\sqrt{g_\perp^{11}} + \sqrt{g_\perp^{22}})^2$, $g_\perp^{nn} = (\sqrt{g_\perp^{11}} - \sqrt{g_\perp^{22}})^2$, and $g_\perp^{mn} = g_\perp^{nm} = g_\perp^{11} - g_\perp^{22}$. In the special case of a perfectly ordered compensated interface with an isotropic contribution from both sublattices ($g_\perp^{11} = g_\perp^{22}$), the models by Cheng et al. and Kamra and Belzig yield entirely different results. One would expect the spin pumping to be dominated by the Néel order parameter in the model by Cheng et al., but this contribution vanishes exactly ($g_\perp^{nn} = 0$) in the model by Kamra and Belzig. It does become finite, however, if disorder or an anisotropy in the transverse spin conductance of the two sublattices ($g_\perp^{11} \neq g_\perp^{22}$) is introduced. The discrepancy between the two models provides a large incentive to study the dependence of spin pumping from antiferromagnets on the sublattice structure at the interface. The physics underlying the difference between the two models can partly be understood through the discussion of a related problem in Chapter 6, Section 6.3.2.

While spin pumping in ferromagnets is now a very common technique, spin pumping has yet to be unequivocally detected from antiferromagnets. An experiment studying the antiferromagnetic material $MnF_2$ has, however, detected a small contribution to the overall signal compatible with the behavior of spin pumping, but further investigation is required to confirm the physical origin of the signal [62, 72]. Because of the challenges in detecting spin pumping from antiferromagnets, one has to be able to find a way to obtain a sufficiently strong spin pumping signal before one can study other aspects, such as how the pumped spin current depends on the interface. The first publication in this thesis [1] studies how the spin pumping from antiferromagnets depends on the different contributions to the micromagnetic energy to examine how one can maximize the spin pumping signal sufficiently to be able to detect it in experiments. We found that the spin pumping signal is expected to be significantly enhanced near the spin-flop transition for uniaxial easy-axis antiferromagnets. This enhancement occurs for the low-frequency mode as the resonance frequency approaches zero. This is in contrast to what was predicted earlier, as one

expected the spin pumping from antiferromagnets to be large due to its fast dynamics [60]. This expectation was based on the fact that the pumped spin current is directly proportional to the frequency of the magnetization dynamics. However, as we just showed for ferromagnets, the DC pumped spin current is also proportional to the area enclosed by the precession of the magnetic moments. At the end of the previous chapter, we mentioned that at resonance, the precession amplitudes in uniaxial easy-axis antiferromagnets are inversely proportional to the resonance frequency. In other words, the enclosed area is proportional to $1/\omega^2$, and the DC pumped spin current is then proportional to $1/\omega$. In linear response, the spin pumping current is therefore expected to diverge near the spin-flop transition in easy-axis antiferromagnets, where the resonance frequency approaches zero.

The model used in Paper [1] (as well as in Paper [2], which is discussed later this chapter) relies on the results of Cheng et al. and considers a compensated interface such that the spin pumping is primarily governed by the Néel order parameter. At first glance, it might appear that the discoveries of Kamra and Belzig discussed earlier in this section could invalidate the model and results in Papers [1, 2]. However, while the spin pumping from the Néel order parameter vanishes exactly in the ideal case in the results of Kamra and Belzig, for a more realistic system with some imperfections, this will still be finite, and the results in Papers [1, 2] can then be described by a renormalization of the parameters. Moreover, if one were to modify the system in these papers to have an uncompensated interface instead of a compensated interface, the results would not change in a significant manner. The dynamics and magnetic susceptibilities in the antiferromagnetic insulator very weakly depend on the interface structure, as the spin pumping is merely a perturbation of the system. Consequently, the only difference should be the spin current pumped into (or absorbed from) the normal metal. However, this should be similar in magnitude for an uncompensated interface in the model by Kamra and Belzig and for a compensated interface in the model by Cheng et al. The two models of antiferromagnetic spin pumping are also in agreement for uncompensated interfaces, where spin pumping from antiferromagnets becomes analogous to spin pumping from ferromagnets [60].

## 3.4 Spin diffusion

When a spin current is generated in a normal metal through the spin Hall effect or by spin pumping from a magnetic insulator into the normal metal, there is a

buildup of a nonequilibrium *spin accumulation* $\boldsymbol{\mu}_s$ inside the normal metal. The spins undergo a diffusive motion given by the spin diffusion equation [73]

$$\frac{\partial \boldsymbol{\mu}_s(\mathbf{r},t)}{\partial t} = |\gamma| \, \mathbf{H}_0 \times \boldsymbol{\mu}_s(\mathbf{r},t) + D_N \boldsymbol{\nabla}^2 \boldsymbol{\mu}_s(\mathbf{r},t) - \frac{\boldsymbol{\mu}_s(\mathbf{r},t)}{\tau_{\text{sf}}}. \tag{3.6}$$

Here, $\gamma$ is the gyromagnetic ratio, $\mathbf{H}_0$ is an external magnetic field, $D_N$ is the diffusion coefficient, and $\tau_{\text{sf}}$ is the spin-flip relaxation time. In a zero magnetic field and when the spin-flip relaxation time is infinite, the spin diffusion equation is analogous to the heat equation. The additional term depending on the magnetic field is a Larmor precession of the spin accumulation, similar to the term appearing in the LLG equation. The last term, which is inversely proportional to $\tau_{\text{sf}}$, leads to a decay of the spin accumulation due to decoherence from relaxation processes. If $\tau_{\text{sf}}$ is much smaller than the other time scales in the system, such as the Larmor precession time $1/|\gamma \mathbf{H}_0|$ and the time evolution of $\boldsymbol{\mu}_s$, we can approximate the spin diffusion equation by the Helmholtz equation

$$\boldsymbol{\nabla}^2 \boldsymbol{\mu}_s(\mathbf{r},t) = \frac{\boldsymbol{\mu}_s(\mathbf{r},t)}{\lambda_{\text{sd}}^2}. \tag{3.7}$$

Here, we introduced the spin-diffusion length $\lambda_{\text{sd}} = \sqrt{D_N \tau_{\text{sf}}}$. This is often a good approximation because the spin-flip relaxation time is for many materials significantly shorter than the time scales of the Larmor precession and magnetic resonance [74]. The differential equation is now independent of time. The time dependence of the spin accumulation then enters through the boundary or initial conditions. This can, for instance, be given by the spin pumping rate or by the frequency of an applied current to the metal.

## 3.5 Spin-transfer torque

When there is an accumulation of spins at the interface of the magnetic insulator due to e.g. a spin current in the adjacent layer, this leads to a torque acting on the magnetization in the magnetic insulator. Just as the magnetic insulator can transfer spin/angular momentum to the normal metal via spin pumping, one can also transfer angular momentum from the normal metal to the magnetic insulator by injecting a spin current. This reciprocal effect is known as a *spin-transfer torque*. Note that this torque is not quite the same as the spin-transfer torque studied by Berger and Slonczewski, as discussed in the introduction to this thesis. The torque studied by Berger and Slonczewski considered the transfer of angular momentum

from conduction electrons to the local magnetization when a polarized charge current passes through a conducting magnetic layer. Here, however, as the magnetic material is insulating, the spin-transfer torque results from a spin accumulation $\boldsymbol{\mu}_s(t)$ at the magnetic interface exerting a torque on the magnetization. The transfer of angular momentum from the normal metal to a ferromagnetic insulator is given by the backflow current

$$\mathbf{I}_s^{\text{backflow}}(t) = -\frac{\text{Re}(g_\perp)}{4\pi}\mathbf{m}(t) \times [\boldsymbol{\mu}_s(t) \times \mathbf{m}(t)] \ . \tag{3.8}$$

Note that $\mathbf{I}_s^{\text{backflow}}$ is defined analogously to $\mathbf{I}_s^{\text{pump}}$ and describes the polarization of the spin current rather than the direction of propagation. The propagation direction is assumed to be along the interface normal. We again disregarded the contribution from the imaginary part of the transverse spin conductance. In Papers [1, 2], we use the model that generalizes this result to two-sublattice systems such as antiferromagnets, where the spin-transfer on the two magnetic sublattices is treated as independent [60, 75]:

$$\mathbf{I}_s^{\text{backflow}}(t) = -\frac{\text{Re}(g_\perp)}{4\pi} \sum_{i=1,2} \mathbf{m}_i(t) \times [\boldsymbol{\mu}_s(t) \times \mathbf{m}_i(t)] \tag{3.9a}$$

$$= -\frac{\text{Re}(g_\perp)}{2\pi} \{\mathbf{m}(t) \times [\boldsymbol{\mu}_s(t) \times \mathbf{m}(t)] + \mathbf{n}(t) \times [\boldsymbol{\mu}_s(t) \times \mathbf{n}(t)]\} \ . \tag{3.9b}$$

This model then assumes that $g_\perp^{11} = g_\perp^{22} \equiv g_\perp$ and $g_\perp^{12} = g_\perp^{21} = 0$, equivalent to the model by Cheng et al. for spin pumping from antiferromagnets [60].

The spin current injected into the magnetic insulator due to spin-transfer torques can have different origins. In spin pumping experiments, one can have a backflow if the pumped spin current is injected into a normal metal that is not a perfect spin sink. This can, for example, occur when the normal metal layer is just a few nanometers thick. In such experiments, it is necessary to take the backflow spin current into account to obtain accurate experimental predictions [74]. One can also use spin-transfer torques as the dynamical source in magnetic resonance experiments. By applying a voltage to the normal metal, one injects a spin current into the magnetic insulator as the charge current is converted to a spin current through the spin Hall effect [2, 76].

## 3.6   Spin-orbit torques and crystal symmetries

Spin-transfer torques originate from a transfer of angular momentum from some source to the local magnetization. These sources can e.g. be a spin-polarized charge

current, as in the spin-transfer torques introduced by Berger and Slonczewski [22–28], or an accumulation of spins at a magnetic interface, as discussed in the previous section. However, if the magnetic material also has an intrinsic spin-orbit coupling and is electrically conducting, applying an unpolarized charge current to the material can also induce a nonequilibrium spin density that exerts torques on the magnetization that do not involve the transfer of angular momentum [77, 78]. These types of torques are denoted as *spin-orbit torques.*

In Ref. [79], Hals and Brataas developed a phenomenological description of the possible spin-orbit torques that were allowed by the underlying symmetry of the material. According to what is known as *Neumann's principle*, we must require that [80]

> *"any type of symmetry which is exhibited by the point group of the crystal is possessed by every physical property of the crystal."*

This is equivalent to requiring that the physical properties be invariant under all the symmetry transformations of the crystal. Consequently, a spin-orbit torque $\boldsymbol{\tau}$ in the extended Landau–Lifshitz–Gilbert equation

$$\dot{\mathbf{m}} = -\left|\gamma\right| \mathbf{m} \times \mathbf{H}_{\text{eff}} + \alpha \mathbf{m} \times \dot{\mathbf{m}} + \boldsymbol{\tau} \tag{3.10}$$

must be invariant under the symmetry operations that define the crystal symmetry group. Let us assume that the crystal is described by a set of unitary symmetry operations given by $\mathcal{R}^{(\alpha)}$ ($\alpha = 1, 2, 3 \ldots$) such as $n$-fold rotations and inversions along various axes, where we have that $\det(\mathcal{R}^{(\alpha)}) = \pm 1$ because all $\mathcal{R}^{(\alpha)}$ are unitary. The physical properties of the system can depend on different tensors, and these tensors can be divided into two main categories. These categories are *polar tensors* and *axial tensors*, and these transform under the unitary transformation $\mathcal{R}$ as [80]

$$\mathcal{T}^{\text{polar}}_{i'j'k'\ldots} = \mathcal{R}_{i'i}\mathcal{R}_{j'j}\mathcal{R}_{k'k}(\ldots)\mathcal{T}^{\text{polar}}_{ijk\ldots}\,, \tag{3.11a}$$

$$\mathcal{T}^{\text{axial}}_{i'j'k'\ldots} = \det(\mathcal{R})\mathcal{R}_{i'i}\mathcal{R}_{j'j}\mathcal{R}_{k'k}(\ldots)\mathcal{T}^{\text{axial}}_{ijk\ldots}\,. \tag{3.11b}$$

In the above notation, the Einstein summation convention is assumed. Examples of polar vectors (rank-1 tensors) are position, momentum, and charge currents, whereas examples of axial vectors are angular momentum, magnetization, and cross products of polar vectors. By performing a tensor expansion of the spin-orbit torque to the first order in the charge current density and higher orders in the magnetization and the magnetization gradient, Hals and Brataas classified the symmetry relations of the different components of the spin-orbit torque, similar to Eq. (3.11). This formalism

can be used to identify forms of the spin-orbit torque that are not described by the conventional LLG equation [81]. This technique was utilized in Paper [5] to describe the current-induced spin-orbit torques for a certain symmetry classification of two-dimensional ferromagnetic materials. We will return to this discussion in Chapter 7, where we examine the physics of Paper [5] in more detail.

## 3.7   Spin Hall magnetoresistance

In magnetic conductors, in addition to the charge current exerting a spin-orbit torque on the magnetic moments, the electric resistance of the charge current depends on the relative orientation of the current and the magnetization in ferromagnets [82] or the Néel order parameter in antiferromagnets [83]. This effect is known as *anisotropic magnetoresistance.* In hybrid structures that consist of a magnetic insulator and a normal metal with a significant spin Hall angle, there is also a recently discovered similar effect known as *spin Hall magnetoresistance* (SMR) [84, 85]. This magnetoresistance is a dependence of the resistance in the normal metal on the orientation of the magnetic order parameter in the magnetic insulator with respect to the current direction in the normal metal. What is peculiar about SMR is that because the magnetic material is insulating, the current is passed through a nonmagnetic material, and the underlying physics is therefore quite different from that of anisotropic magnetoresistance. The origin of SMR is a combination of the effects discussed previously in this chapter. It is a consequence of the interplay between spin-transfer torques, the spin Hall effect, and the inverse spin Hall effect [84]. The underlying physics of SMR is explained in Fig. 3.5.

The contribution of SMR is typically very small compared to the regular resistance in the normal metal, but its contribution can easily be detected. By varying the direction of the magnetic order parameter with respect to the current direction, e.g. by sweeping a magnetic field 360 degrees in a plane, one can measure the angular dependence of the resistance. SMR in ferromagnets has an angular dependence $\cos 2\theta$, where $\theta$ is the angle between the magnetization and the charge current $\mathbf{J}_c$ in the normal metal, and this contribution to the resistance can then be extracted as the regular resistance should be independent of $\theta$. From the $\cos 2\theta$ angular dependence, we find that SMR only depends on which axis the magnetization points along and is equal for the magnetization pointing along either of the two axis directions. Consequently, SMR is expected to be more or less equal for ferromagnets and antiferromagnets because whether the spins in the magnetic insulator are parallel
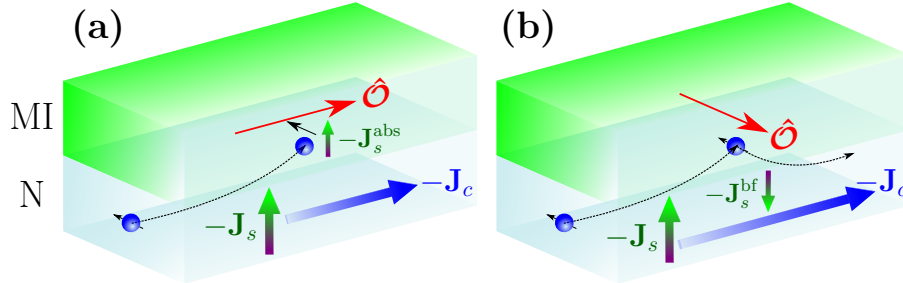
**Figure 3.5.** A charge current in a thin film of normal metal induces a spin current perpendicular to the film through the spin Hall effect. (a) When the spin of the electron in the normal metal is perpendicular to the magnetic order parameter $\hat{\mathcal{O}}$ in the magnetic insulator (magnetization for ferromagnets, Néel order parameter for antiferromagnets), a spin current $\mathbf{J}_s^{\mathrm{abs}}$ can be absorbed into the magnetic insulator. (b) When the electron spin in the normal metal is parallel to $\hat{\mathcal{O}}$, there is no spin current injected into the magnetic insulator. Part of this is instead reflected as a backflow spin current $\mathbf{J}_s^{\mathrm{bf}}$ into the normal metal. Due to the inverse spin Hall effect, this is then transformed into a charge current along the original charge current, thereby enhancing the conductivity in N for this configuration. This illustration is based on a figure in Ref. [84].

or antiparallel is irrelevant. However, the angular dependence of SMR in antiferromagnets is phase shifted by $\pi/2$ compared to ferromagnetic and ferrimagnetic materials when measuring SMR by sweeping a strong magnetic field [86–89]. This is explained by the magnetic field coupling to the magnetization of the antiferromagnet in a canted or spin-flopped state, whereas the SMR in antiferromagnets is primarily due to the Néel order parameter. As indicated by Eq. (2.2), the magnetization and Néel order parameter are perpendicular to each other, explaining the $\pi/2$ phase shift in antiferromagnets compared to ferromagnets [86–89].

### 3.7.1   Spin Hall magnetoresistance at magnetic resonance

SMR has primarily been used to obtain information about static magnetization configurations, but it can also be used to collect information about the magnetization dynamics in magnetic insulators. When the magnetic moments precess at resonance, there is a time-dependent oscillation of the resistance in the normal metal as the direction of the magnetic moments with respect to the current in the normal metal is constantly changing. If the current in the normal metal is also oscillating with the same frequency as the magnetic moments, e.g. if we are in a scenario where the

magnetic resonance is driven by injection of an AC spin current from the normal metal via the spin Hall effect and spin-transfer torques, there will be a mixing of the oscillating resistance and the oscillating current. Depending on the phase difference between the two oscillations, this can lead to a nonzero time-averaged voltage that can be measured and that contains details about the magnetic resonance, such as the resonance frequency and linewidth [90].

In Paper [2], we generalize the work in Ref. [90] to the case of bilayers consisting of a heavy metal and an antiferromagnetic insulator. Building upon the results in Paper [1], we show that the measured signal is also enhanced near the spin-flop transition for exactly the same reasons as we discussed for spin pumping. When the magnetic resonance in these bilayer systems is driven by an injection of a spin current from the normal metal, the magnetic resonance signals originating from the SMR and spin pumping have the same characteristics and an opposite sign. Consequently, the signals compensate each other, which results in a weaker net signal [90]. In Paper [2], we propose a method to separate the signals originating from SMR and spin pumping by utilizing trilayer systems, which can otherwise be extremely challenging in bilayer systems.

## 3.8    Boundary conditions

We have now independently described the spin dynamics in both the magnetic and nonmagnetic layers. To comprehensively discuss the spin dynamics in heterostructures, we need to connect the spin dynamics in the various layers. This is achieved through the boundary conditions at the interfaces between the different layers of the system.

### 3.8.1    Spin current continuity

The main boundary condition that we apply is that we assume the spin current to be continuous across interfaces in the heterostructure [91]. The spin current in the magnetic insulator has contributions from spin pumping and spin-transfer torques, as we considered earlier in this chapter. The spin current in the normal metal also has two main contributions. These contributions are a spin current created through the spin Hall effect by applying a voltage bias to the metal and a spin current due to a gradient in the spin accumulation $\boldsymbol{\mu}_s(\mathbf{r}, t)$. At interfaces between magnetic

insulators and normal metals, we then have the condition

$$\mathbf{I}_s^{\mathrm{MI}}(t)\bigg|_{\mathrm{MI|N}} \equiv \left[\mathbf{I}_s^{\mathrm{pump}}(t) + \mathbf{I}_s^{\mathrm{backflow}}(t)\right]_{\mathrm{MI|N}}$$

$$= \left[\mathbf{I}_s^{\mathrm{SHE}}(t) - \frac{\hbar\sigma A}{4e^2}\boldsymbol{\nabla}\boldsymbol{\mu}_s(\mathbf{r},t)\right]_{\mathrm{MI|N}} \equiv \mathbf{I}_s^{\mathrm{N}}(t)\bigg|_{\mathrm{MI|N}}. \qquad (3.12)$$

Here, $\mathbf{I}_s^{\mathrm{SHE}}(t)$ is the spin current in the normal metal due to the spin Hall effect and $A$ is the interface area between the magnetic insulator (MI) and normal metal (N). All currents are evaluated at the interface.

Another type of interface is an interface with vacuum or a substrate. We assume that there is no spin current in either. For the spin current to be continuous across such interfaces, we must therefore require that the spin current in the magnetic insulator or normal metal vanishes at the edge, i.e.

$$\mathbf{I}_s^{\mathrm{MI}}(t)\bigg|_{\mathrm{MI|Vacuum}} = 0\,, \qquad \text{and} \qquad \mathbf{I}_s^{\mathrm{N}}(t)\bigg|_{\mathrm{N|Vacuum}} = 0\,. \qquad (3.13)$$

Consequently, there is no leaking of the spin current to the environment. The spin current will, however, decay as it propagates through the heterostructure.

### 3.8.2 Standing spin waves

In Chapter 2, we examined the spatially uniform magnetization dynamics in an antiferromagnetic insulator. This will be the dominant type of dynamics when the dynamical source is spatially uniform, such as an oscillating magnetic field. However, in heterostructures, as we are considering here, we can also have dynamical sources that are not spatially uniform. An example of this is by exciting the magnetization dynamics via spin-transfer torques, i.e. by injecting a spin current into a magnetic insulator from a normal metal. The dynamical source is then only at the interface, and the magnetization dynamics then does not have to be uniform in the direction perpendicular to the said interface.

To determine which types of boundary conditions we have for the spatial dependence of the magnetization dynamics, we can integrate the LLG equation in an infinitesimally thin volume around the interface. If we focus on an antiferromagnetic insulator and integrate the LLG equation in Eq. (2.15) and for now disregard interfacial effects such as spin pumping and spin-transfer torques, we obtain the relations
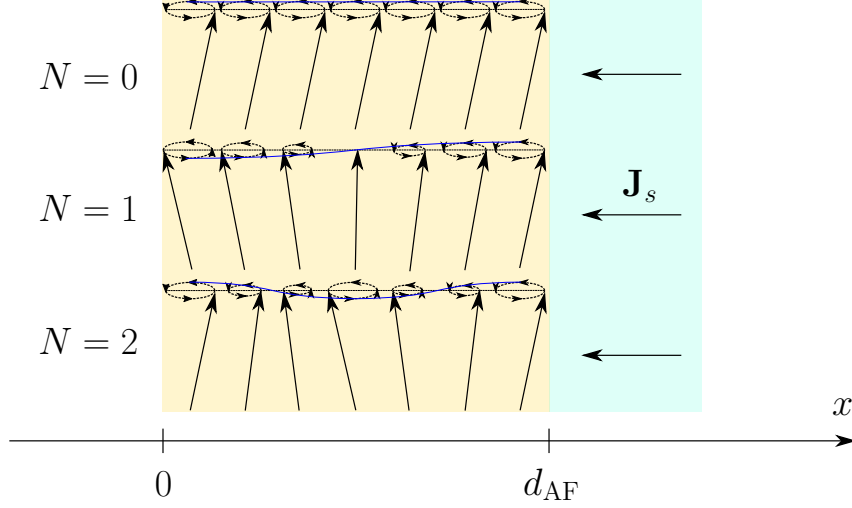
**Figure 3.6.** A nonuniform dynamical source in the form of a spin current $\mathbf{J}_s$ injected into the right side of the antiferromagnetic insulator can induce standing wave resonance modes of the Néel order parameter. Here, we show the three lowest ($N = 0, 1, 2$) standing wave modes, with $N$ being the number of nodes in the standing wave. This figure is reproduced from [2].

$$\pm \left| \tilde{J}_{\mathrm{ex}} \right| \left( \frac{Ma}{2} \right)^2 [\mathbf{m}(\mathbf{r}, t) \times \partial_{\hat{n}} \mathbf{m}(\mathbf{r}, t) + \mathbf{n}(\mathbf{r}, t) \times \partial_{\hat{n}} \mathbf{n}(\mathbf{r}, t)]_{\mathbf{r} \in \mathcal{A}} = 0 \,, \qquad (3.14\mathrm{a})$$

$$\pm \left| \tilde{J}_{\mathrm{ex}} \right| \left( \frac{Ma}{2} \right)^2 [\mathbf{m}(\mathbf{r}, t) \times \partial_{\hat{n}} \mathbf{n}(\mathbf{r}, t) + \mathbf{n}(\mathbf{r}, t) \times \partial_{\hat{n}} \mathbf{m}(\mathbf{r}, t)]_{\mathbf{r} \in \mathcal{A}} = 0 \,. \qquad (3.14\mathrm{b})$$

Here, $\hat{n}$ is a direction normal to the interface, and $\mathcal{A}$ is the interface cross section. These boundary conditions are due to the spin stiffness in the exchange interaction in Eq. (2.5). The sign of the boundary condition depends on which side of the interface the antiferromagnetic insulator is, but this only becomes significant when spin pumping and spin-transfer torques are taken into account.

In the exchange approximation in linear response, we can neglect all contributions to the boundary conditions above, except for the term that goes as $\mathbf{n}(\mathbf{r}, t) \times \partial_{\hat{n}} \mathbf{n}(\mathbf{r}, t)$. This is because the magnetization is typically quite small compared to the Néel order parameter. The boundary conditions in Eq. (3.14) are then reduced to $\mathbf{n}(\mathbf{r}, t) \times \partial_{\hat{n}} \mathbf{n}(\mathbf{r}, t) = 0$, which is satisfied if the spatial derivative of $\mathbf{n}$ in the direction normal to the interfaces vanishes. For an antiferromagnetic film with

a thickness $d_{\mathrm{AF}}$, the Néel order parameter will then be of the form

$$\mathbf{n}(\mathbf{r}, t) = \mathbf{n}_0 + \frac{1}{2} \left\{ \delta\mathbf{n} \cos\left[k_N \left(x - d_{\mathrm{AF}}\right)\right] e^{i\omega t} + \delta\mathbf{n}^* \cos\left[k_N \left(x - d_{\mathrm{AF}}\right)\right] e^{-i\omega t} \right\} . \quad (3.15)$$

Here, we have assumed that the $x$ axis is perpendicular to the interface. The fluctuations $\delta\mathbf{n}$ are perpendicular to the equilibrium direction $\mathbf{n}_0$. The wave numbers $k_N$ take on the values $k_N = N\pi/d_{\mathrm{AF}}$ ($N = 0, 1, 2, \ldots$). This solution describes a set of standing waves of the Néel order parameter inside the antiferromagnetic insulator, as illustrated in Fig. 3.6. The more nodes $N$ that the standing wave resonance mode has, the higher is its resonance frequency. In Paper [2], the source of the magnetic resonance is an injection of a spin current across the interface between the antiferromagnetic insulator and the normal metal. Because the source is spatially inhomogeneous, one can excite these standing waves in the setup considered in Paper [2], unlike in Paper [1], where the source of the magnetic resonance is a spatially uniform oscillating magnetic field. The excitation and detection of these standing waves are studied in more detail in Paper [2].

# 4

# Quantized spin excitations in antiferromagnets

Up to this point, we have considered a microscopic description of magnetization dynamics and spin transport in magnetic systems. However, in some cases, such as when one is studying interactions between the excitations in the system, it can be necessary or more intuitive to consider a quantum mechanical description instead. When moving to the quantum regime, computations tend to become more difficult. In this chapter, we will examine some very useful elementary techniques that will greatly simplify our calculations in the quantum regime. We will not discuss any direct aspects of my own research in this chapter. However, this chapter will lay the groundwork for the Papers [3–5], which will be discussed later in Chapters 5, 6, and 7.

## 4.1 Magnons: quantized spin waves

A very useful trick when describing the spin dynamics of a many-body system in the quantum limit is to map the spin operators to a different set of bosonic operators. At first, this statement might be somewhat perplexing. If we are studying a many-

body system of electrons, which are fermionic particles, why are we then talking about bosons? When studying many-body systems, which consist of a vast sea of particles, it is generally more practical to describe the ripples and waves on that sea instead of every particle in the sea itself. Although these ripples and waves are not particles themselves, we can treat them as some fictional particle: a *quasiparticle*. These quasiparticles are weakly interacting, and it is therefore much more favorable to describe a system of these quasiparticles on top the ground state of our system rather than a system consisting of a vast amount of strongly interacting particles. Ultimately, both methods of describing the system will yield the same result. Note that these quasiparticles are only sensible to discuss in the context of the many-body system. A wave at sea is a very real object, but if you take all the water molecules away, it no longer makes sense to discuss the water wave.

In a many-body system consisting of spins, the ripples in the system will appear as spins pointing slightly away from the equilibrium position. These ripples can be thought of as spin waves, and the elementary quasiparticle excitation is called a *magnon*. In Figures 4.1 and 4.2, we present examples of how a localized and a nonlocalized magnon can be thought of, respectively. In the remaining sections of this chapter, we will discuss how we can model these quasiparticle excitations in a quantum formalism, as well as what type of magnon will be the lowest-energy excitation in an antiferromagnet.

## 4.2    The Holstein–Primakoff transformation

Although there are several ways of describing the quasiparticles in a many-body system of spins, a transformation that is often very convenient is the *Holstein–Primakoff transformation* (HPT) [92]. This transformation is particularly useful when we are studying magnetization dynamics not far from equilibrium, e.g., linear response. This transformation is defined by the following on sublattices $A$ and $B$ of an antiferromagnet:

$$s_{i,+}^A = \sqrt{2s - a_i^\dagger a_i}\, a_i\,, \quad s_{i,-}^A = a_i^\dagger \sqrt{2s - a_i^\dagger a_i}\,, \quad s_{i,z}^A = s - a_i^\dagger a_i \quad, \tag{4.1a}$$

$$s_{j,+}^B = b_j^\dagger \sqrt{2s - b_j^\dagger b_j}\,, \quad s_{j,-}^B = \sqrt{2s - b_j^\dagger b_j}\, b_j\,, \quad s_{i,z}^B = b_j^\dagger b_j - s\,. \tag{4.1b}$$

Here, $s$ is the dimensionless spin number, $i$ and $j$ are lattice sites, $a^{(\dagger)}$ is a magnon annihilation (creation) operator on sublattice $A$, and $b$ and $b^\dagger$ are similar magnon operators on sublattice $B$. We have also introduced $s_\pm = s_x \pm is_y$. This transformation satisfies the spin commutation relation $[s_i, s_j] = i\varepsilon_{ijk}s_k$, with $\varepsilon_{ijk}$ being the
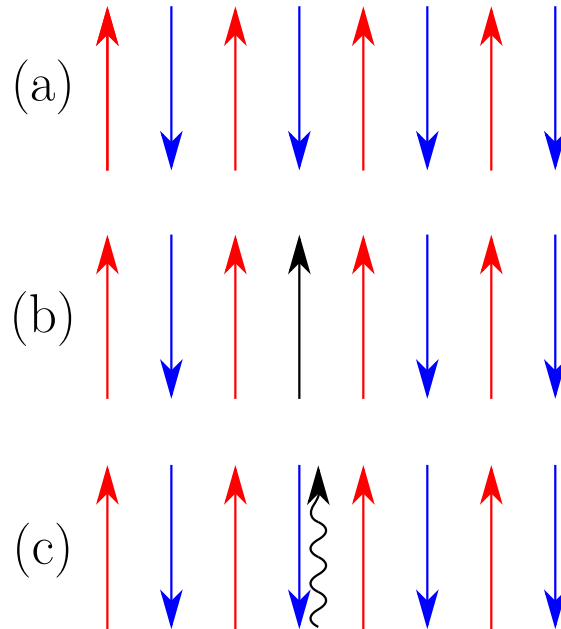
**Figure 4.1.** (a) The ground state of an antiferromagnetic spin chain. (b) An excited state where one spin is flipped with regard to the ground state. (c) The quasiparticle picture of the excited state in (b), where we have the ground state plus a localized magnon. As (b) and (c) must be equivalent, the magnon must have a spin of $+\hbar$, thereby being bosonic like.
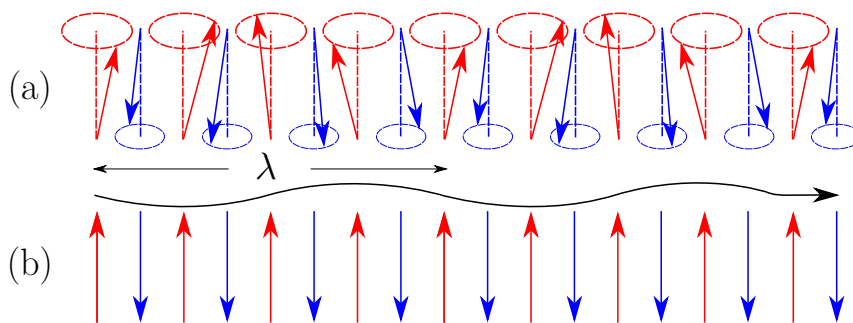


**Figure 4.2.** (a) Periodical precession of antiferromagnetic spins in a chain with wavelength $\lambda$. (b) The quasiparticle picture of (a), where a magnon with wavelength $\lambda$ is passing through the ground state of the spin chain.

Levi-Civita tensor, if $a$, $a^\dagger$, $b$, and $b^\dagger$ obey the bosonic commutation relations, where $\left[a_i, a_j^\dagger\right] = \left[b_i, b_j^\dagger\right] = \delta_{ij}$ and all other commutators are zero. In general, the square roots can make the HPT somewhat cumbersome. However, if we have few magnons

in our system compared to the spin ($\langle a^\dagger a \rangle$, $\langle b^\dagger b \rangle \ll 2s$), we can perform a Taylor expansion of the square roots and only keep terms to some order in the magnon operators. In linear response, we only keep terms to the second order in the magnon operators, which means that we can simply neglect the magnon operators inside the square roots in this approximation.

## 4.3   Local vs collective excitations

In Section 4.1, we showed two different types of spin excitations in our antiferro-magnetic system. In Figure 4.1, we considered a *localized* magnon, where we flipped the spin of a single electron. In Figure 4.2, however, we considered a *collective excitation*, where all the spins in the system are no longer at equilibrium. We will now perform a quick exercise to determine which of the two costs the least amount of energy and will therefore be the most favorable excitation in our system. For simplicity, we consider an isotropic Heisenberg Hamiltonian, given by

$$\mathcal{H} = |J| \sum_{\langle i,j \rangle} \mathbf{S}_i \cdot \mathbf{S}_j + E_0 \,. \tag{4.2}$$

Here, $J$ is the coupling constant between the spins, and $E_0$ is a constant energy level that we choose such that the ground state of the system has zero energy. For the localized magnon, the excitation energy becomes $2z \, |J| \, \hbar^2 s^2$, where $z$ is the number of nearest neighbors. For the collective excitations, we consider periodic waves. To describe these, we perform a Fourier transform of our magnon operators, defined by

$$a_i = \frac{1}{\sqrt{N/2}} \sum_{\mathbf{q}} a_{\mathbf{q}} e^{-i\mathbf{q}\cdot\mathbf{r}_i} \,, \quad b_j = \frac{1}{\sqrt{N/2}} \sum_{\mathbf{q}} b_{\mathbf{q}} e^{-i\mathbf{q}\cdot\mathbf{r}_j} \,. \tag{4.3}$$

Here, the sum over the wave vector $\mathbf{q}$ goes over the Brillouin zone for each sublattice, and $N$ is the number of spins or lattice sites in the system. In terms of the Fourier-transformed operators, the Heisenberg Hamiltonian becomes

$$\mathcal{H} = z \, |J| \, \hbar^2 s \sum_{\mathbf{q}} \left[ a_{\mathbf{q}}^\dagger a_{\mathbf{q}} + b_{\mathbf{q}}^\dagger b_{\mathbf{q}} + \gamma_{\mathbf{q}} \left( a_{\mathbf{q}} b_{-\mathbf{q}} + b_{-\mathbf{q}}^\dagger a_{\mathbf{q}}^\dagger \right) \right] \,, \tag{4.4}$$

with $\gamma_{\mathbf{q}}$ being defined by

$$\gamma_{\mathbf{q}} = \frac{1}{z} \sum_{\boldsymbol{\delta}} e^{i\mathbf{q}\cdot\boldsymbol{\delta}} = \gamma_{-\mathbf{q}} \,, \tag{4.5}$$

and $\boldsymbol{\delta}$ being a vector between two nearest neighbors. Here, we assumed that the material is inversion symmetric.

We note that the Hamiltonian in Eq. (4.4) is not diagonal in the bosonic operators that we have introduced. Consequently, the $a_{\mathbf{q}}$ and $b_{\mathbf{q}}$ magnons from the HPT are interacting quasiparticles. We therefore want to diagonalize this Hamiltonian such that we can determine the energy cost of the noninteracting eigenexcitations. We can accomplish this by introducing new bosonic operators, which we define to be

$$\alpha_{\mathbf{q}} = u_{\mathbf{q}} b_{\mathbf{q}} + v_{\mathbf{q}} a_{-\mathbf{q}}^{\dagger}, \quad \beta_{\mathbf{q}} = u_{\mathbf{q}} a_{\mathbf{q}} + v_{\mathbf{q}} b_{-\mathbf{q}}^{\dagger}. \tag{4.6}$$

Because we enforce these operators to also obey bosonic commutation relations, we have the restriction $|u_{\mathbf{q}}|^2 - |v_{\mathbf{q}}|^2 = 1$. By choosing $u_{\mathbf{q}}$ and $v_{\mathbf{q}}$ such that our Hamiltonian becomes diagonal, we then find that

$$\mathcal{H} = z \, |J| \, \hbar^2 s \sum_{\mathbf{q}} \sqrt{1 - \gamma_{\mathbf{q}}^2} \left[ \alpha_{\mathbf{q}}^{\dagger} \alpha_{\mathbf{q}} + \beta_{\mathbf{q}}^{\dagger} \beta_{\mathbf{q}} \right]. \tag{4.7}$$

If we now consider the case of a 1D spin chain, where $z = 2$ and $\gamma_{\mathbf{q}} = \cos qa$ ($a$ being the lattice spacing between the spins), the energy cost of the localized magnon is $4 \, |J| \, \hbar^2 s^2$, whereas for the collective excitation, it is $2 \, |J| \, \hbar^2 s \, |\sin qa|$. We then see that the collective excitation is more energetically favorable if $|\sin qa| < 2s$. For $s = 1/2$, the collective excitation is then always more or equally energetically favorable. For long-wavelength magnons, the collective excitations have a significantly lower excitation energy and will therefore be the most prevalent excitation in this system.

## 4.4   The Bogoliubov transformation

In the previous section, we diagonalized our Hamiltonian by introducing new bosonic operators in Eq. (4.6) that were a linear combination of our initial HPT bosonic operators. This transformation is known as a *Bogoliubov transformation* and was initially introduced in the case of fermionic operators to solve the Bardeen–Cooper–Schrieffer (BCS) theory of superconductivity [93, 94]. The new operators introduced through this transformation are the eigenexcitations of the system. These are a superposition of creation and annihilation operators of other particles or quasiparticles.

In the previous section, we considered the Bogoliubov transformation of a simple Heisenberg antiferromagnet. In general, we consider a system that also has other interactions, which may make the Hamiltonian harder to diagonalize. For most of the work presented in this thesis, the Hamiltonian of our system can be described by

$$\mathcal{H}_{\mathrm{AF}} = |J| \sum_{\langle i,j \rangle} \mathbf{S}_i \cdot \mathbf{S}_j + \gamma \sum_i \mathbf{H}_0 \cdot \mathbf{S}_i - \frac{k_{\parallel}}{2} \sum_i S_{i,z}^2 + \frac{k_{\perp}}{2} \sum_i S_{i,x}^2 + E_0 \,, \tag{4.8}$$

where $\mathbf{H}_0 = H_0\hat{\mathbf{z}}$ is an external magnetic field along the easy axis and $k_\parallel$ and $k_\perp$ are the easy- and hard-axis anisotropy constants, respectively. After performing an HPT of the spin operators and a Fourier transform of the magnon operators, this Hamiltonian becomes second order in the magnon operators

$$\mathcal{H}_{\mathrm{AF}} = \sum_{\mathbf{q}} \left[ \frac{A}{2} a_{\mathbf{q}}^\dagger a_{\mathbf{q}} + \frac{B}{2} b_{\mathbf{q}}^\dagger b_{\mathbf{q}} + C_{\mathbf{q}} a_{\mathbf{q}} b_{-\mathbf{q}} + D a_{\mathbf{q}} a_{-\mathbf{q}} + D b_{\mathbf{q}} b_{-\mathbf{q}} + \mathrm{H.c.} \right] , \qquad (4.9)$$

where we have introduced

$$A = \hbar \left( \omega_E - \omega_H + \omega_\parallel + \frac{\omega_\perp}{2} \right) , \qquad (4.10\mathrm{a})$$

$$B = \hbar \left( \omega_E + \omega_H + \omega_\parallel + \frac{\omega_\perp}{2} \right) , \qquad (4.10\mathrm{b})$$

$$C_{\mathbf{q}} = \hbar \omega_E \gamma_{\mathbf{q}} , \qquad (4.10\mathrm{c})$$

$$D = \hbar \frac{\omega_\perp}{4} , \qquad (4.10\mathrm{d})$$

as well as the frequencies $\omega_E = |J|\,\hbar s z$, $\omega_H = \gamma H_0$, $\omega_\parallel = k_\parallel \hbar s$, and $\omega_\perp = k_\perp \hbar s$. If the coefficient $D$ vanishes (i.e., there is no hard axis in our system), we can perform a Bogoliubov transformation of this Hamiltonian, similar to the one performed in Eq. (4.6) in the previous section. For this case ($\omega_\perp = 0$), the Bogoliubov coefficients become

$$u_{\mathbf{q}} = \sqrt{\frac{\Gamma_{\mathbf{q}} + 1}{2}} , \quad v_{\mathbf{q}} = \sqrt{\frac{\Gamma_{\mathbf{q}} - 1}{2}} , \qquad (4.11)$$

where we have introduced

$$\Gamma_{\mathbf{q}} = \left[ 1 - \left( \frac{\omega_E \gamma_{\mathbf{q}}}{\omega_E + \omega_\parallel} \right)^2 \right]^{-1/2} . \qquad (4.12)$$

With the presence of the hard-axis anisotropy, the new eigenexcitations become more complicated, and we must generalize the $2 \times 2$ Bogoliubov transformation in Eq. (4.6) to a $4 \times 4$ Bogoliubov transformation. This can be expressed as

$$\boldsymbol{\mu}_{\mathbf{k}} = \begin{pmatrix} \alpha_{\mathbf{k}} \\ \beta_{-\mathbf{k}}^\dagger \\ \alpha_{-\mathbf{k}}^\dagger \\ \beta_{\mathbf{k}} \end{pmatrix} = \begin{pmatrix} u_{\alpha,a} & v_{\alpha,b} & v_{\alpha,a} & u_{\alpha,b} \\ v_{\beta,a}^* & u_{\beta,b}^* & u_{\beta,a}^* & v_{\beta,b}^* \\ v_{\alpha,a}^* & u_{\alpha,b}^* & u_{\alpha,a}^* & v_{\alpha,b}^* \\ u_{\beta,a} & v_{\beta,b} & v_{\beta,a} & u_{\beta,b} \end{pmatrix} \begin{pmatrix} a_{\mathbf{k}} \\ b_{-\mathbf{k}}^\dagger \\ a_{-\mathbf{k}}^\dagger \\ b_{\mathbf{k}} \end{pmatrix} \equiv \underline{B}_4 \mathbf{m}_{\mathbf{k}} , \qquad (4.13)$$

where $\mathbf{k}$ runs over half the vector space of $\mathbf{q}$ [92, 95]. This is to avoid operators with momentum $\mathbf{k}$ and $-\mathbf{k}$ interacting, which will simplify our calculations. Although the constraints on the new Bogoliubov coefficients become more complicated than

previously, the principle behind the constraints remains the same: the new operators must also satisfy bosonic commutation relations. The constraints can be expressed compactly as [95]

$$\underline{Y} = \left[\boldsymbol{\mu}_{\mathbf{k}}, \boldsymbol{\mu}_{\mathbf{k}}^{\dagger}\right] = \underline{B}_4 \left[\mathbf{m}_{\mathbf{k}}, \mathbf{m}_{\mathbf{k}}^{\dagger}\right] \underline{B}_4^{\dagger} = \underline{B}_4 \underline{Y} \underline{B}_4^{\dagger}, \tag{4.14}$$

where $\underline{Y}$ is the matrix

$$\underline{Y} = \begin{pmatrix} 1 & 0 & 0 & 0 \\ 0 & -1 & 0 & 0 \\ 0 & 0 & -1 & 0 \\ 0 & 0 & 0 & 1 \end{pmatrix}. \tag{4.15}$$

The most important constraint that we need to know is

$$|u_{\mu,a}|^2 - |v_{\mu,b}|^2 - |v_{\mu,a}|^2 + |u_{\mu,b}|^2 = 1, \tag{4.16}$$

with $\mu = \alpha, \beta$. The excitation energy of the eigenexcitations can be found through the eigenvalue problem [95]

$$\begin{pmatrix} A & -C_{\mathbf{k}} & -2D & 0 \\ C_{\mathbf{k}} & -B & 0 & 2D \\ 2D & 0 & -A & C_{\mathbf{k}} \\ 0 & -2D & -C_{\mathbf{k}} & B \end{pmatrix} \begin{pmatrix} u_{\mu,a} \\ v_{\mu,b} \\ v_{\mu,a} \\ u_{\mu,b} \end{pmatrix} = \epsilon_{\mu,\mathbf{k}} \begin{pmatrix} u_{\mu,a} \\ v_{\mu,b} \\ v_{\mu,a} \\ u_{\mu,b} \end{pmatrix}, \tag{4.17}$$

which is obtained from the constraint $[\boldsymbol{\mu}_{\mathbf{k}}, \mathcal{H}_{\text{AF}}] = \epsilon_{\mu,\mathbf{k}} \boldsymbol{\mu}_{\mathbf{k}}$. The Bogoliubov coefficients can then be found from the eigenvectors of this eigenvalue problem, with the scaling constant restraint from Eq. (4.16). For the simpler case of an easy-axis antiferromagnet ($\omega_\perp = 0$), the energies become

$$\epsilon_{\alpha,\mathbf{k}} = \hbar \left( \sqrt{(1 - \gamma_{\mathbf{k}}^2)\omega_E^2 + \omega_{\|}(2\omega_E + \omega_{\|})} + \omega_H \right), \tag{4.18a}$$

$$\epsilon_{\beta,\mathbf{k}} = \hbar \left( \sqrt{(1 - \gamma_{\mathbf{k}}^2)\omega_E^2 + \omega_{\|}(2\omega_E + \omega_{\|})} - \omega_H \right). \tag{4.18b}$$

Note that in the long-wavelength limit ($\mathbf{k} = 0 \implies \gamma_{\mathbf{k}} \to 1$), this result is in agreement with the resonance frequencies of the uniform precession mode that we found from the classical treatment through the linear response of the LLG equation in Eq. (2.22). This result is as expected because we are also performing a type of linear response when we only keep terms to second order in the magnon operators from the HPT in our Hamiltonian.
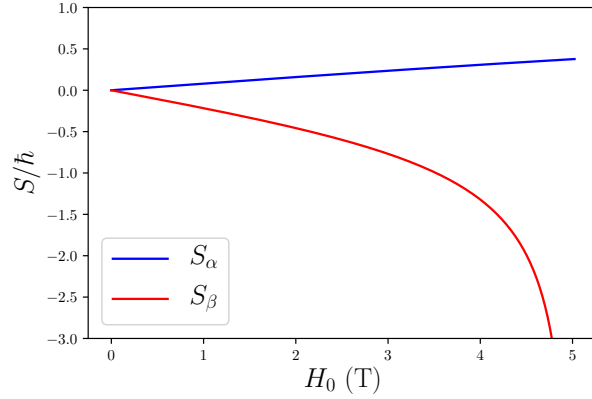
**Figure 4.3.**  The spins of the $\alpha$ and $\beta$ eigenexcitations as a function of external magnetic field $H_0$ along the easy axis of NiO.

## 4.5   The eigenexcitation spin

In Fig. 4.1, we argued that magnons are spin-one quasiparticles ($S = \pm\hbar$), and therefore, they behave as bosons. However, we have now seen that the eigenexcitations of the system are linear superpositions of magnons with spins $+\hbar$ and $-\hbar$. These new magnons can have spins that are neither half integer nor integer, which was recently shown by Kamra et al. [95]. Kamra et al. noted that the Bogoliubov coefficients that combine annihilation and creation operators of the same mode (in our notation, $v_{\alpha,b}$ and $v_{\beta,a}$) lead to *squeezing* (elliptical precession) and an increase in the eigenexcitation spin. Coefficients that combine annihilation (or creation) operators of different modes (in our notation, $u_{\alpha,a}$ and $u_{\beta,b}$) lead to a *hybridization* between magnons with different spins and a decrease in the eigenexcitation spin. The spins of the $\alpha$ and $\beta$ eigenexcitations are [95]

$$S_\alpha = +\hbar \left[ 1 + 2 \left( |v_{\alpha,b}|^2 - |u_{\alpha,a}|^2 \right) \right] , \tag{4.19a}$$

$$S_\beta = -\hbar \left[ 1 + 2 \left( |v_{\beta,a}|^2 - |u_{\beta,b}|^2 \right) \right] . \tag{4.19b}$$

As shown, if the squeezing and hybridization effects do not compensate each other, the eigenexcitations can have a noninteger spin.

Note that for the easy-axis antiferromagnet ($\omega_\perp = 0$), the precessions remain circular, and the eigenexcitations have integer spin ($S_\alpha = +\hbar$, $S_\beta = -\hbar$). This requires perfect uniaxial symmetry, and if this symmetry is broken by, e.g., a small anisotropy perpendicular to the uniaxial anisotropy, the magnons will hybridize

and the spin of the eigenmagnons changes. In the general case of an easy- and hard-axis antiferromagnet, the precessions become elliptical, and the spins of the eigenexcitations are no longer integer. This is illustrated in Fig. 4.3 for the magnons in the easy-plane antiferromagnet NiO. In a zero magnetic field, the eigenmagnons have a linear polarization and zero spin. The effect of the varying spin of the eigenmagnons in NiO can also be observed in a classical calculation using the LLG equation. This can e.g. readily be seen in the results of Paper [1]. In Figs. 2(e) and 2(f) of Paper [1], the pumped spin current vanishes exactly for the right-handed polarization of the microwave source at $H_0 \approx 3.5$ T, which is explained by Fig. 4.3, because at this magnetic field strength, the low-energy $\beta$ eigenmagnons have spin $S = -\hbar$. The eigenmagnons at this point therefore purely consist of left-handed magnons, which cannot be excited by a right-handed microwave source, thereby suppressing the magnetization dynamics and spin pumping for these parameters.

# 5

# Cavity spintronics

The magnon quasiparticle introduced in Chapter 4 can interact with other (quasi)particles and cause interesting physical phenomena. In this chapter, we will study the case where the magnon interacts with other bosons, with an emphasis on one boson in particular: the photon. The magnon and the photon can, for instance, couple to one another via the magnetic field quanta of the photons. The interaction between magnetic matter and photons inside electromagnetic resonators is the foundation for the emerging field of cavity spintronics. Inside these resonators, the photons have discrete frequencies, and if the photon frequency matches the magnetic resonance frequency of the magnons, the magnon and photon can strongly hybridize to form new excitations of the system. When several magnetic subsystems are placed within the electromagnetic resonator, the photons can mediate a nonlocal interaction between the magnetic systems [96, 97], which in turn can be used to manipulate spin currents over macroscopic distances [98].

In this chapter, we will first briefly examine the fundamental concepts and models in quantum optics underlying the interactions between light and matter. We will then present a simple example of an electromagnetic resonator, known as a cavity, and study the magnon-photon system in detail. The last section of this chapter will act as a supplementary material to Paper [3] by providing an in-depth walkthrough

of the methods used therein. In this paper, we show how these electromagnetic resonators can be used to obtain a nonlocal interaction between antiferromagnetic and ferromagnetic materials, inspired by the results of Refs. [96–98]. This is quite interesting because prior to this work, to the best of my knowledge, the only known magnetic interactions between antiferromagnets and ferromagnets were local interactions such as the exchange bias [38].

## 5.1   Interacting harmonic oscillators

The field of cavity spintronics is based on the concept of interacting harmonic oscillators. Before proceeding to the physical system, we will first briefly consider an illustrative example such that we can see what occurs in a system consisting of coupled harmonic oscillators. Let us consider a Hamiltonian that is dependent on some externally adjustable parameter $x$. This Hamiltonian consists of two harmonic oscillators that couple with each other by a coupling strength $g$, and it can be expressed as

$$\mathcal{H}(x) = \hbar\omega_a(x)a^\dagger a + \hbar\omega_b(x)b^\dagger b + \hbar g\left(a^\dagger b + b^\dagger a\right) \tag{5.1a}$$

$$= \begin{pmatrix} a^\dagger & b^\dagger \end{pmatrix} \begin{pmatrix} \hbar\omega_a(x) & \hbar g \\ \hbar g & \hbar\omega_b(x) \end{pmatrix} \begin{pmatrix} a \\ b \end{pmatrix}. \tag{5.1b}$$

In general, we could also imagine the Hamiltonian containing interaction terms that go as $ab + b^\dagger a^\dagger$. We will later argue why these terms contribute less than the interaction terms $a^\dagger b + b^\dagger a$ in many cases. Through a Bogoliubov transformation as discussed in Section 4.4, this Hamiltonian can be diagonalized[1] to the form

$$\mathcal{H}(x) = \mathbf{\Psi}^\dagger \begin{pmatrix} \hbar\omega_- & 0 \\ 0 & \hbar\omega_+ \end{pmatrix} \mathbf{\Psi}, \tag{5.2}$$

where $\omega_\pm = \left(\omega_a(x) + \omega_b(x) \pm \sqrt{\left[\omega_a(x) - \omega_b(x)\right]^2 + 4g^2}\right)/2$ are the energies of the noninteracting system and $\mathbf{\Psi}^\dagger = \begin{pmatrix} \psi_-^\dagger & \psi_+^\dagger \end{pmatrix}$ is a vector of the diagonal eigenstates. If we consider a special case, where $\omega_a(x) = \omega_b(x) \equiv \omega(x_0)$, the vector $\mathbf{\Psi}$ becomes

$$\mathbf{\Psi} = \begin{pmatrix} \psi_- \\ \psi_+ \end{pmatrix} = \frac{1}{\sqrt{2}} \begin{pmatrix} -a + b \\ a + b \end{pmatrix}. \tag{5.3}$$

---

[1]For bilinear bosonic Hamiltonians with terms only consisting of one creation operator and one annihilation operator that are normal ordered as in Eq. (5.1b), the Bogoliubov transformation is equivalent to a standard matrix diagonalization $\mathcal{H} \equiv \mathbf{\Phi}^\dagger M \mathbf{\Phi} = \mathbf{\Phi}^\dagger P D P^{-1} \mathbf{\Phi} \equiv \mathbf{\Psi}^\dagger D \mathbf{\Psi}$. Here, $M$ is a general Hermitian matrix, and the matrix $D$ is a diagonal matrix of the eigenvalues of $M$. Imposing bosonic commutation relations leads to the constraint $P^{-1} = P^\dagger$.
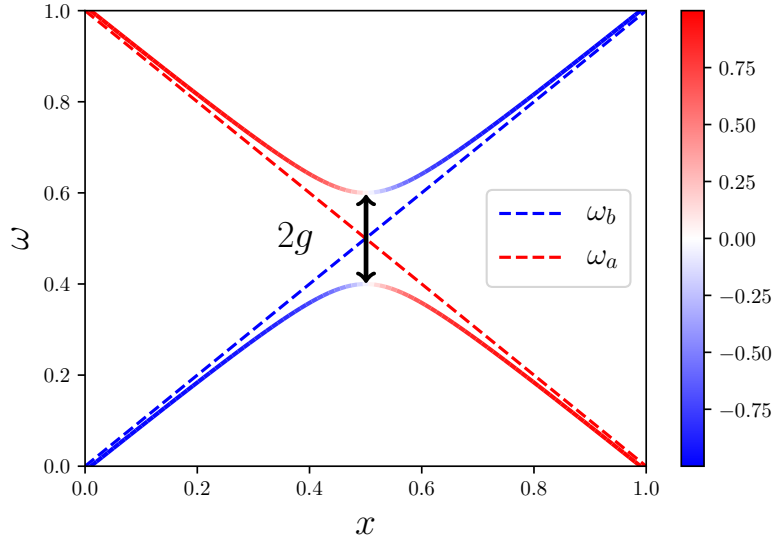
**Figure 5.1.** Dispersion relations for two coupled harmonic oscillators. The uncoupled dispersion relations are shown in dashed lines, with $\omega_a(x) = 1 - x$ and $\omega_b(x) = x$. We consider dimensionless frequencies for simplicity in this illustrative example. The solid lines are the new eigenstates $\omega_\pm$ (where $\omega_+$ is the upper band, and $\omega_-$ is the lower band) of the system with a coupling strength $g = 0.1$. The color gradient of the solid lines shows the composition of the eigenstates $\omega_\pm$ in terms of the uncoupled harmonic oscillators $\omega_{a,b}(x)$. The coupling leads to an anticrossing gap of $2g$ in the dispersion relations.

The new eigenstates of the coupled system in this scenario are superpositions of both harmonic oscillators, with energies $\hbar\omega_\pm = \hbar\omega(x_0) \pm \hbar g$.

Let us now consider a simple example of the dispersion relations $\omega_{a,b}(x)$ and plot the new eigenstate energies of the system together with the energy of the uncoupled eigenstates in Fig. 5.1. We observe that at the crossing point between the initial dispersion relations, the interaction between the harmonic oscillators leads to an anticrossing gap that is linear in the coupling strength between the harmonic oscillators. This is a common feature of interacting harmonic oscillators.

Considering the $\omega_+$ eigenstate, Fig. 5.1 shows that it behaves more or less like the uncoupled harmonic oscillator $a$ far to the left of the crossing point, whereas it behaves like the uncoupled harmonic oscillator $b$ far to the right of the crossing point. This is consistent with what we found when we diagonalized the Hamiltonian at the crossing point: the new eigenstates of the system are superpositions of the harmonic

oscillators and have the properties of both. The anticrossing marks a crossover in behavior where the new eigenstate goes from mostly having the properties of one harmonic oscillator to having the properties of the other.

We have encountered this hybridization between harmonic oscillators previously in this thesis. In Chapter 4, Section 4.5, we observed that when the rotational symmetry of the easy-axis antiferromagnet is broken by e.g. a magnetic anisotropy perpendicular to the easy axis, the eigenmagnons with spin $\pm\hbar$ hybridize and form new linearly polarized spin-0 eigenmagnons. This hybridization has been recently studied experimentally in the ferrimagnet gadolinium iron garnet close to its compensation temperature, where it becomes analogous to an antiferromagnet [99]. In addition to the new eigenmagnons being linearly polarized, the hybridization also leads to a similar anticrossing feature of the magnon dispersion relations as in Fig. 5.1. For the uniaxial easy-axis antiferromagnet, we observed in Eq. (4.18) that the two magnon bands with spin $\pm\hbar$ cross at zero magnetic field. When the rotational symmetry is broken and the magnon modes hybridize, the degeneracy at zero magnetic field is broken, and one will find an anticrossing gap between the two magnon modes at zero magnetic field.

## 5.2 Jaynes–Cummings model and Rabi oscillations

The simple example Hamiltonian in Eq. (5.1a) that we studied in the previous section is very reminiscent of a system called the *Jaynes–Cummings model* [100]. This model was introduced to describe the interaction of a two-level atom with quantized radiation fields and can be expressed as

$$\mathcal{H}_{\mathrm{JC}} = \hbar\omega_c c^\dagger c + \hbar\omega_\sigma \frac{\hat{\sigma}_3}{2} + \frac{\hbar\Omega}{2}\left(c\hat{\sigma}_+ + c^\dagger\hat{\sigma}_-\right). \tag{5.4}$$

Let the two-level atom have a ground state $|g\rangle$ and an excited state $|e\rangle$ separated by an energy $\hbar\omega_\sigma$. We then have that $\hat{\sigma}_3 = |e\rangle\langle e| - |g\rangle\langle g|$, $\hat{\sigma}_+ = |e\rangle\langle g|$, and $\hat{\sigma}_- = |g\rangle\langle e|$. The operators $c$ and $c^\dagger$ describe the annihilation and creation operators of the quantized radiation field, which has an energy $\hbar\omega_c$, and $\hbar\Omega$ describes the interaction strength between the two-level atom and the radiation field. If we assume that we have $n$ radiation quanta in the system, with a frequency $\omega_c = \omega_\sigma + \Delta$, which is detuned from the excitation energy of the atom by a frequency $\Delta$, the energy levels

of this system can be found to be [101]

$$E_\pm = \hbar\omega_c \left(n + \frac{1}{2}\right) \pm \frac{1}{2}\hbar\Omega_\mathrm{R} \,. \tag{5.5}$$

Here, we have introduced the *Rabi frequency* [101]

$$\Omega_\mathrm{R} = \sqrt{\Delta^2 + \Omega^2 \left(n + 1\right)} \,. \tag{5.6}$$

Let us now consider a case where we place a single two-level atom in its excited state inside a constrained space with perfectly reflective boundaries such that radiation quanta cannot be lost from the system. We can determine the wave function $|\psi(t)\rangle$ that describes the state of the two-level atom and the radiation field by solving the time-dependent Schrödinger equation

$$i\hbar\frac{\mathrm{d}}{\mathrm{d}t}|\psi(t)\rangle = \mathcal{H}_\mathrm{JC}|\psi(t)\rangle \,. \tag{5.7}$$

Studying the solution for $|\psi(t)\rangle$, we find that the state of the system oscillates between the initial state with $n$ radiation quanta and the atom in the excited state and a state where the atom has relaxed to the ground state and emitted a radiation quanta. The probability of finding the system in a state where the atom has spontaneously emitted a radiation quanta oscillates between zero and [101]

$$P_\mathrm{emitted}^\mathrm{max} = \frac{\Omega^2(n+1)}{\Delta^2 + \Omega^2(n+1)} = \frac{\Omega^2(n+1)}{\Omega_R^2} \tag{5.8}$$

with the Rabi frequency $\Omega_\mathrm{R}$. The periodical process in which the system emits and reabsorbs a radiation quanta is called a *Rabi oscillation*. We note that in the resonant case where the energy of the radiation quanta equals the excitation energy of the atom ($\Delta = 0$), the probability oscillates between zero and one, and at certain times, we are therefore guaranteed to find the atom in a state where it has emitted a radiation quanta. The reason for this oscillation is that due to the interaction between the atom and the radiation field, the eigenstate of the system is no longer a state with a fixed number of radiation quanta but rather a superposition of the states where the atom is in the excited or ground state and thereby emitted or absorbed a radiation quanta. Consequently, if we prepare the system in a state with a fixed number of radiation quanta (e.g. an excited atom in a vacuum), we are in a quantum superposition of two eigenstates that evolve temporally at different frequencies. The interference between the wave functions causes the Rabi oscillations in the probability of measuring the atom in the ground state or the excited state.

If we compare the example model in Eq. (5.1a) in the previous section to the Jaynes–Cummings model, we find that $2g$ plays the role of the resonant vacuum Rabi frequency $\Omega$. In other words, the coupling strength $g$ provides some indication of how often a Rabi-like oscillation occurs between two coupled harmonic oscillators.

## 5.3   Coherence and coupling regimes

### 5.3.1   Coherence

Although the coupling strength $g$ is an important figure of merit in light-matter interaction systems, it does not contain all the information of interest about a system. In addition to knowing how strongly the light interacts with the matter, we also wish to know about the *coherence* in the system.

Consider a case where we have a system of $N$ two-level atoms in a constrained region (the model describing the coupling between $N$ two-level atoms and the radiation field is called the Dicke model [102] or the Tavis–Cummings model [103, 104]). We then excite all the atoms coherently by e.g. sending a laser pulse into the system. The $N$ atoms will then undergo coherent Rabi oscillations. That is, the individual Rabi oscillations of the atoms will have a constant phase difference between themselves (which we assume to be zero directly after the laser pulse is applied). However, there will be effects in a physical system that will introduce *decoherence* by changing the individual phases of the Rabi oscillations or through loss from the system. One such effect is the spontaneous decay of the atom to its ground state, which emits a radiation quantum. While this sounds similar to the process in a Rabi oscillation, a spontaneous emission will occur at random times, whereas the periodic Rabi oscillations are due to a stimulated emission of the radiation quanta, which we achieve by e.g. exciting the system by a coherent laser pulse. Since the spontaneous decay also emits a radiation quantum, which can later be reabsorbed, the spontaneous emission will only cause a phase shift in the Rabi oscillation. As the atoms will undergo spontaneous decay at different times, this will introduce a phase shift between the Rabi oscillations and thereby a decoherence to the system. Another process that will cause decoherence is the leaking of radiation from the constrained region with the atoms, leaving fewer radiation quanta for the atoms to absorb to continue their Rabi oscillations.

### 5.3.2   Cooperativity as a figure of merit

One way to measure coherence is by the cooperativity of the system. The cooperativity estimates how many Rabi oscillations e.g. an atom will go through on average before it spontaneously decays or the emitted radiation is no longer reabsorbed. The cooperativity will therefore behave as

$$C \sim \frac{g^2}{\Gamma \kappa}, \tag{5.9}$$

where $\Gamma$ is the spontaneous decay rate of the two-level system and $\kappa$ is the loss rate of the radiation. The cooperativity is often a more relevant figure of merit in experiments than the coupling strength $g$ because it also provides some indication about the loss and decay rates of the system.

### 5.3.3   Coupling regimes

Based on the value of the cooperativity and the coupling strength of the system, we can classify the system to be in different coupling regimes [105]. When the coupling strength $g$ is much smaller than the loss rates $\Gamma$ and $\kappa$ of the system, i.e. $C \ll 1$, we are in a *weak coupling regime*. Similarly, when $g$ is much larger than the loss rates ($\Rightarrow C \gg 1$), we are in a *strong coupling regime*. In the strong coupling regime, the system will on average undergo many Rabi oscillations before decoherence becomes significant, unlike the weak coupling regime. The number of coherent Rabi cycles increases with cooperativity.

When the coupling strength $g$ becomes so large that it is comparable to the frequency of the radiation field ($g/\omega_c \gtrsim 0.1$ [105]), we are in a so-called *ultrastrong coupling regime*. In this coupling regime, common approximations such as neglecting the contribution from rapidly rotating terms (e.g. a contribution $\sim \hbar g a^\dagger b^\dagger + \hbar g b a$ to Eq. (5.1a)) no longer hold. (This approximation is called the rotating wave approximation and will be discussed in more detail later in Section 5.5.2). In this thesis, we will assume that we are in the strong coupling regime.

## 5.4   The magnon polariton

Now that we have examined the general case of the coupling between two harmonic oscillators and obtained a physical intuition for this coupling, we will proceed to cavity spintronics, where the harmonic oscillators under consideration are *magnons* and *photons*. Magnons are quantized spin fluctuations that we introduced previously in Chapter 4, whereas photons are quantized electromagnetic waves. We will specifically consider electromagnetic waves in *microwave cavities*. The microwave cavity photons are essentially what we considered in the Jaynes–Cummings model with the radiation quanta in an enclosed region. The microwave cavities are enclosed regions, where the boundary of the region consists of an approximately perfectly conducting material. Due to the boundary condition at the perfectly conducting material, which requires that the component of the electric field parallel to the interface vanishes, there are only certain modes that can exist inside the microwave
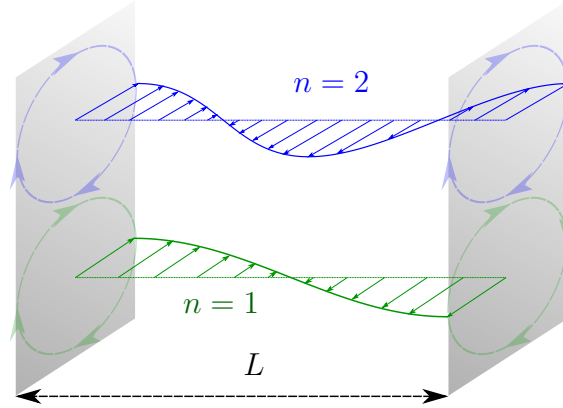
**Figure 5.2.** A simple sketch of a microwave cavity and the quantized magnetic field within. The cavity consists of two perfectly conducting plates separated by a distance $L$. Inside the cavity, only the wavenumbers $n\pi/L$ ($n = 1, 2, \ldots$) perpendicular to the plates are allowed within the cavity. Each mode has two possible polarizations. Here, only one of the circular polarizations is shown, but both circular polarizations (clockwise and counterclockwise) are allowed for each mode $n$.

cavity. The electromagnetic field is then *quantized*. This quantization procedure can be found in introductory textbooks to quantum optics, such as Ref. [101].

A simple model of a cavity can be two parallel conducting plates separated by a distance $L$ in the $z$ direction. This is illustrated in Fig. 5.2. If we only consider photons propagating perpendicular to the plates, the quantized magnetic field inside the microwave cavity becomes

$$\mathbf{H}_{\mathrm{p}}(\mathbf{r}) = i \sum_{n,\lambda} \sqrt{\frac{\hbar\omega_n\mu_0}{V}} \hat{\mathbf{z}} \times \left( p_{n,\lambda}\hat{\mathbf{e}}_\lambda - p_{n,\lambda}^\dagger \hat{\mathbf{e}}_\lambda^* \right) \cos\left(k_n z\right) . \qquad (5.10)$$

Here, $\hat{\mathbf{z}}$ is the propagation direction of the photon, $k_n = n\pi/L$ ($n = 1, 2, \ldots$) are the allowed wave numbers, $\omega_n = k_n c$ is the photon frequency (with $c$ being the speed of light), $V$ is the volume of the cavity, and $\mu_0$ is the vacuum permeability. The operator $p_{n,\lambda}^{(\dagger)}$ is the photon annihilation (creation) operator for the mode with quantum number $n$ and polarization $\lambda$. The vectors $\hat{\mathbf{e}}_\lambda$ are the polarization vectors, which satisfy $\hat{\mathbf{e}}_\lambda \cdot \hat{\mathbf{k}} = \hat{\mathbf{e}}_\lambda \cdot \hat{\mathbf{z}} = 0$ and $|\hat{\mathbf{e}}_\lambda|^2 = 1$, as well as having to form a perpendicular basis. We will consider a circular polarization basis, where $\lambda = \pm$ and $\hat{\mathbf{e}}_\pm = (\hat{\mathbf{x}} \pm i\hat{\mathbf{y}})/\sqrt{2}$.

Recall from Section 2.2 that the magnetization, and thereby spins, interact with magnetic fields through what is called the *Zeeman interaction*. Consequently, there

will be an interaction between the magnetic field quanta of the photons in Eq. (5.10) and the spins in a magnetic material, which can be expressed as

$$\mathcal{H}_{\text{m-p}} = \sum_i \gamma \mathbf{S}_i \cdot \mathbf{H}_{\text{p}}(\mathbf{r}_i) \,. \tag{5.11}$$

Let us first consider the simple case where we only have a single spin interacting with the photons and apply a Holstein–Primakoff transformation as defined in Eq. (4.1); assuming that the spin is located at a point where $\cos(k_n z) = 1$, we find that

$$\mathcal{H}_{\text{m-p}} = \sum_n \hbar\gamma \sqrt{\frac{\hbar\omega_n\mu_0}{2V}} \left[ \left( p_{n,+} - p_{n,-}^\dagger \right) a^\dagger \sqrt{2s - a^\dagger a} + \left( p_{n,+}^\dagger - p_{n,-} \right) \sqrt{2s - a^\dagger a}\, a \right] \,. \tag{5.12}$$

If we assume a sufficiently large spin for the particle under consideration that makes the linearized HPT valid ($2s \gg \langle a^\dagger a \rangle$) and only consider the $\lambda = +$ polarization (we will argue in the next section why we can neglect the $\lambda = -$ polarization in this case), this can then be reduced to

$$\mathcal{H}_{\text{m-p}} = \sum_n \hbar\gamma \sqrt{\frac{\hbar\omega_n\mu_0 s}{V}} \left( p_{n,+} a^\dagger + p_{n,+}^\dagger a \right) \equiv \sum_n \hbar g_n^{(1)} \left( p_{n,+} a^\dagger + p_{n,+}^\dagger a \right) \,. \tag{5.13}$$

We then see that this resembles the interaction term that we considered for the two general coupled harmonic oscillators in Eq. (5.1a), and the localized magnon and photon will therefore hybridize in this system. The resulting new excitations of the system that provide a basis in which the Hamiltonian is diagonal are called *magnon polaritons*.

We will now scale up our system to a case where we have $N$ spins interacting with the photons. For simplicity, we will consider a single-sublattice model, i.e. a ferromagnet. Recall from Chapter 4 that the collective spin excitations (magnons) are the low-energy excitations in magnetic systems. We therefore proceed to a momentum-space basis where

$$a_i = \frac{1}{\sqrt{N}} \sum_{\mathbf{q}} a_{\mathbf{q}} e^{-i\mathbf{q}\cdot\mathbf{r}_i} \,. \tag{5.14}$$

We perform the same approximations as in the single-spin example and only consider HPT of the spin operators to the second order, as well as only consider the $\lambda = +$ polarization of the photons. We also note that the speed of light is much greater than the magnon group velocity, and the photons will therefore primarily couple to the long-wavelength magnons to conserve energy and momentum. We assume that

the photons will only couple to the $|\mathbf{q}| \approx 0$ magnons. We then find that the Zeeman interaction between the magnons and photons is

$$\mathcal{H}_{\text{m-p}} = \sum_n \hbar g_n^{(1)} \left( p_{n,+} a_{\mathbf{0}}^\dagger + p_{n,+}^\dagger a_{\mathbf{0}} \right) \sum_i \frac{1}{\sqrt{N}} = \sum_n \hbar \sqrt{N} g_n^{(1)} \left( p_{n,+} a_{\mathbf{0}}^\dagger + p_{n,+}^\dagger a_{\mathbf{0}} \right) .$$

(5.15)

Note that this is a very important result. In the $N$-spin system, the coupling strength to the cavity photons is enhanced by a factor of $\sqrt{N}$ compared to the single-spin case. This is a general feature that is not restricted to the spin system [106]. In the ferrimagnetic material YIG, which is commonly used in spintronics due to its low damping, the spin density is $\sim 2 \cdot 10^{22}$ cm$^{-3}$ [107]. If we then have a macroscopically sized sample of YIG, the factor of $\sqrt{N}$ can enhance the coupling strength by many orders of magnitude.

The first prediction of magnon polaritons was made a decade ago [108]. A few years later, experiments detected hybridization between ferromagnetic magnons and microwave resonators [109], microwave photons [110], and later optical photons [111–114]. The dispersion relation of ferromagnetic magnons can be tuned externally by applying a magnetic field. By properly choosing the dimensions of the microwave cavity, there will be a crossing point between the dispersion of the ferromagnetic magnons and the cavity photons as a function of the external magnetic field. The hybridization strength between the magnons and the cavity can then be found by measuring the anticrossing gap, as illustrated in Fig. 5.1. This anticrossing gap can e.g. be measured through the transmission and reflection coefficients of the microwave cavity. In the initial experiments, the coupling between the many-body spin system and the photons was on the scale of hundreds of MHz, whereas the coupling strength of the single spin was merely on the order of 38 mHz - 5 Hz [109, 110]. In more recent experiments, coupling strengths of several GHz and a cooperativity of $10^7$ have been measured [115], moving into the ultrastrong coupling regime. It has also been recently predicted that antiferromagnetic magnons can couple to microwaves in cavities [116].

## 5.5   Magnon hybridization between antiferromagnets and ferromagnets

It has been demonstrated experimentally that microwave cavities can be used to obtain a coupling of the magnons in two spatially separated ferromagnets [96, 98].

Whether the same principle can be used to obtain a coupling between an antiferromagnet and a ferromagnet is also of interest. In this section, we will discuss some of the key concepts and results in Paper [3] and elaborate on some of the approximations and methods used in the paper.

### 5.5.1  System Hamiltonian

Let us consider a Hamiltonian that can be divided into the following four parts:

$$\mathcal{H} = \mathcal{H}_{\mathrm{AF}} + \mathcal{H}_{\mathrm{F}} + \mathcal{H}_{\mathrm{p}} + \mathcal{H}_{\mathrm{m\text{-}p}}\,, \tag{5.16}$$

where the first part describes the antiferromagnet, the second describes the ferromagnet, the third describes the microwave cavity, and the last part describes the interaction between the magnons in both magnets and the cavity photons. In Section 4.4, we observed how spin Hamiltonians can be diagonalized through a Bogoliubov transformation for antiferromagnets. The Bogoliubov transformation can also be applied to the ferromagnetic case. We will assume that the magnetic Hamiltonians have already been diagonalized. We will also only consider one of the cavity modes and assume that the cavity has been designed such that the $n = 1$ frequency is relatively close to both the antiferromagnetic and ferromagnetic frequencies. The noninteracting parts of the Hamiltonian can then be written as

$$\mathcal{H}_0 \equiv \mathcal{H}_{\mathrm{AF}} + \mathcal{H}_{\mathrm{F}} + \mathcal{H}_{\mathrm{p}} = \hbar\omega_\alpha \alpha^\dagger\alpha + \hbar\omega_\beta \beta^\dagger\beta + \hbar\omega_\eta \eta^\dagger\eta + \hbar\omega_p \sum_{\lambda=\pm} p_\lambda^\dagger p_\lambda\,. \tag{5.17}$$

Here, $\alpha^{(\dagger)}$ are the diagonal annihilation (creation) operators for the high-energy antiferromagnetic mode, and $\beta$, $\beta^\dagger$, $\eta$, and $\eta^\dagger$ are equivalent operators for the low-energy antiferromagnetic mode and the ferromagnetic mode, respectively.

Our goal is to couple the antiferromagnetic and ferromagnetic magnons indirectly, mediated by the direct coupling to the cavity photons. Therefore, we wish to study a crossing point in the dispersion relation between the antiferromagnetic and ferromagnetic magnons. Fig. 5.3 shows for the simple example of an easy-axis antiferromagnet and a Zeeman-like ferromagnet that a crossing point exists between the low-energy antiferromagnetic magnons and the ferromagnetic magnons. Henceforth, we will therefore only consider the $\beta$ magnons in the antiferromagnet and completely ignore the $\alpha$ magnons. From Eq. (5.12), we can then define a general form of the magnon-photon interaction Hamiltonian:

$$\mathcal{H}_{\mathrm{m\text{-}p}} = \sum_{\lambda=\pm} \hbar \left\{ p_\lambda \left[ g_{\mathrm{AF}}^\lambda \beta^\dagger + \left(g_{\mathrm{AF}}^\lambda\right)^* \beta + g_{\mathrm{F}}^\lambda \eta^\dagger + \left(g_{\mathrm{F}}^\lambda\right)^* \eta \right] \right\} + \mathrm{H.c.}\,, \tag{5.18}$$
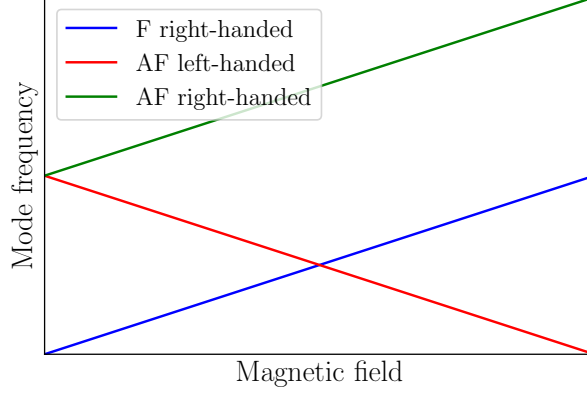
**Figure 5.3.**  Magnon dispersion relations for an easy-axis antiferromagnet and a Zeeman-like ferromagnet as a function of external magnetic field. There is only one type of ferromagnetic magnon with a right-handed polarization with respect to the applied magnetic field but two types of antiferromagnetic magnons with left- and right-handed polarizations.

where $g^\pm_{\mathrm{AF/F}}$ is the coupling strength between the antiferromagnet/ferromagnet and the $\pm$ polarization of the cavity mode. The magnitudes of these coupling strengths are given in Paper [3].

## 5.5.2   Rotating wave approximation

The magnon-photon interaction Hamiltonian in Eq. (5.18) contains 16 individual coupling terms. Before we do anything further with our system Hamiltonian, we wish to see if we can simplify this interaction by determining whether any of the interaction terms can be neglected. If we consider the Hamiltonian in the interaction picture, where we have split the Hamiltonian into the noninteracting and interacting parts $\mathcal{H} = \mathcal{H}_0 + \mathcal{H}_{\mathrm{m\text{-}p}}$, we have

$$\mathcal{H}_\mathrm{I} = e^{i\mathcal{H}_0 t/\hbar} \mathcal{H} e^{-i\mathcal{H}_0 t/\hbar} = \mathcal{H}_0 + e^{i\mathcal{H}_0 t/\hbar} \mathcal{H}_{\mathrm{m\text{-}p}} e^{-i\mathcal{H}_0 t/\hbar}. \tag{5.19}$$

Moreover, in the interaction picture, the bosonic operators are given by

$$\beta_\mathrm{I}(t) = e^{-i\omega_\beta t}\beta\,, \quad \eta_\mathrm{I}(t) = e^{-i\omega_\eta t}\eta\,, \quad p_{\lambda,\mathrm{I}}(t) = e^{-i\omega_p t}p_\lambda\,, \tag{5.20}$$

as well as their Hermitian conjugates. Note that the terms in the interacting part of the Hamiltonian $\mathcal{H}_{\mathrm{m\text{-}p}}$ that pairs a creation operator with an annihilation operator have a time dependence such as $\exp\left[\pm i(\omega_{\beta/\eta} - \omega_p)t\right]$, whereas the terms

that consist of two creation or two annihilation operators have a time dependence $\exp\left[\pm i(\omega_{\beta/\eta} + \omega_p)t\right]$. If we assume that $\left|\omega_{\beta/\eta} - \omega_p\right| \ll \left|\omega_{\beta/\eta} + \omega_p\right|$, the rapidly oscillating terms that consist of pairs of creation or annihilation operators will quickly average out to zero compared to the slowly oscillating terms. This inequality can be enforced by choosing the frequency of the cavity photons to be close to the frequency at the crossing point between the antiferromagnetic and ferromagnetic dispersion relations. By discarding the rapidly oscillating terms from the Hamiltonian and returning to the Schrödinger picture, the magnon-photon interaction Hamiltonian becomes

$$\mathcal{H}_{\text{m-p}}^{\text{RWA}} \approx \hbar\left[p_+\left(g_{\text{AF}}^+\beta^\dagger + g_{\text{F}}^+\eta^\dagger\right) + p_-\left(g_{\text{AF}}^-\beta^\dagger + g_{\text{F}}^-\eta^\dagger\right)\right] + \text{H.c.} \qquad (5.21)$$

This approximation is known as the *rotating wave approximation* (RWA) [101].

### 5.5.3 Unitary transformation

We have now simplified the Hamiltonian in the picture where we have an interaction between the magnons and the photons. However, our goal is to determine whether this magnon-photon interaction can mediate an indirect magnon-magnon interaction between the antiferromagnetic and ferromagnetic magnons. To determine whether this is the case, we perform a unitary transformation of the Hamiltonian. A unitary transformation does not change the eigenvalues of the Hamiltonian [117], and consequently, the physics is also unchanged. On the other hand, by performing a unitary transformation of the Hamiltonian, one can obtain a form where a possible magnon-magnon coupling would be more apparent and easy to identify, as we will see shortly. The magnon-magnon interaction will be the largest where their energies are the same, i.e. at the point where $\omega_\beta = \omega_\eta$. We also assume that the frequency of the cavity photons is detuned from this crossing point by a frequency $\Delta = \omega_p - \omega_{\beta,\eta}$. We will then consider the unitary transformation $\mathcal{H}' = \mathcal{U}\mathcal{H}\mathcal{U}^\dagger$, where we have defined

$$\mathcal{U} = \exp\left\{\sum_{\lambda=\pm} \frac{p_\lambda\left(g_{\text{AF}}^\lambda\beta^\dagger + g_{\text{F}}^\lambda\eta^\dagger\right) - p_\lambda^\dagger\left(g_{\text{AF}}^\lambda\beta + g_{\text{F}}^\lambda\eta\right)}{\Delta}\right\} \equiv \exp\left\{\hat{u}\right\}. \qquad (5.22)$$

We have assumed that the coupling constants $g_{\text{AF/F}}^\lambda$ are real.

In the dispersive limit, where the cavity detuning is assumed to be significantly larger than the magnon-photon coupling strengths (i.e. $\Delta \gg g_{\text{AF,F}}^\pm$), we can perform a series expansion of the Hamiltonian to the second order in $g_{\text{AF,F}}^\pm/\Delta$. To perform

this series expansion, we take advantage of the Hadamard Lemma, which states that

$$e^{\hat{A}}\hat{B}e^{-\hat{A}} \approx \hat{B} + \left[\hat{A}, \hat{B}\right] + \frac{1}{2!}\left[\hat{A}, \left[\hat{A}, \hat{B}\right]\right] + \frac{1}{3!}\left[\hat{A}, \left[\hat{A}, \left[\hat{A}, \hat{B}\right]\right]\right] + \dots \qquad (5.23)$$

Introducing $\mathcal{H}_\Delta = \hbar\Delta\left(p_-^\dagger p_- + p_+^\dagger p_+\right)$, we note the following commutator relations:

$$[\hat{u}, \mathcal{H}_0 - \mathcal{H}_\Delta] = 0\,, \quad [\hat{u}, \mathcal{H}_\Delta] = -\mathcal{H}_{\text{m-p}}^{\text{RWA}}\,. \qquad (5.24)$$

Consequently, to the second order, we have

$$
\begin{aligned}
\mathcal{H}' \approx \quad & \mathcal{H}_0 + \frac{1}{2}\left[\hat{u}, \mathcal{H}_{\text{m-p}}^{\text{RWA}}\right] && (5.25\text{a}) \\
= \quad & \hbar\left[\omega_\beta - \frac{\left(g_{\text{AF}}^-\right)^2 + \left(g_{\text{AF}}^+\right)^2}{\Delta}\right]\beta^\dagger\beta + \hbar\left[\omega_\eta - \frac{\left(g_{\text{F}}^-\right)^2 + \left(g_{\text{F}}^+\right)^2}{\Delta}\right]\eta^\dagger\eta \\
& + \hbar\left[\omega_p + \frac{\left(g_{\text{AF}}^-\right)^2 + \left(g_{\text{F}}^-\right)^2}{\Delta}\right]p_-^\dagger p_- + \hbar\left[\omega_p + \frac{\left(g_{\text{AF}}^+\right)^2 + \left(g_{\text{F}}^+\right)^2}{\Delta}\right]p_+^\dagger p_+ \\
& - \hbar\left(\frac{g_{\text{AF}}^- g_{\text{F}}^- + g_{\text{AF}}^+ g_{\text{F}}^+}{\Delta}\right)\left(\beta^\dagger\eta + \eta^\dagger\beta\right)\,. && (5.25\text{b})
\end{aligned}
$$

In the last line of the above equation, we see that we have a magnon-magnon coupling between the antiferromagnetic and ferromagnetic magnons if ($i$) the magnons couple to the same polarization of the cavity photons and if ($ii$) the two polarization contributions do not cancel each other out. The other correction terms describe a shift in the frequency of the magnons and photons due to the interactions. Notably, the above unitary transformation replaced the explicit magnon-photon couplings by an explicit magnon-magnon coupling.

### 5.5.4   Geometrical aspects of polarization-dependent coupling

We have now found that we can achieve an indirect magnon-magnon coupling if both the antiferromagnetic and ferromagnetic magnons can couple to the same microwave polarization. However, this constitutes a problem; as shown in Fig. 5.3, the crossing point between the dispersion relations is between the left-handed mode of the antiferromagnetic magnons and the ferromagnetic mode, which is right-handed. This means that at the crossing point, the antiferromagnetic magnons and ferromagnetic magnons have opposite spins! Consequently, if we consider a circular polarization basis, the antiferromagnetic magnons will couple to the left-handed circular polarization and not to the right-handed one, whereas the ferromagnetic magnons will
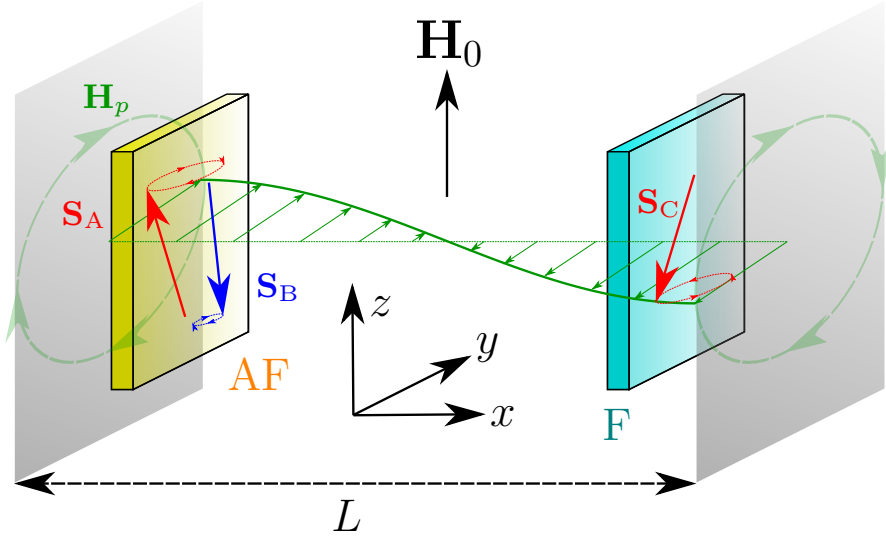
**Figure 5.4.** Illustration of an antiferromagnet (AF) and ferromagnet (F) inside a microwave cavity, given by two perfectly conducting plates separated by a distance $L$. A magnetic field $\mathbf{H}_0$ tunes the magnon frequencies, and the magnetic component $\mathbf{H}_p$ of the quantized electromagnetic field mediates a coupling between the antiferromagnetic and ferromagnetic magnons. Figure taken from Paper [3].

couple to the right-handed polarization and not to the left-handed one. Therefore, in this case, there can be no indirect magnon-magnon coupling mediated by the microwaves because the two polarizations are independent of each other.

The above conclusion assumes that the magnons have integer spin ($S = \pm\hbar$). However, if we have a case where one of the magnon modes is significantly squeezed or hybridized (through e.g. dipolar interactions or nonuniaxial magnetic anisotropies), the magnons will have noninteger spin, as shown in Section 4.5. It can be shown that if a magnon has a noninteger spin, it can couple to both polarizations and not just one. However, it will generally couple much more strongly to one polarization than the other, and the main difference from the integer-spin case is that instead of not coupling to one of the polarizations at all, there is now a small coupling present. Although the case where either (or both) the antiferromagnetic magnons or ferromagnetic magnons have a spin that is noninteger will lead to an indirect magnon-magnon coupling, this coupling will be rather weak.

In addition to considering the polarization of the microwaves, one can also consider the propagation direction of the photons relative to the magnetic moments.

(a)              (b)              (c)              (d)
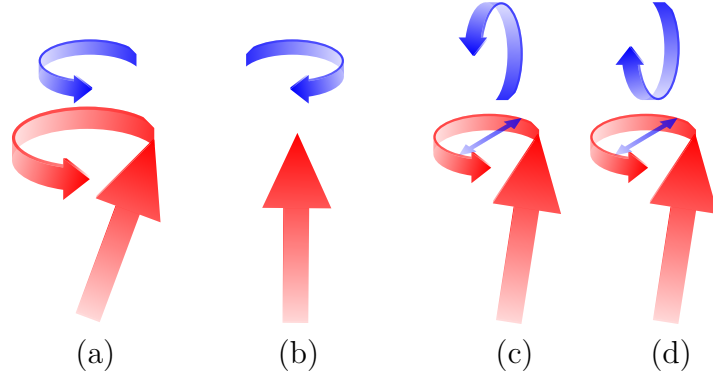
**Figure 5.5.** Coupling between microwaves (blue circular arrows) and ferromagnetic magnons (red circular arrows) for different microwave polarizations and microwave propagation directions. In (a) and (b), the propagation direction of the microwaves is parallel to the magnetization (red arrow), whereas in (c) and (d), it is perpendicular to the magnetization. The right-handed polarization in (a) couples strongly to the magnon, whereas the left-handed polarization in (b) does not couple to the magnon at all. In (c) and (d), both polarizations couple equally strongly to the magnons. This is because the microwaves primarily couple to the transverse component of the magnetization, and the transverse projection of the microwaves (blue arrows) is the same for both polarizations.

In Eq. (5.10), we chose the geometry where the propagation direction of the photons was parallel to the magnetic moments ($z$ direction). We can also consider a geometry where the propagation direction of the photons is perpendicular to the magnetic moments, e.g. a propagation along the $x$ direction. Such a geometry is illustrated in Fig. 5.4. We can then choose a new set of circular polarization vectors, given by $\hat{\mathbf{e}}_{\pm} = (\hat{\mathbf{z}} \pm i\hat{\mathbf{y}})/\sqrt{2}$. The microwaves will now also couple to the longitudinal $z$-component of the magnetic moments, unlike before. Mathematically, this will introduce terms in the magnon-photon interaction Hamiltonian $\mathcal{H}_{\text{m-p}}$ that are linear in the photon annihilation/creation operators, as well as terms that contain one photon operator and two magnon operators (e.g. $\sim p_{n,+}^{\dagger}\eta\eta$). If we assume that $|\omega_p - \omega_{\beta,\eta}| \ll \omega_p$, the linear terms can readily be discarded in the RWA. However, we need to be somewhat more careful with the cubic terms. In principle, these terms can oscillate slowly enough to be significant in the RWA if the magnons couple to the $n = 2$ mode of the microwaves, which has twice the frequency of the cavity mode

that we previously considered. We note that by the following heuristic argument:

$$\sum_i \eta_i^\dagger \eta_i = n_{\text{magnons}} \quad \rightarrow \quad \langle \eta_i^\dagger \eta_i \rangle = \frac{n_{\text{magnons}}}{N_{\text{F}}} \quad \rightarrow \quad \langle \eta_i^{(\dagger)} \rangle \sim \sqrt{\frac{n_{\text{magnons}}}{N_{\text{F}}}}$$

$$\rightarrow \quad \langle \sum_i \eta_i^{(\dagger)} \rangle \sim \sqrt{n_{\text{magnons}} N_{\text{F}}} \quad \rightarrow \quad \frac{\langle \sum_i \eta_i^{(\dagger)} \eta_i^{(\dagger)} \rangle}{\langle \sum_i \eta_i^{(\dagger)} \rangle} \sim \sqrt{\frac{n_{\text{magnons}}}{N_{\text{F}}}}, \tag{5.26}$$

trilinear terms in the Hamiltonian such as $\sim p_{n,+}^\dagger \eta \eta$ contribute, on average, a factor of $\sqrt{n_{\text{magnons}}/N_{\text{F}}}$ less than bilinear terms such as $\sim p_{n,+}^\dagger \eta$, where $N_{\text{F}}$ is the number of spins in the ferromagnet. Because we assume that the number of magnons ($n_{\text{magnons}}$) in the system is much smaller than the number of spins, we conclude that the cubic coupling term's contribution to the magnon-photon coupling can be neglected compared to the contribution from the quadratic coupling term. Consequently, the microwaves effectively do not couple to the longitudinal part of the magnetization to the second order in the magnon operators, and only the transverse projection of the microwaves couple to the magnons. In Fig. 5.5 (c) and (d), we see that this means that both polarizations will have the same coupling to the magnons. Together with our previous result in Eq. (5.25b), this means that in this choice of geometry, we have a significant magnon-magnon coupling!

### 5.5.5   Full dispersion in the rotating wave approximation

Now that we have established that we can obtain a coupling between antiferromagnetic magnons and ferromagnetic magnons inside a microwave cavity by carefully choosing the geometry, it can be useful to investigate how such a coupling will appear in the dispersion relation of the system. In Section 5.1, we found that the interaction between harmonic oscillators typically appears as an anticrossing gap where there would normally be a crossing point in the dispersion relations if the oscillators did not interact. Therefore, a coupling between the antiferromagnetic and ferromagnetic magnons will appear as an anticrossing at the crossing point between their dispersion relations. We will now solve the system exactly and see if this is the case.

The Hamiltonian in Eq. (5.16) can be written as

$$\mathcal{H} = \begin{pmatrix} \beta^\dagger & \eta^\dagger & p_-^\dagger & p_+^\dagger \end{pmatrix} \begin{pmatrix} \hbar\omega_\beta & 0 & \hbar g_{\text{AF}}^- & \hbar g_{\text{AF}}^+ \\ 0 & \hbar\omega_\eta & \hbar g_{\text{F}}^- & \hbar g_{\text{F}}^+ \\ \hbar g_{\text{AF}}^- & \hbar g_{\text{F}}^- & \hbar\omega_p & 0 \\ \hbar g_{\text{AF}}^+ & \hbar g_{\text{F}}^+ & 0 & \hbar\omega_p \end{pmatrix} \begin{pmatrix} \beta \\ \eta \\ p_- \\ p_+ \end{pmatrix}, \tag{5.27}$$
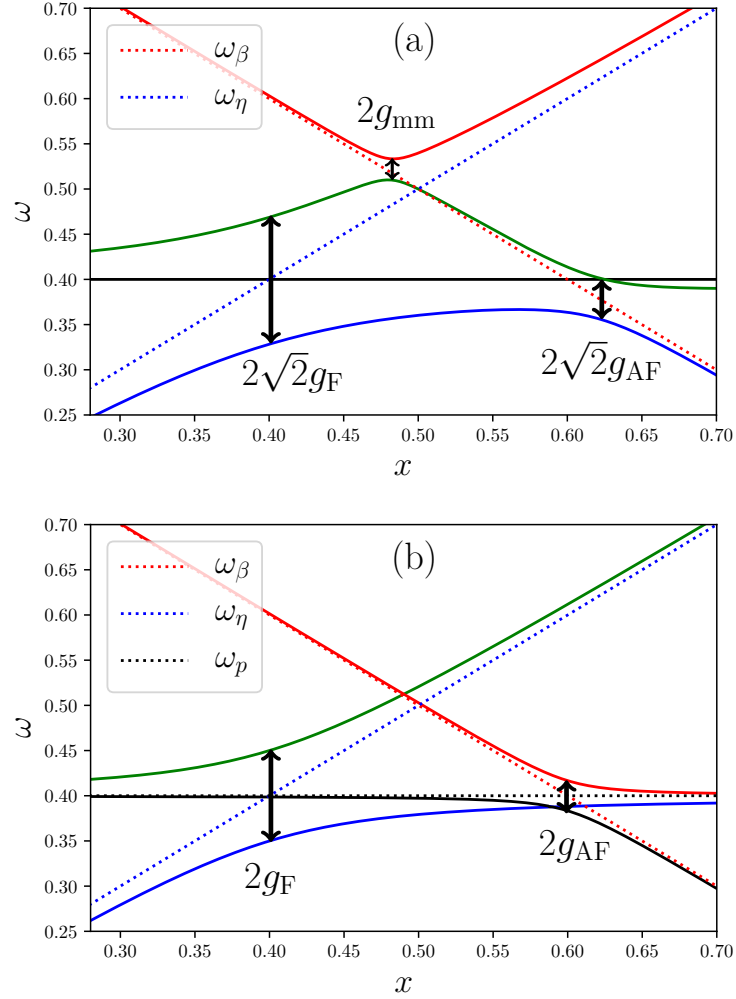
**Figure 5.6.** Example of how direct and indirect couplings manifest in the dispersion relations. The dashed lines are the dispersion relations without interaction in the system, and the solid lines are the new dispersion relations with the magnon-photon interaction present. We consider the case where $\omega_\beta = 1 - x$, $\omega_\eta = x$, and $\omega_p = 0.4$. We use dimensionless frequencies for simplicity in this illustrative example. In (a), both magnons $\beta$ and $\eta$ couple equally to both polarizations of the cavity, with $g_F^\pm \equiv g_F = 0.05$ and $g_{AF}^\pm \equiv g_{AF} = g_F/3$. This leads to an indirect coupling between the magnons, as shown by the anticrossing of magnitude $g_{mm} \approx 2g_{AF}g_F/\Delta$. In (b), we have chosen $g_F^+ = g_F$, $g_{AF}^- = g_F/3$, and $g_F^- = g_{AF}^+ = 0$. We find that this does not lead to an indirect magnon-magnon coupling because the magnons couple to independent cavity modes. The difference of $\sqrt{2}$ between the gap in (a) and (b) is due to the coupling to two polarizations in (a) rather than just one polarization in (b).

assuming a rotating wave approximation. Note that this Hamiltonian only contains explicit couplings between the magnons and the photons and that there is no explicit coupling between the antiferromagnetic and ferromagnetic magnons. Because the Hamiltonian only contains quadratic terms in the bosonic operators, it is possible to diagonalize this Hamiltonian exactly. Diagonalization of this system yields very complicated analytical expressions but can be illustrated nicely in a plot given some numerical values of the energies and coupling strengths. We present a simple example of this case in Fig. 5.6, which illustrates how the magnon-photon interaction affects the dispersion relations and how one can observe the different coupling strengths in the dispersion relations.

In Paper [3], we find that for certain material combinations, it is possible to achieve a significant coupling between antiferromagnetic magnons and ferromagnetic magnons. This coupling strength can be on the order of hundreds of MHz.

## 5.5.6 Coupling strength and cooperativity of antiferromagnets

We have now seen that in principle, one can couple antiferromagnetic magnons both directly to microwave photons and indirectly to ferromagnetic magnons. However, the coupling strength of antiferromagnetic magnons to photons is weaker than the interaction between ferromagnetic magnons and photons due to vanishing magnetization. In easy-axis antiferromagnets, the coupling strength is reduced by an inefficiency factor from the anisotropy to exchange interaction ratio [3]

$$\frac{g_{\mathrm{AF}}}{g_{\mathrm{F}}} \propto \left(\frac{\omega_{\parallel}}{\omega_E}\right)^{1/4} ,$$
(5.28)

assuming that the frequency and spin density are identical for the ferromagnet and antiferromagnet.

For the cooperativity in the system, which describes the coherence, we have $C \sim g^2/(\Gamma\kappa)$ as defined in Eq. (5.9). Here, $\Gamma$ describes the decay rate of the spins and is proportional to the linewidth of the system. In ferromagnets, the linewidth is proportional to $\alpha\omega$, while in antiferromagnets, it is proportional to $\alpha\omega\sqrt{\omega_E/\omega_{\parallel}}$ [2]. Noting that the resonance frequency of the antiferromagnetic magnons is on the order of $\sqrt{\omega_{\parallel}\omega_E}$, the cooperativity of an antiferromagnet is reduced by a factor of

$$\frac{C_{\mathrm{AF}}}{C_{\mathrm{F}}} \propto \frac{\omega_{\parallel}}{\omega_E}$$
(5.29)

compared to a ferromagnet under similar conditions. The reduction in cooperativity is therefore much more significant than the reduction in coupling strength because the ratio $\omega_\parallel/\omega_E$ is typically very small. It can, however, be as large as 7.4% in materials such as $NaNiO_2$ [118]. Note that this reduction in cooperativity also does not account for differences in spin density, Gilbert damping, and so forth. It is not inconceivable that antiferromagnetic materials where these factors would be favorable when taken into account exist, but the lack of experimental data for antiferromagnetic materials makes it difficult to note a general trend here compared to ferromagnetic materials. Experiments have been able to achieve cooperativities as high as $C \sim 10^7$ using YIG [115], which does not have a particularly high spin density compared to other magnetic materials due to the complex structure of its unit cell. With this taken into consideration, the reduction in cooperativity from the anisotropy to exchange ratio needs not necessarily stand in the way of obtaining significant cooperativity values in antiferromagnetic cavity spintronics. The cooperativity values of antiferromagnets should, however, in all likelihood be lower than those of ferromagnets for the most reasonable scenarios.

# 6

# Magnon-mediated fermion interactions

Magnons not only interact with other bosonic quasiparticles but also interact with fermionic particles via their spin. In this chapter, we will study how such interactions can mediate an interaction between two separate fermions. When these magnon-mediated interactions cause the fermions to interact attractively, we can obtain highly exotic states of matter, such as superconductors [119–121]. One way to describe these interactions and the resulting physical phenomena is through thermal quantum field theory. This chapter will introduce this formalism and provide the basis for the results presented in Paper [4]. We will also more closely examine how the magnon-fermion interaction depends on the interface structure of the antiferromagnetic insulator. Since antiferromagnetic insulators have more than one sublattice, these sublattices can form various types of magnetic interfaces, as we have seen previously. In the case of spin pumping in Chapter 3, we observed that the different types of interfaces can lead to very different results. In this chapter, we will more closely examine the underlying physics to better understand how some phenomena highly depend on the magnetic interface structure.

## 6.1   Thermal quantum field theory

In Paper [4], we use a very useful technique in condensed matter theory to study
how fermions can interact via an exchange of magnons. This technique is the use of
*path integrals* in thermal quantum field theory, where we are studying fermionic and
bosonic fields in thermal equilibrium. We will start by providing a brief overview of
the basic ideas in this formalism. However, we leave the mathematical derivations to
the textbooks, as there are several good introductory books to this field, e.g. Refs.
[45, 122]. The basic introduction to the path integral formalism in this section is
based on the description in these textbooks.

Let us start by considering a system described by the Hamiltonian $\mathcal{H}(t)$ pre-
pared in a state $|\Psi_i\rangle$ at some time $t_i$. We focus on many-body systems given by
Hamiltonians in a second-quantization representation. The probability amplitude
of finding the system in some state $|\Psi_f\rangle$ at time $t_f$ is then given by the following
matrix element of the time evolution operator $\hat{\mathcal{U}}(t_f, t_i)$:

$$\langle\Psi_f|\hat{\mathcal{U}}(t_f, t_i)|\Psi_i\rangle \equiv \langle\Psi_f|\mathcal{T}\exp\left[-\frac{i}{\hbar}\int_{t_i}^{t_f} \mathrm{d}t\mathcal{H}(t)\right]|\Psi_i\rangle, \tag{6.1}$$

where $\mathcal{T}$ is the time-ordering operator. We will focus on the special case where we
work in a basis consisting of *coherent states*. It will soon become apparent why we
are free to work in such a basis and why this greatly simplifies the situation. A
coherent state has the peculiar property that it is an eigenstate of the annihilation
operator:

$$\hat{\phi}|\phi\rangle = \phi|\phi\rangle, \quad \langle\bar{\phi}|\hat{\phi}^\dagger = \langle\bar{\phi}|\bar{\phi}. \tag{6.2}$$

Here, $\phi$ is the eigenvalue of the annihilation operator $\hat{\phi}$, and $\bar{\phi}$ is the complex conju-
gate of $\phi$. The coherent state basis is overcomplete and is therefore not an orthonor-
mal basis where $\langle\bar{\phi}_i|\phi_j\rangle = \delta_{ij}$. Although this can occasionally make the situation
more complicated, the advantages of the coherent state greatly outweigh its disad-
vantages in this case. As long as the Hamiltonian is normal ordered, i.e. all the
annihilation operators are to the right of all the creation operators, we can exchange
all the operators in the Hamiltonian in Eq. (6.1) with their eigenvalues. For bosonic
operators, this corresponds to exchanging the operators with complex numbers. For
fermionic operators, the operators can be replaced by so-called *Grassman numbers*
that satisfy a Grassman algebra. This means that the numbers anticommute with
themselves and other fermionic operators but commute with observables [45].

The idea of the path integral formalism is that the expectation value in Eq. (6.1)
can be calculated by summing over each possible path in the phase space spanned
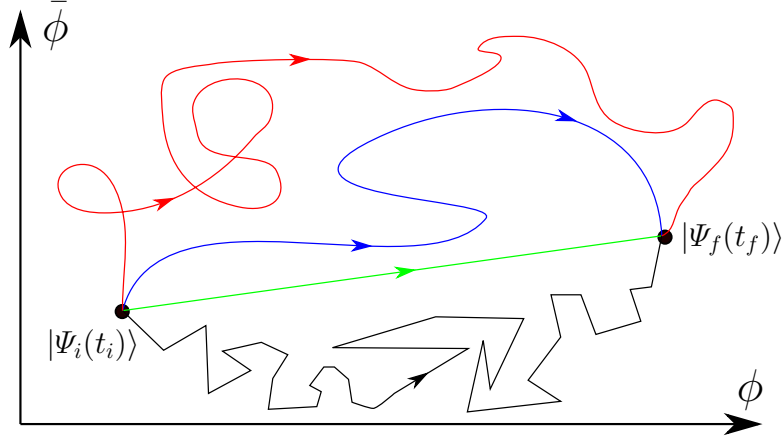
**Figure 6.1.** A state $|\Psi_i(t_i)\rangle$ can evolve to a state $|\Psi_f(t_f)\rangle$ via many different paths in a phase space spanned by the canonical coordinates $\bar{\phi}$ and $\phi$. The most probable path is the path of least action, which is often described as the classical path.

by the canonical coordinates that connect the initial and final states, as illustrated in Fig. 6.1. In a coherent state basis, the eigenvalue $\phi$ of the annihilation operator and its complex conjugate $\bar{\phi}$ effectively play the roles of the canonical coordinates of the system. The contribution of each path to the expectation value in Eq. (6.1) is weighted by the action of the path [45]

$$\langle \Psi_f | \hat{\mathcal{U}}(t_f, t_i) | \Psi_i \rangle = \int_{\text{paths } |\Psi_i\rangle \to |\Psi_f\rangle} \mathcal{D}\phi \mathcal{D}\bar{\phi} \exp\left[ i\mathcal{S}\left(\bar{\phi}, \phi\right)/\hbar \right] , \qquad (6.3)$$

where $\mathcal{S}\left(\bar{\phi}, \phi\right)$ is the action given by

$$\mathcal{S}\left(\bar{\phi}, \phi\right) = \int_{t_i}^{t_f} \mathrm{d}t \mathcal{L}(\bar{\phi}, \phi, t) = \int_{t_i}^{t_f} \mathrm{d}t \left[ i\hbar\bar{\phi}\partial_t\phi - \mathcal{H}(\bar{\phi}, \phi, t) \right] . \qquad (6.4)$$

Here, $\mathcal{L}(\bar{\phi}, \phi, t)$ is the Lagrangian of the system. One of the beautiful aspects of the coherent state path integral formalism is that time ordering occurs *automatically* [45, 122]. Since we replace the operators by their eigenvalues (which are complex numbers and Grassman numbers for bosonic and fermionic operators, respectively) and since these are evaluated at each time step starting at time $t_i$ to time $t_f$ in chronological order along the path, we can simply ignore the time-ordering operator when calculating the expectation value in Eq. (6.1) in the way given in Eq. (6.3).

Let us now move beyond the use of path integrals for the purpose of evaluating the time evolution of quantum states and consider how we can use them to describe

the statistical properties of a system in thermal equilibrium. The primary quantity that we wish to calculate in statistical physics is the *partition function* of the system. This function contains most of the information of interest about the system in thermal equilibrium, meaning that once we have calculated the partition function, we can fairly easily study the properties of the system. The partition function $\mathcal{Z}$ is given by a trace over the Boltzmann weight [45]

$$\mathcal{Z} = \text{Tr}\left[\exp\left(-\beta\mathcal{H}\right)\right] = \sum_\lambda \langle\lambda|\exp\left(-\beta\mathcal{H}\right)|\lambda\rangle, \qquad (6.5)$$

where $\beta = 1/(k_B T)$, with $k_B$ being the Boltzmann constant and $T$ being the temperature of the system. When calculating the trace over the Boltzmann weight, we can use any basis of wave functions that we wish, leaving us free to operate with the coherent states introduced in Eq. (6.2). Interestingly, note that one can relate the partition function in Eq. (6.5) to the time evolution probability amplitude in Eq. (6.1). In thermal equilibrium, the Hamiltonian of the system is independent of time because we do not have any time-dependent driving sources. We then find that each term contributing to the sum on the right-hand side of Eq. (6.5) can be written as a time evolution probability amplitude under the substitution $(t_f - t_i) \to -i\hbar\beta$. In other words, by evolving the initial state to some *imaginary time*, we can use the path integrals to obtain the partition function and thereby the information about the system at thermal equilibrium. The paths contributing to the partition function are periodic, as shown in Eq. (6.5). In a coherent state basis, the partition function can be found to be [45]

$$\mathcal{Z} = \sum_\phi \langle\pm\bar{\phi}|\exp\left(-\beta\mathcal{H}\right)|\phi\rangle, \qquad (6.6)$$

where the positive sign is when the state is a coherent state of bosons and the negative sign is when we have a coherent state of fermions. This negative sign is due to the Grassman algebra of the eigenvalues of the fermionic fields [45, 122]. In other words, for bosons, we sum over all periodic paths that are symmetric under the time evolution to an imaginary time $t_f = t_i - i\hbar\beta$, whereas for fermions, we sum over all antiperiodic paths that are antisymmetric under the same time evolution. In the path integral language of Eq. (6.3), the partition function can then be expressed as

$$\mathcal{Z} = \int_{\text{all (anti)periodic paths}} \mathcal{D}\phi\mathcal{D}\bar{\phi}\exp\left[-\tilde{\mathcal{S}}\left(\bar{\phi},\phi\right)/\hbar\right]. \qquad (6.7)$$

The action is now expressed in imaginary time as

$$\tilde{\mathcal{S}}\left(\bar{\phi},\phi\right) = \int_0^{\hbar\beta} \mathrm{d}\tau\left[\hbar\bar{\phi}\partial_\tau\phi + \mathcal{H}(\bar{\phi},\phi)\right], \qquad (6.8)$$

with $\tau = it$ being imaginary time. Any expectation value of a time-ordered function depending on the bosonic or fermionic fields can then be calculated using the partition function through the identity [45]

$$\langle \mathcal{T} f(\hat{\phi}^\dagger, \hat{\phi}) \rangle = \frac{1}{\mathcal{Z}} \int_{\text{all (anti)periodic paths}} \mathcal{D}\phi \mathcal{D}\bar{\phi} \exp\left[-\tilde{\mathcal{S}}\left(\bar{\phi}, \phi\right)/\hbar\right] f(\bar{\phi}, \phi). \qquad (6.9)$$

To satisfy the periodic boundary conditions of the path integrals, it is often beneficial to work in a *Matsubara basis* of the canonical coordinates $\bar{\phi}$ and $\phi$. Bosonic fields are restricted to obey $\phi_B(\tau = \hbar\beta) = +\phi_B(\tau = 0)$ and similarly for its conjugate, whereas fermionic fields have the antisymmetric relation $\phi_F(\tau = \hbar\beta) = -\phi_F(\tau = 0)$. This periodicity can be enforced by performing a Fourier series expansion of the fields, given by

$$\phi_B(\tau) = \sum_{n=-\infty}^{\infty} \phi_B(i\omega_n)e^{-i\omega_n\tau}, \quad \phi_F(\tau) = \sum_{n=-\infty}^{\infty} \phi_F(i\nu_n)e^{-i\nu_n\tau} \qquad (6.10)$$

for bosonic and fermionic fields, respectively. This series expansion is known as a Matsubara expansion and is given in terms of the bosonic Matsubara frequencies $\omega_n = 2n\pi/(\hbar\beta)$ and fermionic Matsubara frequencies $\nu_n = (2n+1)\pi/(\hbar\beta)$. The inverse relations of the Matsubara expansion are given by

$$\phi_B(i\omega_n) = \frac{1}{\hbar\beta} \int_0^{\hbar\beta} \mathrm{d}\tau \phi_B(\tau)e^{i\omega_n\tau}, \quad \phi_F(i\nu_n) = \frac{1}{\hbar\beta} \int_0^{\hbar\beta} \mathrm{d}\tau \phi_F(\tau)e^{i\nu_n\tau}. \qquad (6.11)$$

Similarly, it is often beneficial to perform a Fourier transform of any spatial dependence of the fields to a momentum representation.

## 6.2    Emission and absorption of magnons at magnetic interfaces

Now that we have a means to calculate the expectation values of bosonic and fermionic fields at thermal equilibrium, the next step in determining how magnon-mediated fermion interactions behave is studying interactions between a single fermion and a magnon. Fermions, such as electrons, can interact with the spin at magnetic interfaces via the *s-d* interaction [123, 124]

$$\mathcal{H}_{s\text{-}d} = -\sum_{\mathbf{r}_i \in \mathcal{A}} J_{s\text{-}d}(\mathbf{r}_i)\hat{\boldsymbol{\rho}}(\mathbf{r}_i) \cdot \mathbf{S}(\mathbf{r}_i). \qquad (6.12)$$

Here, $J_{s\text{-}d}(\mathbf{r}_i)$ is the strength of the interfacial *s-d* exchange coupling at position $\mathbf{r}_i$ (which lies in the interface cross section $\mathcal{A}$), $\mathbf{S}(\mathbf{r}_i)$ is the spin in the magnetic
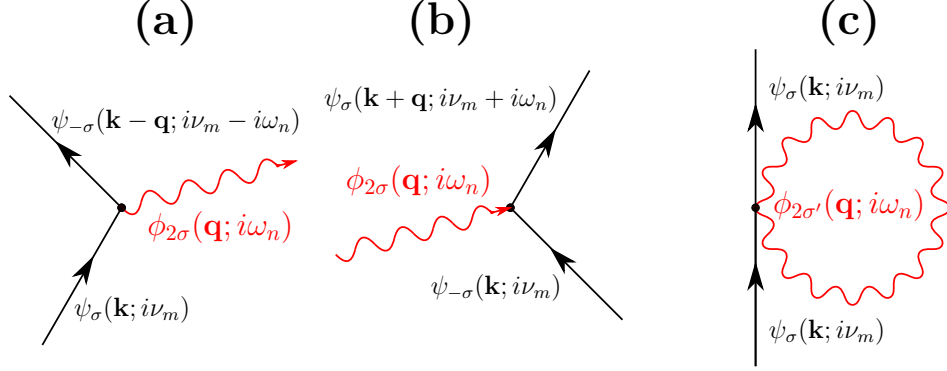
**Figure 6.2.** Feynman diagrams illustrating the different interaction processes between fermions $\psi$ (straight black lines) and magnons $\phi$ (red wavy lines) at magnetic interfaces. The indices $\sigma, \sigma' = \pm\hbar/2$ denote the (quasi)particle spin; the indices $\mathbf{k}$, $\mathbf{q}$ and so forth denote the (quasi)particle momentum; and $i\nu_m$ and $i\omega_n$ are the Matsubara frequencies. **(a)** A fermion flips its spin and thereby emits a magnon with momentum $\mathbf{q}$ and spin $2\sigma$. **(b)** A fermion absorbs a magnon with momentum $\mathbf{q}$ and spin $2\sigma$. **(c)** A fermion instantly emits and reabsorbs a virtual magnon.

insulator, and $\hat{\boldsymbol{\rho}}(\mathbf{r}_i)$ is the electronic spin density operator defined as

$$\hat{\boldsymbol{\rho}}(\mathbf{r}_i) = \frac{1}{2} \sum_{\sigma,\sigma'} \psi_\sigma^\dagger(\mathbf{r}_i) \boldsymbol{\sigma}_{\sigma\sigma'} \psi_{\sigma'}(\mathbf{r}_i) \,, \tag{6.13}$$

where $\boldsymbol{\sigma} = (\sigma_x, \sigma_y, \sigma_z)$ is a vector of the Pauli matrices and $\psi_\sigma^{(\dagger)}(\mathbf{r}_i)$ annihilates (creates) a fermion with spin $\sigma$ at position $\mathbf{r}_i$. The *s-d* interaction in Eq. (6.12) considers the exchange interaction between an itinerant fermion and a localized spin operator. This describes the case at an interface between a nonmagnetic conducting material, such as normal metals and semiconductors where we have freely moving electrons, and magnetic insulators where the electrons are localized. To consider the interaction between a fermion and a magnon, we can perform a "bosonization" of the spin operators $\mathbf{S}(\mathbf{r}_i)$ to a magnon basis, for instance, with the Holstein–Primakoff transformation (HPT) introduced in Section 4.2. If we use the HPT and only keep terms to the second order in the magnon operators, we obtain interaction processes between the fermions and the magnons, as illustrated by the Feynman diagrams in Fig. 6.2. As shown, fermions and magnons can interact at magnetic interfaces via spin flips of the fermions and a corresponding emission or absorption of a magnon. For ferromagnetic insulators, we only have magnons with one spin value in such processes, whereas for antiferromagnetic insulators, these processes

can involve magnons with spins $\pm\hbar$.

## 6.3   Effective magnon-mediated potential

### 6.3.1   Perturbation theory at thermal equilibrium

We now know how a single fermion and magnon can interact. To describe how such processes that involve the emission and absorption of magnons can lead to a magnon-mediated interaction between two fermions, we can treat the interaction between the single fermion and magnon as a perturbative interaction. To obtain a scenario where a magnon can mediate an interaction between two fermions, we need to expand at least to the second order in the processes illustrated in Fig. 6.2. When only considering the dominant contribution to the magnon-mediated fermion-fermion interaction, it is also sufficient to expand to the second order in the fermion-magnon interaction. By studying the vertices in Fig. 6.2, we find that there is only one combination that can lead to an interaction between two separate fermions that is mediated by a magnon. This combination is when the vertices in Fig. 6.2 (a) and Fig. 6.2 (b) are combined. All other combinations will either have vanishing expectation values or only lead to a renormalization of the single-fermion energies due to the presence of the magnons. In other words, from perturbation theory, we find that two fermions can interact through one of them emitting a magnon that is absorbed by the other. Then, by applying the techniques from thermal quantum field theory introduced in Section 6.1, we can perform a thermal average of the magnons in the system when we have thermal equilibrium at some temperature $T$. This allows us to express the process of two fermions interacting via the exchange of a magnon in terms of some effective interaction potential $U_\sigma(\mathbf{q}, i\omega_n)$, as illustrated in Fig. 6.3. We derived this effective magnon-mediated potential between two fermions in Paper [4] for antiferromagnetic magnons. In this manuscript, we applied the potential to study the condensation of so-called *indirect excitons*, where electrons and holes form a coherent state across an insulating barrier. In the remainder of this chapter, we will take a closer look at the behavior of this derived magnon-mediated potential.

### 6.3.2   Interface structure dependence

Because the fermions interact with magnons at a magnetic interface through their spin, the form of the magnon-mediated fermion-fermion interaction is highly dependent on the magnetic structure at the interface(s) to the fermion reservoir(s). This
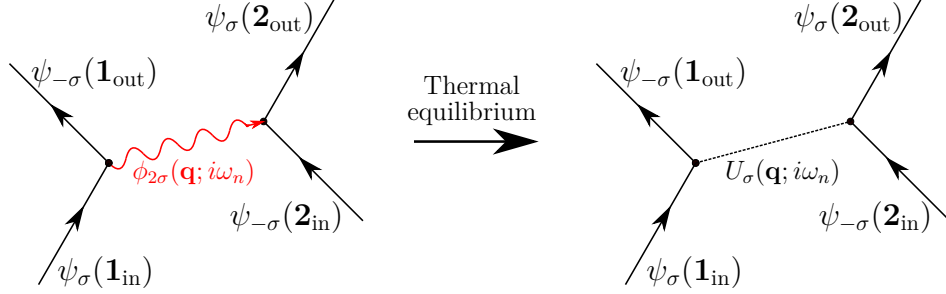
**Figure 6.3.** Two fermions interact via an emission and absorption of a magnon that transfers a momentum $\mathbf{q}$ and a Matsubara frequency $\omega_n$ in addition to a spin $2\sigma$ from one fermion to the other. The states $\mathbf{N}_{\mathrm{in/out}}$ ($\mathbf{N} = \mathbf{1}, \mathbf{2}$) denote the initial and output states of each of the two fermions. By considering the thermal average of the magnons in the system, we can express the interaction via the emission and absorption of magnons in terms of an effective potential $U_\sigma(\mathbf{q}, i\omega_n)$ between the two fermions.

is particularly true for multi-sublattice magnets such as antiferromagnets, where different types of magnetic ordering at the interface are possible, as illustrated in Fig. 3.4.

Let us consider the general case of a compensated interface of an easy-axis antiferromagnetic insulator, where both sublattices are present at the interface, as illustrated in Fig. 3.4 (c). The conclusions for the specific cases of a perfectly compensated interface (equal coupling to both sublattices) and an uncompensated interface (only coupling to one of the sublattices) will naturally follow from this discussion. Note that we will only consider perfectly matched interfaces, where there is a one-to-one matching of the atoms in the nonmagnetic layer and the antiferromagnetic layer. To account for the multiple sublattices present at the interface and that these may couple unequally to the fermion spins via the $s$-$d$ interaction, we split the $s$-$d$ interaction coupling strength $J_{s\text{-}d}$ into two parts. These parts are defined such that they take on the value $J_{s\text{-}d,A}$ ($J_{s\text{-}d,B}$) if the nearest neighbor spin in the magnetic layer is with sublattice $A$ ($B$) and zero otherwise. For a compensated interface, these coupling constants then have a spatial dependence. This can, for

**Table 6.1.** Momentum and Matsubara frequencies of the incoming and outgoing fermionic fields before and after scattering via the magnons for different components of the scattering potential.

| $ss'$ | $\mathbf{1}_{\text{in}}^{ss'}$ | $\mathbf{1}_{\text{out}}^{ss'}$ | $\mathbf{2}_{\text{in}}^{ss'}$ | $\mathbf{2}_{\text{out}}^{ss'}$ |
|---|---|---|---|---|
| $--$ | $\mathbf{k}; i\nu_m$ | $\mathbf{k} - \mathbf{q}; i\nu_m - i\omega_n$ | $\mathbf{k}'; i\nu_l$ | $\mathbf{k}' + \mathbf{q}; i\nu_l + i\omega_n$ |
| $-+$ | $\mathbf{k}; i\nu_m$ | $\mathbf{k} - \mathbf{q} + \mathbf{q}_{\text{AF}}^{(1)}; i\nu_m - i\omega_n$ | $\mathbf{k}'; i\nu_l$ | $\mathbf{k}' + \mathbf{q}; i\nu_l + i\omega_n$ |
| $+-$ | $\mathbf{k}; i\nu_m$ | $\mathbf{k} - \mathbf{q}; i\nu_m - i\omega_n$ | $\mathbf{k}'; i\nu_l$ | $\mathbf{k}' + \mathbf{q} + \mathbf{q}_{\text{AF}}^{(2)}; i\nu_l + i\omega_n$ |
| $++$ | $\mathbf{k}; i\nu_m$ | $\mathbf{k} - \mathbf{q} + \mathbf{q}_{\text{AF}}^{(1)}; i\nu_m - i\omega_n$ | $\mathbf{k}'; i\nu_l$ | $\mathbf{k}' + \mathbf{q} + \mathbf{q}_{\text{AF}}^{(2)}; i\nu_l + i\omega_n$ |

instance, be described by the functions

$$J_{s\text{-}d,A}^{\lambda}(\mathbf{r}) = \frac{J_{s\text{-}d,A}^{\lambda}}{2} \left[ 1 + \cos\left(\frac{\pi}{a}y\right)\cos\left(\frac{\pi}{a}z\right) \right] = \frac{J_{s\text{-}d,A}^{\lambda}}{2}\left( 1 + \frac{1}{4}\sum_{\mathbf{q}_{\text{AF}}} e^{i\mathbf{q}_{\text{AF}}\cdot\mathbf{r}} \right), \quad (6.14\text{a})$$

$$J_{s\text{-}d,B}^{\lambda}(\mathbf{r}) = \frac{J_{s\text{-}d,B}^{\lambda}}{2} \left[ 1 - \cos\left(\frac{\pi}{a}y\right)\cos\left(\frac{\pi}{a}z\right) \right] = \frac{J_{s\text{-}d,B}^{\lambda}}{2}\left( 1 - \frac{1}{4}\sum_{\mathbf{q}_{\text{AF}}} e^{i\mathbf{q}_{\text{AF}}\cdot\mathbf{r}} \right), \quad (6.14\text{b})$$

where $\mathbf{r}$ is a vector located in the interface plane, which we consider to be the $yz$ plane. The exact form of the functions is not crucial to the following discussion; the essential part is that these functions have a periodicity that is determined by the antiferromagnetic sublattice wave vector $\mathbf{q}_{\text{AF}} = \pi(j_y\hat{\mathbf{y}} + j_z\hat{\mathbf{z}})/a$, where $j_y, j_z = \pm$ and $a$ is the antiferromagnetic lattice spacing. We have also added a label $\lambda$ to the $s$-$d$ interaction coupling strengths that denotes which fermion the magnetic spin couples to since we in general can have a magnon-mediated interaction between two distinct types of fermions. This can, for instance, be used to describe fermions in different reservoirs, e.g. in a trilayer structure where the antiferromagnetic insulator is sandwiched between two distinct fermion reservoirs, a system that we will consider in more detail later in this chapter. Using the techniques discussed previously in this chapter, we can express the contribution of the magnon-mediated interactions to the fermionic action as

$$\hbar\beta \sum_{\substack{\lambda\lambda' \\ \eta=\alpha,\beta}} \sum_{\substack{\sigma=\uparrow,\downarrow \\ s,s'=\pm}} \sum_{\substack{lmn \\ \mathbf{k}\mathbf{k}'\mathbf{q}}} \sum_{\mathbf{q}_{\text{AF}}^{(1)},\mathbf{q}_{\text{AF}}^{(2)}} U_{\sigma,\lambda\lambda'}^{\eta,ss'}(\mathbf{q}, i\omega_n) \bar{\psi}_{-\sigma,\lambda'}(\mathbf{1}_{\text{out}}^{ss'}) \bar{\psi}_{\sigma,\lambda}(\mathbf{2}_{\text{out}}^{ss'}) \psi_{-\sigma,\lambda}(\mathbf{2}_{\text{in}}^{ss'}) \psi_{\sigma,\lambda'}(\mathbf{1}_{\text{in}}^{ss'}).$$

$$(6.15)$$

A more detailed calculation showing this in the case of uncompensated interfaces can be found in the Supplementary Material to Paper [4]. The scattering states $\mathbf{1}_{\text{in/out}}^{ss'}$ and $\mathbf{2}_{\text{in/out}}^{ss'}$ of the fermionic fields are listed in Table 6.1. The strength of the interaction between the fermions is given by the effective magnon-mediated potential

$U^{\eta,ss'}_{\sigma,\lambda\lambda'}(\mathbf{q}, i\omega_n)$, which is found to be

$$U^{\alpha,ss'}_{\sigma,\lambda\lambda'}(\mathbf{q}, i\omega_n) = -\frac{\hbar^2 S}{32N} \frac{1}{-\sigma i\hbar\omega_n + \epsilon_{\alpha,\mathbf{q}}} \tilde{J}^s_{\alpha,\lambda}(\mathbf{q}) \tilde{J}^{s'}_{\alpha,\lambda'}(\mathbf{q}) \,, \qquad (6.16a)$$

$$U^{\beta,ss'}_{\sigma,\lambda\lambda'}(\mathbf{q}, i\omega_n) = -\frac{\hbar^2 S}{32N} \frac{1}{\sigma i\hbar\omega_n + \epsilon_{\beta,\mathbf{q}}} \tilde{J}^s_{\beta,\lambda}(\mathbf{q}) \tilde{J}^{s'}_{\beta,\lambda'}(\mathbf{q}) \,. \qquad (6.16b)$$

Here, $S$ is the dimensionless spin number of the magnetic atoms in the antiferromagnetic insulator, $N$ is the number of magnetic atoms in the antiferromagnetic insulator, and $\epsilon_{\alpha/\beta,\mathbf{q}}$ is the energy of an $\alpha/\beta$ eigenmagnon with momentum $\mathbf{q}$, which is given in Eq. (4.18). Note that in the above notation, $\sigma = \uparrow$ is given by $\sigma = +1$ and $\sigma = \downarrow$ by $\sigma = -1$. We have also introduced the effective coupling constants

$$\tilde{J}^{\pm}_{\alpha,\lambda}(\mathbf{q}) \equiv \frac{1}{2} \left( u_{\mathbf{q}} J^\lambda_{s\text{-}d,A} \pm v_{\mathbf{q}} J^\lambda_{s\text{-}d,B} \right) \,, \qquad (6.17a)$$

$$\tilde{J}^{\pm}_{\beta,\lambda}(\mathbf{q}) \equiv \frac{1}{2} \left( v_{\mathbf{q}} J^\lambda_{s\text{-}d,A} \pm u_{\mathbf{q}} J^\lambda_{s\text{-}d,B} \right) \,, \qquad (6.17b)$$

where $u_{\mathbf{q}} > 0$ and $v_{\mathbf{q}} > 0$ are the Bogoliubov coefficients for an easy-axis antiferromagnet defined in Eq. (4.11).

As shown in Table 6.1, the magnon-mediated interaction potential has three distinct scattering processes:

1. Normal scattering of both fermions by a momentum transfer $\mathbf{q}$ (contribution from $ss' = --$ in Eq. (6.15)).

2. One fermion undergoes normal scattering, whereas the other undergoes an *Umklapp scattering* process with the antiferromagnetic sublattice wave vector $\mathbf{q}_{\text{AF}}$ (contributions from $ss' = -+, +-$ in Eq. (6.15)). The Umklapp scattering process is possible when the antiferromagnetic layer has a different periodicity than the nonmagnetic layer. Here, the different periodicity causes the reduced first Brillouin zone of the antiferromagnet to be half the size of the first Brillouin zone in the nonmagnetic layer, assuming a compensated perfectly matched interface.

3. Both fermions undergo an Umklapp scattering process with the antiferromagnetic sublattice (contribution from $ss' = ++$ in Eq. (6.15)).

The scattering processes in Table 6.1 are illustrated in Fig. 6.4 for two different Fermi surfaces. We note that the magnon-mediated fermion interactions are only significant if all the scattered states lie within a thin shell around the Fermi surface, where the thickness of the shell is decided by the magnon energy $\epsilon_{\alpha/\beta,\mathbf{q}}$. This is
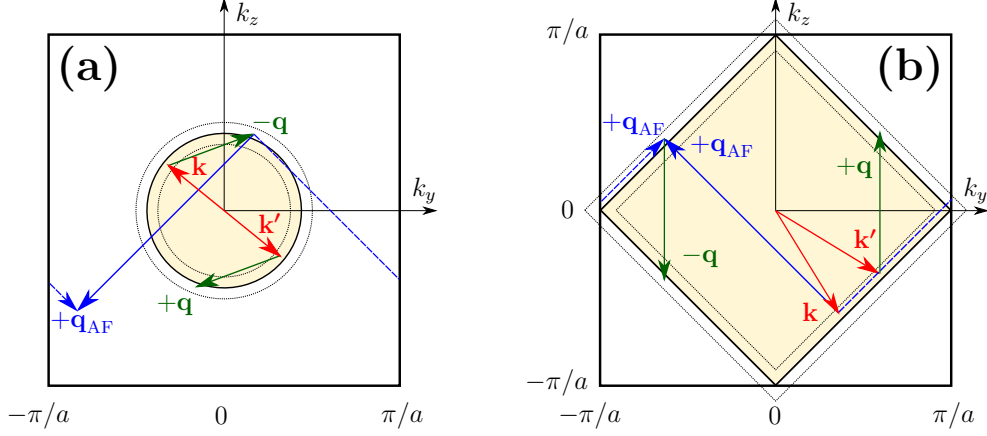
**Figure 6.4.** Illustration of the possible magnon-induced scattering processes in Table 6.1 for different Fermi surfaces. Here, the beige area indicates the occupied states within the Fermi surface of the fermions, and the outer black square is the first Brillouin zone. In **(a)**, the Fermi surface is a circle, whereas in **(b)**, the Fermi surface overlaps with the reduced Brillouin zone of the antiferromagnetic sublattices. The dashed lines around the Fermi surface indicate the thin shell where the magnon-mediated interaction is the most significant. The thickness of this shell is proportional to the magnon energy $\epsilon_{\alpha/\beta,\mathbf{q}}$. Note that only two out of four possible Umklapp scattering processes are illustrated (in solid and dashed blue arrows). The reverse processes ($+\mathbf{q}_{AF} \to -\mathbf{q}_{AF}$) are also possible and will end up in the same point in the Brillouin zone as the two Umklapp processes that are illustrated.

because we need to pair two populated states (i.e. within the surface) with two un-populated states (outside the surface), and the relevant magnon scattering energies are typically much lower than the Fermi energy. We must then find a set of momenta $\mathbf{k}$, $\mathbf{k}'$, and $\mathbf{q}$ such that all the scattered states are within the thin shell. For normal scatterings, the main contributions will come from the case where $\mathbf{k}' = -\mathbf{k}$. This is because for any state $\mathbf{k} - \mathbf{q}$ that lies within the thin shell around the Fermi surface, the state $\mathbf{k}' + \mathbf{q}$ will also lie within the shell (at least if the material is inversion symmetric), as shown in Fig. 6.4 (a). This is the ansatz used in the Bardeen–Cooper–Schrieffer (BCS) theory of superconductivity [125]. However, the situation starts to become complicated when taking processes such as 2 and 3 in the above list into consideration, as we then need to fit states that have undergone an Umklapp scattering with the antiferromagnetic lattice into the thin shell around the Fermi surface. This problem is illustrated in Fig. 6.4 (a) for a circular Fermi surface. For a general Fermi surface, there can be very few, if any, scattering processes where

it is possible to find a set of states within the thin shell. One exception is when
the Fermi surface overlaps with the reduced Brillouin zone of the antiferromagnetic
sublattices, as illustrated in Fig. 6.4 (b). For such Fermi surfaces, one can still ob-
tain a significant magnon-mediated fermion-fermion interaction, as was theoretically
studied in Ref. [126]. In the work presented in this thesis, we will focus on fermions
that are well described by a quadratic dispersion, meaning we that are far away from
the case of half filling that is illustrated in Fig. 6.4 (b). Because processes involving
Umklapp scattering will typically not be significant for small circular Fermi surfaces
for the reasons discussed above, it is most pertinent to instead focus on the normal
scattering process in this scenario.

    As shown in Table 6.1 and Eq. (6.16), normal scattering processes are pro-
portional to $\tilde{J}_{\eta,\lambda}^-(\mathbf{q})\tilde{J}_{\eta,\lambda'}^-(\mathbf{q})$ ($\eta = \alpha, \beta$), which is also somewhat problematic. For
most antiferromagnetic materials, we have that $u_\mathbf{q} \sim v_\mathbf{q}$, meaning that if the $s$-$d$
coupling strengths $J_{s\text{-}d,A}^\lambda$ and $J_{s\text{-}d,B}^\lambda$ to the two antiferromagnetic sublattices take on
similar values, the effective coupling constants $\tilde{J}_{\eta,\lambda}^-(\mathbf{q})$ become very small. However,
if $J_{s\text{-}d,A}^\lambda$ and $J_{s\text{-}d,B}^\lambda$ are very different, $\tilde{J}_{\eta,\lambda}^-(\mathbf{q})$ can in fact become very large. One way
to make these very different is by considering uncompensated interfaces instead of
compensated interfaces, as illustrated in Figs. 3.4 (a) and 3.4 (b). The fermions
then primarily couple to the spins of the sublattice present at the interface, and
we can then neglect the coupling to the other sublattice by setting either $J_{s\text{-}d,A}^\lambda$ or
$J_{s\text{-}d,B}^\lambda$ to zero. The effective coupling constant $\tilde{J}_{\eta,\lambda}^-(\mathbf{q})$ then becomes proportional
to either $J_{s\text{-}d,A}^\lambda$ or $J_{s\text{-}d,B}^\lambda$ and is also enhanced by a Bogoliubov coefficient $u_\mathbf{q}$ or $v_\mathbf{q}$,
which can typically be a relatively large number. This enhancement occurs because
the fermions couple to the spin fluctuations on a single antiferromagnetic sublattice
instead of coupling directly to the net spin of the eigenexcitations in the system.
The spin fluctuations within each antiferromagnetic sublattice can be quite large,
which can be verified rather straightforwardly by studying the inverse of the Bogoli-
ubov transformation in Eq. (4.6). By taking the expectation value of the number of
sublattice magnons $a_\mathbf{q}$ and $b_\mathbf{q}$ living on sublattices $A$ and $B$, respectively, we find

$$\langle a_\mathbf{q}^\dagger a_\mathbf{q} \rangle = |u_\mathbf{q}|^2 \langle \beta_\mathbf{q}^\dagger \beta_\mathbf{q} \rangle + |v_\mathbf{q}|^2 \langle \alpha_{-\mathbf{q}}^\dagger \alpha_{-\mathbf{q}} \rangle, \tag{6.18a}$$

$$\langle b_\mathbf{q}^\dagger b_\mathbf{q} \rangle = |u_\mathbf{q}|^2 \langle \alpha_\mathbf{q}^\dagger \alpha_\mathbf{q} \rangle + |v_\mathbf{q}|^2 \langle \beta_{-\mathbf{q}}^\dagger \beta_{-\mathbf{q}} \rangle. \tag{6.18b}$$

For each eigenmagnon $\alpha_\mathbf{q}$, there is an average number of $|v_\mathbf{q}|^2$ sublattice magnons on
sublattice $A$ and an average number of $|u_\mathbf{q}|^2$ sublattice magnons on sublattice $B$. A
similar result is obtained for the eigenmagnons $\beta_\mathbf{q}$. Using the Bogoliubov coefficients
in Eq. (4.11), we find that in the long-wavelength limit in an exchange approxima-

tion (anisotropy $[\omega_\parallel] \ll$ exchange $[\omega_E]$), the number of sublattice magnons per eigen-magnon is $|u_\mathbf{0}|^2 \approx |v_\mathbf{0}|^2 \approx 2^{-3/2}\sqrt{\omega_E/\omega_\parallel}$. Because the ratio $\omega_E/\omega_\parallel$ can be quite large, this leads to large spin fluctuations on the antiferromagnetic sublattices. When one can couple directly to these large excitations existing on the antiferromagnetic sub-lattices, which can be achieved using uncompensated interfaces as mentioned earlier, this can induce strong interactions between fermions that are mediated by the an-tiferromagnetic magnons. This idea is exploited in Paper [4], where by utilizing uncompensated interfaces, we achieve an enhanced magnon-fermion interaction and thereby an enhanced fermion-fermion interaction mediated by the magnons. This can be used to obtain significant condensation temperatures for e.g. indirect exciton condensates.

The enhancement by coupling to individual magnetic sublattices in antiferro-magnets was suggested in a recent work by Kamra et al. in Ref. [127]. Therein, it is shown that the ground state and eigenexcitations in easy-axis antiferromagnetic insulators are highly squeezed Fock states, with an analogy to squeezed states in quantum optics, and that each eigenexcitation consists of a large excitation at each of the antiferromagnetic sublattices.

Let us briefly return to the discussion of the two different models for spin pumping at antiferromagnetic interfaces in Section 3.3.2, Chapter 3. The present discussion of the interface dependence of the magnon-fermion interaction explains the difference between the two models of spin pumping for antiferromagnets because spin pumping is also a result of magnon-fermion interactions at magnetic interfaces. In the model proposed by Kamra and Belzig [57], they only consider normal scat-tering processes between the magnon and the fermion. As we noted in the previous paragraph, this interaction becomes quite weak for perfectly compensated interfaces. However, in the model proposed by Cheng et al. [60], they include the Umklapp scattering processes and consider a tight-binding model at half filling, which leads to a Fermi surface as in Fig. 6.4 (b). Consequently, the results presented above ex-plain how Cheng et al. are able to find significant spin pumping from compensated interfaces in their considered case.

### 6.3.3 Controlling the sign of the interaction by interface design

In addition to having the benefit of enabling strong magnon-mediated interactions, uncompensated interfaces also have another interesting effect when the fermions

couple to the magnons at two distinct magnetic interfaces. An example of such a system is a trilayer system in which an antiferromagnetic insulator is sandwiched between two fermion reservoirs, as illustrated in Fig. 6.5. As we will soon see, in such systems, it is possible to control whether the magnon-mediated interaction between the two fermion reservoirs is attractive or repulsive by varying the thickness of the antiferromagnet by a single atomic layer. This allows for more variation in the applications of the magnon-mediated interactions. For instance, we can tune the system between having attractive effective electron-electron interactions to the opposite case where the magnons cause the electrons in the two reservoirs to further repel each other. The latter case is investigated in Paper [4]. Moreover, when the magnon-mediated interaction is combined with other interactions, such as the Coulomb interaction, this can be used to control the spin state of the two interacting fermions. Although the Coulomb interaction is independent of spin, the magnon-mediated interaction only works in one spin channel: the $S_z = 0$ spin-triplet channel [4] (i.e. $\left[|\uparrow\downarrow\rangle + |\downarrow\uparrow\rangle\right]/\sqrt{2}$). Assuming that the Coulomb and magnon-mediated interactions can work in the same momentum channels, which is the case for indirect exciton condensation [4], one can then make the $S_z = 0$ spin-triplet pairing more/less favorable by tuning the magnon-mediated potential between being attractive or repulsive.

We will now show how one obtains this tunability of the sign of the magnon-mediated interaction in trilayer systems where an antiferromagnetic insulator is sandwiched between two fermion reservoirs, as shown in Fig. 6.5. Now that we study uncompensated interfaces, the coupling constants to the magnetic sublattices can for simplicity be treated as spatially uniform within each interface, unlike for the case of a compensated interface as in Eq. (6.14). For uncompensated interfaces where we have a perfect one-to-one matching of the atoms in the nonmagnetic and antiferromagnetic layers, the only contribution to the magnon-mediated fermion interaction in Eq. (6.15) is from normal scattering[1] (i.e. $ss' = --$). The magnon-mediated potential for uncompensated interfaces can be written as the potential $U_{\sigma,\lambda\lambda'}^{\eta,--}$ in Eq. (6.16) under the substitution $\tilde{J}_{\eta,\lambda}^{-}(\mathbf{q})\tilde{J}_{\eta,\lambda'}^{-}(\mathbf{q}) \rightarrow J_{\eta}^{\lambda}(\mathbf{q})J_{\eta}^{\lambda'}(\mathbf{q})$, where we have introduced the new effective coupling constants

$$J_{\alpha}^{\lambda}(\mathbf{q}) = v_{\mathbf{q}}J_{s\text{-}d,A}^{\lambda} - u_{\mathbf{q}}J_{s\text{-}d,B}^{\lambda}\,, \tag{6.19a}$$

$$J_{\beta}^{\lambda}(\mathbf{q}) = v_{\mathbf{q}}J_{s\text{-}d,B}^{\lambda} - u_{\mathbf{q}}J_{s\text{-}d,A}^{\lambda}\,. \tag{6.19b}$$

---

[1] In this case, the nonmagnetic and antiferromagnetic layers have the same periodicity and the same first Brillouin zone, and the fermion momentum is therefore invariant under an Umklapp scattering with the antiferromagnetic lattice
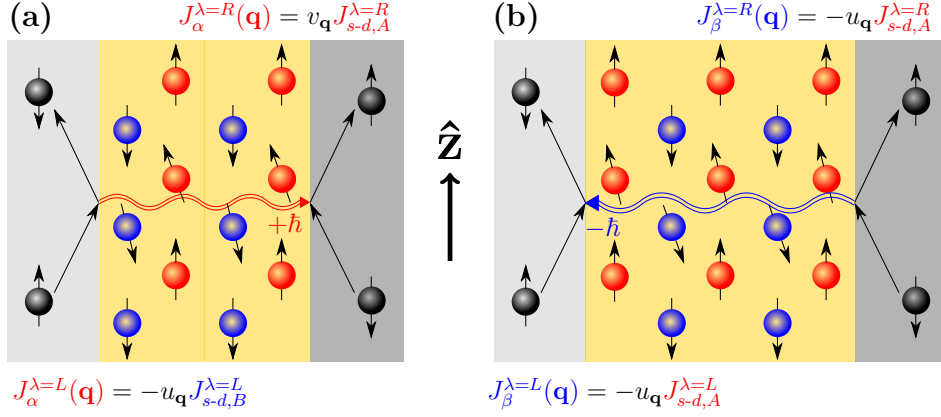
**(a)** $J_{\alpha}^{\lambda=R}(\mathbf{q}) = v_{\mathbf{q}} J_{s\text{-}d,A}^{\lambda=R}$

**(b)** $J_{\beta}^{\lambda=R}(\mathbf{q}) = -u_{\mathbf{q}} J_{s\text{-}d,A}^{\lambda=R}$

$+\hbar$

$\hat{\mathbf{z}}$

$-\hbar$

$J_{\alpha}^{\lambda=L}(\mathbf{q}) = -u_{\mathbf{q}} J_{s\text{-}d,B}^{\lambda=L}$

$J_{\beta}^{\lambda=L}(\mathbf{q}) = -u_{\mathbf{q}} J_{s\text{-}d,A}^{\lambda=L}$

**Figure 6.5.** Interaction of two fermions via the exchange of a magnon through an antiferromagnetic insulator sandwiched between two fermion reservoirs. In (a), a spin $+\hbar$ magnon ($\alpha$ eigenmagnon) propagates from left to right, whereas in (b), a spin $-\hbar$ magnon ($\beta$ eigenmagnon) propagates from right to left. The effective coupling strengths $J_{\alpha/\beta}^{\lambda}(\mathbf{q})$ between the fermions in the left and right reservoirs (denoted by $\lambda = L$ and $\lambda = R$, respectively) to the eigenmagnon are given above and below the interface for the right and left reservoirs, respectively. The figures are reproduced from Paper [4].

The label $\lambda$ on the coupling constant now indicates whether it is the *s-d* interaction at the left interface of antiferromagnetic layer ($\lambda = L$) or the *s-d* interaction at the right interface of the antiferromagnetic layer ($\lambda = R$). Since we have an uncompensated interface, only one of $J_{s\text{-}d,A}^{\lambda}$ and $J_{s\text{-}d,B}^{\lambda}$ is nonzero for a given $\lambda$. Note that $u_{\mathbf{q}}$ and $v_{\mathbf{q}}$ are positive and real according to their definitions in Eq. (4.11). These new effective coupling constants are now defined such that they take on the same sign as $J_{s\text{-}d,A/B}^{\lambda}$ if the spin of the eigenmagnon is in the same direction as the spin of the magnetic atoms at the uncompensated interface of the antiferromagnetic insulator. Similarly, $J_{\alpha}^{\lambda}$ and $J_{\beta}^{\lambda}$ have the opposite sign as $J_{s\text{-}d,A/B}^{\lambda}$ if the eigenmagnon spin is antiparallel to the spins at the uncompensated interface. This is illustrated in Fig. 6.5. As an example, $J_{\alpha}^{\lambda}$ has the same sign as $J_{s\text{-}d,A}^{\lambda}$ at interfaces with sublattice $A$, as the $\alpha$ eigenmagnons have spin $S_z = +\hbar$, and spins on sublattice $A$ point along $+\hat{\mathbf{z}}$ in equilibrium. Here, we have assumed that $S_z > 0$ on sublattice $A$ and $S_z < 0$ on sublattice $B$, in accordance with the definitions in Chapter 4 (e.g. in the Holstein–Primakoff transformation in Eq. (4.1)). Note that the sublattices in Paper [4] are defined oppositely to this, thereby leading to a slightly different definition of the effective coupling constants in the thesis compared to that in the manuscript.

As shown in Eq. (6.19) and Fig. 6.5, when we have two magnetic interfaces, the coupling constants $J_{\alpha/\beta}^{\lambda}(\mathbf{q})$ at the two interfaces can take on opposite or equal signs, as illustrated in Fig. 6.5 (a) and Fig. 6.5 (b), respectively. Since the magnon-mediated potentials $U_{\sigma,LR}^{\eta,--}$ and $U_{\sigma,RL}^{\eta,--}$ are proportional to the product of the coupling constants at the two individual interfaces, we can then have situations where $U_{\sigma,\lambda\lambda'}^{\eta,--} < 0$ and $U_{\sigma,\lambda\lambda'}^{\eta,--} > 0$, depending on what interfaces we have. From Eq. (6.16), $U_{\sigma,\lambda\lambda'}^{\alpha(\beta),--} < 0$ if $J_{\alpha(\beta)}^{\lambda=L}(\mathbf{q})$ and $J_{\alpha(\beta)}^{\lambda'=R}(\mathbf{q})$ have the same sign, and $U_{\sigma,\lambda\lambda'}^{\alpha(\beta),--} > 0$ if $J_{\alpha(\beta)}^{\lambda=L}(\mathbf{q})$ and $J_{\alpha(\beta)}^{\lambda'=R}(\mathbf{q})$ have the opposite sign. In other words, if both fermions couple ferromagnetically ($J_{\alpha/\beta}^{L,R}(\mathbf{q}) > 0$) or antiferromagnetically ($J_{\alpha/\beta}^{L,R}(\mathbf{q}) < 0$) to the same eigenmagnon, the potential has the opposite sign with respect to the case where one fermion couples ferromagnetically to the eigenmagnon, and the other fermion couples antiferromagnetically to the same eigenmagnon. Notably, whether the fermions have a symmetric or asymmetric coupling to the eigenmagnons can readily be enforced by designing the interfaces. This result can be observed by considering two different types of structures:

1. The left and right interfaces are with the opposite sublattices, e.g. the left interface is with sublattice $B$ and the right interface is with sublattice $A$. We assume here and in the next point that $J_{s\text{-}d,A/B}^{\lambda=L,R} > 0$ for simplicity. The $\alpha$ eigenmagnon then couples antiferromagnetically to the fermions in the left reservoir and ferromagnetically to the fermions in the right reservoir. The inverse is true for the $\beta$ eigenmagnons. The couplings are therefore asymmetric for both eigenmagnons, as illustrated in Fig. 6.5 (a).

2. The left and right interfaces have the same sublattice. Considering the case where only sublattice $A$ is present at both interfaces, we have that the $\alpha$ eigenmagnon couples ferromagnetically to the fermions in both reservoirs and that the $\beta$ eigenmagnon couples antiferromagnetically to the fermions in both reservoirs. The couplings are therefore symmetric for both eigenmagnons, as illustrated in Fig. 6.5 (b).

In both of the above scenarios, the contributions from the two eigenmagnons always add constructively (i.e. both eigenmagnons either mediate an attractive or repulsive interaction between the reservoirs). Consequently, one can then find that in the case of uncompensated interfaces, one can vary the potential from attractive to repulsive, or vice versa, by changing the thickness of the antiferromagnetic insulator by a single atomic layer. This allows for great tunability of the magnon-mediated interactions, as discussed previously.

# 7

# Ferromagnetism in two dimensions

Up to this point, we have primarily examined the use of antiferromagnetic insulators in spintronics. However, one of the research papers in this doctoral work, Paper [5], does not directly fall under the scope of the title of this thesis. Instead, this paper focuses on selected ferromagnetic conductors in two dimensions. Specifically, the results of this research show how one can use spin-orbit torques in these materials to control the magnetic phases of the material by applying a charge current. The methods and techniques utilized in this paper have been discussed in the previous chapters of this thesis. To provide a better understanding of the topic itself and of the results presented in Paper [5], this chapter will instead serve as an introduction to the theory of magnetic phases and phase transitions in two dimensions and some key models thereof. We will see that one of these phase transitions can also quite interestingly yield information about the superfluid phase of the indirect exciton condensate briefly mentioned in Chapter 6 and discussed in more detail in Paper [4].

## 7.1   Mermin–Wagner theorem

When studying phases and phase transitions in lower dimensions, a common rule of thumb that states whether a phase transition exists at a finite temperature in a certain dimension is the so-called *Mermin–Wagner theorem*. Mermin and Wagner studied the isotropic Heisenberg model in Eq. (2.3) for various dimensions, and in 1966, they published a paper with the following conclusions [128]:

> *"It is rigorously proved that at, any nonzero temperature, a one- or two-dimensional isotropic spin-S Heisenberg model with finite-range exchange interaction can be neither ferromagnetic nor antiferromagnetic. The method of proof is capable of excluding a variety of types of ordering in one and two dimensions."*

While they focused on the isotropic Heisenberg model, as they state, one can use similar arguments to exclude other types of long-range ordering in one and two dimensions [129]. A more general form of the theorem is that there is no phase transition of a local order parameter at finite temperatures in the form of a spontaneous breaking of a continuous symmetry of the system if the interaction effectively has a finite range and the system is strictly a one- or two-dimensional system.

The key element for the Mermin–Wagner theorem is that fluctuations are much more prevalent in lower dimensions than in higher dimensions, making the energy cost to destroy the order of the system much smaller. This is nicely demonstrated by the density of states of the fluctuations for different dimensions. Consider a quadratic dispersion of the fluctuations in the system (i.e. the excitations from the ordered state have an energy that scales as $(E - E_{\mathrm{gap}}) \propto |\mathbf{k}|^2$), for which the density of states is plotted for one to three dimensions in Fig. 7.1. Here, the energy gap $E_{\mathrm{gap}}$ is the energy cost to excite the lowest-energy fluctuation, which for the quadratic dispersion is the infinite wavelength fluctuation ($|\mathbf{k}| = 0$). For the isotropic Heisenberg model, the excitations, which are magnons as discussed in Chapter 4, are gapless for both ferromagnets and antiferromagnets. This was observed for the antiferromagnetic case in our example calculation of the magnon spectrum of the isotropic Heisenberg model in Section 4.3. One can increase the energy gap required to excite the low-energy magnons by e.g. introducing an easy-axis magnetic anisotropy to the system.

As shown in Fig. 7.1 (a), in one dimension, there is a considerable amount of available excited states just above the energy gap. The density of states actually diverges at the energy gap. In two dimensions, the density of states is just a constant
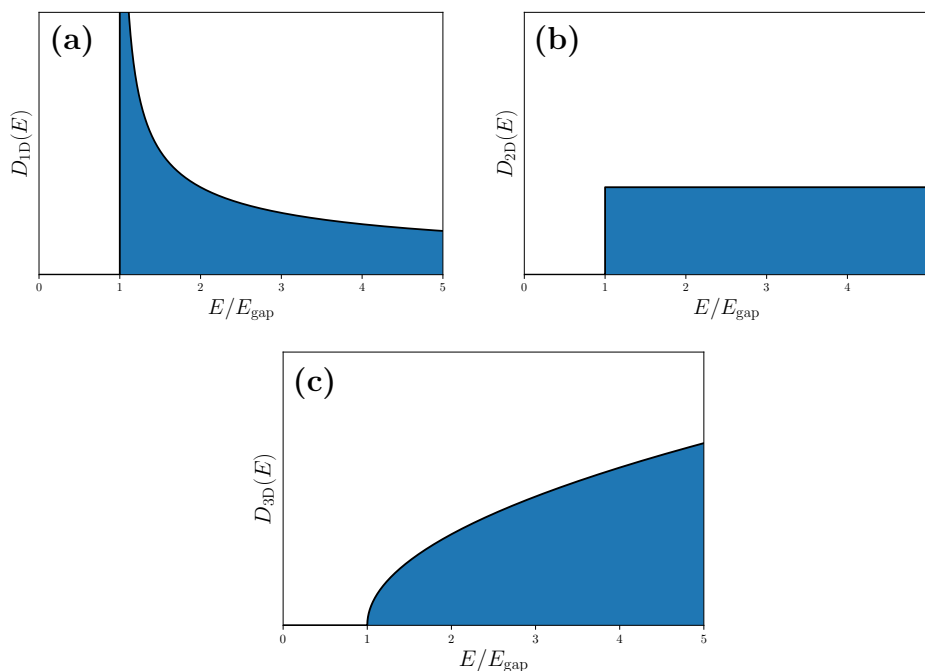
**Figure 7.1.** Density of states $D_{d\mathrm{D}}(E)$ as a function of energy for a quadratic dispersion ($[E - E_{\mathrm{gap}}] \propto |\mathbf{k}|^2$) in $d$ dimensions for (a) $d = 1$, (b) $d = 2$, and (c) $d = 3$. For the quadratic dispersion, the density of states scales as $(E - E_{\mathrm{gap}})^{\frac{d-2}{2}}$. The figures do not share a common $y$ axis.

above the energy gap. In three dimensions, however, the number of low-energy fluctuations above the gap is suppressed compared to the one- and two-dimensional cases. Here, the density of states instead increases with the energy such that more energy is required to excite enough fluctuations to destroy the system order. This enables a phase transition at finite temperatures in three dimensions. The following quote from Ref. [46] nicely summarizes the above discussion and captures the essence of the Mermin–Wagner theorem:

> *"The Mermin–Wagner theorem can be understood as the statement of a competition of energy and entropy."*

## 7.2   Magnetic phases and phase transitions in two dimensions

Despite the pessimistic outlook from the perspective of the Mermin–Wagner theorem, there are several loopholes to the theorem that indeed allow for magnetic phase transitions in two dimensions. We will now briefly go through some of the basics of phase transitions before we study two of the most famous magnetic phase transitions in two dimensions: the 2D Ising model and the 2D $XY$ model. These models exhibit phase transitions at finite temperatures that more or less circumvent the Mermin–Wagner theorem in different manners, which shall be explained later.

### 7.2.1   Phase transitions

A *phase transition* describes a fundamental change in the qualitative ordering or behavior of a state of matter. Most of us are familiar with phase transitions in every day life, such as the melting of ice to water and the boiling of water to steam. There is a plethora of such phase transitions in condensed matter physics, and examples include transitions between different magnetic orders and the transitions to a superconducting or superfluid state. In this chapter, we are primarily interested in magnetic phase transitions in ferromagnetic materials, but we will later see that these transitions also yield considerable information about other phase transitions in nonmagnetic materials.

Phase transitions are typically described by a change in the order parameter of the system. For instance, a ferromagnetic phase is described by the magnetization as an order parameter. Once the ferromagnet undergoes a phase transition to a so-called *paramagnetic* phase, where there is no magnetic ordering in the absence of an external magnetic field, the average magnetization changes from having a finite value in a certain direction to being zero in all directions. We can classify the ferromagnetic and paramagnetic phases, as well as the phase transition, by studying the behavior of the order parameter: the magnetization. This phase transition from the ferromagnetic phase to the paramagnetic phase is caused by the thermal excitation of magnons. At some temperature, the cost of exciting these thermal fluctuations becomes so low that the amount of thermal fluctuations in the system destroys the ferromagnetic ordering. For the ferromagnetic phase transition, this temperature is known as the *Curie temperature*.

Similar to ferromagnets, antiferromagnets have an order parameter that describes the antiferromagnetic phase and phase transitions, which is the Néel order
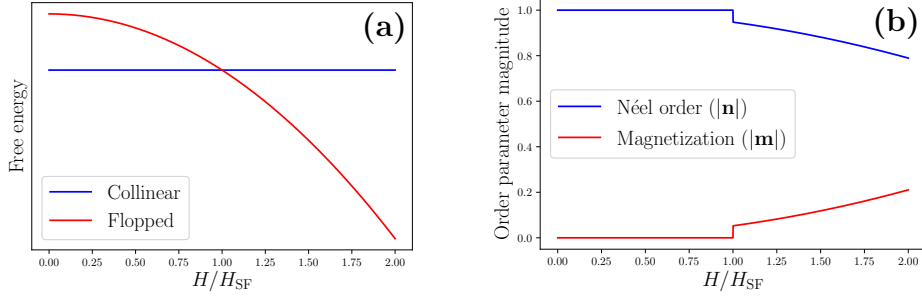
**Figure 7.2.** Underlying the spin-flop transition in antiferromagnets, there are two competing states as a function of an applied magnetic field $H$ along the easy axis: collinear ordering or a flopped/canted ordering. (a) Below the spin-flop field $H_{\mathrm{SF}}$, the collinear state is most favorable, whereas above $H_{\mathrm{SF}}$ the ground state is flopped state. The ground state free energy follows the lowest of the two curves in (a). There is therefore a discontinuity in the first derivative of the free energy at the spin-flop field $H_{\mathrm{SF}}$, causing a discontinuous jump in the order parameters in (b). This is known as a *first-order phase transition*.

parameter[1]. However, to distinguish a collinear antiferromagnetic phase from a canted antiferromagnetic phase or a ferrimagnetic phase (where one also has a net magnetization in both cases), one would have to use two order parameters: the Néel order parameter *and* the magnetization. The relative orientation between the two then decides whether we have a canted antiferromagnet or a ferrimagnet. The spin-flop transition studied in Section 2.3 is a phase transition where the antiferromagnet transitions from a collinear state to a canted state by varying the external magnetic field along the easy axis of the antiferromagnetic insulator. The variation of the free energy and order parameters in the spin-flop transition is studied in Fig. 7.2. As we discussed in Section 2.5.3, the susceptibility of the order parameters in the collinear phase with respect to an applied magnetic field perpendicular to the order parameters becomes very large at the spin-flop transition; in fact, it diverges in a linear response ansatz. This enhancement or divergence of the susceptibility at the phase transition is a common artifact or signature of phase transitions, which we exploited to amplify the signals that one could obtain from e.g. spin pumping and spin Hall magnetoresistance, as discussed in Sections 3.3.2 and 3.7.1.

---

[1]Why the staggered magnetization also has this name is now perhaps more apparent

### 7.2.2   Ising model

Moving to two-dimensional models of ferromagnetism, we will start by considering the Ising model. The Hamiltonian of the Ising model [130] can be written as

$$\mathcal{H}_{\text{Ising}} = -J \sum_{\langle i,j \rangle} S_{i,z} S_{j,z} \,. \tag{7.1}$$

We consider the ferromagnetic Ising model, where $J > 0$ for nearest-neighbor interactions only. The Ising model does not exhibit a phase transition at finite temperatures in one dimension, but quite interestingly, it exhibits one if we move to two dimensions. How can this be the case without violating the Mermin–Wagner theorem? For the Ising model in Eq. (7.1), we note that this model only considers the spins in the $z$ direction. In other words, the spins in the Ising model either point up or down, meaning that there is a discrete and not a continuous symmetry of the system, unlike the isotropic Heisenberg model. This key difference allows us to circumvent the Mermin–Wagner theorem. To obtain a physical intuition of why this is the case, we can consider the following. The Ising model can be viewed as a Heisenberg model with an infinite easy-axis anisotropy along the $z$ axis. This then completely suppresses any small fluctuations away from equilibrium where the spin has a small component in the $xy$ plane. Returning to the discussion in Section 4.3 regarding the energy cost of local fluctuations vs collective excitations, the long-wavelength magnons will no longer be the lowest-energy excitations in the system, and the local spin-flip excitations will instead take this role. As we observed for the antiferromagnetic case in Section 4.3, the local spin-flip excitations cost much more energy than the long-wavelength magnons for the isotropic Heisenberg model. Essentially, this means that in the Ising model, the energy gap for the excitations (see Fig. 7.1 (b)) that destroy the ferromagnetic phase becomes significant such that at sufficiently low temperatures, there are not enough thermal fluctuations to destroy the magnetic order.

Not only does the two-dimensional Ising model exhibit a phase transition at finite temperatures but it also has an analytical solution, as was derived by Lars Onsager in 1944 [131]. The full temperature dependence of the magnetization ($M \propto \langle S_z \rangle$) in the two-dimensional Ising model was found to be [132]

$$\frac{|M|}{M_S} = \left[ 1 - \frac{1}{\sinh\left(2\beta J\right)^4} \right]^{1/8} , \tag{7.2}$$

where $\beta = 1/(k_B T)$ and $M_s$ is the saturation magnetization (i.e. value of the magnetization when all spins point in the same direction). The magnetization vanishes
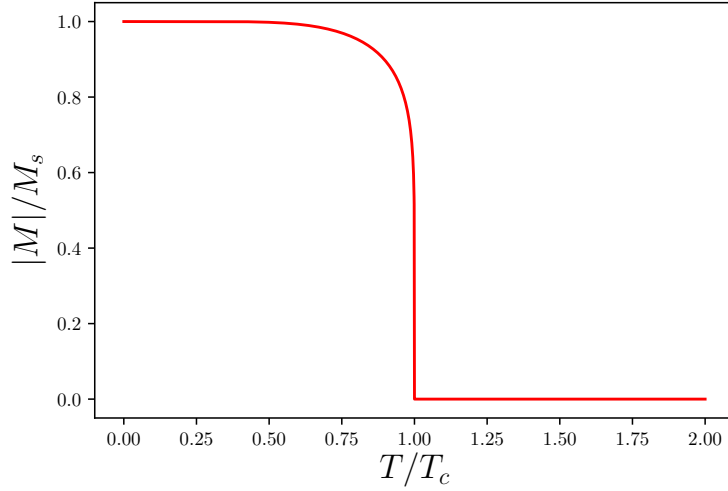
**Figure 7.3.** Normalized magnetization as a function of temperature. The magnetization falls off quickly as it approaches the Curie temperature $T_c$, and it vanishes completely above it.

above the Curie temperature $T_c = 2J/\left[k_B \ln\left(1 + \sqrt{2}\right)\right]$ [131]. The magnetization in the two-dimensional Ising model is plotted as a function of temperature in Fig. 7.3. Notably, if one compares the behavior of the magnetization in the Ising model in Fig. 7.3 to the behavior of the antiferromagnetic order parameters in Fig 7.2 (b) around their respective critical points, one finds that their behavior is qualitatively different. There is a discontinuous jump in the order parameters at the critical point in the antiferromagnetic spin-flop transition; however, in the two-dimensional Ising model, the order parameter is a continuous function of the temperature, but its derivative is discontinuous at the critical point. The phase transition in the two-dimensional Ising model is thus a second-order or *continuous phase transition*. If one introduces the normalized temperature deviation from the Curie temperature $\Delta\tau \equiv (T_c - T)/T_c$ and performs a series expansion of the order parameter (magnetization) just below the critical point to the lowest order in $\Delta\tau$, one finds that

$$\left.\frac{|M|}{M_s}\right|_{T \to T_c^-} \propto \Delta\tau^{\mathcal{B}} + \mathcal{O}\left(\Delta\tau^{\mathcal{B}+1}\right) \tag{7.3}$$

with $\mathcal{B} = 1/8$. Here, $\mathcal{B}$ is a *critical exponent*, describing the leading order behavior

of the order parameter close to the critical point[2].

This power-law dependence close to the critical point is not unique to the order parameter. For continuous phase transitions, one can describe many properties of the system by such power laws close to the critical point. For instance, as mentioned earlier, the susceptibility of the system often diverges at the critical point. In the two-dimensional field-free Ising model, the susceptibility diverges as $\chi \equiv \left(\frac{\partial M}{\partial h}\right)_{h \to 0} \propto |\Delta\tau|^{-\gamma}$ directly above and below the critical temperature, with $\gamma = 7/4$ being the critical exponent for the susceptibility [133]. Here, $h$ is a magnetic field along the spin axis. Another quantity of interest is the spatial dependence of the correlation function

$$G(\mathbf{r} - \mathbf{r}') \equiv \left[\langle S_z(\mathbf{r})S_z(\mathbf{r}')\rangle - \langle S_z(\mathbf{r})\rangle\langle S_z(\mathbf{r}')\rangle\right] \propto \frac{1}{|\mathbf{r} - \mathbf{r}'|^{d-2+\eta}} \exp(-\frac{|\mathbf{r} - \mathbf{r}'|}{\xi}), \quad (7.4)$$

which is a measure of the correlation between the fluctuations in the order parameter at positions $\mathbf{r}$ and $\mathbf{r}'$ [133]. Generally, the correlation between the fluctuations decays exponentially, but exactly at the critical point $T = T_c$, the correlation length $\xi$ diverges as $\xi \propto |\Delta\tau|^{-\nu}$, where $\nu = 1$ is the value of the critical exponent for the two-dimensional Ising model. At the critical point, we then go from having an exponential decay of the correlation in the fluctuations to an algebraic dependence $\propto |\mathbf{r} - \mathbf{r}'|^{-(d-2+\eta)}$, with $d$ being the number of dimensions, and $\eta$ is the critical exponent known as the *anomalous dimension*. The anomalous dimension is the deviation in the algebraic power scaling from what one would obtain using mean field theory. For the two-dimensional Ising model, the anomalous dimension is $\eta = 1/4$. What the divergence in the correlation length means is that while a typical length scale in the fluctuations exists above and below the critical temperature, this is not the case at the critical point. At the point of the phase transition, fluctuations occur at all length scales, and the fluctuations have a long-range correlation over the entire system. This behavior occurs despite the fact that the Ising model we considered only has short-ranged nearest-neighbor interactions! This feature is not only the case for the Ising model but also for all continuous phase transitions.

---

[2]Normally, the symbol $\beta$ is used to describe the critical exponent of the order parameter, but $\mathcal{B}$ is used here instead to avoid confusion with the inverse temperature $\beta = 1/(k_B T)$

### 7.2.3 $XY$ model

Let us now complicate our model and move from the two-dimensional Ising model to the two-dimensional $XY$ model, given by the Hamiltonian

$$\mathcal{H}_{XY} = -J \sum_{\langle i,j \rangle} \left( S_{i,x} S_{j,x} + S_{i,y} S_{j,y} \right) . \tag{7.5}$$

We now allow the spins to lie in a plane instead of just along one axis, as in the Ising model. As in the previous subsection, we consider the ferromagnetic case ($J > 0$) with nearest-neighbor interactions only. The $XY$ model then describes e.g. an easy-plane ferromagnet, but it can also describe physical effects such as superfluidity [134]. For the two-dimensional Ising model, we argued that the discrete values of the order parameter allowed us to circumvent the Mermin–Wagner theorem. However, now that we have allowed for continuous values of the order parameter within a plane, how do we circumvent the Mermin–Wagner theorem for the two-dimensional $XY$ model? Answer: the Mermin–Wagner theorem is *not* circumvented and thereby forbids true long-range magnetic order in this model, meaning that in an infinite system, we have $\langle \mathbf{S} \rangle = \mathbf{0}$ and a vanishing net spin for finite temperatures. Because the average spin/magnetization is zero in any given direction, the magnetic phase of the $XY$ model does not spontaneously break the continuous spin symmetry in the isotropic $xy$ plane. This does not mean, however, that the model does not exhibit interesting magnetic phases or phase transitions. Notably, the two-dimensional $XY$ model exhibits a very interesting phase transition that is very distinct from the more conventional phase transitions in e.g. the Ising model.

We observed in the previous subsection that the phase transition in the Ising model is characterized by the continuous change in the order parameter (magnetization) from a finite value below the Curie temperature $T_c$ to vanishing above $T_c$. This does not occur for the $XY$ model, as the net spin/magnetization is zero for any finite temperature. Instead, the phase transition manifests itself in other properties of the system. For instance, by studying the generalization of the correlation function in Eq. (7.4) to the two-dimensional $XY$ model,

$$G_{XY}^{\mathrm{2D}}(\mathbf{r} - \mathbf{r}') \equiv \langle \mathbf{S}(\mathbf{r}) \cdot \mathbf{S}(\mathbf{r}') \rangle - \langle \mathbf{S}(\mathbf{r}) \rangle \cdot \langle \mathbf{S}(\mathbf{r}') \rangle = \langle \mathbf{S}(\mathbf{r}) \cdot \mathbf{S}(\mathbf{r}') \rangle , \tag{7.6}$$

one finds that it behaves very differently at low and high temperatures. At low temperatures, this correlation function follows an algebraic power law $\sim |\mathbf{r} - \mathbf{r}'|^{-\eta}$ with $\eta = k_B T / 4\pi J$ for sufficiently large $|\mathbf{r} - \mathbf{r}'|$ [135, 136], whereas for high temperatures, the correlation follows an exponential decay $\sim \exp(-|\mathbf{r} - \mathbf{r}'|/\xi)$. As it is

impossible to asymptotically match the power law with the exponential decay, the correlation function has to undergo a qualitative transition at some finite transition temperature. This transition is quite different from the one in the two-dimensional Ising model. In the Ising model, we observed in the previous subsection that the correlation length diverged both above and below the phase transition and that the correlation function in Eq. (7.4) was described by a power law exactly at the Curie temperature. In the $XY$ model, however, the correlation function in Eq. (7.6) is described by a power law in the *entire* low-temperature phase. This power law is described by the anomalous dimension $\eta$, which actually depends on the temperature of the system. The correlation length $\xi$ only diverges from the high-temperature side of the phase transition as $\xi \propto \exp(\text{const}/\sqrt{T - T_{\text{BKT}}})$ [137], which diverges much faster than the algebraic divergence in the Ising model described by the critical exponent $\nu$. Here, $T_{\text{BKT}} = \pi J/k_B$ [136] is the critical temperature of the *Berezinskiĭ–Kosterlitz–Thouless (BKT) phase transition*. Note that at the temperature $T_{\text{BKT}}$, the anomalous dimension in the $XY$ model and Ising model take on the same value, $\eta = 1/4$. By comparing the correlation functions for the Ising model and the $XY$ model, we find that the entire low-temperature phase in the $XY$ model has similarities to the Ising model exactly at the critical point, such as the power law dependence and divergent correlation length. In some sense, one can therefore think of the entire low-temperature phase of the $XY$ model as being critical. In addition to the divergence of the correlation length at $T_{\text{BKT}}$, there is also a jump in the *spin-wave stiffness* (also known as *helicity modulus*) or the *superfluid density* [134, 138]. These can then be used as a measure of the order parameter in the BKT phase transition and can also be used in its experimental detection [139].

The peculiar phase transition in the two-dimensional $XY$ model did not fit into the framework of more conventional phase transitions, such as the melting of ice, or the magnetic phase transitions in the two-dimensional Ising model or three-dimensional isotropic Heisenberg model. The phase transition in the two-dimensional $XY$ model was described by Berezinskiĭ, Kosterlitz, and Thouless in the early 1970s [135–137, 140], and hence the name BKT phase transition. In 2016, Thouless, Kosterlitz, and Haldane won the Nobel prize *"for theoretical discoveries of topological phase transitions and topological phases of matter"* [141], where Thouless and Kosterlitz's description of the phase transition in the two-dimensional $XY$ model was an important part of the reason for them winning the prize. What makes the phase transition in the $XY$ model topological? Berezinskiĭ, Kosterlitz, and Thouless described the phase transition in terms of spin vortices and antivortices, as illustrated
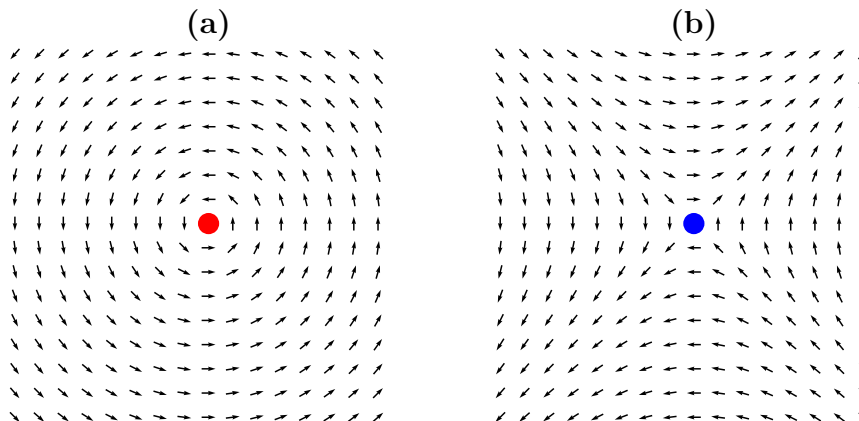
**Figure 7.4.** (a) Spin vortex with winding number +1 and (b) spin antivortex with winding number -1. The winding number is defined as how many multiples of $2\pi$ the spins rotate along an enclosed path around the vortex or antivortex cores, illustrated with red and blue dots, respectively. At the (anti)vortex core, there is a singularity, and the spin is not defined.

in Fig. 7.4. These individual spin structures are topologically protected, meaning that no small perturbation can destroy the topological charge associated with the winding number of the (anti)vortex. What Berezinskiĭ, Kosterlitz, and Thouless discovered was that at low temperatures, the vortices and antivortices form tightly bound vortex-antivortex pairs that have little to no effect on the spin ordering far from the pair. However, at the critical temperature $T_{\mathrm{BKT}}$ of the BKT phase transition, entropy makes it favorable to break up the vortex-antivortex pairs, which causes long-range spin-spin correlations to start dropping exponentially. Above this temperature, it is also energetically favorable to add more vortex-antivortex pairs to the system, which can be done because a topologically trivial state (e.g. a spatially uniform spin structure) is topologically equivalent to a vortex-antivortex pair as the sum of the topological charges is equal to zero for both systems. In the high-temperature phase, vortex-antivortex pairs are then spontaneously created and can then break apart from one another. This process is illustrated in Fig. 7.5.

In the two-dimensional Ising model, we have what is known as *true long-ranged order*; thus, the spin-spin correlation $\langle \mathbf{S}(\mathbf{r}) \cdot \mathbf{S}(\mathbf{r}') \rangle$ is finite regardless of the distance $|\mathbf{r} - \mathbf{r}'|$. This can be understood intuitively by recalling that below the Curie temperature, all spins would like to point in the same direction, and consequently, all spins are correlated with each other. Although true long-ranged order does not exist
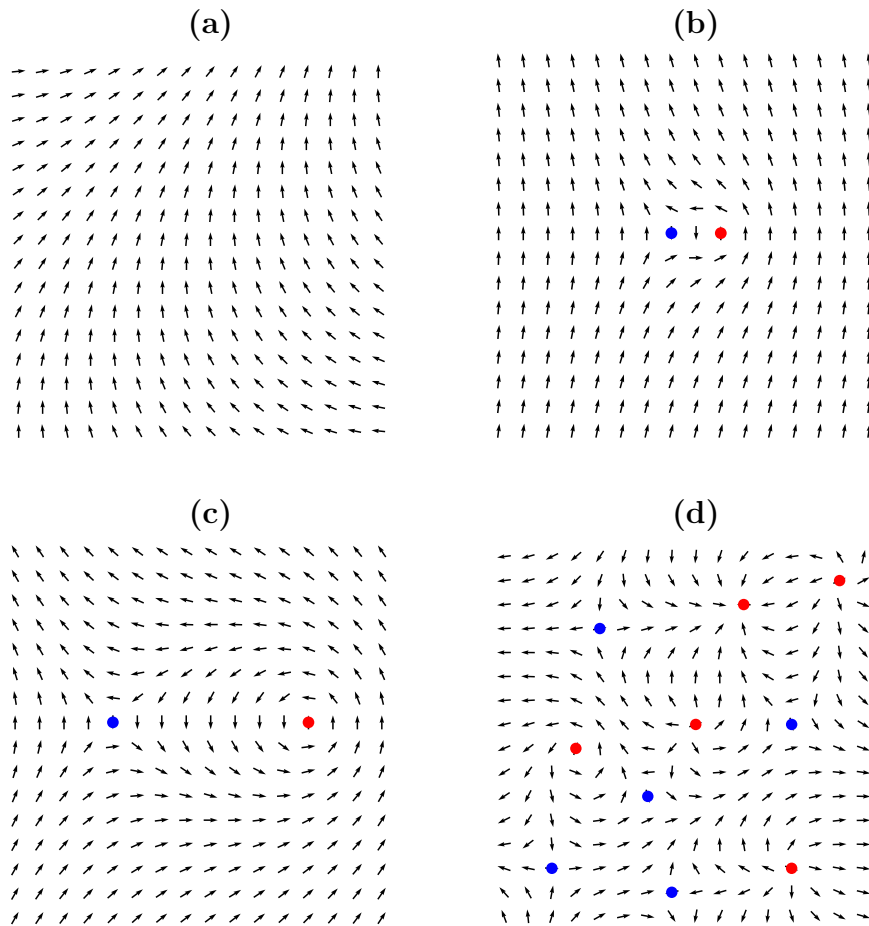
**(a)**

**(b)**

**(c)**

**(d)**



**Figure 7.5.**  Illustration of the BKT phase transition in the two-dimensional $XY$
model. (a) Illustration of what a low-temperature phase of the $XY$ model might look
like for a section of the system.  In (b), we have a tightly bound vortex-antivortex pair
(the cores illustrated with red and blue circles, respectively) on top of a uniform spin
field. This pair causes an energy cost in an area close to the pair, but far away from
the pair, the spins are not affected by them due to the cancellation of the topological
charges.  At the BKT phase transition temperature $T_{\text{BKT}}$, the pairs start unbinding,
as shown in (c), causing larger fluctuations in the system.  In a high-temperature
phase, we then have a "gas" of free vortices and antivortices, as shown in (d), that
make any spin-spin correlations decay exponentially.

in the two-dimensional $XY$ model, there is a so-called *quasi long-ranged order* at low
temperatures. We see that when $k_B T \ll 4\pi J$ ($\eta \ll 1$), the spin-spin correlation is

very weakly decaying as a function of the separation between the spins. This means that while for infinite distances the spin-spin correlation goes to zero, spins can still be highly correlated over very large distances. In other words, while we must have that the net spin of the system vanishes for infinite systems, if we just focus on a smaller segment of the system, we can have a finite value for the net spin. However, the expectation values of such segments that are significantly spatially separated will point in different directions because the Mermin–Wagner theorem forbids any spontaneous breaking of the symmetry for the global system as a whole.

### 7.2.4   Universality classes

Some readers might have been reading about the Ising and $XY$ models and been thinking "this is all well and good, but why should we care that much about the phase transitions in idealistic models such as these? Systems with an infinitely strong easy-axis anisotropy or a perfectly isotropic easy plane will surely not be found in any realistic physical system." This is where the concept of *universality classes* comes in and the theory of phase transitions starts to become *really* interesting. It turns out that the phase transitions in the Ising and $XY$ models can describe critical phenomena in entirely different systems if they belong to the same universality class. In practice, this means that phase transitions in the same universality class share the same critical exponents and behavior close to the critical point. The universality class is decided by the dimensionality of the system and the dimensionality of the order parameter. For the Ising model, we have a scalar order parameter of dimensionality one. Naturally, a uniaxial ferromagnet will have the same dimensionality of the order parameter as the Ising model, even if the uniaxial anisotropy is finite, and they therefore belong to the same universality class. The same applies to a wide variety of nonmagnetic systems, e.g. in the liquid-gas phase transition, we also have a scalar order parameter: the density. Consequently, a liquid-gas phase transition in $d$ spatial dimensions belongs to the same universality class as the Ising model in $d$ spatial dimensions [46].

The reason why such different systems behave exactly the same near a phase transition is that systems are scale invariant at this critical point. This is illustrated by the divergence of the correlation length between the fluctuations at the phase transition. Consequently, the microscopic details and mechanisms of the ordering become irrelevant to the asymptotic behavior of the system as a whole. Note, however, that this universality only applies to the system behavior near the critical point. The location of the critical point depends on the microscopic details, and it is

therefore not universal. As a simple example, a two-dimensional Ising ferromagnet will have a different Curie temperature from a uniaxial ferromagnet with a finite anisotropy. This can be intuitively understood as the Curie temperature has to go to zero when the anisotropy vanishes because an isotropic Heisenberg model has no phase transition in two dimensions according to the Mermin–Wagner theorem.

While the topological BKT phase transition in the two-dimensional *XY* model is very different from phase transitions in models such as the Ising model, the same concept can be found here, and it constitutes its own universality class. The BKT phase transition appears in a number of exotic systems, including the transition in a two-dimensional Coulomb gas from a state of tightly bound electric dipoles (taking the role of the vortex-antivortex pairs) to a plasma of freely moving charged particles [142] and the transition from a normal to superfluid state in two dimensions [139]. In the previous chapter, we briefly discussed the concept of condensation of indirect excitons via magnon-mediated interactions. The indirect exciton condensate also exhibits a BKT phase transition, and it is closely related to the two-dimensional Coulomb gas[3] and superfluids, as a condensate of excitons can have a dissipation-less superfluid transport [143]. Note, however, that the critical phase transition temperature calculated in Paper [4] is not that of the BKT phase transition where the excitons form a superfluid but rather the temperature where the bound pairs of electrons and holes start forming a coherent state. These temperatures are, on the other hand, very similar in the weak coupling limit [144].

## 7.3   Current control of magnetic phases in two-dimensional $Fe_3GeTe_2$

The two-dimensional Ising and *XY* models in magnetic systems have long primarily been of theoretical interest, as manufacturing two-dimensional magnetic materials for experiments has been understandably quite challenging. However, the successful isolation of the two-dimensional material graphene in 2004 [145] paved the way for isolating and studying various two-dimensional materials. Over the past two to three years, one has been able to manufacture two-dimensional materials that exhibit a magnetic ordering at finite temperatures [146–153]. These materials are so-called van der Waals materials, consisting of weakly bound layers. In one of these materials, $Fe_3GeTe_2$ (FGT), experimentalists were able to manufacture samples of

---

[3]An exciton after all is a bound pair of a negatively charged electron and a positively charged electron hole
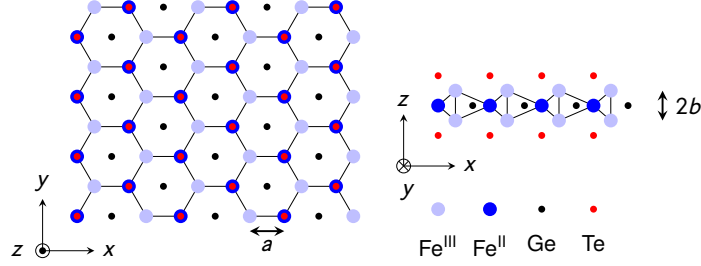
**Figure 7.6.** Crystal structure of two-dimensional Fe$_3$GeTe$_2$. The crystal structure can be seen to have an inversion symmetry along the $y$ and $z$ axes, as well as a threefold rotational symmetry around the $z$ axis. The figure is taken from Paper [5] and redrawn after Ref. [153].

various layer thicknesses down to the monolayer limit and study the layer dependence of the critical exponent $\mathcal{B}$ in the Ising model, as defined in Eq. (7.2). They found that $\mathcal{B}$ varied from taking on a value close to the estimate from the three-dimensional Ising model in the multilayer limit to estimating a range for $\mathcal{B}$ for the monolayer limit that included the value in the two-dimensional Ising model [152]. This shows that they were able to study the crossover from three to two dimensions of the critical exponents in the Ising model. FGT has also been shown to be an interesting material, as other experimentalists have been able to tune the Curie temperature of the monolayer up to room temperature via an ionic gate [153].

In Paper [5], we use Neumann's principle and the method introduced by Hals and Brataas in Ref. [79], as discussed in Section 3.6, to study the spin-orbit torques allowed by symmetry in FGT. The crystal structure of FGT is illustrated in Fig. 7.6, and it is invariant under the symmetry operations [5]

$$\mathcal{R}^y = \begin{pmatrix} 1 & 0 & 0 \\ 0 & -1 & 0 \\ 0 & 0 & 1 \end{pmatrix}, \quad \mathcal{R}^z = \begin{pmatrix} 1 & 0 & 0 \\ 0 & 1 & 0 \\ 0 & 0 & -1 \end{pmatrix}, \quad \mathcal{R}^{3z} = \frac{1}{2} \begin{pmatrix} -1 & \sqrt{3} & 0 \\ -\sqrt{3} & -1 & 0 \\ 0 & 0 & 1 \end{pmatrix}. \quad (7.7)$$

We found that to the first order in the charge-current density and to the second order in the magnetization, the spin-orbit torque can be written as [5]

$$\boldsymbol{\tau} = -|\gamma|\, \mathbf{m} \times \mathbf{H}_{\text{SOT}} \equiv -|\gamma|\, \mathbf{m} \times \Gamma_0 \begin{pmatrix} m_x J_x - m_y J_y \\ -m_y J_x - m_x J_y \\ 0 \end{pmatrix} \quad (7.8)$$

for a spatially uniform magnetization. Here, $J_x$ and $J_y$ are the $x$ and $y$ components of the charge-current density, respectively, and $\Gamma_0$ is a free parameter describing

the strength of the spin-orbit interaction. Note that this form of the spin-orbit torque not only applies to FGT but also to all materials with the same symmetry classification $D_{3h}$, which includes other two-dimensional magnetic materials [154]. In Paper [5], we noted that the spin-orbit torque in Eq. (7.8) could be written as a torque originating from an effective free energy density given by

$$f_{\text{SOT}} = M_s \Gamma_0 \left[ J_y m_x m_y - \frac{1}{2} \left( m_x^2 - m_y^2 \right) \right] = -\frac{M_s \Gamma_0 |J|}{2} \sin^2 \theta \cos \left( 2\phi + \phi_J \right) , \quad (7.9)$$

where $(m_x, m_y, m_z) \equiv (\sin\theta\cos\phi, \sin\theta\sin\phi, \cos\theta)$, $|J| = \sqrt{J_x^2 + J_y^2}$, and $\tan\phi_J \equiv J_y/J_x$. The effective field resulting from this effective free energy density as defined in Eq. (2.11) results in the same spin-orbit torque as defined in (7.8). Notably, this particular spin-orbit torque is controlled by only a single free parameter $\Gamma_0$ and can be interpreted as in-plane current-induced magnetic anisotropies. These anisotropies scale linearly with the applied current density, and the anisotropy axes depend on the direction of the applied current. The anisotropies come in the form of a pair of magnetic easy and hard axes, which are perpendicular to each other. In addition to the current-induced anisotropies, FGT also has a strong easy-axis anisotropy out of the plane, which makes it an Ising-like ferromagnet that also allows for ferromagnetic order in two dimensions.

In Fig. 7.7, we study how the magnetic anisotropies of FGT look for different charge-current density magnitudes. Notably, as we increase the current density, we go from having an out-of-plane easy axis to an in-plane easy axis, and at some critical current density, we obtain a magnetic easy plane. FGT is thus a promising playground for studying the BKT transition in a magnetic $XY$-like system, as well as the crossover from an Ising-like to an $XY$-like system in two dimensions, both of which have not yet been done in magnetic systems to the best of our knowledge. Moreover, as the Curie temperature and $T_{\text{BKT}}$ take on similar values for a given exchange coupling $J$, this shows great potential for observing the BKT transition at elevated temperatures in FGT because of its relatively high Curie temperature $\sim 130\,\text{K}$ [152]. This indicates that the low-temperature phase of easy-plane FGT could potentially be accessed by using liquid oxygen or liquid nitrogen.

The transition from an Ising-like to an $XY$-like system can also be seen by studying the magnon gap (lowest excitation energy of the system) and the Curie temperature as a function of the applied current, as shown in Fig. 7.8. We recall from the discussion in Section 7.2.2 that the finite Curie temperature in the two-dimensional Ising model was due to the suppression of the low-energy fluctuations in the form of an energy gap in the fluctuations (magnons). As shown in Fig. 7.8, in
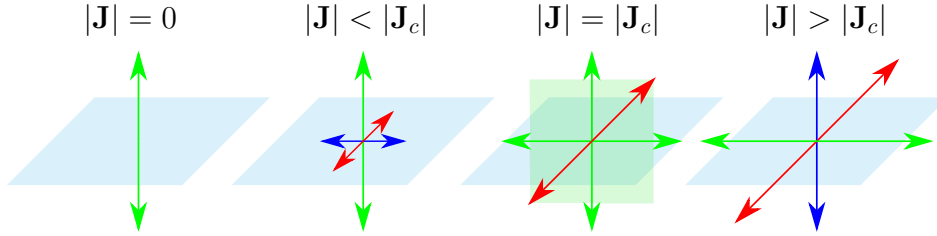
$|\mathbf{J}| = 0$        $|\mathbf{J}| < |\mathbf{J}_c|$        $|\mathbf{J}| = |\mathbf{J}_c|$        $|\mathbf{J}| > |\mathbf{J}_c|$

**Figure 7.7.** At zero applied current, FGT has an out-of-plane magnetic easy axis illustrated by the green arrows. The light blue square indicates the plane of the FGT layer. By passing a charge current through the plane, one breaks the magnetic isotropy in the plane and creates a pair of in-plane easy and hard axes, as illustrated by the blue and red arrows, respectively. However, for low current densities, these anisotropies remain smaller than the equilibrium out-of-plane anisotropy, and the in-plane anisotropy is therefore just an intermediate anisotropy axis (shown in blue to distinguish from the material's easy axis in green). At a critical current density $|\mathbf{J}_c|$, the in-plane anisotropy equals the out-of-plane anisotropy, and we obtain a magnetic easy plane, shown by the opaque green square. Above the critical current density, the in-plane anisotropy becomes the easy axis of the system, and the out-of-plane anisotropy becomes an intermediate anisotropy axis.
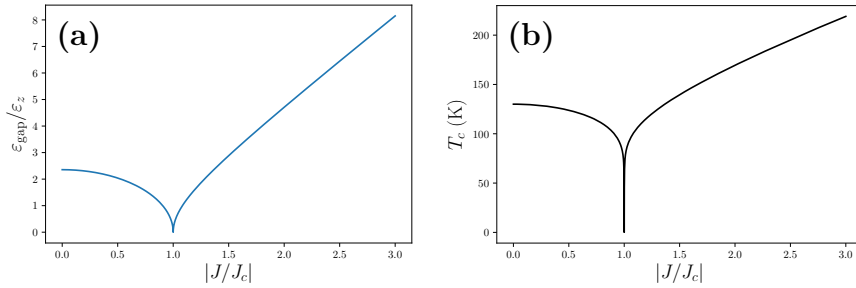


**Figure 7.8.** (a) Magnon gap $\varepsilon_{\mathrm{gap}}$ relative to the equilibrium out-of-plane anisotropy $\varepsilon_z$, and (b) Curie temperature of FGT as a function of applied in-plane current. Note that the Curie temperature is only an estimate calculated from linear response theory, which is explained in greater detail in Paper [5]. Figure (b) is taken from Paper [5].

two dimensions, the Curie temperature, below which we can have a spontaneous net magnetization, is strongly correlated with the magnon gap of the system. As the magnon gap vanishes at the critical current density, so does the Curie temperature since the Mermin–Wagner forbids any spontaneous breaking of symmetry in the easy-plane phase in two dimensions. At this point, we can instead observe the BKT

phase transition. This finding allows for an experimental approach for tuning a system between the Ising and $XY$ universality classes in two dimensions, which should host an abundance of interesting and exotic physics.

# 8

# Conclusion

We have provided the basis for understanding the fundamental concepts that are utilized and discussed in the five research papers in the remaining part of the thesis. These research papers cover a variety of topics of interest for future investigations and applications of antiferromagnetic insulators and two-dimensional ferromagnets.

A focus has been on the electrical detection and generation of spin currents in antiferromagnetic insulators in heterostructures with nonmagnetic conductors. While the theory of spin current detection and generation in ferromagnetic insulators is fairly well understood, similar phenomena with their antiferromagnetic counterpart is still actively under investigation. For instance, spin pumping from antiferromagnets has yet to be unequivocally detected. We have here investigated what materials and conditions are optimal for amplifying the pumped spin current from antiferromagnets, so that experimental detection becomes conceivable. We suggest that easy-axis antiferromagnets with a high anisotropy to exchange ratio near the spin-flop transition are great candidates for spin pumping experiments. This is because the susceptibility of the magnetic moments is significantly enhanced near this phase transition, which leads to a remarkable increase in the pumped spin current. While there has already been an experiment studying the easy-axis anti-ferromagnet $MnF_2$ near the spin-flop transition without the observation of a clear

spin pumping signal [62, 72], we also suggest other means of enhancing the signal by optimizing the polarization of the microwave source and the film thickness of the nonmagnetic conductor. We also show that the electrical generation of spin currents in antiferromagnetic insulators is enhanced for the same type of easy-axis antiferromagnetic insulators near the spin-flop transition.

We have seen that there exist different models of spin pumping from antiferromagnets with very different predictions [57, 60]. The different predictions indicate that spin pumping from antiferromagnets strongly depends on the structure of the magnetic interface. Once spin pumping from antiferromagnets has been experimentally verified, an interesting next step is to investigate the dependence of the spin pumping signal on the interface structure. Such measurements would yield critical information regarding the validity of the models of spin pumping in different regimes and grant a deeper understanding of spin dynamics in antiferromagnetic insulators.

In addition to studying the interface between antiferromagnetic insulator spintronics and conventional electronics, we have also studied a possible bridge between antiferromagnetic and ferromagnetic spintronics. Microwave cavities can induce a nonlocal interaction between distant magnetic systems mediated by the microwave photons in the cavity [96–98]. We have shown how this concept can also cause a nonlocal interaction between a ferromagnet and an antiferromagnet over macroscopic distances, even when the ferromagnetic and antiferromagnetic magnons have opposite spins. This shows great promise for integrating antiferromagnetic spintronics in various hybrid systems.

Antiferromagnetic materials have also shown to have very interesting applications other than their utilization in transport and storage of spin information. Recent proposals suggest that the large magnetic fluctuations in antiferromagnets can be utilized in the formation of quantum matter, such as superconductors. We have considered the interaction between two fermion reservoirs mediated by interactions with antiferromagnetic magnons in an antiferromagnetic insulating barrier, and derived an effective potential that describes this interaction. Interestingly, we show that this interaction can be tuned between being attractive and repulsive by varying the thickness of the antiferromagnetic material by a single atomic layer. Utilizing this, we show how an atomically thin antiferromagnetic insulator sandwiched between two doped two-dimensional semiconductors can be used to generate an indirect exciton condensate, a macroscopic coherent state of electrons and holes separated by an insulating barrier. The magnon-mediated interactions are able to achieve significant condensation temperatures, and can furthermore cooperate with

other interactions such as the Coulomb potential. Due to the strength and tunability of the interaction mediated by the antiferromagnetic fluctuations, antiferromagnetic materials have great potential in future research on strongly correlated fermion systems.

While theoreticians have been fond of modelling two-dimensional systems for a long time, putting the theories to the test has not always been feasible. Recent experimental advances have now made it possible to isolate two-dimensional magnetic materials, enabling the testing of various predictions. In light of this exciting experimental progress, we have analyzed the current-induced spin dynamics in one of these two-dimensional magnetic materials. We show that by tuning the magnitude of the applied charge current it is possible to create a magnetic easy plane in the ferromagnetic material $Fe_3GeTe_2$. This makes it possible to study the famous Berezinskiĭ–Kosterlitz–Thouless phase transition in the magnetic $XY$ model, which will reveal information about e.g. the superfluid phase transition of the indirect exciton condensate mentioned previously, but presumably at significantly higher temperatures that can be accessed by using liquid nitrogen or liquid oxygen.

# 9
# Bibliography

[1] Ø. Johansen and A. Brataas, "Spin pumping and inverse spin Hall voltages from dynamical antiferromagnets," *Phys. Rev. B*, vol. 95, p. 220408, Jun 2017.

[2] Ø. Johansen, H. Skarsvåg, and A. Brataas, "Spin-transfer antiferromagnetic resonance," *Phys. Rev. B*, vol. 97, p. 054423, Feb 2018.

[3] Ø. Johansen and A. Brataas, "Nonlocal Coupling between Antiferromagnets and Ferromagnets in Cavities," *Phys. Rev. Lett.*, vol. 121, p. 087204, Aug 2018.

[4] Ø. Johansen, A. Kamra, C. Ulloa, A. Brataas, and R. A. Duine, "Magnon-Mediated Indirect Exciton Condensation through Antiferromagnetic Insulators," *arXiv:1904.12699*, Apr 2019.

[5] Ø. Johansen, V. Risinggård, A. Sudbø, J. Linder, and A. Brataas, "Current Control of Magnetism in Two-Dimensional $Fe_3GeTe_2$," *Phys. Rev. Lett.*, vol. 122, p. 217203, May 2019.

[6] G. E. Moore, "Cramming more components onto integrated circuits," *Electronics*, vol. 38, Apr 1965.

[7] G. E. Moore, "Progress in digital integrated electronics," *International Electron Devices Meeting, IEEE*, pp. 11–13, 1975.

[8] A. S. G. Andrae and T. Edler, "On Global Electricity Usage of Communication Technology: Trends to 2030," *Challenges*, vol. 6, no. 1, pp. 117–157, 2015.

[9] J. M. D. Coey, *Magnetism and Magnetic Materials.* Cambridge University Press, 2010.

[10] S. A. Wolf, D. D. Awschalom, R. A. Buhrman, J. M. Daughton, S. von Molnár, M. L. Roukes, A. Y. Chtchelkanova, and D. M. Treger, "Spintronics: A Spin-Based Electronics Vision for the Future," *Science*, vol. 294, no. 5546, pp. 1488–1495, 2001.

[11] S. A. Wolf, A. Y. Chtchelkanova, and D. M. Treger, "Spintronics-A retrospective and perspective," *IBM J. Res. Dev.*, vol. 50, pp. 101–110, Jan 2006.

[12] M. N. Baibich, J. M. Broto, A. Fert, F. N. Van Dau, F. Petroff, P. Etienne, G. Creuzet, A. Friederich, and J. Chazelas, "Giant Magnetoresistance of (001)Fe/(001)Cr Magnetic Superlattices," *Phys. Rev. Lett.*, vol. 61, pp. 2472–2475, Nov 1988.

[13] G. Binasch, P. Grünberg, F. Saurenbach, and W. Zinn, "Enhanced magnetoresistance in layered magnetic structures with antiferromagnetic interlayer exchange," *Phys. Rev. B*, vol. 39, pp. 4828–4830, Mar 1989.

[14] "Press release: The Nobel Prize in Physics 2007." `https://www.nobelprize.org/prizes/physics/2007/press-release/`. Accessed: 29/05/2019.

[15] W. P. McCray, "How spintronics went from the lab to the iPod," *Nat. Nanotechnol.*, vol. 4, p. 2, Jan 2009.

[16] M. Julliere, "Tunneling between ferromagnetic films," *Physics Letters A*, vol. 54, no. 3, pp. 225 – 226, 1975.

[17] S. Yuasa, T. Nagahama, A. Fukushima, Y. Suzuki, and K. Ando, "Giant room-temperature magnetoresistance in single-crystal Fe/MgO/Fe magnetic tunnel junctions," *Nat. Mater.*, vol. 3, no. 12, pp. 868–871, 2004.

[18] S. S. P. Parkin, C. Kaiser, A. Panchula, P. M. Rice, B. Hughes, M. Samant, and S.-H. Yang, "Giant tunnelling magnetoresistance at room temperature with MgO (100) tunnel barriers," *Nat. Mater.*, vol. 3, no. 12, pp. 862–867, 2004.

[19] S. Ikeda, J. Hayakawa, Y. Ashizawa, Y. M. Lee, K. Miura, H. Hasegawa, M. Tsunoda, F. Matsukura, and H. Ohno, "Tunnel magnetoresistance of 604% at 300 K by suppression of Ta diffusion in CoFeB/MgO/CoFeB pseudo-spin-valves annealed at high temperature," *Appl. Phys. Lett.*, vol. 93, no. 8, p. 082508, 2008.

[20] T. Song, X. Cai, M. W.-Y. Tu, X. Zhang, B. Huang, N. P. Wilson, K. L. Seyler, L. Zhu, T. Taniguchi, K. Watanabe, M. A. McGuire, D. H. Cobden, D. Xiao, W. Yao, and X. Xu, "Giant tunneling magnetoresistance in spin-filter van der Waals heterostructures," *Science*, vol. 360, no. 6394, pp. 1214–1218, 2018.

[21] H. H. Kim, B. Yang, T. Patel, F. Sfigakis, C. Li, S. Tian, H. Lei, and A. W. Tsen, "One Million Percent Tunnel Magnetoresistance in a Magnetic van der Waals Heterostructure," *Nano Lett.*, vol. 18, pp. 4885–4890, Aug 2018.

[22] L. Berger, "Low-field magnetoresistance and domain drag in ferromagnets," *J. Appl. Phys.*, vol. 49, no. 3, pp. 2156–2161, 1978.

[23] L. Berger, "Domain drag effect in the presence of variable magnetic field or variable transport current," *J. Appl. Phys.*, vol. 50, no. B3, pp. 2137–2139, 1979.

[24] L. Berger, "Exchange interaction between ferromagnetic domain wall and electric current in very thin metallic films," *J. Appl. Phys.*, vol. 55, no. 6, pp. 1954–1956, 1984.

[25] L. Berger, "Motion of a magnetic domain wall traversed by fast-rising current pulses," *J. Appl. Phys.*, vol. 71, no. 6, pp. 2721–2726, 1992.

[26] D. Ralph and M. Stiles, "Spin transfer torques," *J. Magn. Magn. Mater.*, vol. 320, no. 7, pp. 1190 – 1216, 2008.

[27] J. Slonczewski, "Current-driven excitation of magnetic multilayers," *J. Magn. Magn. Mater.*, vol. 159, no. 1, pp. L1 – L7, 1996.

[28] L. Berger, "Emission of spin waves by a magnetic multilayer traversed by a current," *Phys. Rev. B*, vol. 54, no. 13, p. 9353, 1996.

[29] A. D. Kent and D. C. Worledge, "A new spin on magnetic memories," *Nat. Nanotechnol.*, vol. 10, p. 187, Mar 2015.

[30] "Everspin Technologies STT-MRAM products." `https://www.everspin.com/stt-mram-products`. Accessed: 05/06/2019.

[31] S. Datta and B. Das, "Electronic analog of the electro-optic modulator," *Appl. Phys. Lett.*, vol. 56, no. 7, pp. 665–667, 1990.

[32] H. C. Koo, J. H. Kwon, J. Eom, J. Chang, S. H. Han, and M. Johnson, "Control of Spin Precession in a Spin-Injected Field Effect Transistor," *Science*, vol. 325, no. 5947, pp. 1515–1518, 2009.

[33] P. Chuang, S.-C. Ho, L. W. Smith, F. Sfigakis, M. Pepper, C.-H. Chen, J.-C. Fan, J. P. Griffiths, I. Farrer, H. E. Beere, G. A. C. Jones, D. A. Ritchie, and T.-M. Chen, "All-electric all-semiconductor spin field-effect transistors," *Nat. Nanotechnol.*, vol. 10, p. 35, Dec 2014.

[34] A. Dankert and S. P. Dash, "Electrical gate control of spin current in van der Waals heterostructures at room temperature," *Nat. Commun.*, vol. 8, p. 16093, Jul 2017.

[35] Y. Kajiwara, K. Harii, S. Takahashi, J. Ohe, K. Uchida, M. Mizuguchi, H. Umezawa, H. Kawai, K. Ando, K. Takanashi, S. Maekawa, and E. Saitoh, "Transmission of electrical signals by spin-wave interconversion in a magnetic insulator," *Nature*, vol. 464, p. 262, Mar 2010.

[36] L. J. Cornelissen, J. Liu, R. A. Duine, J. B. Youssef, and B. J. van Wees, "Long-distance transport of magnon spin information in a magnetic insulator at room-temperature," *Nat. Phys.*, vol. 11, p. 1022, Sep 2015.

[37] R. Lebrun, A. Ross, S. A. Bender, A. Qaiumzadeh, L. Baldrati, J. Cramer, A. Brataas, R. A. Duine, and M. Kläui, "Tunable long-distance spin transport in a crystalline antiferromagnetic iron oxide," *Nature*, vol. 561, no. 7722, pp. 222–225, 2018.

[38] W. H. Meiklejohn and C. P. Bean, "New Magnetic Anisotropy," *Phys. Rev.*, vol. 102, pp. 1413–1414, Jun 1956.

[39] T. Jungwirth, X. Marti, P. Wadley, and J. Wunderlich, "Antiferromagnetic spintronics," *Nat. Nanotechnol.*, vol. 11, p. 231, Mar 2016.

[40] V. Baltz, A. Manchon, M. Tsoi, T. Moriyama, T. Ono, and Y. Tserkovnyak, "Antiferromagnetic spintronics," *Rev. Mod. Phys.*, vol. 90, p. 015005, Feb 2018.

[41] J. Železný, H. Gao, K. Výborný, J. Zemen, J. Mašek, A. Manchon, J. Wunderlich, J. Sinova, and T. Jungwirth, "Relativistic Néel-Order Fields Induced by Electrical Current in Antiferromagnets," *Phys. Rev. Lett.*, vol. 113, no. 15, p. 157201, 2014.

[42] P. Wadley, B. Howells, J. Železný, C. Andrews, V. Hills, R. P. Campion, V. Novák, K. Olejník, F. Maccherozzi, S. S. Dhesi, S. Y. Martin, T. Wagner, J. Wunderlich, F. Freimuth, Y. Mokrousov, J. Kuneš, J. S. Chauhan, M. J. Grzybowski, A. W. Rushforth, K. W. Edmonds, B. L. Gallagher, and T. Jungwirth, "Electrical switching of an antiferromagnet," *Science*, 2016.

[43] T. Kosub, M. Kopte, R. Hühne, P. Appel, B. Shields, P. Maletinsky, R. Hübner, M. O. Liedke, J. Fassbender, O. G. Schmidt, and D. Makarov, "Purely antiferromagnetic magnetoelectric random access memory," *Nat. Commun.*, vol. 8, p. 13985, Jan 2017.

[44] K. Olejník, T. Seifert, Z. Kašpar, V. Novák, P. Wadley, R. P. Campion, M. Baumgartner, P. Gambardella, P. Němec, J. Wunderlich, J. Sinova, P. Kužel, M. Müller, T. Kampfrath, and T. Jungwirth, "Terahertz electrical writing speed in an antiferromagnetic memory," *Sci. Adv.*, vol. 4, no. 3, 2018.

[45] P. Coleman, *Introduction to Many-Body Physics.* Cambridge University Press, 2015.

[46] A. Altland and B. D. Simons, *Condensed Matter Field Theory.* Cambridge University Press, 2 ed., 2010.

[47] E. H. Lieb and F. Y. Wu, "Absence of Mott Transition in an Exact Solution of the Short-Range, One-Band Model in One Dimension," *Phys. Rev. Lett.*, vol. 20, pp. 1445–1448, Jun 1968.

[48] H. Kramers, "L'interaction Entre les Atomes Magnétogènes dans un Cristal Paramagnétique," *Physica*, vol. 1, no. 1, pp. 182 – 192, 1934.

[49] P. W. Anderson, "Antiferromagnetism. Theory of Superexchange Interaction," *Phys. Rev.*, vol. 79, pp. 350–356, Jul 1950.

[50] E. G. Tveten, T. Müller, J. Linder, and A. Brataas, "Intrinsic magnetization of antiferromagnetic textures," *Phys. Rev. B*, vol. 93, p. 104408, 2016.

[51] R. C. Ohlmann and M. Tinkham, "Antiferromagnetic Resonance in $FeF_2$ at Far-Infrared Frequencies," *Phys. Rev.*, vol. 123, pp. 425–434, Jul 1961.

[52] M. Hagiwara, K. Katsumata, H. Yamaguchi, M. Tokunaga, I. Yamada, M. Gross, and P. Goy, "A Complete Frequency-Field Chart for the Antiferromagnetic Resonance in $MnF_2$," *International Journal of Infrared and Millimeter Waves*, vol. 20, pp. 617–622, Apr 1999.

[53] T. Satoh, S.-J. Cho, R. Iida, T. Shimura, K. Kuroda, H. Ueda, Y. Ueda, B. A. Ivanov, F. Nori, and M. Fiebig, "Spin Oscillations in Antiferromagnetic NiO Triggered by Circularly Polarized Light," *Phys. Rev. Lett.*, vol. 105, p. 077402, Aug 2010.

[54] I. S. Jacobs, "Spin-Flopping in $MnF_2$ by High Magnetic Fields," *J. Appl. Phys.*, vol. 32, no. 3, pp. S61–S62, 1961.

[55] T. L. Gilbert and J. M. Kelly, "Anomalous rotational damping in ferromagnetic sheets," in *Conference on magnetism and magnetic materials: papers presented, Pittsburgh, Pa., June 14-16, 1955*, pp. 253–263, American Institute of Electrical Engineers, 1955.

[56] T. L. Gilbert, "A phenomenological theory of damping in ferromagnetic materials," *IEEE Transactions on Magnetics*, vol. 40, pp. 3443–3449, Nov 2004.

[57] A. Kamra and W. Belzig, "Spin Pumping and Shot Noise in Ferrimagnets: Bridging Ferro- and Antiferromagnets," *Phys. Rev. Lett.*, vol. 119, p. 197201, Nov 2017.

[58] Q. Liu, H. Y. Yuan, K. Xia, and Z. Yuan, "Mode-dependent damping in metallic antiferromagnets due to intersublattice spin pumping," *Phys. Rev. Materials*, vol. 1, p. 061401, Nov 2017.

[59] A. Kamra, R. E. Troncoso, W. Belzig, and A. Brataas, "Gilbert damping phenomenology for two-sublattice magnets," *Phys. Rev. B*, vol. 98, p. 184402, Nov 2018.

[60] R. Cheng, J. Xiao, Q. Niu, and A. Brataas, "Spin pumping and spin-transfer torques in antiferromagnets," *Phys. Rev. Lett.*, vol. 113, p. 057601, 2014.

[61] F. Keffer and C. Kittel, "Theory of Antiferromagnetic Resonance," *Phys. Rev.*, vol. 85, pp. 329–337, Jan 1952.

[62] M. P. Ross, *Spin Dynamics in an Antiferromagnet.* PhD thesis, Technische Universität München, 2013.

[63] T. Kimura, Y. Otani, T. Sato, S. Takahashi, and S. Maekawa, "Room-Temperature Reversible Spin Hall Effect," *Phys. Rev. Lett.*, vol. 98, p. 156601, Apr 2007.

[64] G. Y. Guo, S. Murakami, T.-W. Chen, and N. Nagaosa, "Intrinsic Spin Hall Effect in Platinum: First-Principles Calculations," *Phys. Rev. Lett.*, vol. 100, p. 096401, Mar 2008.

[65] T. Tanaka, H. Kontani, M. Naito, T. Naito, D. S. Hirashima, K. Yamada, and J. Inoue, "Intrinsic spin Hall effect and orbital Hall effect in $4d$ and $5d$ transition metals," *Phys. Rev. B*, vol. 77, p. 165117, Apr 2008.

[66] C.-F. Pai, L. Liu, Y. Li, H. W. Tseng, D. C. Ralph, and R. A. Buhrman, "Spin transfer torque devices utilizing the giant spin Hall effect of tungsten," *Applied Physics Letters*, vol. 101, no. 12, p. 122404, 2012.

[67] L. Liu, C.-F. Pai, Y. Li, H. W. Tseng, D. C. Ralph, and R. A. Buhrman, "Spin-Torque Switching with the Giant Spin Hall Effect of Tantalum," *Science*, vol. 336, no. 6081, pp. 555–558, 2012.

[68] M. I. D'Yakonov and V. I. Perel', "Possibility of Orienting Electron Spins with Current," *JETP Lett.*, vol. 13, p. 467, Jun 1971.

[69] J. E. Hirsch, "Spin Hall Effect," *Phys. Rev. Lett.*, vol. 83, pp. 1834–1837, Aug 1999.

[70] J. Sinova, D. Culcer, Q. Niu, N. A. Sinitsyn, T. Jungwirth, and A. H. MacDonald, "Universal Intrinsic Spin Hall Effect," *Phys. Rev. Lett.*, vol. 92, p. 126603, Mar 2004.

[71] Y. Tserkovnyak, A. Brataas, and G. E. W. Bauer, "Enhanced Gilbert Damping in Thin Ferromagnetic Films," *Phys. Rev. Lett.*, vol. 88, p. 117601, Feb 2002.

[72] P. Ross, M. Schreier, J. Lotze, H. Huebl, R. Gross, and S. T. B. Goennenwein, "Antiferromagentic resonance detected by direct current voltages in $MnF_2/Pt$ bilayers," *J. Appl. Phys.*, vol. 118, no. 23, p. 233907, 2015.

[73] M. Johnson and R. H. Silsbee, "Coupling of electronic charge and spin at a ferromagnetic-paramagnetic metal interface," *Phys. Rev. B*, vol. 37, pp. 5312–5325, Apr 1988.

[74] H. J. Jiao and G. E. W. Bauer, "Spin Backflow and ac Voltage Generation by Spin Pumping and the Inverse Spin Hall Effect," *Phys. Rev. Lett.*, vol. 110, p. 217602, May 2013.

[75] H. V. Gomonay and V. M. Loktev, "Spin-transfer and current-induced switching in antiferromagnets," *Phys. Rev. B*, vol. 81, p. 144427, 2010.

[76] Y.-T. Chen, S. Takahashi, H. Nakayama, M. Althammer, S. T. B. Goennenwein, E. Saitoh, and G. E. W. Bauer, "Theory of spin Hall magnetoresistance," *Phys. Rev. B*, vol. 87, p. 144411, Apr 2013.

[77] A. Manchon and S. Zhang, "Theory of nonequilibrium intrinsic spin torque in a single nanomagnet," *Phys. Rev. B*, vol. 78, p. 212405, Dec 2008.

[78] A. Chernyshov, M. Overby, X. Liu, J. K. Furdyna, Y. Lyanda-Geller, and L. P. Rokhinson, "Evidence for reversible control of magnetization in a ferromagnetic material by means of spin-orbit magnetic field," *Nat. Phys.*, vol. 5, p. 656, Aug 2009.

[79] K. M. D. Hals and A. Brataas, "Phenomenology of current-induced spin-orbit torques," *Phys. Rev. B*, vol. 88, no. 8, p. 085423, 2013.

[80] R. R. Birss, *Symmetry and Magnetism*, vol. 3 of *Selected Topics in Solid State Physics*. North-Holland Publishing Company, 1 ed., 1964.

[81] K. M. D. Hals and A. Brataas, "Spin-motive forces and current-induced torques in ferromagnets," *Phys. Rev. B*, vol. 91, p. 214401, Jun 2015.

[82] W. Thomson, "XIX. On the electro-dynamic qualities of metals:-—Effects of magnetization on the electric conductivity of nickel and of iron," *Proc. R. Soc. Lond.*, vol. 8, pp. 546–550.

[83] I. Fina, X. Marti, D. Yi, J. Liu, J. H. Chu, C. Rayan-Serrao, S. Suresha, A. B. Shick, J. Zelezný, T. Jungwirth, J. Fontcuberta, and R. Ramesh, "Anisotropic magnetoresistance in an antiferromagnetic semiconductor," *Nat. Commun.*, vol. 5, p. 4671, Sep 2014.

[84] H. Nakayama, M. Althammer, Y.-T. Chen, K. Uchida, Y. Kajiwara, D. Kikuchi, T. Ohtani, S. Geprägs, M. Opel, S. Takahashi, R. Gross, G. E. W. Bauer, S. T. B. Goennenwein, and E. Saitoh, "Spin Hall Magnetoresistance Induced by a Nonequilibrium Proximity Effect," *Phys. Rev. Lett.*, vol. 110, p. 206601, May 2013.

[85] C. Hahn, G. de Loubens, O. Klein, M. Viret, V. V. Naletov, and J. Ben Youssef, "Comparative measurements of inverse spin Hall effects and magnetoresistance in YIG/Pt and YIG/Ta," *Phys. Rev. B*, vol. 87, p. 174417, May 2013.

[86] D. Hou, Z. Qiu, J. Barker, K. Sato, K. Yamamoto, S. Vélez, J. M. Gomez-Perez, L. E. Hueso, F. Casanova, and E. Saitoh, "Tunable Sign Change of Spin Hall Magnetoresistance in Pt/NiO/YIG Structures," *Phys. Rev. Lett.*, vol. 118, p. 147202, Apr 2017.

[87] G. R. Hoogeboom, A. Aqeel, T. Kuschel, T. T. M. Palstra, and B. J. van Wees, "Negative spin Hall magnetoresistance of Pt on the bulk easy-plane antiferromagnet NiO," *Appl. Phys. Lett.*, vol. 111, no. 5, p. 052409, 2017.

[88] L. Baldrati, A. Ross, T. Niizeki, C. Schneider, R. Ramos, J. Cramer, O. Gomonay, M. Filianina, T. Savchenko, D. Heinze, A. Kleibert, E. Saitoh, J. Sinova, and M. Kläui, "Full angular dependence of the spin Hall and ordinary magnetoresistance in epitaxial antiferromagnetic NiO(001)/Pt thin films," *Phys. Rev. B*, vol. 98, p. 024422, Jul 2018.

[89] J. Fischer, O. Gomonay, R. Schlitz, K. Ganzhorn, N. Vlietstra, M. Althammer, H. Huebl, M. Opel, R. Gross, S. T. B. Goennenwein, and S. Geprägs, "Spin Hall magnetoresistance in antiferromagnet/heavy-metal heterostructures," *Phys. Rev. B*, vol. 97, p. 014417, Jan 2018.

[90] T. Chiba, G. E. W. Bauer, and S. Takahashi, "Current-Induced Spin-Torque Resonance of Magnetic Insulators," *Phys. Rev. Applied*, vol. 2, p. 034003, Sep 2014.

[91] S. Takahashi, *Physical Principles of Spin Pumping*, pp. 1445–1480. Dordrecht: Springer Netherlands, 2016.

[92] T. Holstein and H. Primakoff, "Field Dependence of the Intrinsic Domain Magnetization of a Ferromagnet," *Phys. Rev.*, vol. 58, pp. 1098–1113, Dec 1940.

[93] J. G. Valatin, "Comments on the theory of superconductivity," *Il Nuovo Cimento (1955-1965)*, vol. 7, pp. 843–857, Mar 1958.

[94] N. N. Bogoljubov, "On a new method in the theory of superconductivity," *Il Nuovo Cimento (1955-1965)*, vol. 7, pp. 794–805, Mar 1958.

[95] A. Kamra, U. Agrawal, and W. Belzig, "Noninteger-spin magnonic excitations in untextured magnets," *Phys. Rev. B*, vol. 96, p. 020411, Jul 2017.

[96] N. J. Lambert, J. A. Haigh, S. Langenfeld, A. C. Doherty, and A. J. Ferguson, "Cavity-mediated coherent coupling of magnetic moments," *Phys. Rev. A*, vol. 93, p. 021803, Feb 2016.

[97] B. Zare Rameshti and G. E. W. Bauer, "Indirect coupling of magnons by cavity photons," *Phys. Rev. B*, vol. 97, p. 014419, Jan 2018.

[98] L. Bai, M. Harder, P. Hyde, Z. Zhang, C.-M. Hu, Y. P. Chen, and J. Q. Xiao, "Cavity Mediated Manipulation of Distant Spin Currents Using a Cavity-Magnon-Polariton," *Phys. Rev. Lett.*, vol. 118, p. 217201, May 2017.

[99] L. Liensberger, A. Kamra, H. Maier-Flaig, S. Geprägs, A. Erb, S. T. B. Goennenwein, R. Gross, W. Belzig, H. Huebl, and M. Weiler, "Exchange-enhanced Ultrastrong Magnon-Magnon Coupling in a Compensated Ferrimagnet," *arXiv:1903.04330*, 2019.

[100] E. T. Jaynes and F. W. Cummings, "Comparison of quantum and semiclassical radiation theories with application to the beam maser," *Proceedings of the IEEE*, vol. 51, pp. 89–109, Jan 1963.

[101] C. Gerry and P. Knight, *Introductory Quantum Optics*. Cambridge University Press, 2004.

[102] R. H. Dicke, "Coherence in Spontaneous Radiation Processes," *Phys. Rev.*, vol. 93, pp. 99–110, Jan 1954.

[103] M. Tavis and F. W. Cummings, "Exact Solution for an $N$-Molecule—Radiation-Field Hamiltonian," *Phys. Rev.*, vol. 170, pp. 379–384, Jun 1968.

[104] M. Tavis and F. W. Cummings, "Approximate Solutions for an $N$-Molecule-Radiation-Field Hamiltonian," *Phys. Rev.*, vol. 188, pp. 692–695, Dec 1969.

[105] Y. Wang and J. Y. Haw, "Bridging the gap between the Jaynes–Cummings and Rabi models using an intermediate rotating wave approximation," *Physics Letters A*, vol. 379, no. 8, pp. 779 – 786, 2015.

[106] M. G. Raizen, R. J. Thompson, R. J. Brecha, H. J. Kimble, and H. J. Carmichael, "Normal-mode splitting and linewidth averaging for two-state atoms in an optical cavity," *Phys. Rev. Lett.*, vol. 63, pp. 240–243, Jul 1989.

[107] M. A. Gilleo and S. Geller, "Magnetic and Crystallographic Properties of Substituted Yttrium-Iron Garnet, $3Y_2O_3 \cdot xM_2O_3 \cdot (5-x)Fe_2O_3$," *Phys. Rev.*, vol. 110, pp. 73–78, Apr 1958.

[108] O. O. Soykal and M. E. Flatté, "Strong Field Interactions between a Nanomagnet and a Photonic Cavity," *Phys. Rev. Lett.*, vol. 104, p. 077202, Feb 2010.

[109] H. Huebl, C. W. Zollitsch, J. Lotze, F. Hocke, M. Greifenstein, A. Marx, R. Gross, and S. T. B. Goennenwein, "High Cooperativity in Coupled Microwave Resonator Ferrimagnetic Insulator Hybrids," *Phys. Rev. Lett.*, vol. 111, p. 127003, Sep 2013.

[110] Y. Tabuchi, S. Ishino, T. Ishikawa, R. Yamazaki, K. Usami, and Y. Nakamura, "Hybridizing Ferromagnetic Magnons and Microwave Photons in the Quantum Limit," *Phys. Rev. Lett.*, vol. 113, p. 083603, Aug 2014.

[111] A. Osada, R. Hisatomi, A. Noguchi, Y. Tabuchi, R. Yamazaki, K. Usami, M. Sadgrove, R. Yalla, M. Nomura, and Y. Nakamura, "Cavity Optomagnonics with Spin-Orbit Coupled Photons," *Phys. Rev. Lett.*, vol. 116, p. 223601, Jun 2016.

[112] X. Zhang, N. Zhu, C.-L. Zou, and H. X. Tang, "Optomagnonic Whispering Gallery Microresonators," *Phys. Rev. Lett.*, vol. 117, p. 123605, Sep 2016.

[113] J. A. Haigh, A. Nunnenkamp, A. J. Ramsay, and A. J. Ferguson, "Triple-Resonant Brillouin Light Scattering in Magneto-Optical Cavities," *Phys. Rev. Lett.*, vol. 117, p. 133602, Sep 2016.

[114] C. Braggio, G. Carugno, M. Guarise, A. Ortolan, and G. Ruoso, "Optical Manipulation of a Magnon-Photon Hybrid System," *Phys. Rev. Lett.*, vol. 118, p. 107205, Mar 2017.

[115] J. Bourhill, N. Kostylev, M. Goryachev, D. L. Creedon, and M. E. Tobar, "Ultrahigh cooperativity interactions between magnons and resonant photons in a YIG sphere," *Phys. Rev. B*, vol. 93, p. 144420, Apr 2016.

[116] H. Y. Yuan and X. R. Wang, "Magnon-photon coupling in antiferromagnets," *Appl. Phys. Lett.*, vol. 110, no. 8, p. 082403, 2017.

[117] F. Haake, *Quantum Signatures of Chaos.* Springer, 2001.

[118] Chappel, E., Núñez-Regueiro, M. D., Dupont, F., Chouteau, G., Darie, C., and Sulpice, A., "Antiferromagnetic resonance and high magnetic field properties of NaNiO$_2$„" *Eur. Phys. J. B*, vol. 17, no. 4, pp. 609–614, 2000.

[119] H. Suhl, "Simultaneous Onset of Ferromagnetism and Superconductivity," *Phys. Rev. Lett.*, vol. 87, p. 167007, Sep 2001.

[120] N. Karchev, "Magnon exchange mechanism of ferromagnetic superconductivity," *Phys. Rev. B*, vol. 67, p. 054416, Feb 2003.

[121] N. Rohling, E. L. Fjærbu, and A. Brataas, "Superconductivity induced by interfacial coupling to magnons," *Phys. Rev. B*, vol. 97, p. 115401, Mar 2018.

[122] H. Stoof, D. Dickerscheid, and K. Gubbels, *Ultracold Quantum Fields.* Theoretical and Mathematical Physics, Springer Netherlands, 2008.

[123] C. Zener, "Interaction Between the *d* Shells in the Transition Metals," *Phys. Rev.*, vol. 81, pp. 440–444, Feb 1951.

[124] T. Kasuya, "A Theory of Metallic Ferro- and Antiferromagnetism on Zener's Model," *Prog. Theor. Phys.*, vol. 16, pp. 45–57, Jul 1956.

[125] J. Bardeen, L. N. Cooper, and J. R. Schrieffer, "Microscopic Theory of Superconductivity," *Phys. Rev.*, vol. 106, pp. 162–164, Apr 1957.

[126] E. L. Fjærbu, N. Rohling, and A. Brataas, "Superconductivity at metal-antiferromagnetic insulator interfaces," *arXiv:1904.00233*, 2019.

[127] A. Kamra, E. Thingstad, G. Rastelli, R. A. Duine, A. Brataas, W. Belzig, and A. Sudbø, "Antiferromagnetic Magnons as Highly Squeezed Fock States underlying Quantum Correlations," *arXiv:1904.04553*, 2019.

[128] N. D. Mermin and H. Wagner, "Absence of ferromagnetism or antiferromagnetism in one- or two-dimensional isotropic Heisenberg models," *Phys. Rev. Lett.*, vol. 17, pp. 1133–1136, Nov 1966.

[129] P. C. Hohenberg, "Existence of Long-Range Order in One and Two Dimensions," *Phys. Rev.*, vol. 158, pp. 383–386, Jun 1967.

[130] E. Ising, "Beitrag zur Theorie des Ferromagnetismus," *Zeitschrift für Physik*, vol. 31, pp. 253–258, Feb 1925.

[131] L. Onsager, "Crystal Statistics. I. A Two-Dimensional Model with an Order-Disorder Transition," *Phys. Rev.*, vol. 65, pp. 117–149, Feb 1944.

[132] C. N. Yang, "The Spontaneous Magnetization of a Two-Dimensional Ising Model," *Phys. Rev.*, vol. 85, pp. 808–816, Mar 1952.

[133] R. Pathria and P. Beale, *Statistical Mechanics.* Elsevier Science, 2011.

[134] P. M. Chaikin and T. C. Lubensky, *Principles of Condensed Matter Physics.* Cambridge University Press, 1995.

[135] V. L. Berezinskiǐ, "Destruction of Long-range Order in One-dimensional and Two-dimensional Systems having a Continuous Symmetry Group I. Classical Systems," *Soviet Phys. JETP*, vol. 32, p. 493, 1971.

[136] J. M. Kosterlitz and D. J. Thouless, "Ordering, metastability and phase transitions in two-dimensional systems," *J. Phys. C: Solid State*, vol. 6, no. 7, p. 1181, 1973.

[137] J. M. Kosterlitz, "The critical properties of the two-dimensional xy model," *Journal of Physics C: Solid State Physics*, vol. 7, pp. 1046–1060, Mar 1974.

[138] D. R. Nelson and J. M. Kosterlitz, "Universal Jump in the Superfluid Density of Two-Dimensional Superfluids," *Phys. Rev. Lett.*, vol. 39, pp. 1201–1205, Nov 1977.

[139] D. J. Bishop and J. D. Reppy, "Study of the Superfluid Transition in Two-Dimensional $^4$He Films," *Phys. Rev. Lett.*, vol. 40, pp. 1727–1730, Jun 1978.

[140] V. L. Berezinskiǐ, "Destruction of Long-range Order in One-dimensional and Two-dimensional Systems Possessing a Continuous Symmetry Group. II. Quantum Systems," *Soviet Phys. JETP*, vol. 34, p. 610, 1972.

[141] "Press release: The Nobel Prize in Physics 2016." `https://www.nobelprize.org/prizes/physics/2016/press-release/`. Accessed: 22/05/2019.

[142] J. Fröhlich and T. Spencer, "The Kosterlitz-Thouless transition in two-dimensional Abelian spin systems and the Coulomb gas," *Communications in Mathematical Physics*, vol. 81, pp. 527–602, Dec 1981.

[143] Y. E. Lozovik and V. I. Yudson, "Feasibility of superfluidity of paired spatially separated electrons and holes; a new superconductivity mechanism," *JETP Lett.*, vol. 22, no. 274, 1975.

[144] D. V. Fil and S. I. Shevchenko, "Electron-hole Superconductivity (Review)," *Low Temp. Phys.*, vol. 44, no. 9, pp. 867–909, 2018.

[145] K. S. Novoselov, A. K. Geim, S. V. Morozov, D. Jiang, Y. Zhang, S. V. Dubonos, I. V. Grigorieva, and A. A. Firsov, "Electric Field Effect in Atomically Thin Carbon Films," *Science*, vol. 306, no. 5696, pp. 666–669, 2004.

[146] J. U. Lee, S. Lee, J. H. Ryoo, S. Kang, T. Y. Kim, P. Kim, C.-H. Park, J.-G. Park, and H. Cheong, "Ising-type magnetic ordering in atomically thin $FePS_3$," *Nano Lett.*, vol. 16, pp. 7433–7438, Dec 2016.

[147] B. Huang, G. Clark, E. Navarro-Moratalla, D. R. Klein, R. Cheng, K. L. Seyler, D. Zhong, E. Schmidgall, M. A. McGuire, D. H. Cobden, W. Yao, D. Xiao, P. Jarillo-Herrero, and X. Xu, "Layer-dependent ferromagnetism in a van der Waals crystal down to the monolayer limit," *Nature*, vol. 546, pp. 270–273, Jun 2017.

[148] C. Gong, L. Li, Z. Li, H. Ji, A. Stern, Y. Xia, T. Cao, W. Bao, C. Wang, Y. Wang, Z. Q. Qiu, R. J. Cava, S. G. Louie, J. Xia, and X. Zhang, "Discovery of intrinsic ferromagnetism in two-dimensional van der Waals crystals," *Nature*, vol. 546, pp. 265–269, Apr 2017.

[149] D. O'Hara, T. Zhu, A. H. Trout, A. S. Ahmed, L. Yunqiu, C. H. Lee, M. R. Brenner, S. Rajan, J. A. Gupta, D. W. McComb, and R. K. Kawakami, "Room temperature intrinsic ferromagnetism in epitaxial manganese selenide films in the monolayer limit," *Nano Lett.*, vol. 18, pp. 3125–3131, Feb 2018.

[150] K. S. Burch, D. Mandrus, and J.-G. Park, "Magnetism in two-dimensional van der Waals materials," *Nature*, vol. 563, pp. 47–52, Nov 2018.

[151] M. Bonilla, S. Kolekar, Y. Ma, H. C. Diaz, V. Kalappattil, R. Das, T. Eggers, H. R. Gutierrez, M.-H. Phan, and M. Batzill, "Strong room-temperature ferromagnetism in VSe$_2$ monolayers on van der Waals substrates," *Nat. Nanotechnol.*, vol. 13, pp. 289–293, Apr 2018.

[152] Z. Fei, B. Huang, P. Malinowski, W. Wang, T. Song, J. Sanchez, W. Yao, D. Xiao, X. Zhu, A. F. May, W. Wu, D. H. Cobden, J.-H. Chu, and X. Xu, "Two-dimensional itinerant ferromagnetism in atomically thin Fe$_3$GeTe$_2$," *Nat. Mater.*, vol. 17, pp. 778–782, Sep 2018.

[153] Y. Deng, Y. Yu, Y. Song, J. Zhang, N. Z. Wang, Z. Sun, Y. Yi, Y. Z. Wu, S. Wu, J. Zhu, J. Wang, X. H. Chen, and Y. Zhang, "Gate-tunable room-temperature ferromagnetism in two-dimensional Fe$_3$GeTe$_2$," *Nature*, vol. 563, pp. 94–99, Nov 2018.

[154] K. M. D. Hals and K. Everschor-Sitte, "Twists in ferromagnetic monolayers with trigonal prismatic symmetry," *Phys. Rev. B*, vol. 99, p. 104422, Mar 2019.

# Paper [1]

**Øyvind Johansen and Arne Brataas**

*"Spin pumping and inverse spin Hall voltages from dynamical antiferromagnets"*
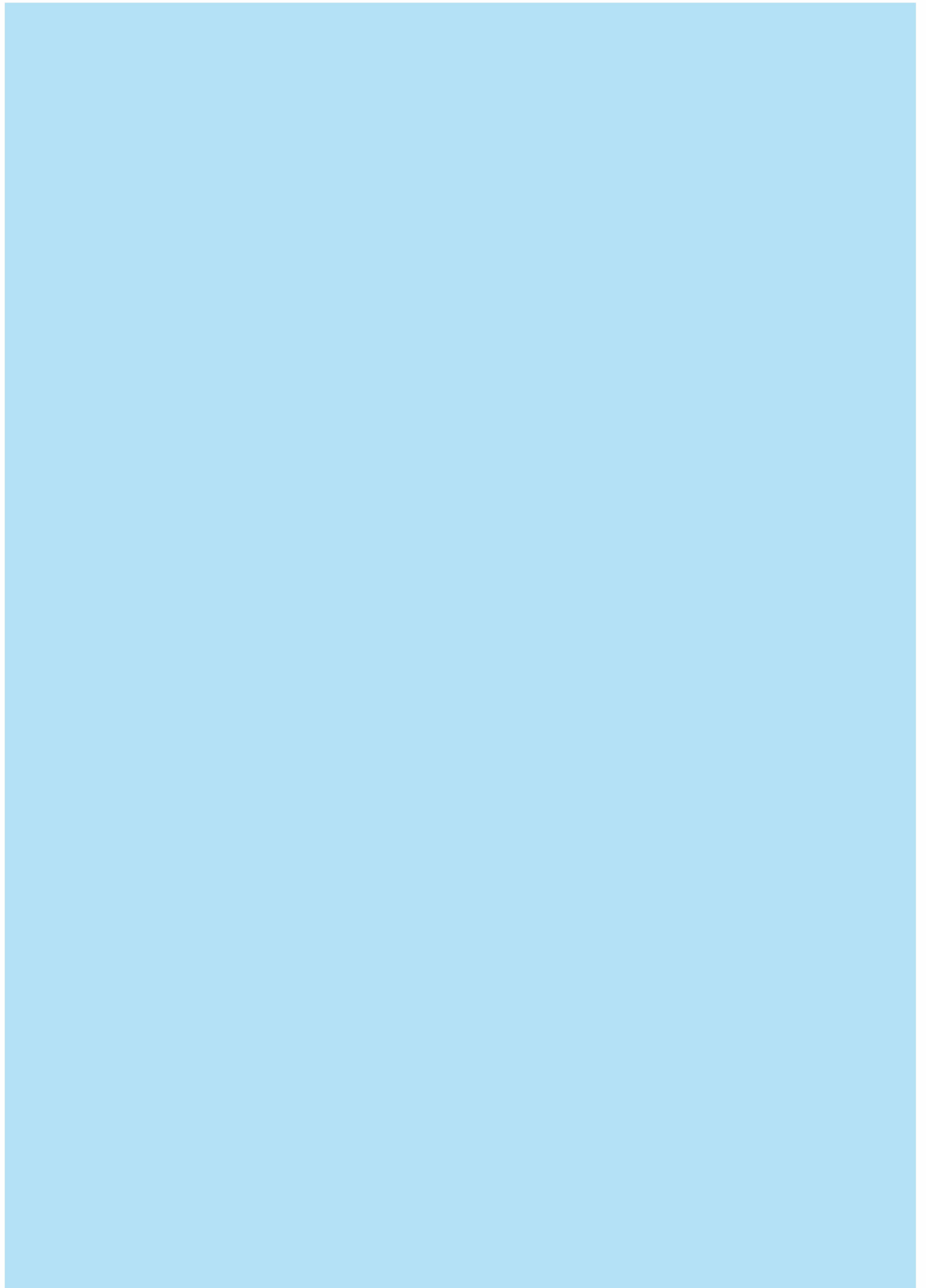
# Spin pumping and inverse spin Hall voltages from dynamical antiferromagnets

Øyvind Johansen[*] and Arne Brataas

*Department of Physics, Norwegian University of Science and Technology, NO-7491 Trondheim, Norway*

(Received 13 February 2017; published 20 June 2017)

Dynamical antiferromagnets can pump spins into adjacent conductors. The high antiferromagnetic resonance frequencies represent a challenge for experimental detection, but magnetic fields can reduce these resonance frequencies. We compute the ac and dc inverse spin Hall voltages resulting from dynamical spin excitations as a function of a magnetic field along the easy axis and the polarization of the driving ac magnetic field perpendicular to the easy axis. We consider the insulating antiferromagnets $MnF_2$, $FeF_2$, and NiO. Near the spin-flop transition, there is a significant enhancement of the dc spin pumping and inverse spin Hall voltage for the uniaxial antiferromagnets $MnF_2$ and $FeF_2$. In the uniaxial antiferromagnets it is also found that the ac spin pumping is independent of the external magnetic field when the driving field has the optimal circular polarization. In the biaxial NiO, the voltages are much weaker, and there is no spin-flop enhancement of the dc component.

DOI: [10.1103/PhysRevB.95.220408](10.1103/PhysRevB.95.220408)

Spin pumping is a versatile tool for probing spin dynamics in ferromagnets [1–6]. The magnitude of the pumped spin currents reveals information about the magnetization dynamics and the electron-magnon coupling at interfaces [7–9]. The precessing spins generate a pure spin flow into adjacent conductors. Inside the conductor, the resulting spin accumulation and currents give insight into the spin-orbit coupling. The inverse spin Hall effect (ISHE) is often used to convert the pure spin current into a charge current, which is detected [10,11]. Additionally, the induced nonequilibrium spins can be probed with x-ray magnetic circular dichroism measurements [12,13].

Antiferromagnets differ strikingly from ferromagnets [14]. There are no stray fields in antiferromagnets, making them more robust against the influence of external magnetic fields. The recent discovery of anisotropic magnetoresistance [15–17], spin-orbit torques [18], and electrical switching of an antiferromagnet [19] demonstrate the feasibility of antiferromagnets as active spintronics components.

The real benefit of antiferromagnets is that they can enable terahertz circuits. Unlike ferromagnets, the resonance frequency of antiferromagnets is also governed by the tremendous exchange energy. We recently demonstrated that the transverse spin conductance, a governing factor of spin pumping, is as large in antiferromagnet–normal metal junctions (AF|N) as in ferromagnet–normal metal junctions [20]. Furthermore, this result is valid even when the magnetic system is insulating. The firm electron-magnon coupling at the interface opens the door for electrical probing of the ultrafast spin dynamics in antiferromagnets [20,21].

Precessing spins in antiferromagnets generate terahertz currents in adjacent conductors. This ability opens new territory in high-frequency spintronics. Such studies could become influential in gathering vital insight into fast electron dynamics and eventually for a broad range of applications. These electric signals also provide further knowledge about the less explored field of antiferromagnetic spin dynamics. This potential requires thorough exploration; we need to establish several critical aspects.

The manner in which spin pumping generates ac and dc inverse spin Hall voltages has yet to be studied in detail.

Furthermore, there is a large variety of antiferromagnets and external field configurations that require knowledge beyond the first predictions of the magnitude of the pumped spin current of Ref. [20]. Recently, researchers explored spin transport through, e.g., the insulating antiferromagnets NiO and $MnF_2$. Unlike the treatment of Ref. [20], in NiO, there are two significant anisotropies to consider. As a starting point in the exploration of high-frequency spintronics, it is also important to tune the resonance frequencies to a lower gigahertz range for easier detection by conventional electronics. The application of an external magnetic field can lower the resonance frequency. However, the details of the magnetic field and its ac component polarization dependence also remain to be classified, a task that we will perform here.

In this Rapid Communication, we compute the inverse spin Hall ac and dc voltages generated by spin pumping. We hope that our studies will further motivate these voltages to be experimentally measured. Such studies will provide a needed deeper insight into antiferromagnetic resonance phenomena, features much less explored than their ferromagnetic counterparts in recent decades.

We consider an insulating antiferromagnet–normal metal bilayer, as illustrated in Fig. 1. We also consider a variety of magnetic anisotropies and magnetic field configurations and strengths. Therefore, the results apply to more complex systems such as biaxial antiferromagnets with elliptical precessional modes. The model also accounts for spin backflow due to the spin accumulation in the metal. We also study how the inverse spin Hall voltages depend on the polarization of the ac magnetic field for different systems, which we find to have a strong influence on the resulting signal. Our main findings are that, when applying an external magnetic field along the easy axis close to the spin-flop transition, we can decrease the resonance frequency while simultaneously significantly increasing the inverse spin Hall signal. The increase in the signal can even overcome the previously anticipated limiting factor in antiferromagnet spin pumping: the ratio of the anisotropic energy to the exchange energy [20].

We consider a small antiferromagnet in the macrospin limit whereby all spin excitations are homogeneous. The antiferromagnet has two sublattices, with temporal magnetizations $\mathbf{M}_1$ and $\mathbf{M}_2$. The dynamics are described by the
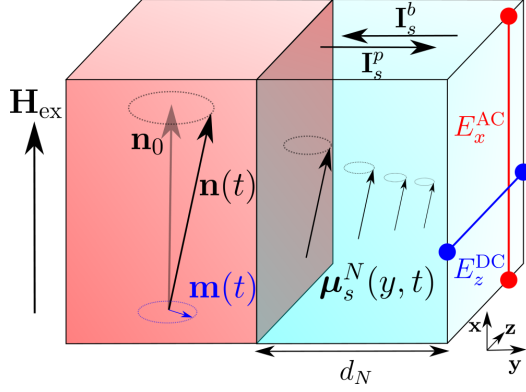
---

[*]Corresponding author: oyvinjoh@ntnu.no

FIG. 1. The precession of **m** and **n** around their equilibrium values pumps spins into the adjacent normal metal of thickness $d_N$. In turn, the spin accumulation $\boldsymbol{\mu}_s^N$ in the normal metal causes a backflow of spins into the antiferromagnet. The spin current in the normal metal causes ac and dc electric fields in the $x$ and $z$ directions, respectively, through the inverse spin Hall effect.

staggered magnetizations $\mathbf{L} = (\mathbf{M}_1 - \mathbf{M}_2)/2 = L\mathbf{n}$ and the magnetization $\mathbf{M} = (\mathbf{M}_1 + \mathbf{M}_2)/2 = L\mathbf{m}$. These fields satisfy the constraints $\mathbf{n}^2 + \mathbf{m}^2 = 1$ and $\mathbf{n} \cdot \mathbf{m} = 0$. At equilibrium, the sublattice magnetizations are antiparallel. An ac magnetic field, with a general polarization, drives the magnetic moments at resonance.

The antiferromagnets that we consider are described by the free energy

$$F = \frac{LV}{\gamma} \left[ \omega_E(\mathbf{m}^2 - \mathbf{n}^2) + \omega_\perp(m_z^2 + n_z^2) - \omega_\parallel(m_x^2 + n_x^2) \right.$$
$$\left. - 2\omega_x m_x - 2\omega_y m_y - 2\omega_z m_z \right], \quad (1)$$

where $\gamma$ is the gyromagnetic ratio, $V$ is the volume of the antiferromagnet, $\omega_E \geqslant 0$ is the exchange frequency, and $\omega_\perp \geqslant 0$ and $\omega_\parallel \geqslant 0$ are the hard axis ($z$ axis) and easy axis ($x$ axis) anisotropy frequencies. The frequency $\omega_x$ quantifies the influence of the external magnetic field along the easy axis, whereas $\omega_y$ and $\omega_z$ quantify the influence of the ac magnetic field in the $yz$ plane. In Table I, we list the exchange and anisotropy frequencies for $MnF_2$, $FeF_2$, and NiO.

The dynamic Landau-Lifshitz-Gilbert (LLG) equations that describe the precession of **n** and **m** are

$$\dot{\mathbf{n}} = \tfrac{1}{2}(\boldsymbol{\omega}_m \times \mathbf{n} + \boldsymbol{\omega}_n \times \mathbf{m}) + \boldsymbol{\tau}_n, \quad (2a)$$

$$\dot{\mathbf{m}} = \tfrac{1}{2}(\boldsymbol{\omega}_n \times \mathbf{n} + \boldsymbol{\omega}_m \times \mathbf{m}) + \boldsymbol{\tau}_m, \quad (2b)$$

TABLE I. Exchange and anisotropy frequencies.

| Material | $\omega_E$ ($10^{12}$ s$^{-1}$) | $\omega_\parallel$ ($10^{12}$ s$^{-1}$) | $\omega_\perp$ ($10^{12}$ s$^{-1}$) |
|---|---|---|---|
| $MnF_2$ [22] | 9.3 | $1.5 \times 10^{-1}$ | |
| $FeF_2$ [23] | 9.5 | 3.5 | |
| NiO [24,25] | $1.7 \times 10^2$ | $2.3 \times 10^{-3}$ | $1.3 \times 10^{-1}$ |

with the effective fields $\boldsymbol{\omega}_n = -(\gamma/L)\partial F/\partial\mathbf{n}$ and $\boldsymbol{\omega}_m = -(\gamma/L)\partial F/\partial\mathbf{m}$. The dissipation and spin-pumping torques are

$$\boldsymbol{\tau}_n = \alpha[\mathbf{n} \times \dot{\mathbf{m}} + \mathbf{m} \times \dot{\mathbf{n}}], \quad (3a)$$

$$\boldsymbol{\tau}_m = \alpha[\mathbf{n} \times \dot{\mathbf{n}} + \mathbf{m} \times \dot{\mathbf{m}}], \quad (3b)$$

where the total Gilbert damping coefficient $\alpha$ is a sum of the intrinsic damping and the spin-pumping-enhanced damping: $\alpha = \alpha_0 + \alpha_{SP}$ [20,26].

A linear response expansion around the equilibrium values of **n** and **m** determines the antiferromagnetic resonance (AFMR) frequencies. For simplicity, we only present the resonance frequencies in the exchange limit $\omega_\parallel, \omega_\perp \ll \omega_E$. This limit is valid for many antiferromagnets but not for $FeF_2$ due to a large anisotropy. In our numerical calculations below, we do not make this approximation. In the exchange limit, the four resonance frequencies below spin flop are [27]

$$\omega_{res}^2 \approx \omega_x^2 + \omega_0^2 \pm \sqrt{\omega_E^2\omega_\perp^2 + 4\omega_x^2\omega_0^2}, \quad (4)$$

where $\omega_0^2 = \omega_E(2\omega_\parallel + \omega_\perp)$. The critical field strength at which the spin-flop transition occurs is $|\omega_x^{crit}| = \sqrt{\omega_\parallel(2\omega_E + \omega_\parallel)}$ in both uniaxial and biaxial antiferromagnets. We will only consider magnetic fields below this value.

Herein, we focus on the right-handed low-energy mode since we want to decrease the resonance frequency. In the absence of an external magnetic field, the resonance frequency of this mode is 0.27 THz for $MnF_2$, 1.41 THz for $FeF_2$, and 0.14 THz for NiO. By applying a magnetic field close to the spin-flop transition, we can reduce these resonance frequencies down to the gigahertz range. Such a reduction should enable detection of AFMR and the resulting significant spin-pumping-induced ac and dc ISHE voltages.

The pumped spin current from a dynamical antiferromagnet into a normal metal is [20]

$$\mathbf{I}_s^p = \frac{\hbar g_\perp}{2\pi}(\mathbf{n} \times \dot{\mathbf{n}} + \mathbf{m} \times \dot{\mathbf{m}}), \quad (5)$$

where $g_\perp$ is the transverse ("mixing") conductance. The spin pumping from the antiferromagnetic insulator causes a spin accumulation in the normal metal, which in turn produces a spin backflow current [11]. In antiferromagnetic insulators, the backflow spin currents within the sublattices add constructively [20,28]:

$$\mathbf{I}_s^b = -\frac{g_\perp}{2\pi}\left[\mathbf{m} \times \left(\boldsymbol{\mu}_s^N \times \mathbf{m}\right) + \mathbf{n} \times \left(\boldsymbol{\mu}_s^N \times \mathbf{n}\right)\right], \quad (6)$$

where $\boldsymbol{\mu}_s^N$ is the spin accumulation in the normal metal.

The most significant contributions to the spin current are second order in the deviations from equilibrium along the easy axis and first order along the perpendicular directions. Nevertheless, the leading-order terms in the total spin current only depend on the first-order deviations of the magnetic moments from their equilibrium values, $\mathbf{n}_0 = \mathbf{e}_x$ and $\mathbf{m}_0 = \mathbf{0}$. It is therefore sufficient to consider the linear response expansions

$$\mathbf{n} = \mathbf{n}_0 + \tfrac{1}{2}(\delta\mathbf{n}e^{i\omega t} + \delta\mathbf{n}^*e^{-i\omega t}), \quad (7a)$$

$$\mathbf{m} = \tfrac{1}{2}(\delta\mathbf{m}e^{i\omega t} + \delta\mathbf{m}^*e^{-i\omega t}), \quad (7b)$$

where the transverse deviations are $\delta\mathbf{n} = \delta n_y \mathbf{e}_y + \delta n_z \mathbf{e}_z$ and $\delta\mathbf{m} = \delta m_y \mathbf{e}_y + \delta m_z \mathbf{e}_z$. $\omega$ is the driving frequency of the ac magnetic field.

The spin accumulation $\boldsymbol{\mu}_s^N$ is a solution of the spin diffusion equation

$$\frac{\partial \boldsymbol{\mu}_s^N(\mathbf{r},t)}{\partial t} = \gamma_N \mathbf{H}_{\mathrm{ex}} \times \boldsymbol{\mu}_s^N + D_N \frac{\partial^2 \boldsymbol{\mu}_s^N}{\partial y^2} - \frac{\boldsymbol{\mu}_s^N}{\tau_{\mathrm{sf}}^N}, \quad (8)$$

where the terms on the right-hand side of Eq. (8) are properties of the normal metal such as the diffusion coefficient $D_N$, the gyromagnetic ratio $\gamma_N$, and the spin-flip relaxation time $\tau_{\mathrm{sf}}^N$, and $\mathbf{H}_{\mathrm{ex}}$ is the external magnetic field. The boundary conditions for $\boldsymbol{\mu}_s^N$ require that the spin current vanishes at the outer edge of the normal metal ($y = d_N$) and that the current is continuous across the antiferromagnet–normal metal interface ($y = 0$). The diffusion equation can be solved in position-frequency space [11,29] in terms of the Fourier components of the total spin current $\mathbf{I}_s^N = \mathbf{I}_s^p + \mathbf{I}_s^b$ at $y = 0$.

The spin current in the normal metal causes a charge current perpendicular to the spin current's direction and polarization through the ISHE. This charge current is given by [30,31]

$$\mathbf{j}_c^{\mathrm{ISHE}}(y,t) = \theta_N \frac{2e}{A\hbar} \mathbf{e}_y \times \mathbf{I}_s^N(y,t), \quad (9)$$

where $\theta_N$ is the spin Hall angle in the normal metal and $A$ is the area of the AF|N interface. Since the system is an open circuit, the charge current accumulates charges at the interfaces. In turn, a generated electric field ensures that the net charge current through the metal vanishes. To determine this electric field, we integrate the charge current $\mathbf{j}_c^{\mathrm{ISHE}}$ over the metallic system to find the electric field needed to cancel the charge current. See the Supplemental Material [32] for the full derivation. The dc component of this electric field becomes

$$E_z^{\mathrm{dc}} = \varepsilon_N \left(1 - \frac{1}{\cosh\left(d_N/\lambda_{\mathrm{sd}}^N\right)}\right) \mu_0^x, \quad (10)$$

the first harmonic ac component is

$$E_x^{\mathrm{ac}}(t) = \varepsilon_N \mathrm{Re}\left[\left(\frac{\mu_1^z + i\mu_1^y}{\cosh[\kappa_3(\omega)d_N]} + \frac{\mu_1^z - i\mu_1^y}{\cosh[\kappa_2(\omega)d_N]} - 2\mu_1^z\right)e^{i\omega t}\right], \quad (11)$$

and the second harmonic ac component is

$$E_z^{\mathrm{ac}}(t) = 2\varepsilon_N \mathrm{Re}\left[\left(1 - \frac{1}{\cosh[\kappa_1(2\omega)d_N]}\right)\mu_2^x e^{2i\omega t}\right]. \quad (12)$$

Here, we have introduced the conversion coefficient $\varepsilon_N = \theta_N e \nu D_N/(\sigma_N d_N)$, where $\sigma_N$ is the conductivity of the normal metal. The factors $\mu_n^{x/y/z}$ are the $n$th Fourier components of the spin accumulation at the AF|N interface ($y = 0$). We compute

that they are

$$\mu_1^y = -\frac{i\hbar\omega g_\perp}{4\pi}\frac{\left[\Gamma_2(\omega) + \frac{g_\perp}{2\pi}\right]\delta n_z + \Gamma_3(\omega)\delta n_y}{\left[\Gamma_2(\omega) + \frac{g_\perp}{2\pi}\right]^2 + \Gamma_3^2(\omega)}, \quad (13a)$$

$$\mu_1^z = \frac{i\hbar\omega g_\perp}{4\pi}\frac{\left[\Gamma_2(\omega) + \frac{g_\perp}{2\pi}\right]\delta n_y - \Gamma_3(\omega)\delta n_z}{\left[\Gamma_2(\omega) + \frac{g_\perp}{2\pi}\right]^2 + \Gamma_3^2(\omega)}, \quad (13b)$$

$$\mu_2^x = \frac{g_\perp}{4\pi\,\Gamma_1(2\omega)}\left(\mu_1^y \delta n_y + \mu_1^z \delta n_z\right) \quad (13c)$$

for the first and second harmonic ac components, and

$$\mu_0^x = \frac{g_\perp}{2\pi\,\Gamma_1(0)}\Big[\mathrm{Re}\big(\mu_1^y \delta n_y^* + \mu_1^z \delta n_z^*\big) - \hbar\omega\,\mathrm{Im}\big(\delta n_y^* \delta n_z + \delta m_y^* \delta m_z\big)\Big] \quad (14)$$

for the dc component. All other components of the spin accumulation vanish. The components of the spin accumulation of Eqs. (13) and (14) are expressed in terms of the functions

$$\Gamma_1(\omega) = \tfrac{1}{2}\hbar\nu A D_N \Lambda_1(\omega), \quad (15a)$$

$$\Gamma_2(\omega) = \tfrac{1}{4}\hbar\nu A D_N[\Lambda_2(\omega) + \Lambda_3(\omega)], \quad (15b)$$

$$\Gamma_3(\omega) = \tfrac{i}{4}\hbar\nu A D_N[\Lambda_2(\omega) - \Lambda_3(\omega)], \quad (15c)$$

with $\Lambda_i(\omega) = \kappa_i(\omega)\tanh[\kappa_i(\omega)d_N]$. Here, we have defined $\kappa_1^2 = (1 + i\omega\tau_{\mathrm{sf}}^N)/(\lambda_{\mathrm{sd}}^N)^2$, $\kappa_{(2,3)}^2 = \kappa_1^2 \mp i\gamma_N H_{\mathrm{ex}}/D_N$, the spin diffusion length $\lambda_{\mathrm{sd}}^N = \sqrt{D_N \tau_{\mathrm{sf}}^N}$, and the one-spin density of state $\nu$. Note that $\mu_2^x$ and consequently $E_z^{\mathrm{ac}}$ vanish in the absence of a magnetic field $[\Gamma_3(\omega) = 0]$ and when the precession of the staggered magnetization is circular ($\delta n_z = \pm i\delta n_y$).

We will now use our model to compute the ISHE signal as a function of external magnetic fields in an AF|Pt bilayer. By inserting the linear response ansatz of Eq. (7) into the LLG equations in Eq. (2), we determine the functions $\delta\boldsymbol{n}$ and $\delta\boldsymbol{m}$. The components of the ac magnetic field that drives these perturbations are given by $\omega_j = |\omega_j| \exp(i\omega t + i\theta_j)$ for $j = y, z$. The phase difference $\theta_z - \theta_y$ determines the polarization of the ac field, and significantly affects the resulting spin current. In our calculations, we let $|\omega_y| = |\omega_z|$.

As the material properties of Pt, we use $\tau_{\mathrm{sf}}^N = 0.01$ ps [11], $\nu = 4.55 \times 10^{47}$ J$^{-1}$ m$^{-3}$ [33], $\sigma_N = 5 \times 10^6$ ($\Omega$ m)$^{-1}$ [34], $\lambda_{\mathrm{sd}}^N = 1.5$ nm, and $\theta_N = 0.075$ [35]. These properties are at 10 K. The transverse spin conductance $g_\perp$ is of the same order of magnitude as that of a ferromagnetic or ferrimagnetic material [20]. We therefore estimate this to be $g_\perp/A = 3 \times 10^{18}$ m$^{-2}$ [36,37]. Experimental measurements of $g_\perp$ are needed and are further motivated by the present calculations.

The magnitude of the ISHE signal depends on the thickness of the Pt layer. It increases approximately linearly with $d_N$ for $d_N/\lambda_{\mathrm{sd}}^N \ll 1$ and is inversely proportional to $d_N$ for $d_N/\lambda_{\mathrm{sd}}^N \gg 1$. This qualitative behavior is similar to that in ferromagnetic/normal metal bilayers (cf. Fig. 3(a) in Ref. [11]). The peak of the ISHE signal is at some value $d_N \sim \lambda_{\mathrm{sd}}^N$, and for our choice of parameters, it peaks at $d_N \approx 0.8\lambda_{\mathrm{sd}}^N = 1.2$ nm.
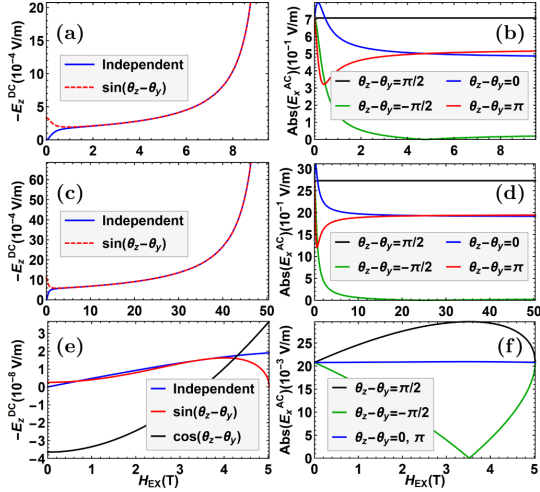
FIG. 2. dc and first harmonic ac components of the ISHE electric field for MnF$_2$ [(a) and (b)], FeF$_2$ [(c) and (d)], and NiO [(e) and (f)] as a function of external magnetic field along the easy axis for different polarizations of the ac magnetic field. The ac field is 1 mT, and $\alpha = 0.01$.

We use this thickness of the Pt layer for the remaining calculations. The optimal thickness $d_N$ weakly depends on the value of $g_\perp/A$ and should therefore be determined experimentally.

Figure 2 plots the dc and the first harmonic ac components of the ISHE electric field as a function of the magnetic field. In the uniaxial antiferromagnets, MnF$_2$ and FeF$_2$, one contribution to the dc signal is independent of the ac magnetic field polarization, and the other contribution is proportional to $\sin(\theta_z - \theta_y)$. At high magnetic fields, these contributions are equal in magnitude but add constructively or destructively, depending on the circular polarization of the ac magnetic field.

Reference [20] demonstrated that the pumped dc spin current in uniaxial antiferromagnets at resonance is suppressed by the factor $\sqrt{\omega_\parallel/\omega_E}$. Since $\sqrt{\omega_\parallel/\omega_E}$ is significantly larger in FeF$_2$ (0.61) than in MnF$_2$ (0.13), it was believed that FeF$_2$ gives a stronger signal than does MnF$_2$. However, with our present additional insight, we reach the opposite conclusion at finite magnetic fields. We find that when $\omega_x \to \omega_x^{\rm crit}$, the dc signal diverges as $(\omega_x^{\rm crit} - \omega_x)^{-1}$. The utilization of the divergence is a better route toward enhancing the ISHE signal than increasing $\sqrt{\omega_\parallel/\omega_E}$. This implies that MnF$_2$ is a more promising candidate than FeF$_2$ because the spin-flop field of MnF$_2$ (9.5 T) is easier to achieve experimentally than is that of FeF$_2$ (50.4 T).

The dc signal diverges because the linear response model breaks down close to the spin-flop transition. By analyzing the magnitude of $|\delta\mathbf{n}|$ we find that it is 0.01 at $\omega_x \approx 0.95\omega_x^{\rm crit}$ and 0.1 at $\omega_x \approx 0.995\omega_x^{\rm crit}$ for the uniaxial antiferromagnets. Consequently, linear response is a good approximation fairly close to the divergence. The enhancement of the dc spin pumping close to the spin-flop transition is therefore a real

phenomenon. We find that the breakdown of the linear response theory is even softer for the biaxial NiO.

Unlike the dc component, the first harmonic ac component is independent of the ac magnetic field polarization in the absence of a uniform external magnetic field and converges toward a finite value as $\omega_x \to \omega_x^{\rm crit}$. The signal when the polarization is circular ($\theta_z - \theta_y = \pi/2$) gives the largest dc signal (and ac signal for sufficiently large magnetic fields). Furthermore, this curve becomes independent of the magnetic field. The origin of this is a complicated compensation between the diverging contributions from the out-of-equilibrium fields and the vanishing resonance frequency around the spin-flop transition.

In NiO, the dominant ac magnetic field contribution is linear in the polarization, which is proportional to $\cos(\theta_z - \theta_y)$. Such a feature appears when there is a hard axis, and the precession is in the easy plane. The linear contribution dominates when $\omega_\perp/\sqrt{\omega_E\omega_\parallel} \gg \alpha$. In biaxial antiferromagnets, we find that the pumped current is governed by the scaling factor $\alpha\omega_\parallel/\omega_\perp$ instead of $\sqrt{\omega_\parallel/\omega_E}$. In discussing the strength of the spin-pumping signals, we should also note that, in both uniaxial and easy-plane antiferromagnets, the signal is inversely proportional to $\omega_E$. Since $\omega_\parallel/\omega_\perp \sim 0.02$ and since $\omega_E$ is exceptionally large in NiO, the dc spin pumping signal is weak in comparison to that of MnF$_2$ and FeF$_2$. In addition, the dc signal in NiO does not exhibit a divergence as $\omega_x \to \omega_x^{\rm crit}$. We do not present the second harmonic ac voltage since it is minimal (and in many cases identically zero). Our results imply that uniaxial antiferromagnets are preferred candidates for the observation of spin pumping compared to hard-axis antiferromagnets such as NiO.

Reference [22] conducted preliminary spin-pumping experiments for a MnF$_2$|Pt system. However, they attributed the dominant dc signal to microwave rectification and not spin pumping. Nevertheless, they observed a small change in the signal upon reversal of the magnetic field, which is consistent with spin pumping.

We propose a different experimental geometry to enhance the spin-pumping signal. The use of the ac magnetic field in a plane perpendicular to the easy axis and a polarization $\theta_z - \theta_y = \pi/2$ increases the dc ISHE signal by a factor of 4. Additionally, by reducing the thickness of the Pt layer from 7 nm to the thickness where the ISHE signal attains its maximum (in our calculations, this is 1.2 nm), we can further amplify the signal by a factor of 2. Together, these improvements will increase the signal strength by an order of magnitude. Whether the signal is due to spin pumping can then easily be tested by the dependence on the polarization of the ac magnetic field according to our model. A circular polarization with $\theta_z - \theta_y = \pi/2$ doubles the signal strength compared to a linear polarization. On the other hand, a circular polarization with $\theta_z - \theta_y = -\pi/2$ results in no dc spin pumping. In contrast, microwave rectification effects should be much less sensitive to the polarization.

In summary, we computed the inverse spin Hall signal as a result of spin pumping and spin backflow in an AF|N bilayer. Our results apply to any polarization of the ac magnetic field and precessional motion of the magnetizations, and the results can also be used in more complex biaxial antiferromagnets. We demonstrate that the dc signal increases substantially near the

spin-flop transition in uniaxial antiferromagnets. Furthermore, the signal strongly depends on the polarization of the ac magnetic field. We also suggest an improved experimental geometry that considerably enhances the dc signal resulting from spin pumping.

[1] S. Mizukami, Y. Ando, and T. Miazaki, Jpn. J. Appl. Phys. **40**, 580 (2001).

[2] R. Urban, G. Woltersdorf, and B. Heinrich, Phys. Rev. Lett. **87**, 217204 (2001).

[3] Y. Tserkovnyak, A. Brataas, and G. E. W. Bauer, Phys. Rev. Lett. **88**, 117601 (2002).

[4] A. Brataas, Y. Tserkovnyak, G. E. W. Bauer, and B. I. Halperin, Phys. Rev. B **66**, 060404 (2002).

[5] B. Heinrich, Y. Tserkovnyak, G. Woltersdorf, A. Brataas, R. Urban, and G. E. W. Bauer, Phys. Rev. Lett. **90**, 187601 (2003).

[6] Y. Tserkovnyak, A. Brataas, G. E. W. Bauer, and B. I. Halperin, Rev. Mod. Phys. **77**, 1375 (2005).

[7] M. V. Costache, M. Sladkov, S. M. Watts, C. H. van der Wal, and B. J. van Wees, Phys. Rev. Lett. **97**, 216603 (2006).

[8] B. Heinrich, C. Burrowes, E. Montoya, B. Kardasz, E. Girt, Y.-Y. Song, Y. Sun, and M. Wu, Phys. Rev. Lett. **107**, 066604 (2011).

[9] A. Kapelrud and A. Brataas, Phys. Rev. Lett. **111**, 097602 (2013).

[10] O. Mosendz, J. E. Pearson, F. Y. Fradin, G. E. W. Bauer, S. D. Bader, and A. Hoffmann, Phys. Rev. Lett. **104**, 046601 (2010).

[11] H. J. Jiao and G. E. W. Bauer, Phys. Rev. Lett. **110**, 217602 (2013).

[12] M. K. Marcham, L. R. Shelford, S. A. Cavill, P. S. Keatley, W. Yu, P. Shafer, A. Neudert, J. R. Childress, J. A. Katine, E. Arenholz, N. D. Telling, G. van der Laan, and R. J. Hicken, Phys. Rev. B **87**, 180403 (2013).

[13] A. A. Baker, A. I. Figueroa, C. J. Love, S. A. Cavill, T. Hesjedal, and G. van der Laan, Phys. Rev. Lett. **116**, 047201 (2016).

[14] T. Jungwirth, X. Marti, P. Wadley, and J. Wunderlich, Nat. Nanotechnol. **11**, 231 (2016).

[15] B. G. Park, J. Wunderlich, X. Martí, V. Holý, Y. Kurosaki, M. Yamada, H. Yamamoto, A. Nishide, J. Hayakawa, H. Takahashi, A. B. Shick, and T. Jungwirth, Nat. Mater. **10**, 347 (2011).

[16] X. Martí, B. G. Park, J. Wunderlich, H. Reichlová, Y. Kurosaki, M. Yamada, H. Yamamoto, A. Nishide, J. Hayakawa, H. Takahashi, and T. Jungwirth, Phys. Rev. Lett. **108**, 017201 (2012).

[17] H. Wang, C. Du, P. C. Hammel, and F. Yang, Phys. Rev. Lett. **113**, 097202 (2014).

[18] J. Železný, H. Gao, K. Výborný, J. Zemen, J. Mašek, A. Manchon, J. Wunderlich, J. Sinova, and T. Jungwirth, Phys. Rev. Lett. **113**, 157201 (2014).

[19] P. Wadley, B. Howells, J. Železný, C. Andrews, V. Hills, R. P. Campion, V. Novák, K. Olejník, F. Maccherozzi, S. S. Dhesi, S. Y. Martin, T. Wagner, J. Wunderlich, F. Freimuth, Y. Mokrousov, J. Kuneš, J. S. Chauhan, M. J. Grzybowski, A. W. Rushforth, K. W. Edmonds, B. L. Gallagher, and T. Jungwirth, Science **351**, 587 (2016).

[20] R. Cheng, J. Xiao, Q. Niu, and A. Brataas, Phys. Rev. Lett. **113**, 057601 (2014).

[21] R. Cheng, D. Xiao, and A. Brataas, Phys. Rev. Lett. **116**, 207603 (2016).

[22] M. P. Ross, Spin dynamics in an antiferromagnet, Ph.D. thesis, Technische Universität München, 2013.

[23] R. C. Ohlmann and M. Tinkham, Phys. Rev. **123**, 425 (1961).

[24] T. Satoh, S.-J. Cho, R. Iida, T. Shimura, K. Kuroda, H. Ueda, Y. Ueda, B. A. Ivanov, F. Nori, and M. Fiebig, Phys. Rev. Lett. **105**, 077402 (2010).

[25] M. T. Hutchings and E. J. Samuelsen, Phys. Rev. B **6**, 3447 (1972).

[26] K. M. D. Hals, Y. Tserkovnyak, and A. Brataas, Phys. Rev. Lett. **106**, 107206 (2011).

[27] K. Yosida, Prog. Theor. Phys. **7**, 25 (1952).

[28] H. V. Gomonay and V. M. Loktev, Phys. Rev. B **81**, 144427 (2010).

[29] M. Johnson and R. H. Silsbee, Phys. Rev. B **37**, 5312 (1988).

[30] E. Saitoh, M. Ueda, H. Miyajima, and G. Tatara, Appl. Phys. Lett. **88**, 182509 (2006).

[31] O. Mosendz, V. Vlaminck, J. E. Pearson, F. Y. Fradin, G. E. W. Bauer, S. D. Bader, and A. Hoffmann, Phys. Rev. B **82**, 214403 (2010).

[32] See Supplemental Material at http://link.aps.org/supplemental/10.1103/PhysRevB.95.220408 for the detailed derivations.

[33] D. Papaconstantopoulos, *Handbook of the Band Structure of Elemental Solids* (Plenum, New York, 1986).

[34] L. Liu, R. A. Buhrman, and D. C. Ralph, arXiv:1111.3702 .

[35] S. Meyer, M. Althammer, S. Geprägs, M. Opel, R. Gross, and S. T. B. Goennenwein, Appl. Phys. Lett. **104**, 242411 (2014).

[36] T. Yoshino, K. Ando, K. Harii, H. Nakayama, Y. Kajiwara, and E. Saitoh, J. Phys.: Conf. Ser. **266**, 012115 (2011).

[37] M. Haertinger, C. H. Back, J. Lotze, M. Weiler, S. Geprägs, H. Huebl, S. T. B. Goennenwein, and G. Woltersdorf, Phys. Rev. B **92**, 054437 (2015).

# Supplementary Material for "Spin Pumping and Inverse Spin Hall Voltages from Dynamical Antiferromagnets"

Øyvind Johansen and Arne Brataas

*Department of Physics, Norwegian University of*

*Science and Technology, NO-7491, Trondheim, Norway*

(Dated: February 13, 2017)

## Abstract

Precessing spins can induce currents between antiferromagnetic insulators and normal metals. We compute these AC and DC spin currents across the interface, including the effects of spin backflow. We also calculate the resulting AC and DC inverse spin Hall electric fields in the normal metal. We express all currents and fields in terms of the dynamics of the staggered field and the magnetization.

**TOTAL SPIN CURRENT AND INVERSE SPIN HALL VOLTAGES**

Spin-pumping is the emission of spin-currents into adjacent conductors from precessing spins. Ref. 1 introduced a quantitative theory for the resulting spin-current through ferromagnet-normal metal interfaces. The spin flow causes a spin accumulation in the normal metal. Ref. 2 computed the resulting DC spin accumulation. There are also AC components and Ref. 3 studied these in detail, and furthermore, included the inverse spin Hall effect in the normal metal. We will generalize this approach by replacing the ferromagnets with antiferromagnetic insulators.

We disregard the imaginary part of the transverse ("mixing") conductance since it is likely to be small in most circumstances[4]. Then, the pumped spin-current is[4]

$$\mathbf{I}_s^p = \frac{\hbar g_\perp}{2\pi} \left( \mathbf{n} \times \dot{\mathbf{n}} + \mathbf{m} \times \dot{\mathbf{m}} \right), \tag{1}$$

where $g_\perp$ is the transverse conductance, $\mathbf{n} = (\mathbf{m}_1 - \mathbf{m}_2)/2$ is the staggered field and $\mathbf{m} = (\mathbf{m}_1 + \mathbf{m}_2)/2$ is the magnetization. At equilibrium, the staggered field is along the easy axis, $\mathbf{n}_0 = \mathbf{e}_x$, and the magnetization vanishes.

Next, we need to take into account the backflow spin current into the antiferromagnet resulting from the spin accumulation. In antiferromagnets, the backflow spin current is similar to the case of ferromagnets since the spin currents from the two sub-lattices add constructively

$$\mathbf{I}_s^b = -\frac{g_\perp}{4\pi} \left[ \mathbf{m}_1 \times \left( \boldsymbol{\mu}_s^N \times \mathbf{m}_1 \right) + \mathbf{m}_2 \times \left( \boldsymbol{\mu}_s^N \times \mathbf{m}_2 \right) \right], \tag{2a}$$

$$= \frac{g_\perp}{2\pi} \left[ \mathbf{m} \left( \boldsymbol{\mu}_s^N \cdot \mathbf{m} \right) + \mathbf{n} \left( \boldsymbol{\mu}_s^N \cdot \mathbf{n} \right) - \boldsymbol{\mu}_s^N \right], \tag{2b}$$

where $\boldsymbol{\mu}_s^N$ is the spin accumulation in the normal metal. The backflow spin current of Eq. (2b) and the pumped spin current of Eq. (1) are related by Onsager reciprocity relations[4].

To compute the spin backflow we need to determine the spatiotemporal variation of the spin accumulation in the normal metal. This spin accumulation should fulfil the spin diffusion equation

$$\frac{\partial \boldsymbol{\mu}_s^N(\mathbf{r}, t)}{\partial t} = \gamma_N \mathbf{H}_{\text{ex}} \times \boldsymbol{\mu}_s^N + D_N \frac{\partial^2 \boldsymbol{\mu}_s^N}{\partial y^2} - \frac{\boldsymbol{\mu}_s^N}{\tau_{\text{sf}}^N}, \tag{3}$$

where the terms on the right hand side of Eq. (3) are properties of the normal metal such as the diffusion coefficient $D_N$, the gyromagnetic ratio $\gamma_N$, the spin-flip relaxation time $\tau_{\text{sf}}^N$, and the external magnetic field $\mathbf{H}_{\text{ex}} = \boldsymbol{e}_x \omega_x / \gamma_{AF}$. We have disregarded the small off-resonance

2

AC component of the magnetic field. As a consequence, the magnetic field only causes spin precession that couples the transverse, $y$- and $z$-components of the spin accumulation.

The spin diffusion equation of Eq. (3) needs to be supplemented by boundary conditions. At the outer edge of the normal metal, $y = d_N$, the spin current vanishes. In contrast, the spin current is continuous across the antiferromagnet-normal metal interface, where $y = 0$. We carry out a Fourier transformation of the spin accumulation in time. With the two boundary conditions, the solution to Eq. (3) is[3,5]:

$$\boldsymbol{\mu}_s^N(y, \omega) = \sum_{i=1}^{3} \mathbf{e}_i \frac{\cosh\left[\kappa_i\left(y - d_N\right)\right]}{\sinh\left[\kappa_i d_N\right]} \frac{2j_{is}\left(y = 0, \omega\right)}{\hbar \nu D_N \kappa_i}. \tag{4}$$

In Eq. (4), we use a circular basis, $\mathbf{e}_1 = \mathbf{e}_x$, $\mathbf{e}_2 = \mathbf{e}_- = (\mathbf{e}_y - i\mathbf{e}_z)/\sqrt{2}$, $\mathbf{e}_3 = \mathbf{e}_+ = (\mathbf{e}_y + i\mathbf{e}_z)/\sqrt{2}$. In this basis, we introduce the spin current density components at the interface: $j_{1s} = I_s^x/A$, $j_{2s} = (I_s^y + iI_s^z)/(\sqrt{2}A)$ and $j_{3s} = (I_s^y - iI_s^z)/(\sqrt{2}A)$, where $A$ is the interface cross section and $I_s^{x/y/z} = \left[\mathbf{I}_s^p(y = 0, \omega) + \mathbf{I}_s^b(y = 0, \omega)\right] \cdot \mathbf{e}_{x/y/z}$ are the cartesian Fourier components of the total spin current at the interface. We have also defined the quantities $\kappa_1^2 = \left(1 + i\omega\tau_{\mathrm{sf}}^N\right)/\left(\lambda_{\mathrm{sd}}^N\right)^2$, $\kappa_{(2,3)}^2 = \kappa_1^2 \mp i\gamma_N\omega_x/\left(\gamma_{AF}D_N\right)$ and the spin diffusion length $\lambda_{\mathrm{sd}}^N = \sqrt{D_N\tau_{\mathrm{sf}}^N}$.

Temporal variations of the staggered field and the magnetization drive the spin currents. We characterize the out-of-equilibrium deviations of these fields by a perturbation parameter $\delta$. We will now consider how the different components scale with the small variations proportional to $\delta$ during the spin dynamics. Since $\mathbf{m}_1$ and $\mathbf{m}_2$ are real unit vectors, $\mathbf{n}$ and $\mathbf{m}$ must fulfil $\mathbf{n}^2 + \mathbf{m}^2 = 1$ and $\mathbf{n} \cdot \mathbf{m} = 0$. These conditions are satisfied to second order in the perturbation parameter $\delta$ when we expand the fields as

$$\mathbf{n} = \left(1 - \delta^2 n_x^{(2)}(t)\right)\mathbf{e}_x + \left(\delta n_y^{(1)}(t) + \delta^2 n_y^{(2)}(t)\right)\mathbf{e}_y + \left(\delta n_z^{(1)}(t) + \delta^2 n_z^{(2)}(t)\right)\mathbf{e}_z, \tag{5a}$$

$$\mathbf{m} = -\delta^2 m_x^{(2)}(t)\mathbf{e}_x + \left(\delta m_y^{(1)}(t) + \delta^2 m_y^{(2)}(t)\right)\mathbf{e}_y + \left(\delta m_z^{(1)}(t) + \delta^2 m_z^{(2)}(t)\right)\mathbf{e}_z, \tag{5b}$$

where the second order longitudinal corrections $\delta^2 n_x^{(2)}(t)$ and $\delta^2 m_x^{(2)}(t)$ must obey

$$\delta^2 n_x^{(2)}(t) = \frac{1}{2}\left[\left(\delta m_y^{(1)}(t)\right)^2 + \left(\delta m_z^{(1)}(t)\right)^2 + \left(\delta n_y^{(1)}(t)\right)^2 + \left(\delta n_z^{(1)}(t)\right)^2\right], \tag{6a}$$

$$\delta^2 m_x^{(2)}(t) = \delta m_y^{(1)}(t)\delta n_y^{(1)}(t) + \delta m_z^{(1)}(t)\delta n_z^{(1)}(t). \tag{6b}$$

We can now insert the expansion of Eq. (5) into the expression for the spin-pumping current in Eq. (1). For the spin current component polarized along the easy axis $\mathbf{e}_x$, we

find that the leading order corrections are of second order in $\delta$. On the other hand, for the spin current components that are polarized transverse to the easy axis, the leading order corrections are first order in $\delta$. Furthermore, all leading order terms only depend on $\delta n_y^{(1)}(t)$, $\delta n_z^{(1)}(t)$, $\delta m_y^{(1)}(t)$ and $\delta m_z^{(1)}(t)$, which simplifies the following discussions considerably.

To leading order, it is then sufficient to only consider the linear corrections in $\mathbf{n}$ and $\mathbf{m}$. In the following analysis, we therefore only use the linear response expansion of the fields that are driven at the frequency $\omega_{\mathrm{AC}}$ of the AC magnetic field

$$\mathbf{n} = \mathbf{n}_0 + \frac{1}{2}\left(\delta\mathbf{n}e^{i\omega_{\mathrm{AC}}t} + \delta\mathbf{n}^*e^{-i\omega_{\mathrm{AC}}t}\right), \tag{7a}$$

$$\mathbf{m} = \frac{1}{2}\left(\delta\mathbf{m}e^{i\omega_{\mathrm{AC}}t} + \delta\mathbf{m}^*e^{-i\omega_{\mathrm{AC}}t}\right). \tag{7b}$$

The out-of-equilibrium deviations $\delta\mathbf{n} = \delta n_y\mathbf{e}_y + \delta n_z\mathbf{e}_z$ and $\delta\mathbf{m} = \delta m_y\mathbf{e}_y + \delta m_z\mathbf{e}_z$ are perpendicular to $\mathbf{n}_0 = \mathbf{e}_x$. In general, these deviations depend on the AC field frequency and the free energy. Their magnitudes are significant only close to the resonance frequencies.

Next, we will consider the contributions to the spin backflow current of Eq. (2b). We note that the backflow current results from the primary source, the pumped spin current of Eq. (1). Therefore, the backflow current cannot exceed the leading order in the pumped spin current. In turn, this implies that the spin accumulation $\boldsymbol{\mu}_s^N(y, \omega)$ component along the $x$-direction is of a second order in $\delta$. On the other hand, the leading contribution to the spin accumulation is of a first order in the spin deviations along the transverse $y$- and $z$-directions.

To proceed, we expand the pumped spin current in a Fourier series

$$\mathbf{I}_s^p = \sum_n \mathbf{I}_n^p e^{in\omega_{\mathrm{AC}}t}. \tag{8}$$

In this series, we decompose the spin-current into a DC term, first AC harmonics, and higher AC harmonics. The pumped DC spin current is of a second order in the deviations from the equilibrium spin configuration and it is polarized along the easy axis:

$$\mathbf{I}_0^p = \frac{i\hbar\omega_{\mathrm{AC}}g_\perp}{4\pi}\left(\delta n_y^*\delta n_z - \delta n_z^*\delta n_y + \delta m_y^*\delta m_z - \delta m_z^*\delta m_y\right)\mathbf{e}_x. \tag{9}$$

The polarization of the first AC harmonic pumped spin current is transverse to the easy axis,

$$\mathbf{I}_1^p = \frac{i\hbar\omega_{\mathrm{AC}}g_\perp}{4\pi}\left(\delta n_y\mathbf{e}_z - \delta n_z\mathbf{e}_y\right) \tag{10}$$

4

and $\mathbf{I}_{-1}^p = (\mathbf{I}_1^p)^*$. To the second order in the spin deviations, the higher harmonics vanish, $\mathbf{I}_n^p = 0$ when ($|n| \geq 2$).

In the expression for the spin backflow current of Eq. (2b), we can disregard the dependence on $\mathbf{m}$ since $\mathbf{m}(\boldsymbol{\mu}_s^N \cdot \mathbf{m})$ is a third order correction. By including terms only up to second order in $\delta\mathbf{m}$ and $\delta\mathbf{n}$, we can then approximate the spin backflow current of Eq. (2b) as

$$\mathbf{I}_s^b \approx \frac{g_\perp}{2\pi} \left[ \mathbf{e}_x \left( \boldsymbol{\mu}_s^N \cdot \mathbf{n} \right) - \boldsymbol{\mu}_s^N \right]. \tag{11}$$

Similar to the spin current, we also Fourier transform the spin accumulation at the interface ($y = 0$) into DC and AC components:

$$\boldsymbol{\mu}_s^N(t) = \sum_n \boldsymbol{\mu}_n e^{in\omega_{\mathrm{AC}}t}. \tag{12}$$

The spin backflow current can also be expanded as

$$\mathbf{I}_s^b = \sum_n \mathbf{I}_n^b e^{in\omega_{\mathrm{AC}}t}, \tag{13}$$

where the harmonic components $\mathbf{I}_n^b$ are

$$\mathbf{I}_n^b = \frac{g_\perp}{2\pi} \begin{pmatrix} \frac{1}{2} \left[ \mu_{n-1}^y \delta n_y + \mu_{n-1}^z \delta n_z + \mu_{n+1}^y \delta n_y^* + \mu_{n+1}^z \delta n_z^* \right] \\ -\mu_n^y \\ -\mu_n^z \end{pmatrix}. \tag{14}$$

Note that $(\mathbf{I}_n^b)^* = \mathbf{I}_{-n}^b$, $\boldsymbol{\mu}_n^* = \boldsymbol{\mu}_{-n}$. The product $\mu_{n-1}^{y/z}\delta n_{y/z}$ ($\mu_{n+1}^{y/z}\delta n_{y/z}^*$) is an $n$-th harmonic contribution since $\delta n_{y/z}$ ($\delta n_{y/z}^*$) contains the first harmonic factor factor $e^{i\omega_{\mathrm{AC}}t}$ ($e^{-i\omega_{\mathrm{AC}}t}$).

We find a closed set of equations for the spin accumulation in the following way. We invert the relation of Eq. (4) to find the total spin current in terms of the spin accumulation. In this inversion process, it is useful to introduce the functions

$$\Gamma_1(y,\omega) = \frac{1}{2}\hbar\nu A D_N \kappa_1(\omega) \frac{\sinh\left[\kappa_1(\omega)(d_N - y)\right]}{\cosh\left[\kappa_1(\omega)d_N\right]}, \tag{15a}$$

$$\Gamma_2(y,\omega) = \frac{\hbar\nu A D_N}{4} \left[ \kappa_2(\omega) \frac{\sinh\left[\kappa_2(\omega)(d_N - y)\right]}{\cosh\left[\kappa_2(\omega)d_N\right]} + \kappa_3(\omega) \frac{\sinh\left[\kappa_3(\omega)(d_N - y)\right]}{\cosh\left[\kappa_3(\omega)d_N\right]} \right], \tag{15b}$$

$$\Gamma_3(y,\omega) = \frac{i\hbar\nu A D_N}{4} \left[ \kappa_2(\omega) \frac{\sinh\left[\kappa_2(\omega)(d_N - y)\right]}{\cosh\left[\kappa_2(\omega)d_N\right]} - \kappa_3(\omega) \frac{\sinh\left[\kappa_3(\omega)(d_N - y)\right]}{\cosh\left[\kappa_3(\omega)d_N\right]} \right], \tag{15c}$$

and $\Gamma_i(\omega) = \Gamma_i(y = 0, \omega)$ ($i = 1, 2, 3$). The resulting expression for the total spin current should equal the sum of the pumped spin current of Eq. (9) and Eq. (10), and the backflow

spin current of Eq. (14). Moreover, the expressions must hold for each component of the Fourier expansion since they should be valid at all times. Then, we find that the spin accumulation along the easy axis at the interface is:

$$\mu_n^x = \frac{1}{\Gamma_1\left(n\omega_{\text{AC}}\right)} \left[ I_n^{p(x)} + \frac{g_\perp}{4\pi} \left( \mu_{n-1}^y \delta n_y + \mu_{n-1}^z \delta n_z + \mu_{n+1}^y \delta n_y^* + \mu_{n+1}^z \delta n_z^* \right) \right]. \qquad (16)$$

We see that the components along the easy axis are coupled to the perpendicular components in the $yz$-plane due to the backflow current in Eq. (14). The magnetic field aligned along the easy axis couples the transverse components of the spin accumulation in the diffusion equation (3). Hence, to find the perpendicular components of the spin accumulation at the interface, we have to solve the matrix equation for the transverse components

$$\begin{pmatrix} \Gamma_2(n\omega_{\text{AC}}) + \frac{g_\perp}{2\pi} & \Gamma_3(n\omega_{\text{AC}}) \\ -\Gamma_3(n\omega_{\text{AC}}) & \Gamma_2(n\omega_{\text{AC}}) + \frac{g_\perp}{2\pi} \end{pmatrix} \begin{pmatrix} \mu_n^y \\ \mu_n^z \end{pmatrix} = \begin{pmatrix} I_n^{p(y)} \\ I_n^{p(z)} \end{pmatrix} = \mathbf{I}_n(y=0, n\omega_{\text{AC}}) - \mathbf{I}_n^b(y=0, n\omega_{\text{AC}}). \tag{17}$$

In the absence of a magnetic field $\Gamma_3(\omega) \to 0$, the coupling between the transverse components $\mu_n^y$ and $\mu_n^z$ vanishes. We solve Eq. (17) for $\mu_n^{y,z}$ and find that

$$\begin{pmatrix} \mu_n^y \\ \mu_n^z \end{pmatrix} = \frac{1}{\left(\Gamma_2\left(n\omega_{\text{AC}}\right) + \frac{g_\perp}{2\pi}\right)^2 + \Gamma_3^2\left(n\omega_{\text{AC}}\right)} \begin{pmatrix} \Gamma_2\left(n\omega_{\text{AC}}\right) + \frac{g_\perp}{2\pi} & -\Gamma_3\left(n\omega_{\text{AC}}\right) \\ \Gamma_3\left(n\omega_{\text{AC}}\right) & \Gamma_2\left(n\omega_{\text{AC}}\right) + \frac{g_\perp}{2\pi} \end{pmatrix} \begin{pmatrix} I_n^{p(y)} \\ I_n^{p(z)} \end{pmatrix}. \tag{18}$$

Since $\left(\Gamma_2\left(n\omega_{\text{AC}}\right) + \frac{g_\perp}{2\pi}\right)^2 + \Gamma_3^2\left(n\omega_{\text{AC}}\right)$ is finite for the parameters of interest and $I_n^{p(y,z)} = 0$ for $|n| \neq 1$, we find that $\mu_n^{y,z} = 0$ for $|n| \neq 1$. We have then determined the spin accumulation at the interface in the normal metal along the transverse $y$ and $z$ directions:

$$\mu_1^y = -\frac{i\hbar\omega_{\text{AC}}g_\perp}{4\pi} \frac{\left(\Gamma_2\left(\omega_{\text{AC}}\right) + \frac{g_\perp}{2\pi}\right)\delta n_z + \Gamma_3\left(\omega_{\text{AC}}\right)\delta n_y}{\left(\Gamma_2\left(\omega_{\text{AC}}\right) + \frac{g_\perp}{2\pi}\right)^2 + \Gamma_3^2\left(\omega_{\text{AC}}\right)}, \qquad (19a)$$

$$\mu_1^z = \frac{i\hbar\omega_{\text{AC}}g_\perp}{4\pi} \frac{\left(\Gamma_2\left(\omega_{\text{AC}}\right) + \frac{g_\perp}{2\pi}\right)\delta n_y - \Gamma_3\left(\omega_{\text{AC}}\right)\delta n_z}{\left(\Gamma_2\left(\omega_{\text{AC}}\right) + \frac{g_\perp}{2\pi}\right)^2 + \Gamma_3^2\left(\omega_{\text{AC}}\right)}. \qquad (19b)$$

These transverse solutions can then be used to obtain the solutions for the longitudinal component, $\mu_n^x$, from Eq. (16). The pumping component $I_n^{p(x)}$ is only non-zero when $n = 0$, thereby only contributing to the DC component $\mu_0^x$. However, there are also second harmonics in the longitudinal component of the spin accumulation. This is caused by the coupling with $\mu_{\pm 1}^{y,z}$ from the backflow, the only finite components of $\mu_n^{y,z}$. In summary, we find that $\mu_n^x$ is finite when $n = 0, \pm 2$, and zero for all other values of $n$.

6

The Fourier components of the total spin current at the interface ($y = 0$) then become

$$\mathbf{I}_0 = \Gamma_1\left(0\right)\mu_0^x\mathbf{e}_x, \tag{20a}$$

$$\mathbf{I}_1 = \left[\Gamma_2\left(\omega_{\mathrm{AC}}\right)\mu_1^y + \Gamma_3\left(\omega_{\mathrm{AC}}\right)\mu_1^z\right]\mathbf{e}_y + \left[\Gamma_2\left(\omega_{\mathrm{AC}}\right)\mu_1^z - \Gamma_3\left(\omega_{\mathrm{AC}}\right)\mu_1^y\right]\mathbf{e}_z, \tag{20b}$$

$$\mathbf{I}_2 = \Gamma_1\left(2\omega_{\mathrm{AC}}\right)\mu_2^x\mathbf{e}_x \tag{20c}$$

and all higher harmonics vanish, $\mathbf{I}_n = 0 \quad (|n| \geq 3)$. Also, $\mathbf{I}_{-n} = \left(\mathbf{I}_n\right)^*$. The total spatiotemporal spin current in the normal metal is then

$$\mathbf{I}_s^N(y,t) = \left[\Gamma_1\left(y,0\right)\mu_0^x + 2\mathrm{Re}\left(\Gamma_1\left(y,2\omega_{\mathrm{AC}}\right)\mu_2^x e^{2i\omega_{\mathrm{AC}}t}\right)\right]\mathbf{e}_x$$
$$+ 2\mathrm{Re}\left[\Gamma_2\left(y,\omega_{\mathrm{AC}}\right)\mu_1^y e^{i\omega_{\mathrm{AC}}t} + \Gamma_3\left(y,\omega_{\mathrm{AC}}\right)\mu_1^z e^{i\omega_{\mathrm{AC}}t}\right]\mathbf{e}_y$$
$$+ 2\mathrm{Re}\left[\Gamma_2\left(y,\omega_{\mathrm{AC}}\right)\mu_1^z e^{i\omega_{\mathrm{AC}}t} - \Gamma_3\left(y,\omega_{\mathrm{AC}}\right)\mu_1^y e^{i\omega_{\mathrm{AC}}t}\right]\mathbf{e}_z. \tag{21}$$

We will now use this result to compute the inverse spin Hall effect (ISHE) to the lowest order in the spin-Hall angle. The charge current in the normal metal generated by the ISHE is[6,7]

$$\mathbf{j}_c^{\mathrm{ISHE}}(y,t) = \theta_N\frac{2e}{A\hbar}\mathbf{e}_y \times \mathbf{I}_s^N(y,t), \tag{22}$$

where $\theta_N$ is the spin Hall angle in the normal metal. This charge current causes a build-up of charge accumulation at the interface. In turn, the charge accumulation generates a counter diffusion charge flow so that the net charge current in the open system vanishes. This electric field is then

$$\mathbf{E}(t) = -\frac{2\theta_N e}{A\hbar\sigma_N d_N}\mathbf{e}_y \times \int_0^{d_N}\mathbf{I}_s^N(y,t)\mathrm{d}y = E_x^{\mathrm{AC}}(t)\mathbf{e}_x + \left(E_z^{\mathrm{DC}} + E_z^{\mathrm{AC}}(t)\right)\mathbf{e}_z, \tag{23}$$

where $\sigma_N$ is the conductivity of the normal metal. From this we find that the DC electric field becomes

$$E_z^{\mathrm{DC}} = \frac{\theta_N e\nu D_N}{\sigma_N d_N}\left(1 - \frac{1}{\cosh\left(d_N/\lambda_{\mathrm{sd}}^N\right)}\right)\mu_0^x. \tag{24}$$

The first harmonic AC component is

$$E_x^{\mathrm{AC}}(t) = \frac{\theta_N e\nu D_N}{\sigma_N d_N}\mathrm{Re}\left[\left(\frac{1}{\cosh\left(\kappa_3(\omega_{\mathrm{AC}})d_N\right)} - \frac{1}{\cosh\left(\kappa_2(\omega_{\mathrm{AC}})d_N\right)}\right)i\mu_1^y e^{i\omega_{\mathrm{AC}}t}\right.$$
$$\left. - \left(2 - \frac{1}{\cosh\left(\kappa_2(\omega_{\mathrm{AC}})d_N\right)} - \frac{1}{\cosh\left(\kappa_3(\omega_{\mathrm{AC}})d_N\right)}\right)\mu_1^z e^{i\omega_{\mathrm{AC}}t}\right] \tag{25}$$

Finally, the second harmonic AC component is

$$E_z^{\mathrm{AC}}(t) = \frac{2\theta_N e\nu D_N}{\sigma_N d_N}\mathrm{Re}\left[\left(1 - \frac{1}{\cosh\left(\kappa_1(2\omega_{\mathrm{AC}})d_N\right)}\right)\mu_2^x e^{2i\omega_{\mathrm{AC}}t}\right]. \tag{26}$$

While the DC component and the second harmonic AC component are quadratic in the spin deviations, the first harmonic AC component is linear in the perturbations.

---

[1] Y. Tserkovnyak, A. Brataas, and G. Bauer, Phys. Rev. Lett. **88** (2002).

[2] A. Brataas, Y. Tserkovnyak, G. E. W. Bauer, and B. I. Halperin, Phys. Rev. B **66**, 060404 (2002).

[3] H. Jiao and G. E. W. Bauer, Phys. Rev. Lett. **110**, 217602 (2013).

[4] R. Cheng, J. Xiao, Q. Niu, and A. Brataas, Phys. Rev. Lett. **113**, 057601 (2014).

[5] M. Johnson and R. H. Silsbee, Phys. Rev. B **37**, 5312 (1988).

[6] E. Saitoh, M. Ueda, H. Miyajima, and G. Tatara, Appl. Phys. Lett. **88**, 182509 (2006).

[7] O. Mosendz, V. Vlaminck, J. E. Pearson, F. Y. Fradin, G. E. W. Bauer, S. D. Bader, and A. Hoffmann, Phys. Rev. B **82**, 214403 (2010).

# Paper [2]

**Øyvind Johansen, Hans Skarsvåg and Arne Brataas**

*"Spin-transfer antiferromagnetic resonance"*

# Spin-transfer antiferromagnetic resonance

Øyvind Johansen,[*] Hans Skarsvåg, and Arne Brataas

*Center for Quantum Spintronics, Department of Physics, Norwegian University of Science and Technology,*
*NO-7491 Trondheim, Norway*

Currents can induce spin excitations in antiferromagnets, even when they are insulating. We investigate how spin transfer can cause antiferromagnetic resonance in bilayers and trilayers that consist of one antiferromagnetic insulator and one or two metals. An ac voltage applied to the metal generates a spin Hall current that drives the magnetic moments in the antiferromagnet. We consider excitation of a sublattice macrospin mode and of transverse standing-spin-wave modes. By solving the Landau-Lifshitz-Gilbert equation in the antiferromagnetic insulator and the spin-diffusion equation in the normal metal, we derive analytical expressions for the spin-Hall-magnetoresistance and spin-pumping inverse-spin-Hall dc voltages. In bilayers, the two contributions compensate each other and cannot easily be distinguished. We present numerical results for a $MnF_2|Pt$ bilayer. Trilayers facilitate separation of the spin-Hall-magnetoresistance and spin-pumping voltages, thereby revealing more information about the spin excitations. We also compute the decay of the pumped spin current through the antiferromagnetic layer as a function of frequency and the thickness of the antiferromagnetic layer.

## I. INTRODUCTION

Antiferromagnets have many qualities that make them attractive for use in spintronic devices. For example, the absence of stray fields allows for dense storage of components without undesired cross talk between the active elements. The most interesting feature of antiferromagnets is that their high resonance frequencies pave the way toward terahertz circuits [1].

Current-induced spin-transfer torques (STTs) can induce ferromagnetic resonance [2] in both metallic and insulating ferromagnets [3,4]. An antidampinglike STT is even under magnetization reversal [5]. Consequently, the magnetic moments in the two sublattices of a collinear antiferromagnetic insulator experience the same STT, which enables STT-driven spin dynamics in antiferromagnets. Current-induced STT is a powerful method for probing the magnetization dynamics in magnetic layers [6,7]. An electric signal can simultaneously drive and detect the magnetization dynamics. An ac voltage leads to an alternating spin current through the spin Hall effect [8], which drives the magnetic moments at resonance. Subsequently, the spin Hall magnetoresistance (SMR) and spin pumping (SP) induce dc voltages through the inverse spin Hall effect (ISHE) [9].

SMR [10,11] is the dependence of the normal-metal resistance on the orientation of the magnetic moments in an adjacent magnetic layer relative to the applied current. When the magnetic moments precess, the resistance of the metal correspondingly oscillates. The mixing of the oscillating resistance and charge current generates a dc voltage bias that can provide insights into the magnetization dynamics. Recent experiments have indicated that SMR also occurs in antiferromagnetic-insulator/normal-metal (AF|N) bilayers [12–16]. Theoretical predictions have also been made for conducting antiferromagnets [17].

Similar to ferromagnets, SP is also active in antiferromagnets [18]. However, to the best of our knowledge, there are no direct experimental detections of antiferromagnetic SP. The lack of direct experimental signatures is possibly due to the high resonance frequencies and low susceptibilities of the magnetic moments in antiferromagnets, which make experimental detection challenging. However, we have recently theoretically shown that the susceptibilities and thus the dc SP substantially increase near the spin-flop transition, where the resonance frequency is low [19]. Therefore, we expect that antiferromagnetic SP will be a prominent effect if we drive our system close to the spin-flop transition.

In this paper, we compute the dc voltages resulting from SMR and SP in antiferromagnetic-insulator/normal-metal bilayers. The driving source is an ac voltage bias on the normal metal. We consider the excitation of a sublattice macrospin mode, henceforth referred to as the macrospin mode, where the magnetization dynamics within each sublattice is spatially uniform throughout the antiferromagnet. In addition to the macrospin mode, we also consider the excitation of transverse standing spin waves. These standing waves have a higher resonance frequency than that of the uniform precession modes, and these waves can be excited by tuning the frequency of the applied voltage bias. The detection of such waves would reveal a wide variety of properties of the antiferromagnetic material. The resonance frequencies can be used to determine contributions to the free energy of the antiferromagnet, such as exchange and anisotropy frequencies and the exchange lengths of the sublattices. The amplitudes and linewidths of the resonance peaks can also be used to determine both the intrinsic and SP-induced damping and thus the transverse spin conductance of the AF|N interface. Finally, we also show how the SMR and SP dc voltages can be separated by sandwiching the antiferromagnetic material between two metals and measuring the dc biases in the metals independently.

---

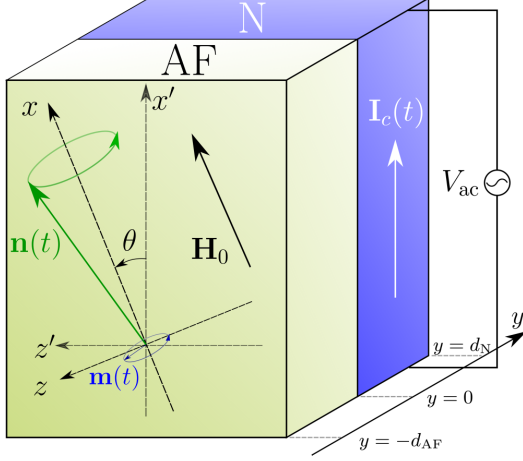[*]Corresponding author: oyvinjoh@ntnu.no

FIG. 1. An ac voltage applied to a normal metal with strong spin-orbit coupling generates spin currents that flow into the antiferromagnetic insulator, exciting the magnetic moments. The direction of the applied voltage and the easy axis of the antiferromagnet are parallel to the AF|N interface, and there is an angle of $\theta$ between them. An external field $\mathbf{H}_0$ along the easy axis of the antiferromagnet controls the resonance frequency and the magnetic susceptibilities.

This approach requires that the dissipation of the pumped spin current through the antiferromagnet is negligible. We therefore study for what thicknesses of the antiferromagnetic layer and for what resonance frequencies this is a valid assumption.

The remainder of this paper is organized as follows. In Sec. II, we present the model that describes the magnetization dynamics in an antiferromagnetic insulator and the accumulation of spins in an adjacent nonmagnetic metal. In that section, we primarily focus on an AF|N bilayer, as illustrated in Fig. 1. The solution of the model for the bilayer system is then presented in Sec. III. This solution is used to obtain analytical expressions for the dc voltages resulting from SP and SMR, given by Eq. (31). These expressions are our main result for the bilayer system. In Sec. IV, we extend the solution of the model presented in Sec. II to a N|AF|N trilayer system (as illustrated in Fig. 4 below). For the trilayer system, our main contribution is illustrating how this system can be used to measure the SP and SMR voltages independently. These contributions cannot be distinguished in the bilayer system because they have the same frequency dependence.

## II. MODEL

### A. Equations of motion

The sublattice magnetizations of the antiferromagnetic insulator are $\mathbf{M}_1$ and $\mathbf{M}_2$. We describe the dynamics of these magnetizations in terms of the dimensionless average magnetization and Néel order parameter vectors $\mathbf{m}$ and $\mathbf{n}$, which are defined as $L\mathbf{m} = (\mathbf{M}_1 + \mathbf{M}_2)/2$ and $L\mathbf{n} = (\mathbf{M}_1 - \mathbf{M}_2)/2$, where $L$ is the saturation magnetization of each sublattice. These vectors satisfy the constraints $\mathbf{m}^2 + \mathbf{n}^2 = 1$ and $\mathbf{m} \cdot \mathbf{n} = 0$. The coupled equations of motion for $\mathbf{m}$ and $\mathbf{n}$ are given by

the Landau-Lifshitz-Gilbert (LLG) equations

$$\dot{\mathbf{m}} = \tfrac{1}{2}(\boldsymbol{\omega}_m \times \mathbf{m} + \boldsymbol{\omega}_n \times \mathbf{n}) + \boldsymbol{\tau}_m^{\mathrm{GD}} + \boldsymbol{\tau}_m^{\mathrm{SP}} + \boldsymbol{\tau}_m^{\mathrm{STT}}, \quad (1a)$$

$$\dot{\mathbf{n}} = \tfrac{1}{2}(\boldsymbol{\omega}_m \times \mathbf{n} + \boldsymbol{\omega}_n \times \mathbf{m}) + \boldsymbol{\tau}_n^{\mathrm{GD}} + \boldsymbol{\tau}_n^{\mathrm{SP}} + \boldsymbol{\tau}_n^{\mathrm{STT}}. \quad (1b)$$

In the LLG equations (1), the Gilbert damping torques are

$$\boldsymbol{\tau}_m^{\mathrm{GD}} = \alpha_0(\mathbf{m} \times \dot{\mathbf{m}} + \mathbf{n} \times \dot{\mathbf{n}}), \quad (2a)$$

$$\boldsymbol{\tau}_n^{\mathrm{GD}} = \alpha_0(\mathbf{m} \times \dot{\mathbf{n}} + \mathbf{n} \times \dot{\mathbf{m}}), \quad (2b)$$

the interfacial SP torques are

$$\boldsymbol{\tau}_m^{\mathrm{SP}} = \alpha' d_{\mathrm{AF}} \delta(y)(\mathbf{m} \times \dot{\mathbf{m}} + \mathbf{n} \times \dot{\mathbf{n}}), \quad (3a)$$

$$\boldsymbol{\tau}_n^{\mathrm{SP}} = \alpha' d_{\mathrm{AF}} \delta(y)(\mathbf{m} \times \dot{\mathbf{n}} + \mathbf{n} \times \dot{\mathbf{m}}), \quad (3b)$$

and the STTs are

$$\boldsymbol{\tau}_m^{\mathrm{STT}} = \frac{\alpha'}{\hbar} d_{\mathrm{AF}} \delta(y) \big\{ \mathbf{m} \times \big[ \mathbf{m} \times \boldsymbol{\mu}_s^{\mathrm{N}}(y,t) \big]$$
$$+ \mathbf{n} \times \big[ \mathbf{n} \times \boldsymbol{\mu}_s^{\mathrm{N}}(y,t) \big] \big\}, \quad (4a)$$

$$\boldsymbol{\tau}_n^{\mathrm{STT}} = \frac{\alpha'}{\hbar} d_{\mathrm{AF}} \delta(y) \big\{ \mathbf{m} \times \big[ \mathbf{n} \times \boldsymbol{\mu}_s^{\mathrm{N}}(y,t) \big]$$
$$+ \mathbf{n} \times \big[ \mathbf{m} \times \boldsymbol{\mu}_s^{\mathrm{N}}(y,t) \big] \big\}. \quad (4b)$$

Here, we have introduced the SP-induced enhanced damping parameter $\alpha' = \hbar \gamma g_\perp / (4\pi L A d_{\mathrm{AF}})$, and $\alpha_0$ is the intrinsic Gilbert damping parameter. $A$ is the AF|N interface area, $\gamma$ is the gyromagnetic ratio, $g_\perp$ is the transverse spin conductance at the AF|N interface, and $d_{\mathrm{AF}}$ is the thickness of the antiferromagnetic layer. The STTs depend on the spin accumulation $\boldsymbol{\mu}_s^{\mathrm{N}}$ in the normal metal.

The frequencies $\boldsymbol{\omega}_{m,n}$ corresponding to the effective fields are $\boldsymbol{\omega}_m = -(\gamma/L) \cdot \delta f/\delta \mathbf{m}$ and $\boldsymbol{\omega}_n = -(\gamma/L) \cdot \delta f/\delta \mathbf{n}$, where $f$ is the free-energy density in a continuum approximation,

$$f = \frac{L}{\gamma} \big\{ \omega_E(\mathbf{m}^2 - \mathbf{n}^2) - 2\omega_H m_x$$
$$- \omega_\| \big[ m_x^2 + n_x^2 - \lambda^2 (\nabla \mathbf{m})^2 - \lambda^2 (\nabla \mathbf{n})^2 \big] \big\}. \quad (5)$$

Here, $\omega_E$ is the exchange frequency, $\omega_\|$ is the easy-axis anisotropy frequency, $\omega_H$ is the frequency that describes the external magnetic field along the easy axis, and $\lambda$ is the exchange length. The exchange length is defined as $\lambda^2 = a^2 \omega_E/(4\omega_\|)$ [20], where $a$ is the length of the antiferromagnetic unit cell.

We will compute the induced dc voltages to the second order in the spin excitations. For this purpose, computing the spin excitations to the first order in their deviations from equilibrium is sufficient. For simplicity, we assume an ideal compensated antiferromagnetic-insulator-metal interface. In this case, we can excite only standing waves in the transversal direction, along the interface normal. Impurities, an uneven interface, or a sufficiently high temperature can also facilitate the excitations of waves in other directions. Within our assumptions, we linearize the LLG equations and use a harmonic transversal standing-wave ansatz of the solutions:

$$\mathbf{m}(y,t) = \tfrac{1}{2}[\delta \mathbf{m}(y)e^{i\omega t} + \delta \mathbf{m}^*(y)e^{-i\omega t}], \quad (6a)$$

$$\mathbf{n}(y,t) = \mathbf{n}_0 + \tfrac{1}{2}[\delta \mathbf{n}(y)e^{i\omega t} + \delta \mathbf{n}^*(y)e^{-i\omega t}], \quad (6b)$$
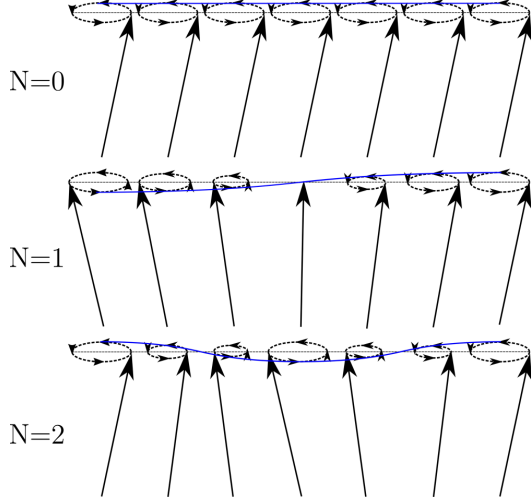
FIG. 2. Standing waves of the Néel order parameter in the transversal direction of the antiferromagnet ($y \in [-d_{\mathrm{AF}}, 0]$) in the limit when $\phi_{m,n}^{y,z} = 0$ and $k_{m,n}^{y,z} d_{\mathrm{AF}} = N\pi$.

where $\omega$ is the frequency of the dynamical source, $\mathbf{n}_0 = \hat{\mathbf{x}}$, and

$$\delta\mathbf{m}(y) = \delta m_y \cos\left[k_m^y(d_{\mathrm{AF}} + y) + \phi_m^y\right]\hat{\mathbf{y}}$$
$$+ \delta m_z \cos\left[k_m^z(d_{\mathrm{AF}} + y) + \phi_m^z\right]\hat{\mathbf{z}}, \quad (7a)$$
$$\delta\mathbf{n}(y) = \delta n_y \cos\left[k_n^y(d_{\mathrm{AF}} + y) + \phi_n^y\right]\hat{\mathbf{y}}$$
$$+ \delta n_z \cos\left[k_n^z(d_{\mathrm{AF}} + y) + \phi_n^z\right]\hat{\mathbf{z}}. \quad (7b)$$

Here, $\delta m_{y,z}$ and $\delta n_{y,z}$ are complex precession amplitudes, $k_{m,n}^{y,z}$ are the wave numbers of the standing waves, and $\phi_{m,n}^{y,z}$ are relative phases. Figure 2 illustrates the different standing waves.

### B. Spin accumulation

The spin-diffusion equation determines the spatiotemporal evolution of the spin accumulation $\boldsymbol{\mu}_s^{\mathrm{N}}(\mathbf{r}, t)$ in the normal metal,

$$\frac{\partial \boldsymbol{\mu}_s^{\mathrm{N}}(\mathbf{r}, t)}{\partial t} = \gamma_{\mathrm{N}} \mathbf{H}_0 \times \boldsymbol{\mu}_s^{\mathrm{N}} + D_{\mathrm{N}} \frac{\partial^2 \boldsymbol{\mu}_s^{\mathrm{N}}}{\partial y^2} - \frac{\boldsymbol{\mu}_s^{\mathrm{N}}}{\tau_{\mathrm{sf}}^{\mathrm{N}}}, \quad (8)$$

where $\gamma_{\mathrm{N}}$ is the gyromagnetic ratio in the normal metal, $\mathbf{H}_0$ is an external magnetic field, $D_{\mathrm{N}}$ is the diffusion constant, and $\tau_{\mathrm{sf}}^{\mathrm{N}}$ is the spin-flip relaxation time. When $\tau_{\mathrm{sf}}^{\mathrm{N}}$ is considerably smaller than the other time scales of the system (applied ac voltage frequency and characteristic magnetic field frequency $\omega_H = \gamma_{\mathrm{N}} |\mathbf{H}_0|$), the spin-diffusion equation can be approximated to be static. This approximation is true for metals such as Pt, which has a spin-flip relaxation time that is as low as 0.01 ps [21]. We use this simplification in our calculations, leaving us with a one-dimensional Helmholtz equation characterized by the spin-diffusion length $\lambda_{\mathrm{sd}}^{\mathrm{N}} = \sqrt{D_{\mathrm{N}} \tau_{\mathrm{sf}}^{\mathrm{N}}}$, with solutions given by hyperbolic functions.

The source of the spin accumulation in the normal metal is an ac voltage. This ac voltage leads to an ac charge current

$\mathbf{I}_c^0(t) = I_c^0(t)\hat{\mathbf{x}}'$ in the metal, which generates an oscillating spin current through the spin Hall effect [8]. We consider a harmonic ac current with frequency $\omega$. The total spin current in the normal metal is then

$$\mathbf{I}_s^{\mathrm{N}}(y, t) = \frac{\hbar \theta_{\mathrm{SH}}}{2e} I_c^0(t)\hat{\mathbf{z}}' - \frac{\hbar \sigma A}{4e^2} \frac{\partial \boldsymbol{\mu}_s^{\mathrm{N}}(y, t)}{\partial y}, \quad (9)$$

where $\theta_{\mathrm{SH}}$ is the spin Hall angle and $\sigma$ is the conductivity of the normal metal.

The boundary conditions that $\boldsymbol{\mu}_s^{\mathrm{N}}$ must satisfy are that the spin current across the normal-metal-vacuum interface must vanish [$\mathbf{I}_s^{\mathrm{N}}(y = d_{\mathrm{N}}, t) = 0$, where $d_{\mathrm{N}}$ is the thickness of the metallic layer] and that the spin current across the AF|N interface is continuous [$\mathbf{I}_s^{\mathrm{N}}(y = 0, t) = \mathbf{I}_s^{\mathrm{AF}}(y = 0, t)$]. The spin current in the antiferromagnetic insulator is given by contributions from SP and STTs, and it is approximated as

$$\mathbf{I}_s^{\mathrm{AF}}(t) \approx \frac{g_{\perp}}{2\pi}\left[\hbar(\mathbf{n} \times \dot{\mathbf{n}}) + \mathbf{n} \times (\mathbf{n} \times \boldsymbol{\mu}_s^{\mathrm{N}})\right]_{y=0} \quad (10)$$

to the leading order in the applied ac voltage bias. We have disregarded contributions from the imaginary part of the transverse spin conductance since it is small in most materials. We also consider the exchange limit ($\omega_{\parallel} \ll \omega_E$), which is a good approximation for many antiferromagnetic materials. In the exchange limit, the antiferromagnet is approximately collinear also at resonance, which means that the net magnetization is negligible. Any SP contributions from the magnetization will therefore be insignificant compared to the SP from the Néel order parameter. By solving the spin-diffusion equation (8) with the boundary conditions, we find that

$$\boldsymbol{\mu}_s^{\mathrm{N}}(y, t) = \mu_{s0}(t)\frac{\sinh\left[(2y - d_{\mathrm{N}})/(2\lambda_{\mathrm{sd}}^{\mathrm{N}})\right]}{\sinh\left[d_{\mathrm{N}}/(2\lambda_{\mathrm{sd}}^{\mathrm{N}})\right]}\hat{\mathbf{z}}'$$
$$+ \frac{1}{1 + \xi}\frac{\cosh\left[(y - d_{\mathrm{N}})/\lambda_{\mathrm{sd}}^{\mathrm{N}}\right]}{\cosh\left[d_{\mathrm{N}}/\lambda_{\mathrm{sd}}^{\mathrm{N}}\right]}$$
$$\times \left[\hbar(\mathbf{n} \times \dot{\mathbf{n}}) - \mu_{s0}(t)\mathbf{n} \times (\mathbf{n} \times \hat{\mathbf{z}}')\right]_{y=0}, \quad (11)$$

where we have introduced the dimensionless parameter

$$\xi = \left[\pi \hbar \sigma A \tanh\left(d_{\mathrm{N}}/\lambda_{\mathrm{sd}}^{\mathrm{N}}\right)\right]/\left(2g_{\perp}e^2\lambda_{\mathrm{sd}}^{\mathrm{N}}\right) \quad (12)$$

and a characteristic spin accumulation

$$\mu_{s0}(t) = 2\theta_{\mathrm{SH}}e\lambda_{\mathrm{sd}}^{\mathrm{N}}\tanh\left(d_{\mathrm{N}}/2\lambda_{\mathrm{sd}}^{\mathrm{N}}\right)I_c^0(t)/(A\sigma). \quad (13)$$

### C. Magnetization dynamics

The magnetization dynamics in the antiferromagnet can be divided into two separate regions: the dynamics at the interfaces and the dynamics in the bulk. At the AF|N interface, the STTs $\boldsymbol{\tau}_{m,n}^{\mathrm{STT}}$ drive the dynamics, and there are also dissipative SP torques $\boldsymbol{\tau}_{m,n}^{\mathrm{SP}}$. By integrating the LLG equations (1) in a low volume around the AF|N interface, we find the boundary conditions for $\mathbf{n}$:

$$d_{\mathrm{AF}}\alpha'\left\{\mathbf{n} \times \dot{\mathbf{n}} + \frac{1}{\hbar}\left[\mathbf{n} \times (\mathbf{n} \times \boldsymbol{\mu}_s^{\mathrm{N}})\right]\right\}_{y=0}$$
$$+ \omega_{\parallel}[\lambda^2 \mathbf{n} \times \partial_y \mathbf{n}]_{y=0} = 0. \quad (14)$$

We assume that the other interface ($y = -d_{\mathrm{AF}}$) connects to vacuum or a substrate with neither SP nor spin transfer.

Subsequently, there is only a contribution to the boundary conditions from the exchange stiffness, which requires that the spatial derivative in the transversal direction vanishes.

By linearizing the boundary condition in Eq. (14) with the ansatz in Eq. (6), we obtain the following constraint on the wave number $k_n^z$:

$$k_n^z d_{\mathrm{AF}} \tan\left(k_n^z d_{\mathrm{AF}}\right) = i\frac{d_{\mathrm{AF}}^2 \alpha' \omega}{\lambda^2 \omega_\parallel}\kappa, \qquad (15)$$

where we have introduced

$$\kappa = \left[1 + \frac{2e^2 g_\perp \lambda_{\mathrm{sd}}^{\mathrm{N}} \coth\left(d_{\mathrm{N}}/\lambda_{\mathrm{sd}}^{\mathrm{N}}\right)}{A\pi\sigma\hbar}\right]^{-1} = \frac{\xi}{\xi+1}. \quad (16)$$

When the term on the right-hand side of Eq. (15) is small, we can expand the solution around the roots where $k_{m,n}^{y,z} d_{\mathrm{AF}} \approx N\pi$ ($N = 0,1,2,\ldots$) to determine the wave numbers. This limit corresponds to the low-damping limit where the decay of the standing waves in the antiferromagnetic layer is negligible. Note that the opposite (high-damping) limit implies that the precessions at the interface (and thus the SP and SMR voltages) become small; therefore, this limit is of little interest.

The constraint from the boundary conditions in Eq. (14) on the wave number $k_n^y$ depends on an amplitude of $\delta\mathbf{n}$,

$$\delta n_y\left[\lambda^2 k_n^y \omega_\parallel \sin\left(k_n^y d_{\mathrm{AF}}\right) - i d_{\mathrm{AF}}\alpha'\kappa\omega\cos\left(k_n^y d_{\mathrm{AF}}\right)\right]$$
$$= d_{\mathrm{AF}}\cos\theta\alpha'\kappa|\mu_{s0}|/\hbar. \qquad (17)$$

Another equation is required to find solutions for $\delta n_y$ and $k_n^y$; therefore, we must solve the LLG equations in the bulk of the antiferromagnet.

In the bulk ($-d_{\mathrm{AF}} < y < 0$), the LLG equation becomes a $4\times 4$ matrix equation. A nontrivial solution requires the determinant of this matrix to be zero because there is no dynamical source in the bulk. The dynamics enters through the boundary conditions at the interface. Because the determinant is independent of the precession amplitudes $\delta\mathbf{m}$ and $\delta\mathbf{n}$, we can use this condition to determine the solutions for $k_n^y$ that allow a nontrivial solution of the precession amplitudes. The amplitude $\delta n_y$ can then be determined from Eq. (17), and the remaining amplitudes $\delta m_y$, $\delta m_z$, and $\delta n_z$ can be determined from the eigenvectors of the LLG bulk equations.

## III. SPIN-TRANSFER-TORQUE-INDUCED ANTIFERROMAGNETIC RESONANCE

### A. Frequency spectrum and susceptibilities

When we are in both the low-damping and exchange limits, the resonance frequencies of the $N$-node standing-wave mode are $|\omega_\pm^{(N)}| = \omega_0^{(N)} \pm |\omega_H|$, where

$$\omega_0^{(N)} = \omega_0\sqrt{1 + \left(\frac{N\pi\lambda}{d_{\mathrm{AF}}}\right)^2} \qquad (18)$$

and $\omega_0 \approx \sqrt{2\omega_E\omega_\parallel}$ is the gap frequency. The solutions of Eq. (17) around the $k_n^{y,z} d_{\mathrm{AF}} = N\pi$ roots are approximately

complex Lorentzians,

$$\delta n_{y,\pm}^{(N)}(\omega) \approx \frac{(-1)^{N+1}\alpha'^{(N)}\kappa\cos\theta|\mu_{s0}|\sqrt{\omega_E}/\left(2\hbar\sqrt{2\omega_\parallel}\right)}{|\omega| - |\omega_\pm^{(N)}| + i\Delta\omega_\pm^{(N)}/2}, \qquad (19)$$

where we have introduced the linewidth

$$\Delta\omega_\pm^{(N)} = 2(\alpha_0 + \alpha'^{(N)}\kappa)|\omega_\pm^{(N)}|\sqrt{\frac{\omega_E}{2\omega_\parallel}}. \qquad (20)$$

We have also introduced the effective SP damping parameter $\alpha'^{(N)}$ for the $N$-mode spin wave, where $\alpha'^{(N=0)} = \alpha'$ and $\alpha'^{(N\neq 0)} = 2\alpha'$, which is analogous to the result for ferromagnetic spin waves [22].

The Lorentzian approximation in Eqs. (19) and (20) is valid to the lowest order in $\alpha_0$ and $\alpha'$ under the assumption that $\lambda/d_{\mathrm{AF}} \ll 1$. If the antiferromagnet is so thin that the thickness becomes comparable to the exchange length, then the gap between the resonance frequencies of the macrospin mode and the higher-order standing-wave modes approaches the exchange frequency $\omega_E$. This is the upper bound of the resonance frequency; thus, in the limit $d_{\mathrm{AF}} \sim \lambda$, we can excite only the macrospin mode. Because we also want to study the higher-order standing waves, we consider only the limit where $d_{\mathrm{AF}} \gg \lambda$.

Note that even though the linewidth is enhanced by a factor of $\sqrt{\omega_E/\omega_\parallel}$, the maximum amplitude of the precessions is not suppressed by the inverse of this factor. This differs from the case where the source of the dynamics is a magnetic field, where the amplitudes are suppressed by a factor of $\sqrt{\omega_\parallel/\omega_E}$. For the spin-transfer-driven case, the only suppression arises from the high resonance frequencies of the antiferromagnet, and this suppression is also present in the magnetic-field-driven case in addition to the $\sqrt{\omega_\parallel/\omega_E}$ factor.

The $z$ component of the Néel order parameter is related to the $y$ component by

$$\cos\left(k_n^z d_{\mathrm{AF}}\right)\delta n_{z,\pm}^{(N)} = \mp\mathrm{sgn}(\omega_H)i\cos\left(k_n^y d_{\mathrm{AF}}\right)\delta n_{y,\pm}^{(N)}. \quad (21)$$

This is obtained through the eigenvectors of the bulk LLG equations in Eq. (1) in the region where $-d_{\mathrm{AF}} < y < 0$. The magnetization $\delta\mathbf{m}$ also has a circular polarization for uniaxial antiferromagnets, and its amplitude is suppressed by a factor of $\propto\sqrt{\omega_\parallel/\omega_E}$ compared to the Néel order parameter. This suppression factor justifies our discarding the contributions from the magnetization in the antiferromagnet to the spin accumulation in the metal. We now assume that the separation between the resonance frequencies $|\omega_\pm^{(N)}|$ is considerably greater than the linewidths $|\Delta\omega_\pm^{(N)}|$ and that the real part of the eigenfrequency is much greater than the imaginary part. The frequency spectrum for, e.g., $\delta n_y(\omega)$ can then be approximated by a sum of the complex Lorentzians in Eq. (19):

$$\delta n_y(\omega) = \sum_{N=0}^{\infty}\sum_{i=\pm}\delta n_{y,i}^{(N)}(\omega), \qquad (22)$$

with similar notation for the other amplitudes.

### B. Spin Hall magnetoresistance and spin pumping dc voltages

We can now use our solutions of the spin accumulation in Eq. (11) and precession amplitudes in Eqs. (19) and (21) to

determine the total charge current resulting from the applied voltage and interaction with the antiferromagnet driven at resonance. This charge current density is [11]

$$\mathbf{j}_c(y,t) = \frac{I_c^0(t)}{A}\hat{\mathbf{x}}' + \frac{\theta_{\mathrm{SH}}\sigma}{2e}\hat{\mathbf{y}} \times \frac{\partial \boldsymbol{\mu}_s^{\mathrm{N}}(y,t)}{\partial y}. \quad (23)$$

By averaging over the normal metal, $\overline{\mathbf{j}}_c(t) = d_{\mathrm{N}}^{-1}\int_0^{d_{\mathrm{N}}}\mathbf{j}_c(y,t)\mathrm{d}y$, we find that the contributions to the $x'$ direction are

$$\overline{\mathbf{j}}_c(t)\cdot\hat{\mathbf{x}}' = j_{c,x'}^{\mathrm{SMR}}(t) + j_{c,x'}^{\mathrm{SP}}(t), \quad (24)$$

where

$$j_{c,x'}^{\mathrm{SMR}}(t) = \frac{I_c^0(t)}{A}\left[1 - \frac{\Delta\rho_0}{\rho} - \frac{\Delta\rho_{\mathrm{S}}}{\rho}\left(1 - n_{z'}^2\right)\right]_{y=0}, \quad (25)$$

$$j_{c,x'}^{\mathrm{SP}}(t) = -\frac{\theta_{\mathrm{SH}}\hbar\sigma}{2d_{\mathrm{N}}e}\eta[(\mathbf{n}\times\dot{\mathbf{n}})_{z'}]_{y=0}. \quad (26)$$

Here, we have introduced

$$\Delta\rho_0 = -\rho\theta_{\mathrm{SH}}^2\frac{2\lambda_{\mathrm{sd}}^{\mathrm{N}}}{d_{\mathrm{N}}}\tanh\left(\frac{d_{\mathrm{N}}}{2\lambda_{\mathrm{sd}}^{\mathrm{N}}}\right), \quad (27)$$

$$\eta = \frac{1}{1+\xi}\tanh\left(\frac{d_{\mathrm{N}}}{2\lambda_{\mathrm{sd}}^{\mathrm{N}}}\right)\tanh\left(\frac{d_{\mathrm{N}}}{\lambda_{\mathrm{sd}}^{\mathrm{N}}}\right), \quad (28)$$

and the SMR $\Delta\rho_{\mathrm{S}} = -\eta\Delta\rho_0/2$. $\rho = 1/\sigma$ is the resistivity of the normal metal. The contributions from both the SMR and the SP induce a dc component in the resulting ISHE voltage in the normal metal. Assuming that $I_c^0(t) = I_c^0\cos(\omega t)$, we find that

$$\langle j_{c,x'}^{\mathrm{SMR}}(t)\rangle_t = \frac{\Delta\rho_{\mathrm{S}}I_c^0}{2\rho A}\sin 2\theta\,\mathrm{Re}\big[\delta n_z\cos\left(k_n^z d_{\mathrm{AF}}\right)\big]. \quad (29)$$

To find the dc contributions from SP, we study the dc component of $\langle(\mathbf{n}\times\dot{\mathbf{n}})_{z'}\rangle_t$, and we compute that

$$\langle(\mathbf{n}\times\dot{\mathbf{n}})_{z'}\rangle_t = -\omega\,\mathrm{Im}\Big\{\big[\delta n_y\cos\left(k_n^y d_{\mathrm{AF}}\right)\big]^* \\ \times \delta n_z\cos\left(k_n^z d_{\mathrm{AF}}\right)\Big\}\sin\theta. \quad (30)$$

Let us now compare the results for the dc components of $j_{c,x'}^{\mathrm{SMR}}$ and $j_{c,x'}^{\mathrm{SP}}$ in Eqs. (25) and (26) to the ferromagnetic case [3]. We observe that the results are exactly the same when $\mathbf{n}\leftrightarrow\hat{\mathbf{M}}$ and $G_r \to 2G_r$, where $\hat{\mathbf{M}}$ is the magnetization unit vector in the ferromagnet and $G_r$ is the real transverse spin conductance in Ref. [3].

Experiments measuring the SMR in NiO|Pt heterostructures indicate that the SMR is negative for antiferromagnets [13–16]. Because the only key difference between the antiferromagnetic case and the ferromagnetic case is that the Néel order parameter, not the magnetization, causes the SMR, the negative sign must be due to some property of the Néel order parameter. This is in agreement with the reasoning in Ref. [14], where the negative SMR is explained by the coupling of the Néel order parameter to the magnetic field. They typically couple perpendicularly to each other, whereas for ferromagnets, the magnetization couples along the magnetic field. The perpendicular coupling gives rise to a $\pi/2$ phase shift relative to the ferromagnetic case and a negative sign in the measured SMR.

If we consider the case in which the susceptibility of the Néel order parameter is of the same order of magnitude as

the susceptibility of the magnetization in a ferromagnet, then the SMR and SP voltages in an antiferromagnet should be comparable to those in a ferromagnet. Equation (19) shows that the susceptibility scales with the inverse of the resonance frequency. The susceptibility of the Néel order parameter therefore becomes comparable to that of the magnetization in a ferromagnet when the system is driven close to the spin-flop transition, where the resonance frequency is small [19].

Inserting our solutions of the frequency-dependent amplitudes in Eqs. (19) and (21), the dc voltages as a function of applied ac voltage frequency become approximately

$$V_{\mathrm{dc}}^{\mathrm{SMR}}(\omega) = \mathrm{sgn}(\omega_H)K\sin 2\theta\cos\theta\left(\frac{I_c^0}{A}\right)^2 \\ \times \sum_{N=0}^{\infty}\sum_{j=\pm}\frac{\alpha'^{(N)}}{2(\alpha_0+\kappa\alpha'^{(N)})}\frac{jL_j^{(N)}(\omega)}{\left|\omega_j^{(N)}\right|}, \quad (31a)$$

$$V_{\mathrm{dc}}^{\mathrm{SP}}(\omega) = -\mathrm{sgn}(\omega_H)\kappa K\sin 2\theta\cos\theta\left(\frac{I_c^0}{A}\right)^2 \\ \times \sum_{N=0}^{\infty}\sum_{j=\pm}\left[\frac{\alpha'^{(N)}}{2(\alpha_0+\kappa\alpha'^{(N)})}\right]^2\frac{jL_j^{(N)}(\omega)}{\left|\omega_j^{(N)}\right|}, \quad (31b)$$

where $V_{\mathrm{dc}}^{\mathrm{SMR/SP}} = l\rho\langle j_{c,x}^{\mathrm{SMR/SP}}(t)\rangle_t$ and $l$ is the length of the bilayer in the direction of the applied voltage. We have also introduced the symmetric Lorentzian

$$L_{\pm}^{(N)}(\omega) = \frac{\left(\Delta\omega_{\pm}^{(N)}/2\right)^2}{\left(|\omega| - \left|\omega_{\pm}^{(N)}\right|\right)^2 + \left(\Delta\omega_{\pm}^{(N)}/2\right)^2} \quad (32)$$

and the constant

$$K = \frac{l\kappa\eta\theta_{\mathrm{SH}}^3 e(\lambda_{\mathrm{sd}}^{\mathrm{N}})^2}{\hbar d_{\mathrm{N}}\sigma^2}\tanh^2\left[\frac{d_{\mathrm{N}}}{2\lambda_{\mathrm{sd}}^{\mathrm{N}}}\right]. \quad (33)$$

In our model, the SMR and SP voltages as functions of frequency are described via symmetric Lorentzians. However, we have not included the contributions from the Oersted field to the dynamics. The charge current causes an oscillating magnetic field that leads to an antisymmetric Lorentzian component [3]. One therefore needs to filter out the antisymmetric component before comparing experimental data with our model. We did not take the Oersted field in the free energy into account since the susceptibility associated with this magnetic field is a factor of $\sim\sqrt{\omega_{\parallel}/\omega_E}$ smaller than the susceptibility associated with the spin accumulation [23]. Moreover, because the Oersted field is approximately uniform in a sufficiently thin antiferromagnetic film, it can couple only to the $N = 0$ mode. The symmetric Lorentzian can therefore be expected to be the dominant component of the signal for most antiferromagnetic materials and should be the only component for the $N \neq 0$ modes.

Next, we will compute the dc voltages for a MnF$_2$|Pt bilayer using the parameters in Tables I and II. Direct measurements

TABLE I. Material parameters for MnF$_2$.

| $\omega_E$ (s$^{-1}$) [24] | $\omega_{\parallel}$ (s$^{-1}$) [24] | $L$ (A/m) [25] |
|---|---|---|
| $9.3\times 10^{12}$ | $1.5\times 10^{11}$ | 47 862 |

TABLE II. Material parameters for Pt.

| $\theta_{SH}$ [26] | $\lambda_{sd}^{Pt}$ (nm) [27] | $\sigma$ ($[\Omega \, m]^{-1}$) [28] |
|---|---|---|
| 0.12 | 1.5 | $5 \times 10^6$ |

of some of the parameters are lacking. We therefore use these missing material parameters from similar systems. We use the Gilbert damping of NiO, $\alpha_0 = 2.1 \times 10^{-4}$ [29]. The transverse conductance at AF|N interfaces has been predicted to be of the same order of magnitude as the conductance at interfaces consisting of ferromagnets or ferrimagnets and a normal metal [18]. We therefore use a typical value of the transverse conductance for ferromagnet-normal-metal systems, $g_\perp/A \sim 3 \times 10^{18}$ m$^{-2}$ (ferromagnet|Pt [30]). MnF$_2$ has a tetragonal crystal structure and therefore two lattice constants. The length $a$ of the antiferromagnetic unit cell is therefore not uniquely defined for this material. The value of $a$ used to evaluate the exchange length $\lambda$ [given by $\lambda^2 = a^2 \omega_E/(4\omega_\parallel)$] will be the length of the unit cell in the propagation direction of the spin waves, i.e., the $y$ direction in our geometry. In our calculations, we use the average of the two lattice constants for our characteristic length $a$. The two lattice constants for MnF$_2$ are $a_1 = 4.88$ Å and $a_2 = 3.32$ Å [31], providing the average value $a = 4.10$ Å. This value results in an estimated exchange length of 1.6 nm. We note, however, that this value depends on the orientation of the antiferromagnet. The exchange length should therefore be estimated by measuring the separation between the resonance peaks.

The results obtained using these parameters are presented in Fig. 3, where we have used $l = 100 \, \mu$m, $d_N = 2\lambda_{sd}^{Pt}$, and $I_c^0/A = 10^{10}$ A/m$^2$. For the angle $\theta$ between the applied voltage and the easy axis of the antiferromagnetic material, we use a value of $\theta = 35°$. Optimally, one would have the ac voltage source along the easy axis direction and another pair of electrodes for detecting the resulting dc voltage perpendicular to the easy axis. However, realizing such an experimental setup with two pairs of electrodes may be impractical. When measuring the signal along the same direction as the applied voltage source, as considered here, $\theta \approx 35°$ is the most efficient angle for simultaneously exciting and detecting the resonance. The SMR and SP dc voltages always have opposite signs, whereas their frequency dependence is exactly the same. The partial cancellation leads to a smaller net signal. The contributions from SMR and SP cannot be distinguished from one another in this bilayer system. We also observe that the SP voltage is always smaller than the SMR voltage. For a given direction of the external magnetic field, here assuming that $\omega_H > 0$, the signs of the dc signals depend solely on whether the precessions are right handed ($\omega_{res} > 0$, + mode) or left handed ($\omega_{res} < 0$, − mode). The dc voltages resulting from the higher-energy modes are not particularly large for our choice of parameters. This is primarily due to the high resonance frequencies of these modes. The standing waves will be easier to detect in materials with a gap frequency $\omega_0$ lower than that of MnF$_2$. Examples of antiferromagnets with a low gap frequency are RbMnF$_3$, which has a gap of $\omega_0/2\pi = 9$ GHz [32], and GdFe$_3$(BO$_3$)$_4$, which has a gap of $\omega_0/2\pi = 29$ GHz [33]. For comparison, the gap frequency of MnF$_2$ is $\omega_0/2\pi = 267$ GHz.
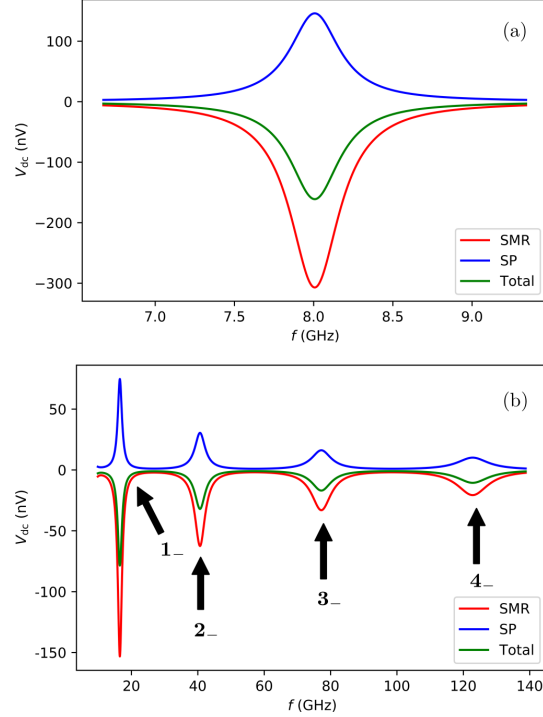


FIG. 3. Resonance spectrum for a MnF$_2$ film of thickness $d_{AF} = 20$ nm in an external magnetic field $\omega_H = 0.97\omega_0$ ($|\mathbf{H}_0| = 9.24$ T). The dc voltages for the low-energy macrospin mode ($0_-$) are shown in (a), while some of the higher-energy left-handed $N_-$ modes are shown in (b).

As an alternative to finding materials with lower resonance frequencies, one can apply a stronger voltage to enhance the signals because the measured dc voltages are quadratic in the applied ac voltage.

In the next section, we will discuss a trilayer system that allows separating the SMR and SP voltages. Separating these voltages yields more information about the system, such as the ratio between the intrinsic damping and the SP-enhanced damping.

## IV. SEPARATION OF SPIN-HALL-MAGNETORESISTANCE AND SPIN-PUMPING VOLTAGES

### A. N|AF|N system

We now extend and generalize our considerations to an antiferromagnetic insulator sandwiched between two normal metals, as illustrated in Fig. 4. We apply an ac voltage with a constant amplitude to an active normal metal as in the previous sections. Additionally, we use a passive normal metal to detect the SP contributions from the antiferromagnet. Because the passive normal metal does not exhibit any SMR dc voltage to the leading order in the applied voltage source, we measure the SMR and SP voltages independently.
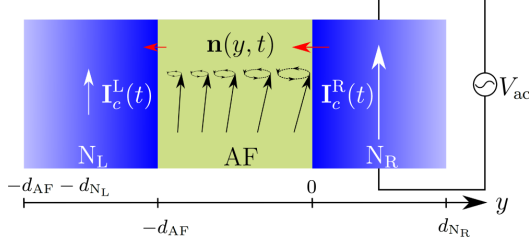
FIG. 4. An antiferromagnet sandwiched between two normal metals. Magnetization dynamics in the antiferromagnet is induced by applying an ac voltage with a constant amplitude on the normal metal to the right, which leads to a spin current into the antiferromagnet. A spin current is then pumped into the left normal metal, which induces a charge current through the inverse spin Hall effect.

Taking advantage of the symmetry of our system, the spin accumulation in the passive normal metal can readily be obtained from Eq. (11). Because the only source for the spin accumulation is SP from the antiferromagnet, we find the spin accumulation to be

$$\boldsymbol{\mu}_s^{N_L}(y,t) = \frac{\hbar}{1+\xi_L}[\mathbf{n}\times\dot{\mathbf{n}}]_{y=-d_{AF}}\big(\cosh\big[d_{N_L}/\lambda_{sd}^{N_L}\big]\big)^{-1}$$
$$\times \cosh\big[(y+d_{N_L}+d_{AF})/\lambda_{sd}^{N_L}\big]. \tag{34}$$

Here, the index L implies that the value should be evaluated using the properties of the passive normal metal $N_L$ and the $N_L|AF$ interface. These parameters are defined analogously to those of the bilayer system but will potentially take on different values than the active normal metal $N_R$ and the $AF|N_R$ interface. Consequently, the average charge current in the passive normal metal along the $x'$ direction becomes

$$j_{c,x'}^L(t) = \overline{\mathbf{j}_c^L}\cdot\hat{\mathbf{x}}' = \frac{\theta_{SH}^L\hbar\sigma_L}{2d_{N_L}e}\eta_L[(\mathbf{n}\times\dot{\mathbf{n}})_{z'}]_{y=-d_{AF}}. \tag{35}$$

If we, for simplicity, assume no decay of the spin current in the antiferromagnet, then we can observe from Eq. (26) that

$$\big\langle j_{c,x'}^L(t)\big\rangle_t = -\frac{\theta_{SH}^L\sigma_L\eta_Ld_{N_R}}{\theta_{SH}^R\sigma_R\eta_Rd_{N_L}}\big\langle j_{c,x'}^{SP}(t)\big\rangle_t. \tag{36}$$

In other words, when the properties of both metallic layers are known, we can indirectly measure the SMR dc voltage by measuring the ratio of the dc voltage in the passive normal metal $N_L$ relative to the dc voltage in the active normal metal $N_R$. This indirect measurement of the SMR voltage assumes that the decay of the pumped spin current is insignificant. We will now determine in what region this approximation holds.

### B. Spin-current decay

The nonzero spin current across the left AF interface implies that the boundary conditions at $y=-d_{AF}$ must be extended to include SP and STTs:

$$d_{AF}\alpha_L'\bigg\{\mathbf{n}\times\dot{\mathbf{n}} + \frac{1}{\hbar}\big[\mathbf{n}\times(\mathbf{n}\times\boldsymbol{\mu}_s^{N_L})\big]\bigg\}_{y=-d_{AF}}$$
$$- \omega_\parallel[\lambda^2\mathbf{n}\times\partial_y\mathbf{n}]_{y=-d_{AF}} = 0. \tag{37}$$

The boundary conditions at $y=0$ remain unchanged and are given by Eq. (14). As a result of the new boundary conditions at $y=-d_{AF}$, the solutions for the phases $\phi_{m,n}^{y,z}$ in our linear response ansatz in Eq. (7) are no longer zero as they were in the bilayer system. The phases will now have a finite correction in $\alpha'$. We can rewrite our boundary conditions at $y=0,-d_{AF}$ as the following constraints on the wave numbers and phases:

$$k_n^{y,z}d_{AF}\tan\phi_n^{y,z} = -i\frac{d_{AF}^2\omega}{\lambda^2\omega_\parallel}\alpha_L'\kappa_L, \tag{38a}$$

$$k_n^zd_{AF}\tan\big(k_n^zd_{AF}+\phi_n^z\big) = i\frac{d_{AF}^2\omega}{\lambda^2\omega_\parallel}\alpha_R'\kappa_R. \tag{38b}$$

We can decouple the above equations to obtain constraints that are dependent on only the wave number $k_n^z$,

$$\tan\big(k_n^zd_{AF}\big)\bigg[k_n^zd_{AF} + \frac{1}{k_n^zd_{AF}}\bigg(\frac{d_{AF}^2\omega}{\lambda^2\omega_\parallel}\bigg)^2\alpha_L'\alpha_R'\kappa_L\kappa_R\bigg]$$
$$\approx k_n^zd_{AF}\tan\big(k_n^zd_{AF}\big) = 2i\frac{d_{AF}^2\omega}{\lambda^2\omega_\parallel}\overline{\alpha'\kappa}, \tag{39}$$

where we have introduced $\overline{\alpha'\kappa}=(\alpha_L'\kappa_L+\alpha_R'\kappa_R)/2$. This constraint is similar to the constraint for the AF|N bilayer in Eq. (15) to the lowest order in $\alpha'$, except that $\alpha'\kappa\to 2\overline{\alpha'\kappa}$. The enhanced damping due to SP is because we now pump spins across two interfaces rather than across one interface. The last constraint on $k_n^y$ is equivalent to Eq. (17), where we now also have to take the nonzero phase $\phi_n^y$ into account; thus, the boundary condition becomes

$$d_{AF}\cos\theta\alpha_R'\kappa_R|\mu_{s0}^R|/\hbar = \delta n_y\big[\lambda^2 k_n^y\omega_\parallel\sin\big(k_n^yd_{AF}+\phi_n^y\big)$$
$$- id_{AF}\alpha_R'\kappa_R\omega\cos\big(k_n^yd_{AF}+\phi_n^y\big)\big]. \tag{40}$$

The decay of the spin current in the antiferromagnetic insulator is related to the imaginary components of $d_{AF}k_n^{y,z}$. At resonance and to the lowest order in $\alpha'$ and $\alpha_0$, we find these to be

$$\big|\mathrm{Im}\big(d_{AF}k_{n,N=0}^z\big)\big| = \sqrt{\frac{d_{AF}^2\overline{\alpha'\kappa}\omega}{\lambda^2\omega_\parallel}}, \tag{41a}$$

$$\big|\mathrm{Im}\big(d_{AF}k_{n,N=0}^y\big)\big| = \sqrt{\frac{d_{AF}^2(\overline{\alpha'\kappa}+\alpha_0)\omega}{\lambda^2\omega_\parallel}} \tag{41b}$$

for the macrospin mode and

$$\big|\mathrm{Im}\big(d_{AF}k_{n,N>0}^z\big)\big| = \frac{2d_{AF}^2\overline{\alpha'\kappa}\omega}{\lambda^2 N\pi\omega_\parallel}, \tag{42a}$$

$$\big|\mathrm{Im}\big(d_{AF}k_{n,N>0}^y\big)\big| = \frac{d_{AF}^2(2\overline{\alpha'\kappa}+\alpha_0)\omega}{\lambda^2 N\pi\omega_\parallel} \tag{42b}$$

for the standing-wave modes, respectively.

Let us now study how the imaginary components in Eqs. (41) and (42) scale with $d_{AF}$ and the resonance frequency $\omega$. Since the SP-induced damping $\alpha'\propto 1/d_{AF}$, $\mathrm{Im}(d_{AF}k_{n,N}^z)$ scales as $\propto(d_{AF}\omega)^\zeta$, where $\zeta=1/2$ for the macrospin mode and $\zeta=1$ for the standing waves ($N>0$). In the limit where
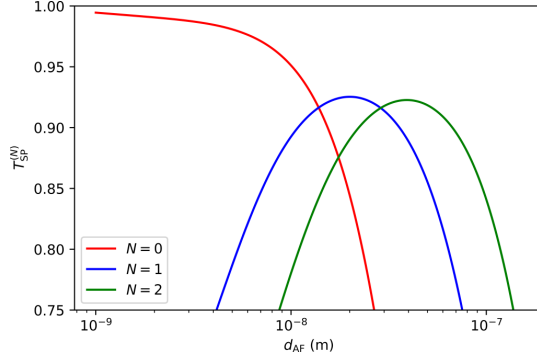
FIG. 5. Ratio of the spin pumping at the passive AF|N interface relative to the spin pumping at the active AF|N interface as a function of $d_{AF}$ for three of the low-energy left-handed $N_-$ modes at $\omega_H = 0.97\omega_0$ ($|\mathbf{H}_0| = 9.24$ T).

$\alpha_0 \ll \alpha'$, when the bulk damping is small compared to the interface damping, $\text{Im}(d_{AF}k_{n,N}^y)$ scales as $\text{Im}(d_{AF}k_{n,N}^z)$. However, when $\alpha_0$ becomes large compared to $\alpha'$, the bulk damping dominates, and $\text{Im}(d_{AF}k_{n,N}^y)$ scales as $\propto (d_{AF}^2\omega)^\zeta$. We can then observe, as expected, that the spin current decays faster as a function of $d_{AF}$ for thicker films where the bulk damping dominates. Based on these scaling relations, we observe that we can minimize the decay of the spin current, thereby keeping the magnitude of the SP at the two interfaces similar to each other, by (i) keeping the antiferromagnetic layer sufficiently thin and (ii) reducing the resonance frequency by driving the system close to the spin-flop transition.

Assuming that the SP is dominated by the dynamics of $\mathbf{n}$, which is a good assumption for most collinear antiferromagnets, the transmission of the pumped spin current through the antiferromagnetic layer can be defined as

$$T_{SP}^{(N)} = \left| \frac{\langle(\mathbf{n} \times \dot{\mathbf{n}})_{y=-d_{AF}}\rangle_t}{\langle(\mathbf{n} \times \dot{\mathbf{n}})_{y=0}\rangle_t} \right|. \tag{43}$$

This describes the ratio of the SP at the passive interface relative to the active interface where we excite the dynamics by injecting a spin current. When this ratio is close to unity, it is a good assumption that we are in the low-decay regime, and the pumped spin current across the two interfaces will be approximately the same. In the low-decay regime, the SMR and SP dc voltages can be separated by measuring the dc voltage in both normal metals independently.

We plot the transmission of the pumped spin current as a function of $d_{AF}$ in Fig. 5 for the three lowest energy modes. We use the same values for the system parameters as for the bilayer system in Sec. III B, and for simplicity, we let the properties of both metallic layers be identical. As shown, the pumped spin current of the modes with the lowest energy exhibits the fastest decay with increasing thickness of the antiferromagnetic layer. This result is as expected from the scaling behaviors in Eqs. (41) and (42), as $d_{AF}^2\omega\overline{\alpha'\kappa}/(\lambda^2\omega_\parallel)$ is a small dimensionless number for the choice of parameters that we have previously considered. If $d_{AF}^2\omega\overline{\alpha'\kappa}/(\lambda^2\omega_\parallel)$ is of order unity or larger, then we are in the large-damping limit, and we

can therefore expect the decay of the spin-wave amplitudes to become significant. We also observe that the $N > 0$ modes decay in both the thin-film limit ($d_{AF} \sim \lambda$) and in the thick-film limit ($d_{AF} \gg \lambda$), in contrast to the behavior of the macrospin mode. This result is due to the high resonance frequencies of the standing waves when the thickness of the AF layer approaches the exchange length, as one can see from Eq. (18). As the standing waves ($N > 0$ modes) decay considerably due to a high resonance frequency in the thin-film limit and due to the long transport distances in the thick-film limit, there will be a finite optimal-transmission thickness for these modes, as indicated by the transmission peaks in Fig. 5. For the macrospin mode, $T_{SP}^{(N)} \approx 1$ is a good approximation when the thickness of the antiferromagnetic layer is comparable to the exchange length. For the standing-wave modes there is always a notable decay for our choice of parameters. However, a transmission close to 90% is possible for thin AFs if the resonance frequency is relatively low.

To study the cause of the decay of the spin current, we compare the different contributions to the damping. For our choice of parameters, we have that $\alpha' = \alpha_0$ at $d_{AF} = 440$ nm. As shown in Fig. 5, there is a significant decay of the spin current well below this thickness. This means that for our choice of parameters, the observed decay of the spin current is not primarily due to the intrinsic Gilbert damping in the bulk of the antiferromagnet. The noteworthy decay observed for relatively thin films is a consequence of the short exchange length of MnF$_2$. The spin waves are rather soft in this material. For stiffer materials with longer exchange lengths, i.e., materials with a larger exchange to anisotropy ratio, it is expected that the decay lengths will also be longer. The disadvantage of having long exchange lengths, however, is that this will also increase the resonance frequencies of the standing-wave modes, thereby making their detection more challenging. This is not the case for the macrospin mode, where the exchange length affects only the decay length of the spin waves.

Based on our results, one can observe that $T_{SP}^{(N)} \approx 1$ is a good approximation when $\text{Im}(d_{AF}k_n^{y,z}) \ll 1$. We can then utilize the analytical expressions for these imaginary components in Eqs. (41) and (42) to evaluate whether we are in a low-decay regime, where the SMR and SP dc voltages can be separated.

## V. CONCLUSIONS

We have studied STT-induced antiferromagnetic resonance in bilayers that consist of an antiferromagnetic insulator and a normal metal and in a metal-antiferromagnetic-insulator-metal trilayer. We considered excitations of the uniform mode and of the transverse standing waves. The dc voltages have contributions from the SMR and SP, similar to ferromagnetic systems. In the antiferromagnetic system, the dynamics of the Néel order parameter causes these effects. A challenge in an antiferromagnetic system is the weak signals due to the low susceptibility of the Néel order parameter. We demonstrate how the signals are enhanced by driving the system close to the spin-flop transition, where the resonance frequency is lower. In trilayer systems, the contributions due to SP and SMR can be separated when the antiferromagnetic layer is thin.

*Note added.* Recently, an independent study of spin-transfer antiferromagnetic resonance was reported [23]. Reference [23] computes the spin accumulation and frequency dependence of the conductivity in the normal metal for the macrospin mode. A main point and difference in our work is that we consider a magnetic field that importantly reduces the frequency and enhances the output signal. This facilitates experimental detection in an experimentally feasible frequency range. Additionally, we study the excitation of standing spin waves and a trilayer system that can be utilized to separate the output signals resulting from SP and SMR.

[1] R. Cheng, D. Xiao, and A. Brataas, Phys. Rev. Lett. **116**, 207603 (2016).

[2] L. Liu, T. Moriyama, D. C. Ralph, and R. A. Buhrman, Phys. Rev. Lett. **106**, 036601 (2011).

[3] T. Chiba, G. E. W. Bauer, and S. Takahashi, Phys. Rev. Appl. **2**, 034003 (2014).

[4] M. Schreier, T. Chiba, A. Niedermayr, J. Lotze, H. Huebl, S. Geprägs, S. Takahashi, G. E. W. Bauer, R. Gross, and S. T. B. Goennenwein, Phys. Rev. B **92**, 144411 (2015).

[5] J. Slonczewski, J. Magn. Magn. Mater. **159**, L1 (1996).

[6] J. Sklenar, W. Zhang, M. B. Jungfleisch, W. Jiang, H. Chang, J. E. Pearson, M. Wu, J. B. Ketterson, and A. Hoffmann, Phys. Rev. B **92**, 174406 (2015).

[7] C. He, A. Navabi, Q. Shao, G. Yu, D. Wu, W. Zhu, C. Zheng, X. Li, Q. L. He, S. A. Razavi, K. L. Wong, Z. Zhang, P. K. Amiri, and K. L. Wang, Appl. Phys. Lett. **109**, 202404 (2016).

[8] M. Dyakonov and V. Perel, Phys. Lett. A **35**, 459 (1971).

[9] E. Saitoh, M. Ueda, H. Miyajima, and G. Tatara, Appl. Phys. Lett. **88**, 182509 (2006).

[10] H. Nakayama, M. Althammer, Y.-T. Chen, K. Uchida, Y. Kajiwara, D. Kikuchi, T. Ohtani, S. Geprägs, M. Opel, S. Takahashi, R. Gross, G. E. W. Bauer, S. T. B. Goennenwein, and E. Saitoh, Phys. Rev. Lett. **110**, 206601 (2013).

[11] Y.-T. Chen, S. Takahashi, H. Nakayama, M. Althammer, S. T. B. Goennenwein, E. Saitoh, and G. E. W. Bauer, Phys. Rev. B **87**, 144411 (2013).

[12] J. H. Han, C. Song, F. Li, Y. Y. Wang, G. Y. Wang, Q. H. Yang, and F. Pan, Phys. Rev. B **90**, 144431 (2014).

[13] D. Hou, Z. Qiu, J. Barker, K. Sato, K. Yamamoto, S. Vélez, J. M. Gomez-Perez, L. E. Hueso, F. Casanova, and E. Saitoh, Phys. Rev. Lett. **118**, 147202 (2017).

[14] G. R. Hoogeboom, A. Aqeel, T. Kuschel, T. T. M. Palstra, and B. J. van Wees, Appl. Phys. Lett. **111**, 052409 (2017).

[15] L. Baldrati, A. Ross, T. Niizeki, C. Schneider, R. Ramos, J. Cramer, O. Gomonay, M. Filianina, T. Savchenko, D. Heinze *et al.*, arXiv:1709.00910.

[16] J. Fischer, O. Gomonay, R. Schlitz, K. Ganzhorn, N. Vlietstra, M. Althammer, H. Huebl, M. Opel, R. Gross, S. T. B. Goennenwein, and S. Geprägs, Phys. Rev. B **97**, 014417 (2018).

[17] A. Manchon, Phys. Status Solidi RRL **11**, 1600409 (2017).

[18] R. Cheng, J. Xiao, Q. Niu, and A. Brataas, Phys. Rev. Lett. **113**, 057601 (2014).

[19] Ø. Johansen and A. Brataas, Phys. Rev. B **95**, 220408(R) (2017).

[20] E. G. Tveten, T. Müller, J. Linder, and A. Brataas, Phys. Rev. B **93**, 104408 (2016).

[21] H. J. Jiao and G. E. W. Bauer, Phys. Rev. Lett. **110**, 217602 (2013).

[22] A. Kapelrud and A. Brataas, Phys. Rev. Lett. **111**, 097602 (2013).

[23] V. Sluka, Phys. Rev. B **96**, 214412 (2017).

[24] M. P. Ross, Ph.D. thesis, Technische Universität München, 2013.

[25] J. P. Kotthaus and V. Jaccarino, Phys. Rev. Lett. **28**, 1649 (1972).

[26] M. Obstbaum, M. Härtinger, H. G. Bauer, T. Meier, F. Swientek, C. H. Back, and G. Woltersdorf, Phys. Rev. B **89**, 060407 (2014).

[27] S. Meyer, M. Althammer, S. Geprägs, M. Opel, R. Gross, and S. T. B. Goennenwein, Appl. Phys. Lett. **104**, 242411 (2014).

[28] L. Liu, R. A. Buhrman, and D. C. Ralph, arXiv:1111.3702.

[29] T. Kampfrath, A. Sell, G. Klatt, A. Pashkin, S. Mahrlein, T. Dekorsy, M. Wolf, M. Fiebig, A. Leitenstorfer, and R. Huber, Nat. Photonics **5**, 31 (2011).

[30] T. Yoshino, K. Ando, K. Harii, H. Nakayama, Y. Kajiwara, and E. Saitoh, J. Phys. Conf. Ser. **266**, 012115 (2011).

[31] E. Dormann, J. R. D. Copley, and V. Jaccarino, J. Phys. C **10**, 2767 (1977).

[32] W. J. Ince, J. Appl. Phys. **37**, 1132 (1966).

[33] A. I. Pankrats, G. A. Petrakovskii, L. N. Bezmaternykh, and O. A. Bayukov, J. Exp. Theor. Phys. **99**, 766 (2004).

# Paper [3]

**Øyvind Johansen and Arne Brataas**

*"Nonlocal Coupling between Antiferromagnets and Ferromagnets in Cavities"*

# Nonlocal Coupling between Antiferromagnets and Ferromagnets in Cavities

Øyvind Johansen[*] and Arne Brataas

*Center for Quantum Spintronics, Department of Physics, Norwegian University of Science and Technology,*
*NO-7491 Trondheim, Norway*

Microwaves couple to magnetic moments in both ferromagnets and antiferromagnets. Although the magnons in ferromagnets and antiferromagnets radically differ, they can become entangled via strong coupling to the same microwave mode in a cavity. The equilibrium configuration of the magnetic moments crucially governs the coupling between the different magnons, because the antiferromagnetic and ferromagnetic magnons have opposite spins when their dispersion relations cross. We derive analytical expressions for the coupling strengths and find that the coupling between antiferromagnets and ferromagnets is comparable to the coupling between two ferromagnets. Our findings reveal a robust link between cavity spintronics with ferromagnets and antiferromagnets.

Magnets and photons can couple strongly and coherently on the quantum level [1]. This coupling has been observed as hybridizations between ferromagnetic magnons and either microwave resonators [2], microwave photons [3], or optical photons [4–7]. Together, these findings constitute the birth of *cavity spintronics*, a new interdisciplinary field with roots in spintronics, cavity quantum electrodynamics, and quantum optics. Shortly after the initial observations of magnon-photon hybridization, experiments also achieved ultrastrong coupling between magnons and microwaves [8–11]. One can tune the coupling strength by changing the temperature of the system [12,13]. The cooperativity of the hybridization, namely, the ratio of the coupling strength to the loss rates, is a measure of the coherence in the system and can be as large as $10^7$ [10]. The transmission and reflection coefficients of a cavity are measures of the magnon-photon coupling. Brillouin light scattering [14] or spin pumping [15–17] can provide additional information. Although the focus thus far has been placed on the hybridization between ferromagnetic magnons and photons, theory predicts that there should also be a significant coupling between antiferromagnetic magnons and photons [18]. Recently, a robust coupling between microwave photons and antiferromagnetic fluctuations in an organic magnet has been observed [19].

When two ferromagnets or ferrimagnets couple to the same cavity mode or the same photons, a nonlocal interaction between the magnons emerges [20,21]. The quantized magnetic field of the cavity mode or photons mediates this indirect coupling. In turn, this coupling facilitates the coherent transport of magnons over macroscopic distances.

The magnons in ferromagnets and antiferromagnets strongly differ. Nevertheless, we will demonstrate that a strong nonlocal coupling can also arise between the magnons in an antiferromagnet and those in a ferromagnet.

This link opens the door toward long-range spin communication between antiferromagnetic and ferromagnetic spintronic devices. Such a connection has so far been elusive, because the vanishing magnetization of the antiferromagnet renders it invisible to dipolar interactions with the ferromagnet. The need for and interest in such a long-range coupling between dissimilar magnetic materials have increased with the recent emergence of antiferromagnetic spintronics [22–26]. Our findings open a path toward integrating these new components with existing ferromagnetic ones.

To study the cavity-mediated coupling between an antiferromagnet and a ferromagnet, we consider the setup depicted in Fig. 1. The Hamiltonian consists of four components:



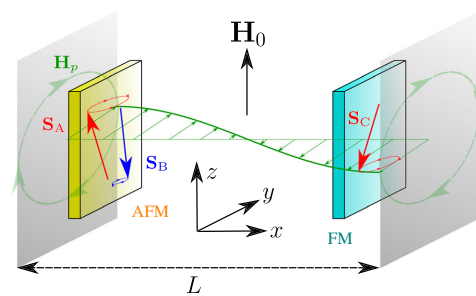FIG. 1. A microwave cavity consisting of two perfect conductors separated by a distance $L$. The magnons in an antiferromagnet (with sublattice spins $S_A$ and $S_B$) and those in a ferromagnet (with spins $S_C$) couple via the quantized magnetic field $H_p$. An external magnetic field $H_0$ along the equilibrium direction of the magnetic moments tunes the resonance frequencies of the magnons to be in the same frequency range.

$$H = H_{\text{AFM}} + H_{\text{FM}} + H_{\text{ph}} + H_{\text{m-ph}}, \qquad (1)$$

where $H_{\text{AFM}}$ describes the antiferromagnet, $H_{\text{FM}}$ the ferromagnet, $H_{\text{ph}}$ the cavity modes, and $H_{\text{m-ph}}$ the coupling of the magnons in both the antiferromagnet and the ferromagnet to the cavity modes. We consider an antiferromagnet described by the Hamiltonian

$$H_{\text{AFM}} = J \sum_{\langle i,j \rangle \in \text{AFM}} \mathbf{S}_i \cdot \mathbf{S}_j + |\gamma| \sum_{i \in \text{AFM}} \mathbf{H}_0 \cdot \mathbf{S}_i$$
$$- \frac{K_{\parallel}}{2} \sum_{i \in \text{AFM}} (S_i^z)^2 + \frac{K_{\perp}}{2} \sum_{i \in \text{AFM}} (S_i^x)^2, \qquad (2)$$

where $J > 0$ is the exchange coupling between the spins $\mathbf{S}$, $\gamma$ is the gyromagnetic ratio, $\mathbf{H}_0 = H_0 \hat{\mathbf{z}}$ is an external magnetic field (in units of Tesla) along the easy axis, and $K_{\parallel} > 0$ and $K_{\perp} \geq 0$ are the easy- and hard-axis anisotropy constants, respectively. For the ferromagnet, we consider energy contributions from the Zeeman and dipolar interactions. It will become clear that the photons couple only to homogeneous magnetic excitations. We can therefore use a simplified expression for the dipolar interaction, resulting in a ferromagnetic Hamiltonian of

$$H_{\text{FM}} = |\gamma| \sum_{i \in \text{FM}} \mathbf{H}_0 \cdot \mathbf{S}_i + \frac{\mu_0}{2} \int_{V_{\text{FM}}} dV \sum_{i=x,y,z} N_i M_i^2. \quad (3)$$

Here, $N_{x,y,z}$ are the elements of the diagonal demagnetization tensor, $V_{\text{FM}}$ is the volume of the ferromagnet, $\mu_0$ is the vacuum permeability, and $M_i$ is the $i$th component of the magnetization. The magnetization is related to the spins by $\mathbf{M} = -|\gamma| \sum_{i \in \text{FM}} \mathbf{S}_i / V_{\text{FM}}$.

Now, let us rewrite the two magnetic Hamiltonians in terms of magnon operators. We perform a Holstein-Primakoff transformation [27] of the spin operators $\mathbf{S}_i$, retaining terms of up to second order in the magnon operators in the resulting Hamiltonian. Following this procedure, we perform a Fourier transformation from spatial coordinates into a momentum representation. To diagonalize the antiferromagnetic and ferromagnetic Hamiltonians, we also perform Bogoliubov transformations.

In terms of the initial Holstein-Primakoff antiferromagnetic magnon annihilation (creation) operators $a_{\mathbf{q}}^{(\dagger)}$ and $b_{\mathbf{q}}^{(\dagger)}$ within sublattices $A$ and $B$, respectively (see Fig. 1), the Bogoliubov transformation into the diagonal eigenmode magnons $\alpha_{\mathbf{q}}^{(\dagger)}$ and $\beta_{\mathbf{q}}^{(\dagger)}$ is [28]

$$\begin{pmatrix} \alpha_{\mathbf{q}} \\ \beta_{-\mathbf{q}}^{\dagger} \\ \alpha_{-\mathbf{q}}^{\dagger} \\ \beta_{\mathbf{q}} \end{pmatrix} = \begin{pmatrix} u_{\alpha,a} & v_{\alpha,b} & v_{\alpha,a} & u_{\alpha,b} \\ v_{\beta,a}^* & u_{\beta,b}^* & u_{\beta,a}^* & v_{\beta,b}^* \\ v_{\alpha,a}^* & u_{\alpha,b}^* & u_{\alpha,a}^* & v_{\alpha,b}^* \\ u_{\beta,a} & v_{\beta,b} & v_{\beta,a} & u_{\beta,b} \end{pmatrix} \begin{pmatrix} a_{\mathbf{q}} \\ b_{-\mathbf{q}}^{\dagger} \\ a_{-\mathbf{q}}^{\dagger} \\ b_{\mathbf{q}} \end{pmatrix}. \quad (4)$$

Here, $\mathbf{q}$ is the wave vector of the magnons. To determine the elements of the Bogoliubov transformation, we impose the requirement that the operators $\alpha_{\mathbf{q}}^{(\dagger)}$ and $\beta_{\mathbf{q}}^{(\dagger)}$ must satisfy bosonic commutation relations as well as the relations $[\alpha_{\mathbf{q}}, H_{\text{AFM}}] = \hbar \omega_\alpha \alpha_{\mathbf{q}}$ and $[\beta_{\mathbf{q}}, H_{\text{AFM}}] = \hbar \omega_\beta \beta_{\mathbf{q}}$. Here, $\omega_{\alpha,\beta}$ are the eigenfrequencies of the antiferromagnet. The excitations in the antiferromagnet are then

$$H_{\text{AFM}} = \sum_{\mathbf{q}} (\hbar \omega_\alpha \alpha_{\mathbf{q}}^{\dagger} \alpha_{\mathbf{q}} + \hbar \omega_\beta \beta_{\mathbf{q}}^{\dagger} \beta_{\mathbf{q}}). \qquad (5)$$

Let us define the frequencies $\omega_E = \hbar J s Z$, $\omega_H = |\gamma| H_0$, $\omega_{\parallel} = \hbar s K_{\parallel}$, and $\omega_{\perp} = \hbar s K_{\perp}$, where $s$ is the spin number and $Z$ is the number of nearest neighbors in the antiferromagnet; then, we can express the eigenfrequencies as

$$\omega_{\pm}^2 \approx \omega_E (2\omega_{\parallel} + \omega_{\perp}) + \omega_H^2$$
$$\pm \sqrt{\omega_E^2 \omega_{\perp}^2 + 4\omega_H^2 \omega_E (2\omega_{\parallel} + \omega_{\perp})}, \qquad (6)$$

where $\omega_\alpha = \omega_+$ and $\omega_\beta = \omega_-$. For simplicity, we have here included only terms to the lowest order in the anisotropy frequencies $\omega_{\parallel/\perp}$, as these are typically much smaller than the exchange frequency $\omega_E$. We also assume that the wavelength of the magnons is much larger than the atomic length scale.

In the long-wavelength limit ($\mathbf{q} = \mathbf{0}$), the quantized ferromagnetic Hamiltonian can be expressed as [28,29]

$$H_{\text{FM}} = A_{\text{FM}} c^{\dagger} c + B_{\text{FM}} (cc + c^{\dagger} c^{\dagger}), \qquad (7)$$

where $A_{\text{FM}} = \hbar[\omega_H + \omega_M(N_{xz} + N_{yz})/2]$ and $B_{\text{FM}} = \hbar \omega_M N_{xy}/4$. Here, we have defined $\omega_M = |\gamma| \mu_0 M_s$, where $M_s$ is the saturation magnetization of the ferromagnet, and $N_{ij} = N_i - N_j$. We have also introduced the ferromagnetic magnon annihilation (creation) operator $c^{(\dagger)}$ from the initial Holstein-Primakoff transformation for the ferromagnet. This Hamiltonian can be diagonalized through a Bogoliubov transformation defined by $\eta = u_{\text{FM}} c + v_{\text{FM}} c^{\dagger}$. Imposing bosonic commutation relations on $\eta^{(\dagger)}$ yields the constraint $u_{\text{FM}}^2 - v_{\text{FM}}^2 = 1$. The elements of the Bogoliubov transformation are [29]

$$v_{\text{FM}} = 2 B_{\text{FM}} \Big/ \sqrt[4]{(A_{\text{FM}} + \hbar \omega_\eta)^2 - 4 B_{\text{FM}}^2}, \qquad (8a)$$

$$u_{\text{FM}} = v_{\text{FM}} (A_{\text{FM}} + \hbar \omega_\eta)/(2 B_{\text{FM}}). \qquad (8b)$$

We assume a thin-film geometry with $N_x = 1$ and $N_y = N_z = 0$. The resonance frequency is then $\omega_\eta = \sqrt{\omega_H(\omega_H + \omega_M)}$.

Now, let us consider the cavity. We first introduce a simple geometry. We will later argue that the simple geometry also captures the essential physics in more

complex cavities. We describe the microwave cavity as two perfect conductor plates separated by a distance $L$ in the $x$ direction. The plates are located at $x = 0$ and $x = L$. The boundary conditions near the conducting plates cause a quantization of the electromagnetic modes in the $x$ direction. The allowed wave numbers in this direction are $n\pi/L$ ($n = 1, 2, \ldots$). We assume that the microwaves propagate only in the direction perpendicular to the conducting plates, i.e., along the $x$ axis. The resulting quantized magnetic field is

$$\mathbf{H}_p(\mathbf{r}) = \sum_{n,\lambda} i \cos\left(\frac{n\pi x}{L}\right)\left(\frac{\hbar\omega_n\mu_0}{V}\right)^{1/2}$$
$$\times (p_{n,\lambda}\hat{\mathbf{x}} \times \hat{\mathbf{e}}_\lambda - p_{n,\lambda}^\dagger\hat{\mathbf{x}} \times \hat{\mathbf{e}}_\lambda^*). \quad (9)$$

Here, $p_{n,\lambda}^{(\dagger)}$ is the boson annihilation (creation) operator associated with a cavity mode with quantum numbers $n$ and $\lambda$. $\hat{\mathbf{e}}_\lambda$ is the polarization unit vector, where $\lambda$ is the polarization. $V$ is the volume of the cavity, $\omega_n = n\pi c/L$ is the cavity mode frequency, and $c$ is the speed of light. The cavity Hamiltonian is

$$H_{\mathrm{ph}} = \sum_{n,\lambda} \hbar\omega_n\left(p_{n,\lambda}^\dagger p_{n,\lambda} + \frac{1}{2}\right). \quad (10)$$

The cavity modes can couple to the magnons in both antiferromagnets [18] and ferromagnets [2,3]. The interaction is represented by a Zeeman term between the quantized magnetic field $\mathbf{H}_p$ in Eq. (9) and the spins in the magnetic materials. This interaction is described by the magnon-photon Hamiltonian $H_{\mathrm{m-ph}}$.

We use a circular polarization basis, $\lambda = \pm$ and $\hat{\mathbf{e}}_\lambda = \hat{\mathbf{e}}_\pm = (\hat{\mathbf{z}} \pm i\hat{\mathbf{y}})/\sqrt{2}$, for the cavity modes. Since the speed of light is much greater than the group velocity of the magnons, the cavity modes couple only to magnons of approximately $|\mathbf{q}| = 0$. For simplicity, we assume that the cavity couples only to the $\mathbf{q} = \mathbf{0}$ modes. We also use the rotating wave approximation (RWA) to simplify the magnon-photon interaction. In the RWA, rapidly oscillating terms, e.g., pairs of creation operators or pairs of annihilation operators, are disregarded, because their average contributions quickly become small.

We tune the system size such that the $n = 1$ cavity mode has a frequency near the crossing of the ferromagnetic and antiferromagnetic dispersion relations. The coupling between the ferromagnet and the antiferromagnet is significant only near this crossing region. Therefore, we disregard any contributions from the high-energy $n > 1$ cavity modes and $\alpha$ magnons of the antiferromagnet. There are also three-particle (and higher-order) interactions in which pairs of magnon creation or annihilation operators couple to the cavity mode, i.e., terms such as $\beta^\dagger\beta^\dagger p_{n,\lambda}$ and $\beta\beta p_{n,\lambda}^\dagger$. Such couplings to the $n = 2$ cavity mode, for

example, oscillate sufficiently slowly to be significant in the RWA. However, these higher-order contributions scale more weakly with the number of spins in the ferromagnet or antiferromagnet ($N_{\mathrm{FM/AFM}}$) than the two-particle interactions do. Such terms can therefore be safely disregarded.

With these approximations and simplifications, the magnon-photon interaction Hamiltonian reduces to

$$H_{\mathrm{m-ph}} = \hbar(\tilde{g}_{\mathrm{AFM}}\beta^\dagger - \tilde{g}_{\mathrm{FM}}\eta^\dagger)(p_+ + p_-) + \mathrm{H.c.} \quad (11)$$

Here, we have introduced the ferromagnetic coupling strength $\tilde{g}_{\mathrm{FM}} = g_{\mathrm{FM}}(u_{\mathrm{FM}} + v_{\mathrm{FM}})$ and the antiferromagnetic coupling strength $\tilde{g}_{\mathrm{AFM}} = g_{\mathrm{AFM}}(u_{\beta,a} - v_{\beta,b} + v_{\beta,a} - u_{\beta,b})/\sqrt{2}$, where $g_{\mathrm{FM/AFM}} = |\gamma|\sqrt{\hbar\omega_p\mu_0 s N_{\mathrm{FM/AFM}}/(4V)}$, with $\omega_p = \omega_{n=1}$ being the microwave frequency. In addition, the coupling strength in a cavity depends on the overlap of the cavity mode with the magnetic materials [15]. More general geometries are described by substituting $g_{\mathrm{FM/AFM}} \to \xi_{\mathrm{FM/AFM}}g_{\mathrm{FM/AFM}}$, where $\xi_{\mathrm{FM/AFM}}$ is a geometrical overlap factor of order one for the ferromagnet or antiferromagnet [13]. In the following illustrations, we consider a perfect overlap between the cavity mode and each magnetic material; i.e., we set $\xi_{\mathrm{FM,AFM}} = 1$. In general, the elements of the Bogoliubov transformation for the antiferromagnetic magnons ($u_{\beta,a}$, $v_{\beta,b}$, $v_{\beta,a}$, and $u_{\beta,b}$—see Ref. [28] for how to calculate them) are complicated functions of the parameters of the antiferromagnetic Hamiltonian expressed in Eq. (2). We therefore present the coupling strengths between the antiferromagnetic magnons and the cavity for only two particular scenarios. In the first scenario, the antiferromagnet is uniaxial ($\omega_\perp = 0$), and we find that the coupling strength is

$$\frac{\tilde{g}_{\mathrm{AFM}}}{g_{\mathrm{AFM}}} \approx \left(\frac{\omega_\parallel}{8\omega_E}\right)^{1/4}. \quad (12)$$

In the second scenario, the antiferromagnet has an easy-plane anisotropy such as that in NiO, where $\mathcal{O}(\omega_\perp) \sim \mathcal{O}(\sqrt{\omega_\parallel\omega_E})$ [30,31]. The coupling strength is then

$$\frac{\tilde{g}_{\mathrm{AFM}}}{g_{\mathrm{AFM}}} \approx \frac{\omega_H}{\sqrt{2\omega_E}(2\omega_E\omega_\parallel - \omega_H^2)^{1/4}}. \quad (13)$$

The expressions given in (12) and (13) are valid to the lowest order in $\omega_\parallel/\omega_E$. Note that, for the uniaxial antiferromagnet, the suppression from the anisotropy-to-exchange ratio is rather weak (only to the power of $1/4$). In spin pumping from antiferromagnets, for example, the suppression from the large exchange interaction is stronger (to the power of $1/2$). This is promising for achieving a significant coupling between the antiferromagnetic magnons and the microwaves.

We consider two geometries. In the first case, the magnetic moments of the ferromagnet and antiferromagnet are

perpendicular to the propagation direction of the cavity modes, as in Fig. 1. In this geometry, which is the one we have considered so far, the magnons couple to both circular polarizations with the same strength, as seen in Eq. (11). This is because, in the RWA and to leading order in the spin fluctuations, the component of the quantized magnetic field along the magnetic moments does not influence the dynamics of the magnetic moments. Since the magnets experience an oscillating magnetic field along only one axis, they effectively couple to a cavity mode that is linearly polarized. The coupling of antiferromagnetic and ferromagnetic magnons requires that they couple to the same cavity mode with quantum numbers $n$ and $\lambda$. Linearly polarized microwaves couple to magnons with different spins and can therefore couple equally strongly to both antiferromagnetic and ferromagnetic magnons. Consequently, this geometry enables a magnon-magnon interaction between an antiferromagnet and a ferromagnet.

In the second geometry, the magnetic moments are collinear with the propagation direction of the cavity modes. In such a geometry, the coupling strengths strongly depend on the cavity mode polarization. Each magnon couples to the microwave mode with the same spin. At the crossing, the antiferromagnetic and ferromagnetic magnons therefore couple to different polarization states $\lambda$ of the cavity modes. Cavity modes with different polarizations $\lambda = \pm$ are independent. This geometry therefore does not lead to a magnon-magnon coupling. This lack of indirect coupling can be circumvented when at least one of the magnon modes is squeezed or hybridized (i.e., it has a noninteger spin [28]). In this case, the magnons have finite, but dissimilar, couplings to both polarizations of the cavity mode. Although this generates a finite magnon-magnon coupling, this coupling will typically be rather weak, because the magnons still primarily couple to different cavity mode polarizations. We therefore focus on the former geometry, illustrated in Fig. 1. In this geometry, there are equally strong couplings to both polarizations and, consequently, a stronger coupling between the magnons.

More complex cavity structures can be effectively reduced to our planar cavity geometry when there is only one mode with a frequency near the crossing point of the magnon dispersion relations. The magnon-magnon coupling is then dominated by this mode. The overlap factors $\xi_{FM,AFM}$ depend on the details of the cavity structure.

We now wish to determine the coupling strength between the ferromagnetic and antiferromagnetic magnons. We consider a dispersive regime, in which the frequency of the cavity mode is slightly detuned from the crossing point between the ferromagnetic and antiferromagnetic magnon dispersion relations. We assume that this detuning $\Delta = \omega_p - \omega_\eta = \omega_p - \omega_\beta$ is much larger than the coupling strengths $\tilde{g}_{FM,AFM}$ and that the frequency of the cavity mode is sufficiently close to the crossing point where $\omega_\eta = \omega_\beta$. We can then determine the magnon-magnon

coupling by performing a unitary transformation of the Hamiltonian given in Eq. (1) and then applying the second-order degenerate perturbation theory, with $\tilde{g}_{FM,AFM}$ as the perturbation parameters. We thus compute that, at the crossing point between the antiferromagnetic and ferromagnetic magnon dispersion relations, the transformed Hamiltonian describing the excitations is

$$H' = \hbar \left( \omega_\beta - \frac{2\tilde{g}_{AFM}^2}{\Delta} \right) \beta^\dagger \beta + \hbar \left( \omega_\eta - \frac{2\tilde{g}_{FM}^2}{\Delta} \right) \eta^\dagger \eta$$
$$+ \hbar \left( \omega_p + \frac{\tilde{g}_{FM}^2 + \tilde{g}_{AFM}^2}{\Delta} \right) (p_-^\dagger p_- + p_+^\dagger p_+)$$
$$+ 2\hbar \frac{\tilde{g}_{FM}\tilde{g}_{AFM}}{\Delta} (\beta^\dagger \eta + \eta^\dagger \beta) \quad (14)$$

to second order in $\tilde{g}_{FM,AFM}$. The first three terms in Eq. (14) describe shifts in the frequencies of both the magnon and cavity modes, whereas the last term describes a dispersive coupling between the ferromagnetic and antiferromagnetic magnons. This dispersive coupling means that the eigenstate of the system becomes a linear combination of both magnons and can therefore no longer be described as a purely ferromagnetic or antiferromagnetic magnon.

It is instructive to find numerical estimates of the effective coupling strengths for different combinations of materials. We consider a scenario in which the volume of each of the magnetic materials constitutes 1% of the volume of the cavity; this magnitude is similar to that in previous experiments involving ferromagnets in spherical cavities [20,21]. As ferromagnets, we consider yttrium-iron-garnet (YIG) and Co-Fe alloys. These materials can have a damping on the order of $10^{-4}$ [32,33]. The spin density $sN_{FM}/V_{FM}$ in YIG is $\sim 2 \times 10^{22}$ cm$^{-3}$ [34]. In a Co-Fe alloy, it is possible to achieve a spin density as high as $\sim 2 \times 10^{23}$ cm$^{-3}$, where we have estimated the magnitude of the spin density as $M_s/\mu_B$, with $\mu_B$ being the Bohr magneton. The saturation magnetizations of these ferromagnetic materials are $\mu_0 M_s = 0.247$ T for YIG [35] and $\mu_0 M_s \approx 2.4$ T for the Co-Fe alloy [33]. As antiferromagnets, we consider the uniaxial antiferromagnetic materials MnF$_2$ and NaNiO$_2$ as well as the easy-plane antiferromagnetic material NiO. Estimates of the spin densities in MnF$_2$, NaNiO$_2$, and NiO yield $\sim 10^{22}$ [36], $\sim 5 \times 10^{22}$ [37], and $\sim 10^{23}$ cm$^{-3}$ [38], respectively. The exchange and anisotropy frequencies of the antiferromagnetic materials are listed in Table I. Using these parameters and choosing

TABLE I. Exchange and anisotropy frequencies of the antiferromagnets.

| Material | $\omega_E$ ($10^{12}$ s$^{-1}$) | $\omega_\parallel$ ($10^{12}$ s$^{-1}$) | $\omega_\perp$ ($10^{12}$ s$^{-1}$) |
|---|---|---|---|
| MnF$_2$ [39] | 9.3 | $1.5 \times 10^{-1}$ | $\cdots$ |
| NaNiO$_2$ [37] | $8.4 \times 10^{-1}$ | $6.2 \times 10^{-2}$ | $\cdots$ |
| NiO [30,31] | $1.7 \times 10^2$ | $2.3 \times 10^{-3}$ | $1.3 \times 10^{-1}$ |

TABLE II.  Coupling strengths for different combinations of ferromagnets and antiferromagnets.

| Materials (AFM/FM) | $\tilde{g}_{AFM}/(2\pi)$ (GHz) | $\tilde{g}_{FM}/(2\pi)$ (GHz) |
| --- | --- | --- |
| $MnF_2$/YIG | 0.31 | 2.30 |
| $MnF_2$/Co-Fe | 0.33 | 7.67 |
| $NaNiO_2$/YIG | 0.44 | 1.28 |
| $NaNiO_2$/Co-Fe | 0.50 | 5.03 |
| NiO/YIG | 0.17 | 2.03 |
| NiO/Co-Fe | 0.15 | 6.88 |

the $n = 1$ frequency mode of the cavity to lie at the crossing point between the antiferromagnetic and ferromagnetic dispersion relations, we obtain the coupling strengths given in Table II. A plot of the dispersion relations and the interpretation of the coupling constants $\tilde{g}_{FM,AFM}$ is given in Fig. 2 for the material combination $NaNiO_2$/YIG.

Our results reveal that the coupling strength of the cavity with the antiferromagnet is typically an order of magnitude lower than that with the ferromagnet. This is due to the weak interaction between antiferromagnets and magnetic fields, which gives rise to a suppression factor from the high exchange energy, as seen in Eqs. (12) and (13). Importantly, it is still possible to achieve a sizable magnon-magnon coupling between the antiferromagnet and the ferromagnet. If we detune the cavity from the crossing point of the magnon dispersion relations by $\Delta = 5\tilde{g}_{FM}$, then the magnon-magnon coupling becomes $\approx 2\tilde{g}_{AFM}/5$. For $MnF_2$/Co-Fe, this would correspond to a coupling strength of 132 MHz; for $NaNiO_2$/Co-Fe, the corresponding value is 200 MHz, and for NiO/YIG, it is 68 MHz. These magnitudes are similar to the coupling strength observed between two YIG spheres [20,21]. The inefficiency of the coupling between the antiferromagnet and the cavity is compensated for by the high frequency at the crossing point between the magnon dispersion relations, with a
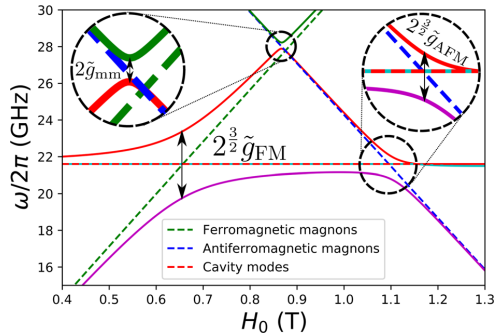


FIG. 2.  Dispersion relations for $NaNiO_2$ and YIG in a cavity, with $\Delta = -5\tilde{g}_{FM}$. The magnon-magnon coupling is $\tilde{g}_{mm} \approx 2\tilde{g}_{FM}\tilde{g}_{AFM}/\Delta$. The dashed lines show the dispersion relations in the absence of the magnon-photon coupling, whereas the solid lines are the dispersion relations in the interacting system.

proportionality of $\tilde{g}_{FM/AFM} \propto \sqrt{\omega}$. The magnon dispersion relations cross at 148 GHz ($H_0 = 4.2$ T) for $MnF_2$/Co-Fe, at 36 GHz ($H_0 = 0.6$ T) for $NaNiO_2$/Co-Fe, and at 100 GHz ($H_0 = 3.5$ T) for NiO/YIG.

Although the linewidths of many ferromagnets have been extensively studied, there are very few similar measurements available for antiferromagnets. It is possible that the linewidth may become larger in antiferromagnets, since the exchange energy often dominates. If this is the case, the cooperativity (which is a measure of the coherence within the system) will be lower in systems involving antiferromagnets than in systems consisting solely of ferromagnets.

In summary, we have shown that, despite having opposite spins, antiferromagnetic magnons and ferromagnetic magnons can be coupled inside a microwave cavity. This coupling is strongest when the magnetic moments in the antiferromagnet and ferromagnet are perpendicular to the propagation direction of the cavity modes at equilibrium. In this geometry, the cavity mode couples to both the antiferromagnetic and ferromagnetic magnons, resulting in a robust nonlocal magnon-magnon coupling. The magnitude of this coupling is similar to that of the nonlocal interaction between two ferromagnets.

*Corresponding author.
oyvinjoh@ntnu.no

[1] O. O. Soykal and M. E. Flatté, Strong Field Interactions between a Nanomagnet and a Photonic Cavity, Phys. Rev. Lett. 104, 077202 (2010).

[2] H. Huebl, C. W. Zollitsch, J. Lotze, F. Hocke, M. Greifenstein, A. Marx, R. Gross, and S. T. B. Goennenwein, High Cooperativity in Coupled Microwave Resonator Ferrimagnetic Insulator Hybrids, Phys. Rev. Lett. 111, 127003 (2013).

[3] Y. Tabuchi, S. Ishino, T. Ishikawa, R. Yamazaki, K. Usami, and Y. Nakamura, Hybridizing Ferromagnetic Magnons and Microwave Photons in the Quantum Limit, Phys. Rev. Lett. 113, 083603 (2014).

[4] A. Osada, R. Hisatomi, A. Noguchi, Y. Tabuchi, R. Yamazaki, K. Usami, M. Sadgrove, R. Yalla, M. Nomura, and Y. Nakamura, Cavity Optomagnonics with Spin-Orbit Coupled Photons, Phys. Rev. Lett. 116, 223601 (2016).

[5] X. Zhang, N. Zhu, C.-L. Zou, and H. X. Tang, Optomagnonic Whispering Gallery Microresonators, Phys. Rev. Lett. 117, 123605 (2016).

[6] J. A. Haigh, A. Nunnenkamp, A. J. Ramsay, and A. J. Ferguson, Triple-Resonant Brillouin Light Scattering in

Magneto-Optical Cavities, Phys. Rev. Lett. **117,** 133602 (2016).

[7] C. Braggio, G. Carugno, M. Guarise, A. Ortolan, and G. Ruoso, Optical Manipulation of a Magnon-Photon Hybrid System, Phys. Rev. Lett. **118,** 107205 (2017).

[8] X. Zhang, C.-L. Zou, L. Jiang, and H. X. Tang, Strongly Coupled Magnons and Cavity Microwave Photons, Phys. Rev. Lett. **113,** 156401 (2014).

[9] M. Goryachev, W. G. Farr, D. L. Creedon, Y. Fan, M. Kostylev, and M. E. Tobar, High-Cooperativity Cavity QED with Magnons at Microwave Frequencies, Phys. Rev. Applied **2,** 054002 (2014).

[10] J. Bourhill, N. Kostylev, M. Goryachev, D. L. Creedon, and M. E. Tobar, Ultrahigh cooperativity interactions between magnons and resonant photons in a YIG sphere, Phys. Rev. B **93,** 144420 (2016).

[11] N. Kostylev, M. Goryachev, and M. E. Tobar, Superstrong coupling of a microwave cavity to yttrium iron garnet magnons, Appl. Phys. Lett. **108,** 062402 (2016).

[12] H. Maier-Flaig, M. Harder, S. Klingler, Z. Qiu, E. Saitoh, M. Weiler, S. Geprägs, R. Gross, S. T. B. Goennenwein, and H. Huebl, Tunable magnon-photon coupling in a compensating ferrimagnet—from weak to strong coupling, Appl. Phys. Lett. **110,** 132401 (2017).

[13] I. Boventer, M. Pfirrmann, J. Krause, Y. Schön, M. Kläui, and M. Weides, Complex temperature dependence of coupling and dissipation of cavity magnon polaritons from millikelvin to room temperature, Phys. Rev. B **97,** 184420 (2018).

[14] S. Klingler, H. Maier-Flaig, R. Gross, C.-M. Hu, H. Huebl, S. T. B. Goennenwein, and M. Weiler, Combined Brillouin light scattering and microwave absorption study of magnon-photon coupling in a split-ring resonator/YIG film system, Appl. Phys. Lett. **109,** 072402 (2016).

[15] Y. Cao, P. Yan, H. Huebl, S. T. B. Goennenwein, and G. E. W. Bauer, Exchange magnon-polaritons in microwave cavities, Phys. Rev. B **91,** 094423 (2015).

[16] L. Bai, M. Harder, Y. P. Chen, X. Fan, J. Q. Xiao, and C.-M. Hu, Spin Pumping in Electrodynamically Coupled Magnon-Photon Systems, Phys. Rev. Lett. **114,** 227201 (2015).

[17] L. Bai, M. Harder, P. Hyde, Z. Zhang, C.-M. Hu, Y. P. Chen, and J. Q. Xiao, Cavity Mediated Manipulation of Distant Spin Currents Using a Cavity-Magnon-Polariton, Phys. Rev. Lett. **118,** 217201 (2017).

[18] H. Y. Yuan and X. R. Wang, Magnon-photon coupling in antiferromagnets, Appl. Phys. Lett. **110,** 082403 (2017).

[19] M. Mergenthaler, J. Liu, J. J. Le Roy, N. Ares, A. L. Thompson, L. Bogani, F. Luis, S. J. Blundell, T. Lancaster, A. Ardavan, G. A. D. Briggs, P. J. Leek, and E. A. Laird, Strong Coupling of Microwave Photons to Antiferromagnetic Fluctuations in an Organic Magnet, Phys. Rev. Lett. **119,** 147701 (2017).

[20] N. J. Lambert, J. A. Haigh, S. Langenfeld, A. C. Doherty, and A. J. Ferguson, Cavity-mediated coherent coupling of magnetic moments, Phys. Rev. A **93,** 021803 (2016).

[21] B. Zare Rameshti and G. E. W. Bauer, Indirect coupling of magnons by cavity photons, Phys. Rev. B **97,** 014419 (2018).

[22] R. Cheng, J. Xiao, Q. Niu, and A. Brataas, Spin Pumping and Spin-Transfer Torques in Antiferromagnets, Phys. Rev. Lett. **113,** 057601 (2014).

[23] X. Marti, I. Fina, C. Frontera, J. Liu, P. Wadley, Q. He, R. J. Paull, J. D. Clarkson, J. Kudrnovský, I. Turek, J. Kunes, D. Yi, J.-H. Chu, C. T. Nelson, L. You, E. Arenholz, S. Salahuddin, J. Fontcuberta, T. Jungwirth, and R. Ramesh, Room-temperature antiferromagnetic memory resistor, Nat. Mater. **13,** 367 (2014).

[24] R. Cheng, D. Xiao, and A. Brataas, Terahertz Antiferromagnetic Spin Hall Nano-Oscillator, Phys. Rev. Lett. **116,** 207603 (2016).

[25] T. Jungwirth, X. Marti, P. Wadley, and J. Wunderlich, Antiferromagnetic spintronics, Nat. Nanotechnol. **11,** 231 (2016).

[26] V. Baltz, A. Manchon, M. Tsoi, T. Moriyama, T. Ono, and Y. Tserkovnyak, Antiferromagnetic spintronics, Rev. Mod. Phys. **90,** 015005 (2018).

[27] T. Holstein and H. Primakoff, Field dependence of the intrinsic domain magnetization of a ferromagnet, Phys. Rev. **58,** 1098 (1940).

[28] A. Kamra, U. Agrawal, and W. Belzig, Noninteger-spin magnonic excitations in untextured magnets, Phys. Rev. B **96,** 020411 (2017).

[29] A. Kamra and W. Belzig, Super-Poissonian Shot Noise of Squeezed-Magnon Mediated Spin Transport, Phys. Rev. Lett. **116,** 146601 (2016).

[30] T. Satoh, S.-J. Cho, R. Iida, T. Shimura, K. Kuroda, H. Ueda, Y. Ueda, B. A. Ivanov, F. Nori, and M. Fiebig, Spin Oscillations in Antiferromagnetic NiO Triggered by Circularly Polarized Light, Phys. Rev. Lett. **105,** 077402 (2010).

[31] M. T. Hutchings and E. J. Samuelsen, Measurement of spin-wave dispersion in NiO by inelastic neutron scattering and its relation to magnetic properties, Phys. Rev. B **6,** 3447 (1972).

[32] H. Kurebayashi, O. Dzyapko, V. E. Demidov, D. Fang, A. J. Ferguson, and S. O. Demokritov, Controlled enhancement of spin-current emission by three-magnon splitting, Nat. Mater. **10,** 660 (2011).

[33] M. A. W. Schoen, D. Thonig, M. L. Schneider, T. J. Silva, H. T. Nembach, O. Eriksson, O. Karis, and J. M. Shaw, Ultra-low magnetic damping of a metallic ferromagnet, Nat. Phys. **12,** 839 (2016).

[34] M. A. Gilleo and S. Geller, Magnetic and crystallographic properties of substituted yttrium-iron garnet, $3Y_2O_3 \cdot xM_2O_3 \cdot (5-x)Fe_2O_3$, Phys. Rev. **110,** 73 (1958).

[35] P. Hansen, P. Röschmann, and W. Tolksdorf, Saturation magnetization of gallium-substituted yttrium iron garnet, J. Appl. Phys. **45,** 2728 (1974).

[36] J. P. Kotthaus and V. Jaccarino, Antiferromagnetic-Resonance Linewidths in $MnF_2$, Phys. Rev. Lett. **28,** 1649 (1972).

[37] E. Chappel, M. D. Núñez-Regueiro, F. Dupont, G. Chouteau, C. Darie, and A. Sulpice, Antiferromagnetic resonance and high magnetic field properties of $NaNi O_2$, Eur. Phys. J. B **17,** 609 (2000).

[38] A. Schrön and F. Bechstedt, Spin-dependent properties and images of MnO, FeO, CoO, and NiO(001) surfaces, Phys. Rev. B **92,** 165112 (2015).

[39] M. P. Ross, Spin Dynamics in an Antiferromagnet, Ph.D. thesis, Technische Universität München, 2013.
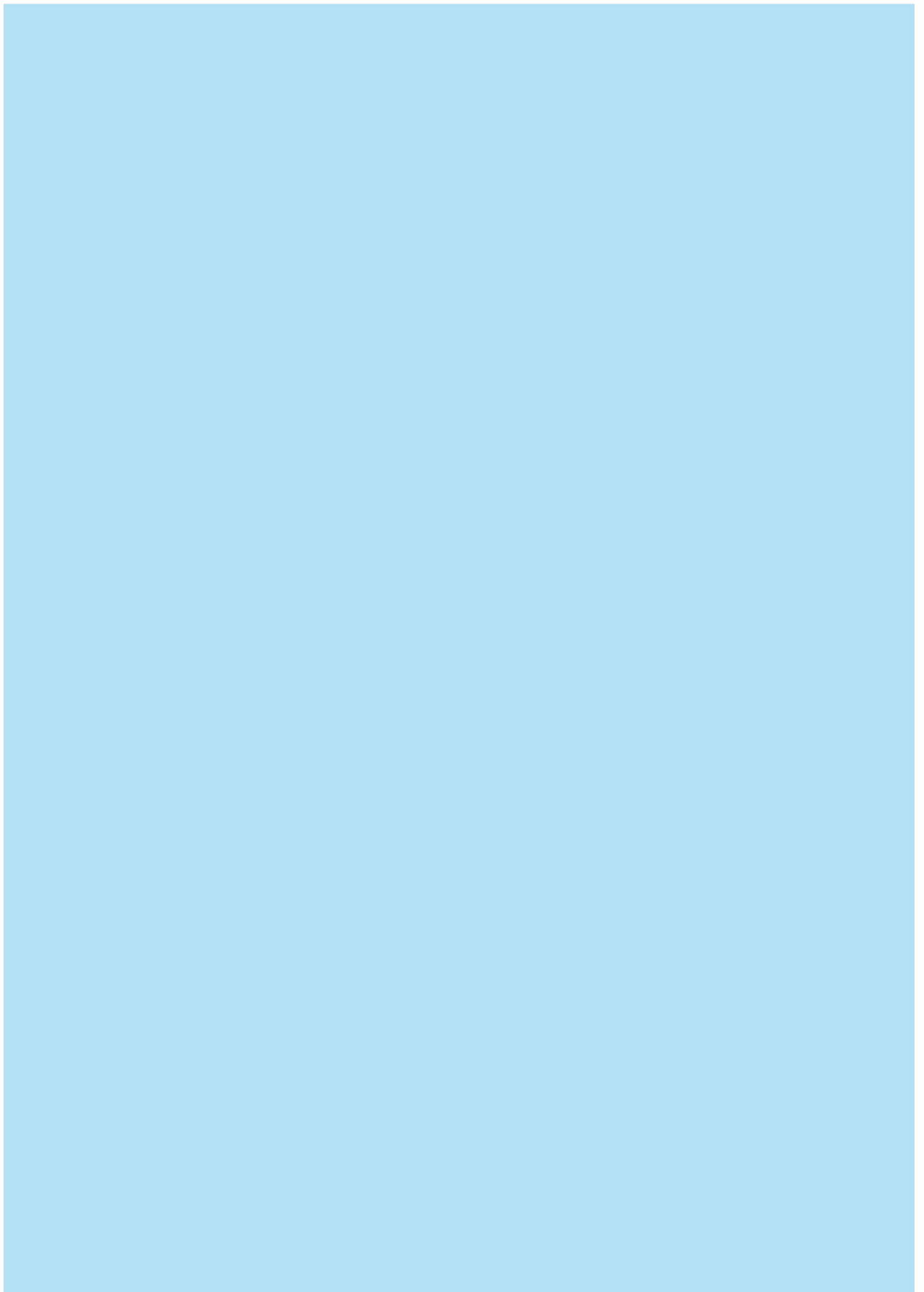
# Paper [4]

**Øyvind Johansen, Akashdeep Kamra, Camilo Ulloa,
Arne Brataas, and Rembert A. Duine**

*"Magnon-Mediated Indirect Exciton Condensation
through Antiferromagnetic Insulators"*

# Magnon-Mediated Indirect Exciton Condensation through Antiferromagnetic Insulators

Øyvind Johansen,[1, *] Akashdeep Kamra,[1] Camilo Ulloa,[2] Arne Brataas,[1] and Rembert A. Duine[1, 2, 3]

[1]*Center for Quantum Spintronics, Department of Physics,*
*Norwegian University of Science and Technology, NO-7491 Trondheim, Norway*
[2]*Institute for Theoretical Physics, Utrecht University, Princetonplein 5, 3584 CC Utrecht, the Netherlands*
[3]*Department of Applied Physics, Eindhoven University of Technology,*
*P.O. Box 513, 5600 MB Eindhoven, The Netherlands*
(Dated: July 26, 2019)

Electrons and holes residing on the opposing sides of an insulating barrier and experiencing an attractive Coulomb interaction can spontaneously form a coherent state known as an indirect exciton condensate. We study a trilayer system where the barrier is an antiferromagnetic insulator. The electrons and holes here additionally interact via interfacial coupling to the antiferromagnetic magnons. We show that by employing magnetically uncompensated interfaces, we can design the magnon-mediated interaction to be attractive or repulsive by varying the thickness of the antiferromagnetic insulator by a single atomic layer. We derive an analytical expression for the critical temperature $T_c$ of the indirect exciton condensation. Within our model, anisotropy is found to be crucial for achieving a finite $T_c$, which increases with the strength of the exchange interaction in the antiferromagnetic bulk. For realistic material parameters, we estimate $T_c$ to be around 7 K, the same order of magnitude as the current experimentally achievable exciton condensation where the attraction is solely due to the Coulomb interaction. The magnon-mediated interaction is expected to cooperate with the Coulomb interaction for condensation of indirect excitons, thereby providing a means to significantly increase the exciton condensation temperature range.

*Introduction.*—Interactions between fermions result in exotic states of matter. Superconductivity is a prime example, where the negatively charged electrons can have an overall attractive coupling mediated by individual couplings to the vibrations, known as phonons, of the positively charged lattice. In addition to charge, the electron also has a spin degree of freedom. The electron spin can interact with localized magnetic moments through an exchange interaction exciting the magnetic moment by transfer of angular momentum. These excitations are quasiparticles known as magnons. Theoretical predictions of electron-magnon interactions have shown that these can also induce effects such as superconductivity [1–10].

Research interest in antiferromagnetic materials is surging [11, 12]. This enthusiasm is due to the promising properties of antiferromagnets such as high resonance frequencies in the THz regime and a vanishing net magnetic moment. Much of this research focuses on interactions involving magnons or spin waves at magnetic interfaces in hybrid structures. Examples of this are spin pumping [13–19], spin transfer [15, 20–22], and spin Hall magnetoresistance [23–28] at normal metal interfaces, and magnon-mediated superconductivity [9, 10]. Recently, an experiment has also demonstrated spin transport in an antiferromagnetic insulator over distances up to 80 μm [29]. Moreover, antiferromagnetic materials are also of interest since it is believed that high-temperature superconductivity in cuprates is intricately linked to magnetic fluctuations near an antiferromagnetic Mott insulating phase [30, 31]. Thus it is crucial to achieve a good understanding of antiferromagnetic magnon-electron interactions, as well as electron-electron interactions mediated by antiferromagnetic magnons.

In this Letter, we theoretically demonstrate the application of antiferromagnetic insulators to condensation of indirect excitons. An exciton is a bound state consisting of an electron and a hole. The excitons interact attractively through the Coulomb interaction due to their opposite charges [32]. Initially predicted many decades ago [33, 34], the exciton condensate has been surprisingly elusive. A challenge is that the exciton lifetime is too short to form a condensate due to exciton-exciton annihilation processes such as Auger recombination [35–38]. The problem of short exciton lifetimes can be solved by having a spatial separation between the electrons and holes in a trilayer system, where the electrons and holes are separated by an insulating barrier [39–41] to drastically lower the recombination rate. Excitons in such systems are often referred to as (spatially) indirect excitons, and these are ideal to observe the exciton condensate. Herein, we consider a system where the insulating barrier is an antiferromagnetic insulator, as shown in Fig. 1. The insulating barrier can then serve a dual purpose: in addition
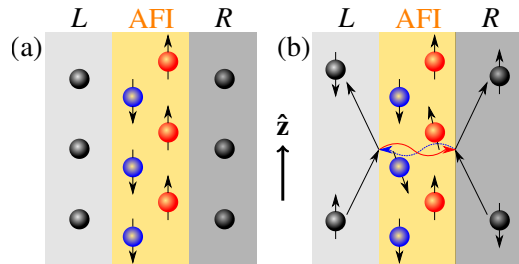


Figure 1. (a) An antiferromagnetic insulator (AFI) sandwiched between two separate fermion reservoirs, denoted by $L$ and $R$. We let the spins on sublattice $A$ (illustrated in blue) be down, and the spins on sublattice $B$ (illustrated in red) be up. (b) The fermions in the two reservoirs can interact through emission and absorption of magnons. For the process in the figure we have that either a spin-up fermion in $L$ emits a $S_z = +\hbar$ magnon (red arrow) which is absorbed by a spin-down fermion in $R$, or a spin-down fermion in $R$ emits a $S_z = -\hbar$ magnon (blue dashed arrow) absorbed by a spin-up fermion in $L$.

to increasing the exciton lifetime, the spin fluctuations in the antiferromagnet mediate an additional attractive interaction between the electrons and the holes. This magnon-mediated interaction cooperates with the Coulomb interaction thereby enabling an increase of the temperature range for observing exciton condensation in experiments.

The indirect exciton condensate has two main experimental signatures. The first is a dissipationless counterflow of electric currents in the two layers [42–44]. When the exciton condensate moves in one direction, the resulting charge currents in the individual layers are antiparallel due to the oppositely charged carriers in the two layers. The second signature is a large enhancement of the zero-bias tunneling conductance between the layers [45, 46], reminiscent of the Josephson effect in superconductors. These experimental signatures can be used to observe the existence of the indirect condensate in our proposed system.

The exciton condensate is expected to exist when the number of electrons in one layer equals the number of holes in the other. Thus far, to the best of our knowledge, experiments with an unequivocal detection of the exciton condensate have utilized quantum Hall systems with a half filling of the lowest Landau level to satisfy this criterion [47–51]. Such systems rely on high external magnetic fields. A recent experiment studying double-bilayer graphene systems has, however, been able to detect the enhanced zero-bias tunneling conductance signature of indirect exciton condensation without any magnetic field, by controlling the electron and hole populations through gate voltages [52]. This is an indication of the possible existence of an exciton condensate, and shows promise for finding a magnetic-field free exciton condensate.

In this Letter, we show that the magnon-mediated interaction between the electrons and holes can be attractive or repulsive depending on whether the two magnetic interfaces are with the same or opposite magnetic sublattices. In turn, this enables an unprecedented control over the interaction nature via the variation of the antiferromagnetic insulator thickness by a single atomic layer. Consequently, when the magnon-mediated interaction is paired with the Coulomb interaction, this can be used to control the favored spin structure of the excitons. In our model, we find that the critical temperature for condensation is enhanced by the exchange interaction in the antiferromagnet, and that a finite magnetic anisotropy is needed to have an attractive interaction around the Fermi level. Our results suggest that if one lets the insulating barrier in indirect exciton condensation experiments be an antiferromagnetic insulator, the magnon-mediated interactions can significantly strengthen the correlations between the electrons and the holes.

*Model.*—We consider a trilayer system where an antiferromagnetic insulator is sandwiched between two fermion reservoirs, as illustrated in Fig. 1 (a). We will then later consider the case where one of these reservoirs is populated by electrons, and the other by holes. This system can be described by the Hamiltonian $\mathcal{H} = \mathcal{H}_{el} + \mathcal{H}_{mag} + \mathcal{H}_{int}$, where $\mathcal{H}_{el}$ describes the electronic part of the system in the fermion reservoirs, $\mathcal{H}_{mag}$ describes the spins in the antiferromagnetic insulator, and $\mathcal{H}_{int}$

describes the interfacial interaction between the fermions and magnons. We assume all three layers to be atomically thin, and thus two-dimensional, for simplicity.

We consider a uniaxial easy-axis antiferromagnetic insulator described by the Hamiltonian

$$\mathcal{H}_{mag} = J \sum_{\langle i,j \rangle} \mathbf{S}_i \cdot \mathbf{S}_j - \frac{K}{2} \sum_i S_{iz}^2 . \qquad (1)$$

Here $J > 0$ is the strength of the nearest-neighbor exchange interaction between the spins which have a magnitude $|\mathbf{S}_i| = \hbar S$ for all $i$, and $K > 0$ is the easy-axis anisotropy constant. Next, we perform a Holstein–Primakoff transformation (HPT) [53] of the spin operators on each sublattice, denoted by sublattices $A$ and $B$, as defined in Fig. 1. From the HPT, we have that the operator $a_i^{(\dagger)}$ annihilates (creates) a magnon at $\mathbf{r}_i$ when $\mathbf{r}_i \in A$, and equivalently $b_i^{(\dagger)}$ annihilates (creates) a magnon at $\mathbf{r}_i$ when $\mathbf{r}_i \in B$. The magnetic Hamiltonian can be diagonalized through Fourier and Bogoliubov transformations to the form $\mathcal{H}_{mag} = \sum_{\mathbf{k}} \varepsilon_{\mathbf{k}} \left( \mu_{\mathbf{k}}^{\dagger} \mu_{\mathbf{k}} + v_{\mathbf{k}}^{\dagger} v_{\mathbf{k}} \right)$. The magnon energy is given by $\varepsilon_{\mathbf{k}} = \hbar \sqrt{(1 - \gamma_{\mathbf{k}}^2)\omega_E^2 + \omega_{\parallel}(2\omega_E + \omega_{\parallel})}$, where $\mathbf{k}$ is the magnon momentum, $\gamma_{\pm \mathbf{k}} = z^{-1} \sum_{\boldsymbol{\delta}} \exp(i\mathbf{k} \cdot \boldsymbol{\delta})$, $\boldsymbol{\delta}$ a set of vectors to each nearest neighbor, $z$ the number of nearest neighbors, $\omega_E = \hbar J S z$, and $\omega_{\parallel} = \hbar K S$. The eigenmagnon operators $\mu_{\mathbf{k}}^{(\dagger)}$ and $v_{\mathbf{k}}^{(\dagger)}$ are related to the HPT magnon operators through the Bogoliubov transformation $\mu_{\mathbf{k}} = u_{\mathbf{k}} a_{\mathbf{k}} + v_{\mathbf{k}} b_{-\mathbf{k}}^{\dagger}$, $v_{\mathbf{k}} = u_{\mathbf{k}} b_{\mathbf{k}} + v_{\mathbf{k}} a_{-\mathbf{k}}^{\dagger}$. The Bogoliubov coefficients $u_{\mathbf{k}}$ and $v_{\mathbf{k}}$ are given by $u_{\mathbf{k}} = \sqrt{(\Gamma_{\mathbf{k}} + 1)/2}$ and $v_{\mathbf{k}} = \sqrt{(\Gamma_{\mathbf{k}} - 1)/2}$, with $\Gamma_{\mathbf{k}} = \{1 - [\omega_E \gamma_{\mathbf{k}}/(\omega_E + \omega_{\parallel})]^2\}^{-1/2}$.

The interfacial exchange interaction between the fermions and magnons at the two magnetic interfaces is modeled by the *s-d* interaction [54, 55]

$$\mathcal{H}_{int} = - \sum_{j=L,R} \sum_{k=A,B} \sum_{i \in \mathcal{A}_k^j} J_k^j(\mathbf{r}_i) \hat{\boldsymbol{\rho}}_j(\mathbf{r}_i) \cdot \mathbf{S}(\mathbf{r}_i), \qquad (2)$$

which has been successfully applied to describe interactions at magnetic interfaces in similar systems [19, 56–59]. Here $\mathcal{A}_k^{L(R)}$ is the interface section between the left (right) fermion reservoir and the $k$-th ($k = A, B$) sublattice of the antiferromagnetic insulator. The interfacial exchange coupling constants $J_k^j(\mathbf{r}_i)$ are defined so that they take on the value $J_k^j(\mathbf{r}_i) = J_k^j$ if $\mathbf{r}_i \in \mathcal{A}_k^j$, and zero otherwise. We have also defined the electronic spin density

$$\hat{\boldsymbol{\rho}}_j(\mathbf{r}_i) = \frac{1}{2} \sum_{\sigma,\sigma'} \psi_{\sigma,j}^{\dagger}(\mathbf{r}_i) \boldsymbol{\sigma}_{\sigma\sigma'} \psi_{\sigma',j}(\mathbf{r}_i) \qquad (3)$$

with $\psi_{\sigma,j}^{(\dagger)}$ annihilating (creating) a fermion with spin $\sigma$ in the $j$-th ($j = L, R$) fermion reservoir, and $\boldsymbol{\sigma} = (\sigma_x, \sigma_y, \sigma_z)$ being a vector of Pauli matrices.

*Effective magnon potential.*—We will now use a path integral approach where we treat the magnon-fermion interaction as a perturbation, and integrate out the magnonic fields that

give rise to processes as illustrated in Fig. 1 (b) to express the interaction as an effective potential between the fermion reservoirs. We consider the coherent-state path integral $\mathcal{Z} = \int \mathcal{D}^2 \psi_L \mathcal{D}^2 \psi_R \mathcal{D}^2 \mu \mathcal{D}^2 \nu \exp(-\mathcal{S}/\hbar)$ in imaginary time, where $\mathcal{D}^2 \mu \equiv \mathcal{D}\mu \mathcal{D}\mu^*$ *etc.* The action $\mathcal{S}$ is given by

$$\mathcal{S} = \int_0^{\hbar\beta} d\tau \left\{ \hbar \sum_i \left[ \sum_{\sigma=\uparrow,\downarrow} \sum_{j=L,R} \psi_{\sigma,j}^*(\mathbf{r}_i, \tau)\partial_\tau \psi_{\sigma,j}(\mathbf{r}_i, \tau) \right. \right.$$
$$\left. \left. + \sum_{\eta=\mu,\nu} \eta^*(\mathbf{r}_i, \tau)\partial_\tau \eta(\mathbf{r}_i, \tau) \right] + \mathcal{H}(\tau) \right\}, \quad (4)$$

where $\tau = it$ is imaginary time, and $\beta = 1/(k_B T)$ with $k_B$ being the Boltzmann constant and $T$ the temperature. Note that in the coherent-state path integral we can replace fermion operators by Grassman numbers (*e.g.* $\psi^\dagger \to \psi^*$) and boson operators by complex numbers (*e.g.* $\eta^\dagger \to \eta^*$).

We now treat $\mathcal{H}_{\text{int}}$ as a perturbation, and keep terms up to second order. We discard any terms that only contribute to intralayer interactions, as we are interested in the interlayer potential between the fermion reservoirs. By discarding the intralayer terms, we effectively assume that the interlayer interactions will dominate over the intralayer interactions, which is the case for a system designed for indirect exciton condensation. Next, we integrate out the magnon fields $\mu^{(*)}$ and $\nu^{(*)}$, and write the path integral over the fermion reservoirs as $\mathcal{Z} \approx \int \mathcal{D}^2 \psi_L \mathcal{D}^2 \psi_R \exp(-\mathcal{S}_{\text{eff}}/\hbar)$. In the momentum and Matsubara-frequency bases, the effective action $\mathcal{S}_{\text{eff}}$ is given by [60]

$$\mathcal{S}_{\text{eff}} = \mathcal{S}_{\text{el}} + \hbar\beta \sum_{\sigma=\uparrow,\downarrow} \sum_{lmn} \sum_{\mathbf{k}\mathbf{k}'\mathbf{q}} U_\sigma(\mathbf{q}, i\omega_n)\psi_{\sigma,L}^*(\mathbf{k}' + \mathbf{q}, i\nu_l + i\omega_n)$$
$$\times \psi_{-\sigma,L}(\mathbf{k}', i\nu_l)\psi_{-\sigma,R}^*(\mathbf{k} - \mathbf{q}, i\nu_m - i\omega_n)\psi_{\sigma,R}(\mathbf{k}, i\nu_m), \quad (5)$$

where we have here introduced the fermionic and bosonic Matsubara frequencies, $\nu_n = (2n+1)\pi/(\hbar\beta)$ and $\omega_n = 2\pi n/(\hbar\beta)$ respectively. The action $\mathcal{S}_{\text{el}}$ describes the contribution of the fermionic fields to the action in Eq. (4), except for the contributions from $\mathcal{H}_{\text{int}}$. The latter term, $\mathcal{H}_{\text{int}}$, is instead described by the contribution of the magnon-mediated interlayer-fermion potential

$$U_\sigma(\mathbf{q}, i\omega_n) \equiv -\frac{\hbar^2 S}{N} \left[ \frac{J_\mu^L(\mathbf{q})J_\mu^R(\mathbf{q})}{-\sigma i\hbar\omega_n + \varepsilon_{\mathbf{q}}} + \frac{J_\nu^L(\mathbf{q})J_\nu^R(\mathbf{q})}{\sigma i\hbar\omega_n + \varepsilon_{\mathbf{q}}} \right] \quad (6)$$

to the effective action, where $N$ is the total number of spin sites in the antiferromagnet. We assume the two magnetic interfaces are uncompensated, *i.e.* each interface is only with one of the antiferromagnetic sublattices [25, 61, 62] as shown in Fig. 1. We compute that the coupling constants $J_{\mu,\nu}^{L,R}(\mathbf{q})$ describing the effective exchange coupling strength between the spin of the fermions in reservoirs $L, R$ to the spin of the eigenmagnons $\mu_{\mathbf{q}}, \nu_{\mathbf{q}}$ are $J_\mu^{L/R}(\mathbf{q}) = v_{\mathbf{q}} J_B^{L/R}(\mathbf{r}_{L/R}) - u_{\mathbf{q}} J_A^{L/R}(\mathbf{r}_{L/R})$ and $J_\nu^{L/R}(\mathbf{q}) = v_{\mathbf{q}} J_A^{L/R}(\mathbf{r}_{L/R}) - u_{\mathbf{q}} J_B^{L/R}(\mathbf{r}_{L/R})$. Since each interface is with only one sublattice, $J_\mu^L(\mathbf{q}) = -u_{\mathbf{q}} J_A^L$ if the left interface is with sublattice $A$, and $J_\mu^L(\mathbf{q}) = v_{\mathbf{q}} J_B^L$ if the left

interface is with sublattice $B$. We get analogous results for the right interface. We see that the effective coupling constants $J_{\mu,\nu}^{L,R}(\mathbf{q})$ can have the same or opposite sign as the coupling constants $J_{A,B}^{L,R}$ depending on which sublattice is at the interface. This has to do with the spin projection of the eigenmagnon relative to the equilibrium spin direction of the sublattice at the interface. The effective coupling constants $J_{\mu,\nu}^{L,R}(\mathbf{q})$ are also enhanced by a Bogoliubov coefficient $u_{\mathbf{q}}$ or $v_{\mathbf{q}}$ with respect to the coupling constants $J_{A,B}^{L,R}$. These are typically large numbers. For $\mathbf{q} = \mathbf{0}$ we have $u_{\mathbf{0}} \approx v_{\mathbf{0}} \approx 2^{-3/4} \times (\omega_E/\omega_\parallel)^{1/4}$ to lowest order in the small ratio $\omega_\parallel/\omega_E$. The enhancement is due to large spin fluctuations at each sublattice of the antiferromagnet per eigenmagnon in the system, since the eigenmagnons are squeezed states [9, 63].

By studying Eq. (6), we note that we have $\text{Re}[U_\sigma(\mathbf{q}, i\omega_n)] < 0$ for identical uncompensated interfaces, whereas for a system where one of the interfaces is with sublattice $A$ and the other with sublattice $B$, we have $\text{Re}[U_\sigma(\mathbf{q}, i\omega_n)] > 0$. Consequentially, this allows us to control whether the magnon-mediated interlayer-fermion potential $U_\sigma(\mathbf{q}, i\omega_n)$ is attractive or repulsive by designing the interfaces. Whether this potential is attractive or repulsive can depend on a single atomic layer. This allows for an unprecedented high degree of control and tunability of the interlayer-fermion interactions. The sign difference of the potential can be explained by how the two fermions coupled by the magnon interact with the eigenmagnon spin. For $\text{Re}[U_\sigma(\mathbf{q}, i\omega_n)] < 0$ we have processes where the fermions couple symmetrically to the magnon spin, *i.e.* both fermions couple either ferromagnetically or antiferromagnetically to its spin. On the other hand, for $\text{Re}[U_\sigma(\mathbf{q}, i\omega_n)] > 0$ we have an asymmetric coupling, where one fermion couples ferromagnetically to the eigenmagnon spin and the other fermion couples antiferromagnetically to the eigenmagnon spin.

*Indirect exciton condensation.*—We will now study spontaneous condensation of spatially-indirect excitons where the attraction is mediated by the antiferromagnetic magnons. We consider the left (right) reservoir to be an n-doped (p-doped) semiconductor. We describe the semiconductors by the Hamiltonian

$$\mathcal{H}_{\text{el}}(\tau) = \sum_{j=L,R} \sum_{\mathbf{k}} \sum_{\sigma=\uparrow,\downarrow} \epsilon_j(\mathbf{k})\psi_{\sigma,j}^\dagger(\mathbf{k}, \tau)\psi_{\sigma,j}(\mathbf{k}, \tau), \quad (7)$$

with $\epsilon_L(\mathbf{k}) = -\epsilon_R(\mathbf{k}) = \hbar^2 k^2/(2m) - \epsilon_F \equiv \epsilon(\mathbf{k})$. Here $m$ is the effective electron and hole mass, which we assume to be equal, and $\epsilon_F$ is the Fermi level. While the operator $\psi_{\sigma,L/R}^\dagger$ creates an electron with spin $\sigma$ in the left/right layer, we note that due to the negative dispersion in the right layer the excitations in this layer are effectively described by electron holes. We also note that we have not included a Coulomb interaction between the electron and the holes in our model. The effect of the Coulomb potential on indirect exciton condensation has been widely studied in previous literature [64]. We will later argue why the magnon-mediated potential is expected to cooperate with the Coulomb potential in the case of indirect exciton condensation.

The interaction in Eq. (5) is too complicated for us to solve

for the exciton condensation. We then do an approximation similar to the Bardeen–Cooper–Schrieffer (BCS) theory of superconductivity [65, 66], and assume that the dominant contribution to the interaction arises when the excitons have zero net momentum ($\boldsymbol{k} + \boldsymbol{k}' = \boldsymbol{q}$), and similarly for the Matsubara frequencies ($i\nu_l + i\nu_m = i\omega_n$). Next, we introduce the order parameter

$$\Delta_\sigma(\boldsymbol{k}, i\nu_m) \equiv -\sum_n \sum_{\boldsymbol{k}'} U_\sigma(\boldsymbol{k} - \boldsymbol{k}', i\nu_m - i\nu_n)$$
$$\times \psi^*_{\sigma,R}(\boldsymbol{k}', i\nu_n)\psi_{\sigma,L}(\boldsymbol{k}', i\nu_n) \qquad (8)$$

and its Hermitian conjugate, and perform a Hubbard–Stratonovich transformation of the effective action. By doing a saddle-point approximation and integrating over the fermionic fields [60], we then obtain the gap equation

$$\Delta_{-\sigma}(\boldsymbol{k}', i\nu_n) = \sum_m \sum_{\boldsymbol{k}} \beta^{-1} U_\sigma(\boldsymbol{k} - \boldsymbol{k}', i\nu_m - i\nu_n)$$
$$\times \frac{\Delta_\sigma(\boldsymbol{k}, i\nu_m)}{|\Delta_\sigma(\boldsymbol{k}, i\nu_m)|^2 + \epsilon(\boldsymbol{k})^2 + (\hbar\nu_m)^2} . \qquad (9)$$

We note that the magnon-mediated potential is attractive when $U_\sigma(\boldsymbol{q}, i\omega_n) > 0$ in the case of indirect exciton condensation, which can be seen from rearranging the fermionic fields in Eq. (5).

We now use Eq. (9) to find an analytical expression for the critical temperature $T_c$ below which the excitons spontaneously form a condensate. To obtain an analytical solution, we focus on the case when the gap functions and the magnon-mediated potential are independent of momentum and frequency. This corresponds to an instantaneous contact interaction, and we therefore assume that the gap functions have an $s$-wave pairing. Moreover, we see that the gap equation in Eq. (9) only has a solution when $\Delta_\sigma$ and $\Delta_{-\sigma}$ have the same sign. In the case where spin-degeneracy is unbroken, it is fair to assume that $\Delta_\sigma = \Delta_{-\sigma}$, indicating triplet-like pairing. In superconductivity, $s$-wave and triplet pairing are mutually exclusive for even frequency order parameters, but in the case of indirect excitons the same symmetry restrictions on the order parameter do not apply, as the composite boson does not consist of identical particles. In other words, for indirect excitons the symmetries in momentum space and spin space are decoupled from one another. As both the magnon-mediated potential and the Coulomb potential are in the $s$-wave channel and the Coulomb potential is independent of spin, the magnon-mediated potential works together with the Coulomb potential enhancing the attractive exciton pairing interaction. The fact that we can design whether the magnon-mediated potential is attractive or repulsive allows us to control which spin channel is the most favorable for the excitons to condensate.

To determine $T_c$ we perform a BCS-like calculation [60, 66] and restrict the sum over Matsubara frequencies to a thin shell around the Fermi level ($|\hbar\nu_m| < \varepsilon_0$), where the magnon-mediated potential is attractive. The analytical expression for

$T_c$ is found to be

$$T_c = \frac{2e^{\gamma_{EM}}\varepsilon_0}{\pi k_B} \exp\left(-\frac{2\pi\varepsilon_0}{Su_0 v_0 ma^2 J_A^L J_B^R}\right), \qquad (10)$$

where $\gamma_{EM} \approx 0.577$ is the Euler–Mascheroni constant and $a$ the lattice constant of the semiconductors. Here we have assumed that the left and right magnetic interfaces consist of opposite sublattices. This leads to an attractive exciton interaction. If we assume the exchange energy among the spins in the bulk is much larger than the interface coupling ($\hbar\omega_E \gg Sma^2 J_A^L J_B^R$), the value of the anisotropy that maximizes $T_c$ is

$$\hbar\omega_\parallel^{(opt)} \equiv \frac{Sma^2 J_A^L J_B^R}{16\pi} . \qquad (11)$$

The full dependence of $T_c$ on the magnetic anisotropy is shown in Fig. 2. The critical temperature for indirect exciton condensation is largest for a nonzero and finite magnetic anisotropy. This is because in the limit $\omega_\parallel \to 0$ the magnon gap in the antiferromagnetic insulator vanishes, and consequentially so does the thin shell around the Fermi level where the magnon-mediated potential is attractive. In the case of a large anisotropy, $\omega_\parallel \gg \omega_\parallel^{(opt)}$, the enhancement of the magnon-mediated potential due to magnon squeezing is lost [63]. When the anisotropy takes on its optimal value, the critical temperature becomes

$$T_c^{(opt)} \equiv \frac{\sqrt{\hbar\omega_E Sma^2 J_A^L J_B^R}}{\sqrt{2}\pi^{3/2} k_B} e^{\gamma_{EM}-1/2} . \qquad (12)$$

Notably, we see that the critical temperature increases monotonously with increasing strength of the exchange interaction $\hbar\omega_E$. The optimal choice of an antiferromagnetic insulator would then be a material with a magnetic anisotropy ($\hbar\omega_\parallel$) on an energy scale proportional to the exchange coupling at the interface ($\hbar J_{A,B}^{L,R}$), and a very strong exchange interaction in the bulk of the antiferromagnetic insulator ($\hbar\omega_E$).

To show how high the $T_c$ of indirect exciton condensation in our model can be using only the magnon-mediated interaction,
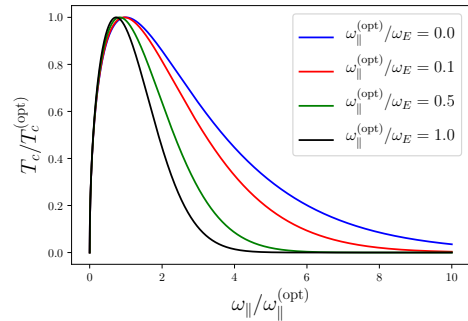


Figure 2. Dependence of the normalized critical temperature on the strength of the normalized magnetic anisotropy.

we give a numerical estimate for realistic material parameters. Using the parameters $S = 1$, $m$ equal the electron mass, $a = 5\,\text{Å}$, $\hbar J_A^L = \hbar J_B^R = 10\,\text{meV}$ [7], $\omega_E = 8.6 \cdot 10^{13}\,\text{s}^{-1}$ [67], and assuming the magnetic anisotropy takes on its optimal value $\omega_\parallel^{\text{(opt)}} = 9.9 \cdot 10^9\,\text{s}^{-1}$, we obtain a $T_c^{\text{(opt)}}$ of approximately 7 K. Antiferromagnetic insulators that can be suitable for the proposed experiment are $Cr_2O_3$ [61], $\alpha$-$Fe_2O_3$ [29], and NiO [67]. In comparison, a recent experiment studying double bilayer graphene in the quantum Hall regime found the Coulomb-mediated exciton condensation to have an activation energy of $\sim 8\,\text{K}$ [51], which was ten times higher than what was found in an experiment using GaAs [68]. This demonstrates that the potential mediated by the antiferromagnetic magnons is capable of creating strong correlations between the electrons and holes that could significantly increase the critical temperature for condensation compared to when the excitons are just bound through the Coulomb interaction.

---

* oyvinjoh@ntnu.no

[1] H. Suhl, "Simultaneous onset of ferromagnetism and superconductivity," Phys. Rev. Lett. 87, 167007 (2001).

[2] N. Karchev, "Magnon exchange mechanism of ferromagnetic superconductivity," Phys. Rev. B 67, 054416 (2003).

[3] H. Funaki and H. Shimahara, "Odd- and even-frequency superconductivities mediated by ferromagnetic magnons," J. Phys. Soc. Jpn. 83, 123704 (2014).

[4] R. Kar, T. Goswami, B. C. Paul, and A. Misra, "On magnon mediated Cooper pair formation in ferromagnetic superconductors," AIP Advances 4, 087126 (2014).

[5] M. Kargarian, D. K. Efimkin, and V. Galitski, "Amperean pairing at the surface of topological insulators," Phys. Rev. Lett. 117, 076806 (2016).

[6] X. Gong, M. Kargarian, A. Stern, D. Yue, H. Zhou, X. Jin, V. M. Galitski, V. M. Yakovenko, and J. Xia, "Time-reversal symmetry-breaking superconductivity in epitaxial bismuth/nickel bilayers," Science Advances 3 (2017), 10.1126/sciadv.1602579.

[7] N. Rohling, E. L. Fjærbu, and A. Brataas, "Superconductivity induced by interfacial coupling to magnons," Phys. Rev. B 97, 115401 (2018).

[8] H. G. Hugdal, S. Rex, F. S. Nogueira, and A. Sudbø, "Magnon-induced superconductivity in a topological insulator coupled to ferromagnetic and antiferromagnetic insulators," Phys. Rev. B 97, 195438 (2018).

[9] E. Erlandsen, A. Kamra, A. Brataas, and A. Sudbø, "Enhancement of superconductivity mediated by antiferromagnetic squeezed magnons," arXiv (2019), arXiv:1903.01470v2.

[10] E. L. Fjærbu, N. Rohling, and A. Brataas, "Superconductivity at metal-antiferromagnetic insulator interfaces," arXiv (2019), arXiv:1904.00233.

[11] T. Jungwirth, X. Marti, P. Wadley, and J. Wunderlich, "Antiferromagnetic spintronics," Nat. Nanotechnol. 11, 231 (2016).

[12] V. Baltz, A. Manchon, M. Tsoi, T. Moriyama, T. Ono, and Y. Tserkovnyak, "Antiferromagnetic spintronics," Rev. Mod. Phys. 90, 015005 (2018).

[13] Y. Tserkovnyak, A. Brataas, and G. E. W. Bauer, "Enhanced Gilbert damping in thin ferromagnetic films," Phys. Rev. Lett. 88, 117601 (2002).

[14] M. P. Ross, Spin Dynamics in an Antiferromagnet, Ph.D. thesis, Technische Universität München (2013).

[15] R. Cheng, J. Xiao, Q. Niu, and A. Brataas, "Spin pumping and spin-transfer torques in antiferromagnets," Phys. Rev. Lett. 113, 057601 (2014).

[16] S. Takei, B. I. Halperin, A. Yacoby, and Y. Tserkovnyak, "Superfluid spin transport through antiferromagnetic insulators," Phys. Rev. B 90, 094408 (2014).

[17] P. Ross, M. Schreier, J. Lotze, H. Huebl, R. Gross, and S. T. B. Goennenwein, "Antiferromagentic resonance detected by direct current voltages in $MnF_2$/Pt bilayers," J. Appl. Phys. 118, 233907 (2015).

[18] Ø. Johansen and A. Brataas, "Spin pumping and inverse spin Hall voltages from dynamical antiferromagnets," Phys. Rev. B 95, 220408 (2017).

[19] A. Kamra and W. Belzig, "Spin pumping and shot noise in ferrimagnets: Bridging ferro- and antiferromagnets," Phys. Rev. Lett. 119, 197201 (2017).

[20] R. Cheng, D. Xiao, and A. Brataas, "Terahertz antiferromagnetic spin Hall nano-oscillator," Phys. Rev. Lett. 116, 207603 (2016).

[21] V. Sluka, "Antiferromagnetic resonance excited by oscillating electric currents," Phys. Rev. B 96, 214412 (2017).

[22] Ø. Johansen, H. Skarsvåg, and A. Brataas, "Spin-transfer antiferromagnetic resonance," Phys. Rev. B 97, 054423 (2018).

[23] J. H. Han, C. Song, F. Li, Y. Y. Wang, G. Y. Wang, Q. H. Yang, and F. Pan, "Antiferromagnet-controlled spin current transport in $SrMnO_3$/Pt hybrids," Phys. Rev. B 90, 144431 (2014).

[24] D. Hou, Z. Qiu, J. Barker, K. Sato, K. Yamamoto, S. Vélez, J. M. Gomez-Perez, L. E. Hueso, F. Casanova, and E. Saitoh, "Tunable sign change of spin Hall magnetoresistance in Pt/NiO/YIG structures," Phys. Rev. Lett. 118, 147202 (2017).

[25] G. R. Hoogeboom, A. Aqeel, T. Kuschel, T. T. M. Palstra, and B. J. van Wees, "Negative spin Hall magnetoresistance of Pt on the bulk easy-plane antiferromagnet NiO," Appl. Phys. Lett. 111, 052409 (2017).

[26] A. Manchon, "Spin Hall magnetoresistance in antiferromagnet/normal metal bilayers," Phys. Status Solidi RRL 11, 1600409 (2017).

[27] J. Fischer, O. Gomonay, R. Schlitz, K. Ganzhorn, N. Vlietstra, M. Althammer, H. Huebl, M. Opel, R. Gross, S. T. B. Goennenwein, and S. Geprägs, "Spin Hall magnetoresistance in antiferromagnet/heavy-metal heterostructures," Phys. Rev. B 97, 014417 (2018).

[28] L. Baldrati, A. Ross, T. Niizeki, C. Schneider, R. Ramos, J. Cramer, O. Gomonay, M. Filianina, T. Savchenko, D. Heinze, A. Kleibert, E. Saitoh, J. Sinova, and M. Kläui, "Full angular dependence of the spin Hall and ordinary magnetoresistance in epitaxial antiferromagnetic NiO(001)/Pt thin films," Phys. Rev. B 98, 024422 (2018).

[29] R. Lebrun, A. Ross, S. A. Bender, A. Qaiumzadeh, L. Baldrati, J. Cramer, A. Brataas, R. A. Duine, and M. Kläui, "Tunable long-distance spin transport in a crystalline antiferromagnetic iron oxide," Nature 561, 222–225 (2018).

[30] D. A. Bonn, "Are high-temperature superconductors exotic?" Nat. Phys. 2, 159 (2006).

[31] "Towards a complete theory of high $T_c$," Nat. Phys. 2, 138 (2006).

[32] G. H. Wannier, "The structure of electronic excitation levels in insulating crystals," Phys. Rev. 52, 191–197 (1937).

[33] J. M. Blatt, K. W. Böer, and W. Brandt, "Bose-Einstein condensation of excitons," Phys. Rev. 126, 1691–1692 (1962).

[34] R. C. Casella, "A criterion for exciton binding in dense electron—hole systems—application to line narrowing observed in GaAs," J. Appl. Phys. 34, 1703–1705 (1963).

[35] K. E. O'Hara, L. Ó Súilleabháin, and J. P. Wolfe, "Strong nonradiative recombination of excitons in Cu$_2$O and its impact on Bose-Einstein statistics," Phys. Rev. B 60, 10565–10568 (1999).

[36] V. I. Klimov, A. A. Mikhailovsky, D. W. McBranch, C. A. Leatherdale, and M. G. Bawendi, "Quantization of multiparticle Auger rates in semiconductor quantum dots," Science 287, 1011–1013 (2000).

[37] F. Wang, G. Dukovic, E. Knoesel, L. E. Brus, and T. F. Heinz, "Observation of rapid Auger recombination in optically excited semiconducting carbon nanotubes," Phys. Rev. B 70, 241403 (2004).

[38] F. Wang, Y. Wu, M. S. Hybertsen, and T. F. Heinz, "Auger recombination of excitons in one-dimensional systems," Phys. Rev. B 73, 245424 (2006).

[39] Y. E. Lozovik and V. I. Yudson, "Feasibility of superfluidity of paired spatially separated electrons and holes; a new superconductivity mechanism," JETP Lett. 22 (1975).

[40] Y. E. Lozovik and V. I. Yudson, "Superconductivity at dielectric pairing of spatially separated quasiparticles," Solid State Commun. 19, 391 – 393 (1976).

[41] Y. E. Lozovik and V. I. Yudson, "Electron—hole superconductivity. Influence of structure defects," Solid State Commun. 21, 211 – 215 (1977).

[42] E. Tutuc, M. Shayegan, and D. A. Huse, "Counterflow measurements in strongly correlated GaAs hole bilayers: Evidence for electron-hole pairing," Phys. Rev. Lett. 93, 036802 (2004).

[43] M. Kellogg, J. P. Eisenstein, L. N. Pfeiffer, and K. W. West, "Vanishing Hall resistance at high magnetic field in a double-layer two-dimensional electron system," Phys. Rev. Lett. 93, 036801 (2004).

[44] D. Nandi, A. D. K. Finck, J. P. Eisenstein, L. N. Pfeiffer, and K. W. West, "Exciton condensation and perfect Coulomb drag," Nature 488, 481 (2012).

[45] I. B. Spielman, J. P. Eisenstein, L. N. Pfeiffer, and K. W. West, "Resonantly enhanced tunneling in a double layer quantum Hall ferromagnet," Phys. Rev. Lett. 84, 5808–5811 (2000).

[46] I. B. Spielman, J. P. Eisenstein, L. N. Pfeiffer, and K. W. West, "Observation of a linearly dispersing collective mode in a quantum Hall ferromagnet," Phys. Rev. Lett. 87, 036803 (2001).

[47] J. P. Eisenstein and A. H. MacDonald, "Bose-Einstein condensation of excitons in bilayer electron systems," Nature 432, 691 (2004).

[48] R. D. Wiersma, J. G. S. Lok, S. Kraus, W. Dietsche, K. von Klitzing, D. Schuh, M. Bichler, H.-P. Tranitz, and W. Wegscheider, "Activated transport in the separate layers that form the $\nu_T = 1$ exciton condensate," Phys. Rev. Lett. 93, 266805 (2004).

[49] J.P. Eisenstein, "Exciton condensation in bilayer quantum Hall systems," Annu. Rev. Condens. Matter Phys. 5, 159–181 (2014).

[50] J. I. A. Li, T. Taniguchi, K. Watanabe, J. Hone, and C. R. Dean, "Excitonic superfluid phase in double bilayer graphene," Nat. Phys. 13, 751 (2017).

[51] X. Liu, K. Watanabe, T. Taniguchi, B. I. Halperin, and P. Kim, "Quantum Hall drag of exciton condensate in graphene," Nat. Phys. 13, 746 (2017).

[52] G. W. Burg, N. Prasad, K. Kim, T. Taniguchi, K. Watanabe, A. H. MacDonald, L. F. Register, and E. Tutuc, "Strongly enhanced tunneling at total charge neutrality in double-bilayer graphene-WSe$_2$ heterostructures," Phys. Rev. Lett. 120, 177702 (2018).

[53] T. Holstein and H. Primakoff, "Field dependence of the intrinsic domain magnetization of a ferromagnet," Phys. Rev. 58, 1098–1113 (1940).

[54] C. Zener, "Interaction between the $d$ shells in the transition metals," Phys. Rev. 81, 440–444 (1951).

[55] T. Kasuya, "A Theory of Metallic Ferro- and Antiferromagnetism on Zener's Model," Prog. Theor. Phys. 16, 45–57 (1956).

[56] S Takahashi, E Saitoh, and S Maekawa, "Spin current through a normal-metal/insulating-ferromagnet junction," Journal of Physics: Conference Series 200, 062030 (2010).

[57] Y. Kajiwara, K. Harii, S. Takahashi, J. Ohe, K. Uchida, M. Mizuguchi, H. Umezawa, H. Kawai, K. Ando, K. Takanashi, S. Maekawa, and E. Saitoh, "Transmission of electrical signals by spin-wave interconversion in a magnetic insulator," Nature 464, 262 (2010).

[58] S. S.-L. Zhang and S. Zhang, "Spin convertance at magnetic interfaces," Phys. Rev. B 86, 214424 (2012).

[59] S. A. Bender and Y. Tserkovnyak, "Interfacial spin and heat transfer between metals and magnetic insulators," Phys. Rev. B 91, 140402 (2015).

[60] See the Supplemental Material, which includes Ref. [69], for the full derivation of the effective potential, gap equation, and critical temperature.

[61] X. He, Y. Wang, N. Wu, A. N. Caruso, E. Vescovo, K. D. Belashchenko, P. A. Dowben, and C. Binek, "Robust isothermal electric control of exchange bias at room temperature," Nat. Mater. 9, 579 (2010).

[62] A. Kamra, A. Rezaei, and W. Belzig, "Spin splitting induced in a superconductor by an antiferromagnetic insulator," Phys. Rev. Lett. 121, 247702 (2018).

[63] A. Kamra, E. Thingstad, G. Rastelli, R. A. Duine, A. Brataas, W. Belzig, and A Sudbø, "Antiferromagnetic Magnons as Highly Squeezed Fock States underlying Quantum Correlations," arXiv (2019), arXiv:1904.04553.

[64] D. V. Fil and S. I. Shevchenko, "Electron-hole superconductivity (review)," Low Temp. Phys. 44, 867–909 (2018).

[65] J. Bardeen, L. N. Cooper, and J. R. Schrieffer, "Microscopic theory of superconductivity," Phys. Rev. 106, 162–164 (1957).

[66] N. Kopnin, Theory of Nonequilibrium Superconductivity, International Series of Monographs on Physics (Clarendon Press, 2001).

[67] T. Satoh, S.-J. Cho, R. Iida, T. Shimura, K. Kuroda, H. Ueda, Y. Ueda, B. A. Ivanov, F. Nori, and M. Fiebig, "Spin oscillations in antiferromagnetic NiO triggered by circularly polarized light," Phys. Rev. Lett. 105, 077402 (2010).

[68] M. Kellogg, I. B. Spielman, J. P. Eisenstein, L. N. Pfeiffer, and K. W. West, "Observation of quantized Hall drag in a strongly correlated bilayer electron system," Phys. Rev. Lett. 88, 126804 (2002).

[69] P. Coleman, Introduction to Many-Body Physics (Cambridge University Press, 2015).

# "Magnon-Mediated Indirect Exciton Condensation through Antiferromagnetic Insulators"

Øyvind Johansen,[1, *] Akashdeep Kamra,[1] Camilo Ulloa,[2] Arne Brataas,[1] and Rembert A. Duine[1, 2, 3]

[1]*Center for Quantum Spintronics, Department of Physics,*
*Norwegian University of Science and Technology, NO-7491 Trondheim, Norway*
[2]*Institute for Theoretical Physics, Utrecht University, Princetonplein 5, 3584 CC Utrecht, the Netherlands*
[3]*Department of Applied Physics, Eindhoven University of Technology,*
*P.O. Box 513, 5600 MB Eindhoven, The Netherlands*
(Dated: July 26, 2019)

## I. INTERACTING SYSTEM

In these notes we will consider a trilayer system consisting of an antiferromagnetic insulator (AFI) sandwiched between two fermion reservoirs (FR|AFI|FR). The magnons in the AFI effectively couple the fermions in the different reservoirs. Here we aim to calculate the magnon-mediated effective interaction between the reservoirs mediated by the magnons by using the path integral formalism.

### One interface

Let us first analyze a single fermion reservoir placed at the interface of an AFI. We will later generalize our calculation to the trilayer system. The Hamiltonian consists of three contributions,

$$\mathcal{H} = \mathcal{H}_{\text{el}} + \mathcal{H}_{\text{mag}} + \mathcal{H}_{\text{int}}, \tag{1}$$

where the first two terms describe the fermions in the reservoir and the magnons in the AFI, respectively. The interfacial coupling between the fermions and magnons is expressed by the *s-d* exchange interaction

$$\mathcal{H}_{\text{int}} = -\sum_{j=A,B} \sum_{i \in \mathcal{A}_j} J_j(\boldsymbol{r}_i) \, \hat{\boldsymbol{\rho}}(\boldsymbol{r}_i) \cdot \boldsymbol{S}(\boldsymbol{r}_i) \,. \tag{2}$$

Here $\mathcal{A}_{A(B)}$ is the cross section of the interface with sublattice $A$ ($B$). The interfacial exchange coupling constant $J_{A/B}(\boldsymbol{r}_i)$ is defined as

$$J_j(\boldsymbol{r}_i) = \begin{cases} J_j, & \text{if } \boldsymbol{r}_i \in \mathcal{A}_j \\ 0, & \text{otherwise} \end{cases} \,, \tag{3}$$

and

$$\hat{\boldsymbol{\rho}}(\boldsymbol{r}_i) = \frac{1}{2} \sum_{\sigma,\sigma'} \psi_\sigma^\dagger(\boldsymbol{r}_i) \boldsymbol{\sigma}_{\sigma\sigma'} \psi_{\sigma'}(\boldsymbol{r}_i) \tag{4}$$

denotes the spin density. Here $\psi_\sigma^\dagger$ ($\psi_\sigma$) creates (annihilates) a fermion with spin $\sigma$, and $\boldsymbol{\sigma} = (\sigma_x, \sigma_y, \sigma_z)$ is a vector of Pauli matrices given by

$$\sigma_x = \begin{pmatrix} 0 & 1 \\ 1 & 0 \end{pmatrix}, \quad \sigma_y = \begin{pmatrix} 0 & -i \\ i & 0 \end{pmatrix}, \quad \sigma_z = \begin{pmatrix} 1 & 0 \\ 0 & -1 \end{pmatrix}. \tag{5}$$

The direction of the spin $\boldsymbol{S}$ appearing in Eq. (2) depends on the sublattice of the antiferromagnet. We perform a Holstein–Primakoff transformation (HPT) of the spin operators in each sublattice, which for a small number of magnons ($\langle a_i^\dagger a_i \rangle$, $\langle b_i^\dagger b_i \rangle \ll 2S$) yields

$$S_{i,A}^x = \frac{\hbar\sqrt{2S}}{2}\left(a_i^\dagger + a_i\right), \quad S_{i,A}^y = \frac{\hbar\sqrt{2S}}{2i}\left(a_i^\dagger - a_i\right), \quad S_{i,A}^z = \hbar\left(a_i^\dagger a_i - S\right), \tag{6a}$$

$$S_{i,B}^x = \frac{\hbar\sqrt{2S}}{2}\left(b_i^\dagger + b_i\right), \quad S_{i,B}^y = \frac{\hbar\sqrt{2S}}{2i}\left(b_i - b_i^\dagger\right), \quad S_{i,B}^z = \hbar\left(S - b_i^\dagger b_i\right). \tag{6b}$$

---

[*] oyvinjoh@ntnu.no

We use the HPT in Eq. (6a) if $\boldsymbol{r}_i$ lies in sublattice $A$, and the HPT in Eq. (6b) if $\boldsymbol{r}_i$ lies in sublattice $B$. The interaction Hamiltonian at the AFI|FR interface can then be written as $\mathcal{H}_{\text{int}} = \mathcal{H}_{\text{int}}^A + \mathcal{H}_{\text{int}}^B$, where

$$\mathcal{H}_{\text{int}}^A = -J_A \sum_{i \in \mathcal{A}_A} \left[ \frac{\hbar\sqrt{2S}}{2} \left( \psi_\uparrow^\dagger \psi_\downarrow a + \psi_\downarrow^\dagger \psi_\uparrow a^\dagger \right) + \frac{\hbar}{2} \left( \psi_\uparrow^\dagger \psi_\uparrow - \psi_\downarrow^\dagger \psi_\downarrow \right) \left( a^\dagger a - S \right) \right], \tag{7a}$$

$$\mathcal{H}_{\text{int}}^B = -J_B \sum_{i \in \mathcal{A}_B} \left[ \frac{\hbar\sqrt{2S}}{2} \left( \psi_\uparrow^\dagger \psi_\downarrow b^\dagger + \psi_\downarrow^\dagger \psi_\uparrow b \right) - \frac{\hbar}{2} \left( \psi_\uparrow^\dagger \psi_\uparrow - \psi_\downarrow^\dagger \psi_\downarrow \right) \left( b^\dagger b - S \right) \right], \tag{7b}$$

and we are summing over the part of the sublattice cross section $\mathcal{A}_{A/B}$ of sublattice $A/B$ that is in contact with the reservoir of fermions described by $\psi$. Note that the operators $\psi$, $a$ and $b$ have an implicit site index $i$. The interaction Hamiltonian $\mathcal{H}_{\text{int}}$ depends on the interface structure of the antiferromagnetic insulator. In general, we can express the interaction Hamiltonian as

$$\mathcal{H}_{\text{int}} = - \sum_{i \in (\mathcal{A}_A + \mathcal{A}_B)} \left\{ \frac{\hbar\sqrt{2S}}{2} \left[ \psi_\uparrow^\dagger \psi_\downarrow \left( J_A(\boldsymbol{r}_i)a + J_B(\boldsymbol{r}_i)b^\dagger \right) \psi_\downarrow^\dagger \psi_\uparrow \left( J_A(\boldsymbol{r}_i)a^\dagger + J_B(\boldsymbol{r}_i)b \right) \right] \right.$$
$$\left. + \frac{\hbar}{2} \left( \psi_\uparrow^\dagger \psi_\uparrow - \psi_\downarrow^\dagger \psi_\downarrow \right) \times \left[ J_A(\boldsymbol{r}_i)a^\dagger a - J_B(\boldsymbol{r}_i)b^\dagger b + (J_B(\boldsymbol{r}_i) - J_A(\boldsymbol{r}_i)) S \right] \right\}, \tag{8}$$

where the sum now runs over the entire reservoir interface. The interface structure is now encoded in the spatial dependence of the interfacial coupling constants $J_{A,B}(\boldsymbol{r}_i)$. From here on we omit the explicit notation of the $\boldsymbol{r}$ dependence of the coupling constants $J_{A,B}(\boldsymbol{r}_i)$. In our notation, $J_{A,B}$ depends on $\boldsymbol{r}_i$ if it is inside the sum, and it is constant if it is outside the sum.

## II. PATH INTEGRAL

### A. One interface

Now we calculate the coherent state integral in imaginary time

$$\mathcal{Z} = \int \mathcal{D}\psi \mathcal{D}\psi^* \mathcal{D}\mu \mathcal{D}\mu^* \mathcal{D}\nu \mathcal{D}\nu^* \exp\left(-\mathcal{S}/\hbar\right). \tag{9}$$

where we have introduced the eigenstates $\mu$ and $\nu$ which diagonalize the two-sublattice magnetic Hamiltonian. The dependence of these eigenstates on the Holstein–Primakoff magnons $a$ and $b$ will be discussed in the following section. The action of the bilayer system is $\mathcal{S} = \mathcal{S}_{\text{el}} + \mathcal{S}_{\text{mag}} + \mathcal{S}_{\text{int}}$, with

$$\mathcal{S}_{\text{el}} = \int_0^{\hbar\beta} d\tau \left[ \hbar \sum_i \sum_\sigma \psi_\sigma^*(\boldsymbol{r}_i, \tau)\dot{\psi}_\sigma(\boldsymbol{r}_i, \tau) + \mathcal{H}_{\text{el}} \right], \tag{10a}$$

$$\mathcal{S}_{\text{mag}} = \int_0^{\hbar\beta} d\tau \left[ \hbar \sum_i \sum_{\eta=\mu,\nu} \eta^*(\boldsymbol{r}_i, \tau)\dot{\eta}(\boldsymbol{r}_i, \tau) + \mathcal{H}_{\text{mag}} \right], \tag{10b}$$

$$\mathcal{S}_{\text{int}} = \int_0^{\hbar\beta} d\tau \quad \mathcal{H}_{\text{int}}, \tag{10c}$$

where $\dot{\eta} = \partial\eta/\partial\tau$, $\tau = it$ ($t$ being real time), and $\beta = 1/(k_B T)$ with $k_B$ being the Boltzmann constant and $T$ the temperature. Note that from now on $\psi^{(*)}$ are Grassman variables such that $\psi^{(\dagger)} = \psi^{(*)}$, and $\{\mu^{(*)}, \nu^{(*)}, a^{(*)}, b^{(*)}\}$ are complex numbers. We treat the interaction term as a perturbation and perform an expansion up to second order in the interaction term of the action

$$\mathcal{Z} = \int \mathcal{D}^2\psi \mathcal{D}^2\mu \mathcal{D}^2\nu \exp\left(-\frac{\mathcal{S}_{\text{el}} + \mathcal{S}_{\text{mag}}}{\hbar}\right) \exp\left(-\frac{\mathcal{S}_{\text{int}}}{\hbar}\right) \approx \int \mathcal{D}^2\psi \mathcal{D}^2\mu \mathcal{D}^2\nu \exp\left(-\frac{\mathcal{S}_{\text{el}} + \mathcal{S}_{\text{mag}}}{\hbar}\right) \gamma_{\text{int}} \tag{11}$$

where $\gamma_{\text{int}} = 1 - \mathcal{S}_{\text{int}}/\hbar + (\mathcal{S}_{\text{int}}/\hbar)^2/2$. We from now on also use the shorthand notation $\mathcal{D}^2\psi = \mathcal{D}\psi\mathcal{D}\psi^*$ etc. The first order term in $\gamma_{\text{int}}$ that is linear in $\mathcal{S}_{\text{int}}$ is neglected, as all the processes in Eq. (8) are only between a single fermion and a magnon. Such processes to first order can therefore not mediate an interaction between two separate fermions, which are the processes we are interested in later on.
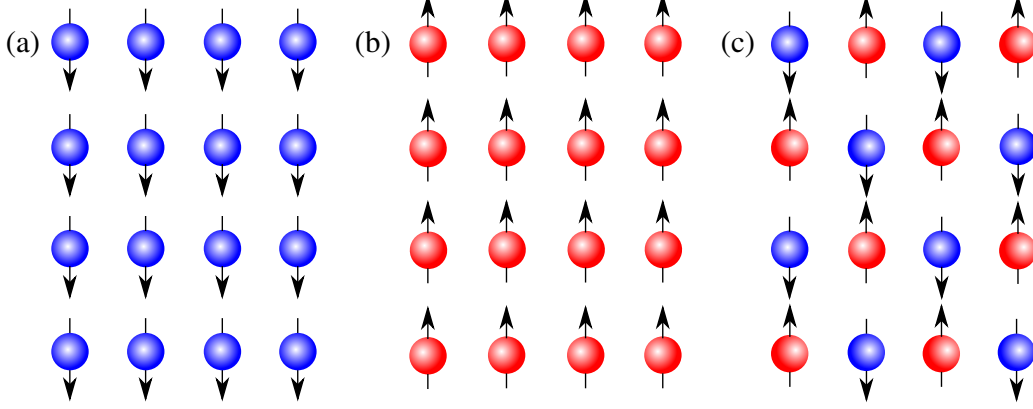
Figure 1. The spin structures of the atoms in the AFI in the plane closest to the fermion reservoir as seen from the fermion reservoir. (a) and (b) are fully uncompensated interfaces with sublattices $A$ and $B$ respectively, where only one of the sublattices is present at the interface. (c) is a compensated interface where both sublattices are present at the interface, in a chessboard pattern.

Let us now analyze the second order term, and evaluate

$$\mathcal{S}_{\text{int}}^2 = \int \mathrm{d}\tau \mathrm{d}\tau' \mathcal{H}_{\text{int}}(\tau) \mathcal{H}_{\text{int}}(\tau') . \tag{12}$$

We write $\psi_\sigma \equiv \psi_\sigma(\tau, \boldsymbol{r}_i)$ and $\underline{\psi}_\sigma \equiv \psi_\sigma(\tau', \boldsymbol{r}_j)$, and the same convention for $a$, $b$, and $J_{A,B}(\boldsymbol{r}_i)$. Let us first consider a general type of interface, and use $\mathcal{H}_{\text{int}}$ in (8). The interface structure is then encoded in the spatial dependencies of $J_{A,B}(\boldsymbol{r}_i)$. Note that the two limits of a fully uncompensated interface (either with sublattice $A$ or sublattice $B$, as defined in Fig. 1) can easily be recovered from the general expression by setting either $J_A$ or $J_B$ to zero. We then find

$$\mathcal{H}_{\text{int}}(\tau)\mathcal{H}_{\text{int}}(\tau') = \sum_{i,j \in (\mathcal{A}_A + \mathcal{A}_B)} \left[ \frac{\hbar^2 S}{2} \left( A_{AA} J_A \underline{J}_A + A_{AB} J_A \underline{J}_B + A_{BA} J_B \underline{J}_A + A_{BB} J_B \underline{J}_B \right) \right.$$
$$\left. + \frac{\hbar^2}{4} \left( B_{AA} J_A \underline{J}_A + B_{AB} J_A \underline{J}_B + B_{BA} J_B \underline{J}_A + B_{BB} J_B \underline{J}_B \right) \right], \tag{13}$$

where we have defined

$$A_{AA} = \psi_\uparrow^\dagger \psi_\downarrow \underline{\psi}_\uparrow^\dagger \underline{\psi}_\downarrow a\underline{a} + \psi_\uparrow^\dagger \psi_\downarrow \underline{\psi}_\downarrow^\dagger \underline{\psi}_\uparrow a\underline{a}^\dagger + \psi_\downarrow^\dagger \psi_\uparrow \underline{\psi}_\uparrow^\dagger \underline{\psi}_\downarrow a^\dagger \underline{a} + \psi_\downarrow^\dagger \psi_\uparrow \underline{\psi}_\downarrow^\dagger \underline{\psi}_\uparrow a^\dagger \underline{a}^\dagger , \tag{14a}$$

$$A_{AB} = \psi_\uparrow^\dagger \psi_\downarrow \underline{\psi}_\uparrow^\dagger \underline{\psi}_\downarrow a\underline{b}^\dagger + \psi_\uparrow^\dagger \psi_\downarrow \underline{\psi}_\downarrow^\dagger \underline{\psi}_\uparrow a\underline{b} + \psi_\downarrow^\dagger \psi_\uparrow \underline{\psi}_\uparrow^\dagger \underline{\psi}_\downarrow a^\dagger \underline{b}^\dagger + \psi_\downarrow^\dagger \psi_\uparrow \underline{\psi}_\downarrow^\dagger \underline{\psi}_\uparrow a^\dagger \underline{b} , \tag{14b}$$

$$A_{BA} = \psi_\uparrow^\dagger \psi_\downarrow \underline{\psi}_\uparrow^\dagger \underline{\psi}_\downarrow b^\dagger \underline{a} + \psi_\uparrow^\dagger \psi_\downarrow \underline{\psi}_\downarrow^\dagger \underline{\psi}_\uparrow b^\dagger \underline{a}^\dagger + \psi_\downarrow^\dagger \psi_\uparrow \underline{\psi}_\uparrow^\dagger \underline{\psi}_\downarrow b\underline{a} + \psi_\downarrow^\dagger \psi_\uparrow \underline{\psi}_\downarrow^\dagger \underline{\psi}_\uparrow b\underline{a}^\dagger , \tag{14c}$$

$$A_{BB} = \psi_\uparrow^\dagger \psi_\downarrow \underline{\psi}_\uparrow^\dagger \underline{\psi}_\downarrow b^\dagger \underline{b}^\dagger + \psi_\uparrow^\dagger \psi_\downarrow \underline{\psi}_\downarrow^\dagger \underline{\psi}_\uparrow b^\dagger \underline{b} + \psi_\downarrow^\dagger \psi_\uparrow \underline{\psi}_\uparrow^\dagger \underline{\psi}_\downarrow b\underline{b}^\dagger + \psi_\downarrow^\dagger \psi_\uparrow \underline{\psi}_\downarrow^\dagger \underline{\psi}_\uparrow b\underline{b} , \tag{14d}$$

$$B_{AA} = \left( \psi_\uparrow^\dagger \psi_\uparrow \underline{\psi}_\uparrow^\dagger \underline{\psi}_\uparrow - \psi_\uparrow^\dagger \psi_\uparrow \underline{\psi}_\downarrow^\dagger \underline{\psi}_\downarrow - \psi_\downarrow^\dagger \psi_\downarrow \underline{\psi}_\uparrow^\dagger \underline{\psi}_\uparrow + \psi_\downarrow^\dagger \psi_\downarrow \underline{\psi}_\downarrow^\dagger \underline{\psi}_\downarrow \right) \times \left( a^\dagger a \underline{a}^\dagger \underline{a} - S a^\dagger a - S \underline{a}^\dagger \underline{a} + S^2 \right) \tag{14e}$$

$$B_{AB} = \left( \psi_\uparrow^\dagger \psi_\uparrow \underline{\psi}_\uparrow^\dagger \underline{\psi}_\uparrow - \psi_\uparrow^\dagger \psi_\uparrow \underline{\psi}_\downarrow^\dagger \underline{\psi}_\downarrow - \psi_\downarrow^\dagger \psi_\downarrow \underline{\psi}_\uparrow^\dagger \underline{\psi}_\uparrow + \psi_\downarrow^\dagger \psi_\downarrow \underline{\psi}_\downarrow^\dagger \underline{\psi}_\downarrow \right) \times \left( -a^\dagger a \underline{b}^\dagger \underline{b} + S a^\dagger a + S \underline{b}^\dagger \underline{b} - S^2 \right) \tag{14f}$$

$$B_{BA} = \left( \psi_\uparrow^\dagger \psi_\uparrow \underline{\psi}_\uparrow^\dagger \underline{\psi}_\uparrow - \psi_\uparrow^\dagger \psi_\uparrow \underline{\psi}_\downarrow^\dagger \underline{\psi}_\downarrow - \psi_\downarrow^\dagger \psi_\downarrow \underline{\psi}_\uparrow^\dagger \underline{\psi}_\uparrow + \psi_\downarrow^\dagger \psi_\downarrow \underline{\psi}_\downarrow^\dagger \underline{\psi}_\downarrow \right) \times \left( -b^\dagger b \underline{a}^\dagger \underline{a} + S \underline{a}^\dagger \underline{a} + S b^\dagger b - S^2 \right) \tag{14g}$$

$$B_{BB} = \left( \psi_\uparrow^\dagger \psi_\uparrow \underline{\psi}_\uparrow^\dagger \underline{\psi}_\uparrow - \psi_\uparrow^\dagger \psi_\uparrow \underline{\psi}_\downarrow^\dagger \underline{\psi}_\downarrow - \psi_\downarrow^\dagger \psi_\downarrow \underline{\psi}_\uparrow^\dagger \underline{\psi}_\uparrow + \psi_\downarrow^\dagger \psi_\downarrow \underline{\psi}_\downarrow^\dagger \underline{\psi}_\downarrow \right) \times \left( b^\dagger b \underline{b}^\dagger \underline{b} - S b^\dagger b - S \underline{b}^\dagger \underline{b} + S^2 \right) . \tag{14h}$$

The contributions from terms that are odd in the number of magnon operators are neglected because they correspond to disconnected diagrams whose expectation values will vanish. The terms $A_{AB}$, $A_{BA}$ are not discarded as $a$ and $b$ are not

eigenexcitations, and the product of the two might still contain contributing terms that are even in the eigenmagnon operators. From this point on we also disregard terms of order $a^4$ and $b^4$ and higher to be consistent with the linear expansion of the HPT. Moreover, the interactions proportional to $aa$, $ab^\dagger$, $bb$, and their Hermitian conjugates vanish once the magnon operators are diagonalized. This is because these processes do not conserve spin.

### B. Two interfaces

We now want to generalize to the case where we have two fermion reservoirs $L$ and $R$ connected through the magnetic insulator. Similar to the case with only one fermion reservoir, there is no contribution of interest from the first order perturbation in $\mathcal{S}_{\text{int}}$ as these processes can not mediate an interaction between the two fermion reservoirs. Moreover, the processes represented by $B_{ij}$ ($i, j = A, B$) for the one-interface case in Eq. (14) also cannot couple the fermion reservoirs. This is because there are no processes in $B_{ij}$ where a magnon is emitted at one point and absorbed at another, only processes where a magnon is instantaneously emitted and absorbed at the same point. These interactions (first order in $\mathcal{S}_{\text{int}}$ and processes proportional to $B_{ij}$) will only contribute to a renormalization of the energy at each interface. As we are only interested in contributions that can mediate a coupling between the two reservoirs, we henceforth drop all contributions that are first order in $\mathcal{S}_{\text{int}}$ or included in $B_{ij}$.

The second order contribution can be expressed as

$$\left(\frac{\mathcal{S}_{\text{int}}}{\hbar}\right)^2 = \int d\tau d\tau' \left\{ \sum_{\substack{i,j=L,R \\ i \neq j}} \sum_{k,l=A,B} \sum_{\substack{m \in \mathcal{A}_i \\ n \in \mathcal{A}_j}} J_k^i(\boldsymbol{r}_m) \underline{J}_l^j(\boldsymbol{r}_n) \left[\hat{\rho}_i(\boldsymbol{r}_m,\tau) \cdot \boldsymbol{S}(\boldsymbol{r}_m,\tau)\right] \left[\underline{\hat{\rho}}_j(\boldsymbol{r}_n,\tau') \cdot \underline{\boldsymbol{S}}(\boldsymbol{r}_n,\tau')\right] \right\}, \tag{15}$$

with $\mathcal{A}_{L(R)} = \mathcal{A}_A^{L(R)} + \mathcal{A}_B^{L(R)}$, and $\hat{\rho}_i$ is the spin density defined in Eq. (4) in the $i$-th ($i = L, R$) fermion reservoir. For consistency with the contributions we have previously neglected, we only sum over the contributions where the fermions are located in different layers ($i \neq j$). We also allow for the interfaces to be different, and have generalized the definition of the interfacial exchange couplings in Eq. (3) to

$$J_k^i(\boldsymbol{r}_m) = \begin{cases} J_k^i, & \text{if } \boldsymbol{r}_m \in \mathcal{A}_k^i \\ 0, & \text{otherwise} \end{cases}. \tag{16}$$

From this point on, we only consider uncompensated magnetic interfaces, corresponding to either Fig. 1 (a) or (b). In other words, if we have the left interface being an uncompensated interface with sublattice $A$, we have $J_A^L(\boldsymbol{r}) = J_A^L$ for all $\boldsymbol{r} \in \mathcal{A}_L$ as well as $J_B^L(\boldsymbol{r}) = 0$ for all $\boldsymbol{r} \in \mathcal{A}_L$. However, we make no assumptions about which sublattice is at the interface, and whether the two interfaces are with identical or opposite sublattices.

We see that the result for one interface can easily be generalized to two interfaces with different fermion reservoirs. We can define

$$\gamma_{\text{int}}^{(2)} = 1 + \frac{S}{4} \int d\tau d\tau' \sum_{\substack{i,j=L,R \\ i \neq j}} \sum_{k,l=A,B} \sum_{\substack{m \in \mathcal{A}_i \\ n \in \mathcal{A}_j}} A_{kl}^{ij} J_k^i(\boldsymbol{r}_m) \underline{J}_l^j(\boldsymbol{r}_n), \tag{17}$$

where the coefficients $A_{kl}^{ij}$ are as in the one-reservoir case, but now with two different reservoir labels. As an example, we have

$$A_{AA}^{LR} = \psi_{\uparrow,L}^\dagger \psi_{\downarrow,L} \underline{\psi}_{\uparrow,R}^\dagger \underline{\psi}_{\downarrow,R} a\underline{a} + \psi_{\uparrow,L}^\dagger \psi_{\downarrow,L} \underline{\psi}_{\downarrow,R}^\dagger \underline{\psi}_{\uparrow,R} a\underline{a}^\dagger + \psi_{\downarrow,L}^\dagger \psi_{\uparrow,L} \underline{\psi}_{\uparrow,R}^\dagger \underline{\psi}_{\downarrow,R} a^\dagger \underline{a} + \psi_{\downarrow,L}^\dagger \psi_{\uparrow,L} \underline{\psi}_{\downarrow,R}^\dagger \underline{\psi}_{\uparrow,R} a^\dagger \underline{a}^\dagger, \tag{18}$$

where $\psi_{\uparrow,L}^\dagger$ creates a fermion with spin up in the left fermion reservoir, and so on. $\gamma_{\text{int}}^{(2)}$ takes the role of $\gamma_{\text{int}}$ in the path integral in Eq. (11) for the two-reservoir case. This path integral is also extended by an integration over the fermionic fields in the second fermion reservoir, *i.e.* $\mathcal{D}^2\psi \to \mathcal{D}^2\psi_L \mathcal{D}^2\psi_R$.

### III. MAGNETIC HAMILTONIAN

Now that we have considered how the fermions interact with the magnons in the HPT-magnon basis, we wish to find how these $a$ and $b$ magnons relate to the eigenexcitations of the system (the $\mu$ and $\nu$ magnons, which we integrate over in the path integral in Eq. (9)). We consider an easy-axis antiferromagnetic insulator, which is described by the Hamiltonian

$$\mathcal{H}_{\text{mag}} = J \sum_{\langle i,j \rangle} \boldsymbol{S}_i \cdot \boldsymbol{S}_j - \frac{K}{2} \sum_i S_{iz}^2. \tag{19}$$

where $J$ and $K$ are the strengths of the exchange interaction and magnetic anisotropy, respetively. Performing a HPT of the spin operators as defined in Eq. (6), disregarding any constant terms in the Hamiltonian and only keeping terms to second order in the magnon-operators, we find

$$\mathcal{H}_{\text{mag}} = \frac{J\hbar^2 S}{2} \sum_{\delta} \left[ \sum_{i \in A} \left( a_i^\dagger a_i + b_{i+\delta}^\dagger b_{i+\delta} + 2a_i^\dagger b_{i+\delta}^\dagger \right) + \sum_{i \in B} \left( b_i^\dagger b_i + a_{i+\delta}^\dagger a_{i+\delta} + 2b_i a_{i+\delta} \right) \right] + \hbar^2 KS \left( \sum_{i \in A} a_i^\dagger a_i + \sum_{i \in B} b_i^\dagger b_i \right). \quad (20)$$

Here $\delta$ is a set of nearest-neighbor vectors from site $i$. Next, we perform a Fourier transformation of the magnon operators, given by

$$a(\boldsymbol{r}_i, \tau) = \frac{1}{\sqrt{N_A}} \sum_{\boldsymbol{k}} a_{\boldsymbol{k}}(\tau) e^{i\boldsymbol{k} \cdot \boldsymbol{r}_i}, \quad a^\dagger(\boldsymbol{r}_i, \tau) = \frac{1}{\sqrt{N_A}} \sum_{\boldsymbol{k}} a_{\boldsymbol{k}}^\dagger(\tau) e^{-i\boldsymbol{k} \cdot \boldsymbol{r}_i}, \quad (21\text{a})$$

$$b(\boldsymbol{r}_i, \tau) = \frac{1}{\sqrt{N_B}} \sum_{\boldsymbol{k}} b_{\boldsymbol{k}}(\tau) e^{i\boldsymbol{k} \cdot \boldsymbol{r}_i}, \quad b^\dagger(\boldsymbol{r}_i, \tau) = \frac{1}{\sqrt{N_B}} \sum_{\boldsymbol{k}} b_{\boldsymbol{k}}^\dagger(\tau) e^{-i\boldsymbol{k} \cdot \boldsymbol{r}_i}. \quad (21\text{b})$$

where $N_{A/B}$ is the number of spins in sublattice $A/B$. The momentum $\boldsymbol{k}$ in each sum runs over the sublattice Brillouin zone. For an antiferromagnet, we have $N_A = N_B$.

If we assume that $N_A$ is macroscopic, the terms in the Hamiltonian transform as

$$\sum_{j \in A} a^\dagger(\boldsymbol{r}_j, \tau) a(\boldsymbol{r}_j, \tau) = \sum_{\boldsymbol{k}} a_{\boldsymbol{k}}^\dagger(\tau) a_{\boldsymbol{k}}(\tau). \quad (22)$$

Transforming the remaining terms in the Hamiltonian to momentum space, we find it to be

$$\mathcal{H}_{\text{mag}} = \sum_{\boldsymbol{k}} \left\{ \hbar^2 S (Jz + K) \left[ a_{\boldsymbol{k}}^\dagger(\tau) a_{\boldsymbol{k}}(\tau) + b_{\boldsymbol{k}}^\dagger(\tau) b_{\boldsymbol{k}}(\tau) \right] + \hbar^2 S Jz \left[ \gamma_{\boldsymbol{k}} a_{\boldsymbol{k}}^\dagger(\tau) b_{-\boldsymbol{k}}^\dagger(\tau) + \gamma_{-\boldsymbol{k}} a_{\boldsymbol{k}}(\tau) b_{-\boldsymbol{k}}(\tau) \right] \right\}, \quad (23)$$

where $z$ is the number of nearest neighbours, and

$$\gamma_{\boldsymbol{k}} = z^{-1} \sum_{\delta} e^{i\boldsymbol{k} \cdot \delta} = \gamma_{-\boldsymbol{k}}. \quad (24)$$

We now want to diagonalize the Hamiltonian in Eq. (23). We use a Bogoliubov transformation given by

$$\mu_{\boldsymbol{k}}(\tau) = u_{\boldsymbol{k}} a_{\boldsymbol{k}}(\tau) + v_{\boldsymbol{k}} b_{-\boldsymbol{k}}^\dagger(\tau), \quad \nu_{\boldsymbol{k}}(\tau) = u_{\boldsymbol{k}} b_{\boldsymbol{k}}(\tau) + v_{\boldsymbol{k}} a_{-\boldsymbol{k}}^\dagger(\tau), \quad (25)$$

where the new bosonic operators $\mu$ and $\nu$ also satisfy bosonic commutation relations. Introducing the quantities $\omega_E = J\hbar Sz$ and $\omega_\parallel = K\hbar S$, we find that

$$\mathcal{H}_{\text{mag}} = \sum_{\boldsymbol{k}} \left[ \varepsilon_{\boldsymbol{k},\mu} \mu_{\boldsymbol{k}}^\dagger(\tau) \mu_{\boldsymbol{k}}(\tau) + \varepsilon_{\boldsymbol{k},\nu} \nu_{\boldsymbol{k}}^\dagger(\tau) \nu_{\boldsymbol{k}}(\tau) \right]. \quad (26)$$

The energies are

$$\varepsilon_{\boldsymbol{k},\mu} = \varepsilon_{\boldsymbol{k},\nu} \equiv \varepsilon_{\boldsymbol{k}} = \hbar \sqrt{\left(1 - \gamma_{\boldsymbol{k}}^2\right) \omega_E^2 + \omega_\parallel \left(2\omega_E + \omega_\parallel\right)}. \quad (27)$$

The Bogoliubov coefficients are

$$u_{\boldsymbol{k}} = \sqrt{\frac{\Gamma_{\boldsymbol{k}} + 1}{2}}, \quad v_{\boldsymbol{k}} = \sqrt{\frac{\Gamma_{\boldsymbol{k}} - 1}{2}}, \quad (28)$$

where we have introduced

$$\Gamma_{\boldsymbol{k}} = \frac{1}{\sqrt{1 - \left(\frac{\omega_E \gamma_{\boldsymbol{k}}}{\omega_E + \omega_\parallel}\right)^2}}. \quad (29)$$

## IV. MAGNON GREEN'S FUNCTIONS

Now that we can express the fermion-magnon interaction in terms of the eigenmagnons $\mu$ and $\nu$, over which we integrate, we can proceed by performing the integrals over the magnon fields to express the interaction as an effective fermion-fermion interaction mediated by the magnons. Let us introduce the (inverse) Green's function so that the partition function for the magnons becomes

$$\mathcal{Z}_{\mathrm{mag}} = \int \mathcal{D}^2\mu \mathcal{D}^2\nu \exp\left[\int_0^{\hbar\beta} \mathrm{d}\tau \mathrm{d}\tau' \sum_{i,j} \mathbf{\Phi}^\dagger(\mathbf{r}_i, \tau) \mathcal{G}_{\mathrm{mag}}^{-1}(\mathbf{r}_i, \tau; \mathbf{r}_j, \tau') \mathbf{\Phi}(\mathbf{r}_j, \tau')\right], \tag{30}$$

where we have

$$\mathbf{\Phi}^\dagger(\mathbf{r}, \tau) = (\mu^*(\mathbf{r}, \tau), \quad \nu^*(\mathbf{r}, \tau)). \tag{31}$$

To describe the (imaginary) time dependence of the magnon fields we do a Matsubara expansion and go to frequency space,

$$\mu(\mathbf{r}, \tau) = \frac{1}{\sqrt{N_A}} \sum_{n=-\infty}^{\infty} \sum_{\mathbf{k}} \mu_{\mathbf{k},n} e^{i(\mathbf{k}\cdot\mathbf{r} - \omega_n \tau)}, \tag{32}$$

where $\omega_n = 2\pi n/(\hbar\beta)$ is the Matsubara frequency for bosons.

In a momentum and frequency representation, the partition function can alternatively be expressed as

$$\mathcal{Z}_{\mathrm{mag}} = \int \mathcal{D}^2\mu \mathcal{D}^2\nu \exp\left(-\frac{\mathcal{S}_{\mathrm{mag}}}{\hbar}\right) = \int \mathcal{D}^2\mu \mathcal{D}^2\nu \exp\left[\sum_{\mathbf{k},\mathbf{k}'} \sum_{n,n'} \mathbf{\Phi}^\dagger_{\mathbf{k},n} \mathcal{G}_{\mathrm{mag}}^{-1}(\mathbf{k}, i\omega_n; \mathbf{k}', i\omega_{n'}) \mathbf{\Phi}_{\mathbf{k}',n'}\right], \tag{33}$$

with

$$\mathbf{\Phi}^\dagger_{\mathbf{k},n} = \left(\mu^*_{\mathbf{k},n}, \quad \nu^*_{\mathbf{k},n}\right). \tag{34}$$

Performing the Matsubara expansion of our fields, and using our Hamiltonian as shown in Eq. (26) in terms of the Matsubara modes, we note that the action in Eq. (10b) becomes

$$\mathcal{S}_{\mathrm{mag}} = \hbar\beta \sum_{\mathbf{k}} \sum_n \sum_{\eta=\mu,\nu} \left(-i\hbar\omega_n + \varepsilon_{\mathbf{k},\eta}\right) \eta^*_{\mathbf{k},n} \eta_{\mathbf{k},n}, \tag{35}$$

where we have used the identity

$$\int_0^{\hbar\beta} \mathrm{d}\tau \frac{e^{i(\omega_{n'} - \omega_n)\tau}}{\hbar\beta} = \delta_{n,n'}. \tag{36}$$

Consequentially, we find the Green's function in the Matsubara basis to be

$$\mathcal{G}_{\mathrm{mag}}(\mathbf{k}, i\omega_n; \mathbf{k}', i\omega_{n'}) = -\frac{\hbar}{\hbar\beta} \delta_{\mathbf{k}\mathbf{k}'} \delta_{n,n'} \left(\begin{matrix} \left(-i\hbar\omega_n + \varepsilon_{\mathbf{k},\mu}\right)^{-1} & 0 \\ 0 & \left(-i\hbar\omega_n + \varepsilon_{\mathbf{k},\nu}\right)^{-1} \end{matrix}\right) = -\left(\begin{matrix} \langle\mu^*_{\mathbf{k},n}\mu_{\mathbf{k}',n'}\rangle & 0 \\ 0 & \langle\nu^*_{\mathbf{k},n}\nu_{\mathbf{k}',n'}\rangle \end{matrix}\right). \tag{37}$$

Now we wish to calculate expectation values such as

$$\langle\mu^*(\mathbf{r}, \tau)\mu(\mathbf{r}', \tau')\rangle = \mathcal{Z}_{\mathrm{mag}}^{-1} \int \mathcal{D}^2\mu \mathcal{D}^2\nu \exp\left(-\frac{\mathcal{S}_{\mathrm{mag}}}{\hbar}\right) \mu^*(\mathbf{r}, \tau)\mu(\mathbf{r}', \tau'). \tag{38}$$

We once again do a Fourier transform and a Matsubara expansion, and using the results above we find that

$$\begin{aligned} \langle\mu^*(\mathbf{r}, \tau)\mu(\mathbf{r}', \tau')\rangle &= \frac{1}{N_A} \sum_{\mathbf{k},\mathbf{k}'} \sum_{n,n'} e^{i(\mathbf{k}'\cdot\mathbf{r}' - \mathbf{k}\cdot\mathbf{r})} e^{i(\omega_n\tau - \omega_{n'}\tau')} \mathcal{Z}_{\mathrm{mag}}^{-1} \int \mathcal{D}^2\mu \mathcal{D}^2\nu \exp\left(-\frac{\mathcal{S}_{\mathrm{mag}}}{\hbar}\right) \mu^*_{\mathbf{k},n}\mu_{\mathbf{k}',n'} \\ &= \frac{1}{N_A} \sum_{\mathbf{k},\mathbf{k}'} \sum_{n,n'} e^{i(\mathbf{k}'\cdot\mathbf{r}' - \mathbf{k}\cdot\mathbf{r})} e^{i(\omega_n\tau - \omega_{n'}\tau')} \langle\mu^*_{\mathbf{k},n}\mu_{\mathbf{k}',n'}\rangle \\ &= \frac{1}{\hbar\beta N_A} \sum_{\mathbf{k}} \sum_n \frac{\hbar}{-i\hbar\omega_n + \varepsilon_{\mathbf{k},\mu}} e^{i\mathbf{k}\cdot(\mathbf{r}'-\mathbf{r})} e^{-i\omega_n(\tau'-\tau)} \\ &\equiv \sum_{\mathbf{k}} \langle\mu^*_{\mathbf{k}}(\mathbf{r}, \tau)\mu_{\mathbf{k}}(\mathbf{r}', \tau')\rangle = -\mathcal{G}_{\mathrm{mag}}(\mathbf{r}, \tau; \mathbf{r}', \tau'). \end{aligned} \tag{39}$$

A similar result is obtained for $\langle v^*(\boldsymbol{r}, \tau) v(\boldsymbol{r}', \tau') \rangle$, and all other expectation values vanish.

Previously we expressed the interaction in terms of the sublattice magnon operators $a$ and $b$. The expectation values of these magnons are related to the expectation values of the diagonal magnons by the following:

$$\langle a^*(\boldsymbol{r}, \tau) a(\boldsymbol{r}', \tau') \rangle = \sum_{\boldsymbol{k}} \left[ u_{\boldsymbol{k}}^2 \langle \mu_{\boldsymbol{k}}^*(\boldsymbol{r}, \tau) \mu_{\boldsymbol{k}}(\boldsymbol{r}', \tau') \rangle + v_{\boldsymbol{k}}^2 \langle v_{\boldsymbol{k}}^*(\boldsymbol{r}', \tau') v_{\boldsymbol{k}}(\boldsymbol{r}, \tau) \rangle \right], \tag{40a}$$

$$\langle b^*(\boldsymbol{r}, \tau) b(\boldsymbol{r}', \tau') \rangle = \sum_{\boldsymbol{k}} \left[ v_{\boldsymbol{k}}^2 \langle \mu_{\boldsymbol{k}}^*(\boldsymbol{r}', \tau') \mu_{\boldsymbol{k}}(\boldsymbol{r}, \tau) \rangle + u_{\boldsymbol{k}}^2 \langle v_{\boldsymbol{k}}^*(\boldsymbol{r}, \tau) v_{\boldsymbol{k}}(\boldsymbol{r}', \tau') \rangle \right], \tag{40b}$$

$$\langle a(\boldsymbol{r}, \tau) b(\boldsymbol{r}', \tau') \rangle = -\sum_{\boldsymbol{k}} u_{\boldsymbol{k}} v_{\boldsymbol{k}} \left[ \langle \mu_{\boldsymbol{k}}^*(\boldsymbol{r}', \tau') \mu_{\boldsymbol{k}}(\boldsymbol{r}, \tau) \rangle + \langle v_{\boldsymbol{k}}^*(\boldsymbol{r}, \tau) v_{\boldsymbol{k}}(\boldsymbol{r}', \tau') \rangle \right], \tag{40c}$$

$$\langle a^*(\boldsymbol{r}, \tau) b^*(\boldsymbol{r}', \tau') \rangle = -\sum_{\boldsymbol{k}} u_{\boldsymbol{k}} v_{\boldsymbol{k}} \left[ \langle \mu_{\boldsymbol{k}}^*(\boldsymbol{r}, \tau) \mu_{\boldsymbol{k}}(\boldsymbol{r}', \tau') \rangle + \langle v_{\boldsymbol{k}}^*(\boldsymbol{r}', \tau') v_{\boldsymbol{k}}(\boldsymbol{r}, \tau) \rangle \right]. \tag{40d}$$

The other expectation values vanish.

## V. EFFECTIVE POTENTIAL

Using the results found previously, we integrate out the magnons and find that

$$\mathcal{Z} = \mathcal{Z}_{\text{mag}} \int \mathcal{D}^2 \psi_L \mathcal{D}^2 \psi_R \exp\left( -\mathcal{S}_{\text{el}}^{\text{eff}} / \hbar \right) \equiv \int \mathcal{D}^2 \psi_L \mathcal{D}^2 \psi_R \exp\left( -\mathcal{S}_{\text{el}} / \hbar \right) \int \mathcal{D}^2 \mu \mathcal{D}^2 v \exp(-\mathcal{S}_{\text{mag}} / \hbar) \gamma_{\text{int}}^{(2)}, \tag{41}$$

where $\gamma_{\text{int}}^{(2)}$ is defined in Eq. (17), and we have defined the effective action of the fermionic system:

$$\mathcal{S}_{\text{el}}^{\text{eff}} = \int_0^{\hbar\beta} d\tau \left[ \hbar \sum_{i=L,R} \sum_{\boldsymbol{r}_j \in i} \sum_{\sigma=\uparrow,\downarrow} \psi_{\sigma,i}^*(\boldsymbol{r}_j, \tau) \dot{\psi}_{\sigma,i}(\boldsymbol{r}_j, \tau) + \mathcal{H}_{\text{el}} \right] + \hbar \left( 1 - \gamma_{\text{int}}^G \right).$$

We have here reintroduced the interaction term in the exponent.

The interaction term can be expressed as following:

$$\hbar \left( 1 - \gamma_{\text{int}}^G \right) = \sum_{\substack{i,j=L,R \\ i \neq j}} \int d\tau d\tau' \sum_{\substack{k \in \mathcal{A}_i \\ l \in \mathcal{A}_j}} \sum_{\sigma=\uparrow,\downarrow} V_{\sigma,-\sigma}^{ij}(\boldsymbol{r}_k, \boldsymbol{r}_l, \tau - \tau') \psi_{\sigma,i}^*(\boldsymbol{r}_k, \tau) \psi_{-\sigma,i}(\boldsymbol{r}_k, \tau) \psi_{-\sigma,j}^*(\boldsymbol{r}_l, \tau') \psi_{\sigma,j}(\boldsymbol{r}_l, \tau'). \tag{42}$$

The effective potential $V_{\sigma,-\sigma}^{ij}(\boldsymbol{r}, \boldsymbol{r}', \tau - \tau')$ describes a spin-flip interaction of two fermions located in reservoirs $i$ and $j$ mediated by a magnon in the magnetic insulator. One fermion flips its spin and thereby emits a magnon. This magnon is then absorbed by a fermion that is located in the reservoir on the opposing side of the insulating barrier with respect to the fermion that emitted the magnon. We then write down the effective spin-flip potential as

$$V_{\uparrow,\downarrow}^{ij}(\boldsymbol{r}, \boldsymbol{r}', \tau - \tau') = V_{\downarrow,\uparrow}^{ji}(\boldsymbol{r}', \boldsymbol{r}, \tau' - \tau) \tag{43a}$$

$$= -\frac{\hbar S}{4} \left[ \langle a^*(\boldsymbol{r}', \tau') a(\boldsymbol{r}, \tau) \rangle J_A^i(\boldsymbol{r}) J_A^j(\boldsymbol{r}') + \langle a(\boldsymbol{r}, \tau) b(\boldsymbol{r}', \tau') \rangle J_A^i(\boldsymbol{r}) J_B^j(\boldsymbol{r}') \right.$$

$$\left. + \langle a^*(\boldsymbol{r}', \tau') b^*(\boldsymbol{r}, \tau) \rangle J_A^i(\boldsymbol{r}') J_B^j(\boldsymbol{r}) + \langle b^*(\boldsymbol{r}, \tau) b(\boldsymbol{r}', \tau') \rangle J_B^i(\boldsymbol{r}) J_B^j(\boldsymbol{r}') \right] \tag{43b}$$

$$= -\frac{S}{4\beta N_A} \sum_{\boldsymbol{k}} \sum_n \frac{\hbar}{-i\hbar\omega_n + \varepsilon_{\boldsymbol{k},\mu}} \left[ v_{\boldsymbol{k}} J_B^i(\boldsymbol{r}) - u_{\boldsymbol{k}} J_A^i(\boldsymbol{r}) \right] \left[ v_{\boldsymbol{k}} J_B^j(\boldsymbol{r}') - u_{\boldsymbol{k}} J_A^j(\boldsymbol{r}') \right] e^{i\boldsymbol{k}\cdot(\boldsymbol{r}-\boldsymbol{r}')} e^{-i\omega_n(\tau-\tau')}$$

$$- \frac{S}{4\beta N_A} \sum_{\boldsymbol{k}} \sum_n \frac{\hbar}{-i\hbar\omega_n + \varepsilon_{\boldsymbol{k},v}} \left[ v_{\boldsymbol{k}} J_A^i(\boldsymbol{r}) - u_{\boldsymbol{k}} J_B^i(\boldsymbol{r}) \right] \left[ v_{\boldsymbol{k}} J_A^j(\boldsymbol{r}') - u_{\boldsymbol{k}} J_B^j(\boldsymbol{r}') \right] e^{i\boldsymbol{k}\cdot(\boldsymbol{r}'-\boldsymbol{r})} e^{-i\omega_n(\tau'-\tau)} \tag{43c}$$

We now do a Fourier transformation and Matsubara expansion of the fermionic fields, so that

$$\psi_{\sigma,i}(\boldsymbol{r}, \tau) = \frac{1}{\sqrt{N_i}} \sum_n \sum_{\boldsymbol{k}} \psi_{\sigma,i}(\boldsymbol{k}, i\nu_n) e^{i\boldsymbol{k}\cdot\boldsymbol{r} - i\nu_n\tau}. \tag{44}$$

Here $N_i$ is the number of sites in reservoir $i$ ($i = L, R$), and $\boldsymbol{k}$ now runs over the Brillouin zone of the fermion reservoirs. The Matsubara expansion of the fermionic fields is defined in terms of the fermionic Matsubara frequencies $\nu_n = (2n + 1)\pi/(\hbar\beta)$. With these transformations, we rewrite the magnon-mediated interaction as

$$\sum_{\substack{i,j=L,R \\ i \neq j}} \sum_{\sigma=\uparrow,\downarrow} \int d\tau d\tau' \sum_{\substack{k \in \mathcal{A}_i \\ l \in \mathcal{A}_j}} V_{\sigma,-\sigma}^{ij}(\boldsymbol{r}_k, \boldsymbol{r}_l, \tau - \tau') \psi_{\sigma,i}^*(\boldsymbol{r}_k, \tau) \psi_{-\sigma,i}(\boldsymbol{r}_k, \tau) \psi_{-\sigma,j}^*(\boldsymbol{r}_l, \tau') \psi_{\sigma,j}(\boldsymbol{r}_l, \tau')$$

$$= \sum_{\substack{i,j=L,R \\ i \neq j}} \sum_{\sigma=\uparrow,\downarrow} (\hbar\beta)^2 \sum_{lmn} \sum_{\boldsymbol{k}\boldsymbol{k}'\boldsymbol{q}} V_{\sigma,\mu\nu}^{ij}(\boldsymbol{q}, i\omega_n) \psi_{\sigma,i}^*(\boldsymbol{k}' + \boldsymbol{q}, i\nu_l + i\omega_n) \psi_{-\sigma,i}(\boldsymbol{k}', i\nu_l) \psi_{-\sigma,j}^*(\boldsymbol{k} - \boldsymbol{q}, i\nu_m - i\omega_n) \psi_{\sigma,j}(\boldsymbol{k}, i\nu_m). \quad (45)$$

Here we have defined

$$V_{\sigma,-\sigma}^{ij}(\boldsymbol{r}, \boldsymbol{r}', \tau - \tau') \equiv \sum_{\boldsymbol{q}} \sum_n V_{\sigma,\mu\nu}^{ij}(\boldsymbol{q}, i\omega_n) e^{i\boldsymbol{q}\cdot(\boldsymbol{r}-\boldsymbol{r}')} e^{-i\omega_n(\tau-\tau')}, \quad (46)$$

with

$$V_{\sigma,\mu\nu}^{ij}(\boldsymbol{q}, i\omega_n) \equiv -\frac{\hbar S}{4\hbar\beta N_A} \left\{ \frac{\hbar}{-\sigma i\hbar\omega_n + \varepsilon_{\boldsymbol{q},\mu}} \left[ v_{\boldsymbol{q}} J_B^i(\boldsymbol{r}_i) - u_{\boldsymbol{q}} J_A^i(\boldsymbol{r}_i) \right] \left[ v_{\boldsymbol{q}} J_B^j(\boldsymbol{r}_j) - u_{\boldsymbol{q}} J_A^j(\boldsymbol{r}_j) \right] \right.$$

$$\left. + \frac{\hbar}{\sigma i\hbar\omega_n + \varepsilon_{\boldsymbol{q},\nu}} \left[ v_{\boldsymbol{q}} J_A^i(\boldsymbol{r}_i) - u_{\boldsymbol{q}} J_B^i(\boldsymbol{r}_i) \right] \left[ v_{\boldsymbol{q}} J_A^j(\boldsymbol{r}_j) - u_{\boldsymbol{q}} J_B^j(\boldsymbol{r}_j) \right] \right\}. \quad (47)$$

While at first glance the potential in the above equation seemingly also depends on position, we note that since we are only considering uncompensated interfaces (see Fig. 1 (a) and (b)) the interfacial coupling constants $J_{A,B}^{L,R}(\boldsymbol{r})$ can only take on the constant values $J_{A,B}^{L,R}$ or zero for all positions $\boldsymbol{r}$ at each interface. As an example, $J_A^L(\boldsymbol{r}_L \in \mathcal{A}_L) = J_A^L$ if the interface with reservoir $L$ is an uncompensated interface with sublattice $A$, but $J_A^L(\boldsymbol{r}_L \in \mathcal{A}_L) = 0$ if the interface with reservoir $L$ is an uncompensated interface with sublattice $B$. However, if one is considering a compensated interface such as in Fig. 1 (c), the interfacial coupling constants have a periodic spatial dependence at that interface, and they would then also need to be Fourier transformed accordingly. Since we are only considering uncompensated interfaces, we do not have to take this into consideration.

We have previously assumed an inversion symmetry in the magnetic insulator, so that $\varepsilon_{\boldsymbol{k},\mu/\nu} = \varepsilon_{-\boldsymbol{k},\mu/\nu}$. With this in mind, the Fourier transform of the effective magnon potential has the following symmetries:

$$V_{\sigma,\mu\nu}^{ij}(\boldsymbol{k}, i\omega_n) = V_{\sigma,\mu\nu}^{ji}(\boldsymbol{k}, i\omega_n), \quad V_{\sigma,\mu\nu}^{ij}(\boldsymbol{k}, i\omega_n) = V_{\sigma,\mu\nu}^{ij}(-\boldsymbol{k}, i\omega_n), \quad V_{-\sigma,\mu\nu}^{ij}(\boldsymbol{k}, i\omega_n) = V_{\sigma,\mu\nu}^{ij}(\boldsymbol{k}, -i\omega_n). \quad (48)$$

Through these symmetries, and some relabelling of the momenta and Matsubara frequencies, one can see that the interactions in (45) are pairwise identical. The interactions are paired through the substitutions $L \leftrightarrow R$, $\sigma \to -\sigma$. Consequently, we can perform the sums over layers (only considering interlayer interactions) in (45), and reduce the result to

$$2(\hbar\beta)^2 \sum_{\sigma=\uparrow,\downarrow} \sum_{lmn} \sum_{\boldsymbol{k}\boldsymbol{k}'\boldsymbol{q}} V_{\sigma,\mu\nu}^{LR}(\boldsymbol{q}, i\omega_n) \psi_{\sigma,L}^*(\boldsymbol{k}' + \boldsymbol{q}, i\nu_l + i\omega_n) \psi_{-\sigma,L}(\boldsymbol{k}', i\nu_l) \psi_{-\sigma,R}^*(\boldsymbol{k} - \boldsymbol{q}, i\nu_m - i\omega_n) \psi_{\sigma,R}(\boldsymbol{k}, i\nu_m). \quad (49)$$

To have a more intuitive form of the magnon-mediated potential, we define the quantity

$$U_\sigma(\boldsymbol{q}, i\omega_n) \equiv 2\hbar\beta V_{\sigma,\mu\nu}^{LR}(\boldsymbol{q}, i\omega_n), \quad (50)$$

which has units Joule.

## VI. EXCITON INTERACTION

We will now use the effective action to look at interlayer exciton condensation. It is then advantageous to reorder the fermionic fields on the following form:

$$-\hbar\beta \sum_{\sigma=\uparrow,\downarrow} \sum_{lmn} \sum_{\boldsymbol{k}\boldsymbol{k}'\boldsymbol{q}} U_\sigma(\boldsymbol{q}, i\omega_n) \psi_{\sigma,L}^*(\boldsymbol{k}' + \boldsymbol{q}, i\nu_l + i\omega_n) \psi_{\sigma,R}(\boldsymbol{k}, i\nu_m) \psi_{-\sigma,R}^*(\boldsymbol{k} - \boldsymbol{q}, i\nu_m - i\omega_n) \psi_{-\sigma,L}(\boldsymbol{k}', i\nu_l). \quad (51)$$

We can simplify this further by only considering the case where the exciton has a net zero momentum ($\boldsymbol{k}' + \boldsymbol{q} - \boldsymbol{k} = 0$). Moreover, we assume that the electronic fields in an exciton pair has the same Matsubara frequency ($i\nu_l + i\omega_n = i\nu_m$) as well as momentum. The simplified interaction we consider is then

$$-\hbar\beta \sum_{mn} \sum_{\boldsymbol{k}\boldsymbol{k}'} \sum_\sigma U_\sigma(\boldsymbol{k} - \boldsymbol{k}', i\nu_m - i\nu_n) \psi_{\sigma,L}^*(\boldsymbol{k}, i\nu_m) \psi_{\sigma,R}(\boldsymbol{k}, i\nu_m) \psi_{-\sigma,R}^*(\boldsymbol{k}', i\nu_n) \psi_{-\sigma,L}(\boldsymbol{k}', i\nu_n). \quad (52)$$

## VII. HUBBARD–STRATONOVICH TRANSFORMATION

To simplify the Hamiltonian, we can reduce the effective electronic Hamiltonian to a bilinear Hamiltonian by introducing an auxiliary Hubbard–Stratonovich field. To introduce the new Hubbard–Stratonovich fields, we first multiply our path integral by a unity path integral, given by the path integral over a white-noise field $\alpha$ [1]:

$$\mathcal{Z}_\alpha = \int \mathcal{D}^2 \alpha \exp\left[ -\sum_\sigma \sum_{mn} \sum_{kk'} \alpha_\sigma^\dagger(k, i\nu_m) \beta U_\sigma^{-1}(k - k', i\nu_m - i\nu_n) \alpha_{-\sigma}(k', i\nu_n) \right]. \tag{53}$$

Defining the bilinears $A_\sigma(k, i\nu_n) = \psi_{\sigma,R}^*(k, i\nu_n)\psi_{\sigma,L}(k, i\nu_n)$ and its Hermitian conjugate in the fermionic fields, we can shift the white-noise field variables by introducing the Hubbard–Stratonovich field

$$\Delta_\sigma(k, i\nu_m) = \alpha_\sigma(k, i\nu_m) - \sum_n \sum_{k'} U_\sigma(k - k', i\nu_m - i\nu_n) A_\sigma(k', i\nu_n), \tag{54}$$

and its Hermitian conjugate. Noting that the inverse matrix $U_\sigma^{-1}(k - k', i\nu_m - i\nu_n)$ is defined so that it satisfies the relation

$$\sum_l \sum_k U_\sigma^{-1}(k - k', i\nu_l - i\nu_m) U_\sigma(k - k'', i\nu_l - i\nu_n) = \delta_{k',k''}\delta_{m,n}, \tag{55}$$

we can rewrite the sum of the interaction and white-noise fields in the effective action as

$$\begin{aligned}
&- \hbar\beta \sum_{mn} \sum_{kk'} A_\sigma^\dagger(k, i\nu_m) U_\sigma(k - k') A_{-\sigma}(k', i\nu_n) \\
&+ \hbar\beta \sum_{mn} \sum_{kk'} \alpha_\sigma^\dagger(k, i\nu_m) U_\sigma^{-1}(k - k', i\nu_m - i\nu_n) \alpha_{-\sigma}(k', i\nu_n) \\
&= \hbar\beta \sum_n \sum_k \Delta_\sigma^\dagger(k, i\nu_n) A_{-\sigma}(k, i\nu_n) + \hbar\beta \sum_n \sum_k A_\sigma^\dagger(k, i\nu_n) \Delta_{-\sigma}(k, i\nu_n) \\
&+ \hbar\beta \sum_{mn} \sum_{kk'} \Delta_\sigma^\dagger(k, i\nu_m) U_\sigma^{-1}(k - k', i\nu_m - i\nu_n) \Delta_{-\sigma}(k', i\nu_n).
\end{aligned} \tag{56}$$

The path integral in its entirety can then be written as

$$\mathcal{Z} = \int \mathcal{D}^2 \Delta \exp\left[ -\beta \sum_\sigma \sum_{mn} \sum_{kk'} \Delta_\sigma^\dagger(k, i\nu_m) U_\sigma^{-1}(k - k', i\nu_m - i\nu_n) \Delta_{-\sigma}(k', i\nu_n) \right] \int \mathcal{D}^2\psi_L \int \mathcal{D}^2\psi_R \exp\left( -\frac{\tilde{S}_{\text{eff}}}{\hbar} \right), \tag{57}$$

where we have defined

$$\tilde{S}_{\text{eff}} = \int_0^{\hbar\beta} d\tau \left[ \hbar \sum_{i=L,R} \sum_{\sigma=\uparrow,\downarrow} \sum_{j\in V_i} \psi_{\sigma,i}^*(r_j, \tau) \dot{\psi}_{\sigma,i}(r_j, \tau) + \mathcal{H}_{\text{el}} \right] + \hbar\beta \sum_\sigma \sum_n \sum_k \left[ \Delta_\sigma^\dagger(k) A_{-\sigma}(k, i\nu_n) + A_\sigma^\dagger(k, i\nu_n) \Delta_{-\sigma}(k) \right]. \tag{58}$$

Assuming the electron and hole Hamiltonians to be diagonalized on the form

$$\mathcal{H}_{\text{el}} = \sum_n \sum_k \epsilon(k) \sum_\sigma \left[ \psi_{\sigma,L}^*(k, i\nu_n)\psi_{\sigma,L}(k, i\nu_n) - \psi_{\sigma,R}^*(k, i\nu_n)\psi_{\sigma,R}(k, i\nu_n) \right], \tag{59}$$

we can do Fourier and Matsubara expansions of the kinetic term to write the effective electronic action as

$$\begin{aligned}
\tilde{S}_{\text{eff}} = \hbar\beta \sum_{\sigma,n,k} \Big\{ &\psi_{\sigma,L}^*(k, i\nu_n) [-i\hbar\nu_n + \epsilon(k)] \psi_{\sigma,L}(k, i\nu_n) + \psi_{\sigma,R}^*(k, i\nu_n) [-i\hbar\nu_n - \epsilon(k)] \psi_{\sigma,R}(k, i\nu_n) \\
&+ \Delta_\sigma^\dagger(k, i\nu_n)\psi_{-\sigma,R}^*(k, i\nu_n)\psi_{-\sigma,L}(k, i\nu_n) + \psi_{\sigma,L}^*(k, i\nu_n)\psi_{\sigma,R}(k, i\nu_n)\Delta_{-\sigma}(k, i\nu_n) \Big\}.
\end{aligned} \tag{60}$$

Here $\epsilon(k)$ is the energy of the fermions in the left reservoir as a function of momentum, and the negative energy of the fermions in the right reservoir.

## VIII. SADDLE-POINT APPROXIMATION

Under the path integral, the Hubbard–Stratonovich transformation is exact. We have now successfully made our action bilinear in the fermionic fields, but this came at the cost of introducing another path integral over a bosonic Hubbard–Stratonovich field. To simplify our calculations, we make a mean-field approximation where we assume that the path integral over the Hubbard–Stratonovich field is dominated by the values of $\Delta_\sigma(\boldsymbol{k})$ and $\Delta_\sigma^*(\boldsymbol{k})$ that minimize the total action

$$S_\Delta = \hbar\beta \sum_\sigma \sum_{mn} \sum_{\boldsymbol{kk'}} \Delta_{-\sigma}^\dagger(\boldsymbol{k}, i\nu_m) U_\sigma^{-1}(\boldsymbol{k} - \boldsymbol{k'}, i\nu_m - i\nu_n) \Delta_\sigma(\boldsymbol{k'}, i\nu_n) + \tilde{S}_{\text{eff}}. \tag{61}$$

The path integral is then approximated by

$$\mathcal{Z} \approx \exp\left[-\beta \sum_\sigma \sum_{mn} \sum_{\boldsymbol{kk'}} \Delta_{-\sigma}^*(\boldsymbol{k}, i\nu_m) U_\sigma^{-1}(\boldsymbol{k} - \boldsymbol{k'}, i\nu_m - i\nu_n) \Delta_\sigma(\boldsymbol{k'}, i\nu_n)\right] \int \mathcal{D}^2\psi_L \int \mathcal{D}^2\psi_R \exp\left(-\frac{\tilde{S}_{\text{eff}}}{\hbar}\right), \tag{62}$$

where we the Hubbard–Stratonovich fields are no longer integrated over, but now take on constant values that satisfy $\delta S_\Delta / \delta[\Delta_\sigma^{(*)}(\boldsymbol{k}, i\nu_m)] = 0$. This is known as the saddle-point approximation.

## IX. GAP EQUATION

The effective action $\tilde{S}_{\text{eff}}$ now only consists of bilinear terms in the fermionic fields, and can therefore be written on the form

$$\tilde{S}_{\text{eff}} = \hbar\beta \sum_n \sum_{\boldsymbol{k}} \boldsymbol{\Psi}^\dagger(\boldsymbol{k}, i\nu_n) \left[-i\hbar\nu_n \underline{1} + \underline{h}_\Psi(\boldsymbol{k}, i\nu_n)\right] \boldsymbol{\Psi}(\boldsymbol{k}, i\nu_n), \tag{63}$$

where $\underline{1}$ is the identity matrix, and we have defined

$$\underline{h}_\Psi(\boldsymbol{k}, i\nu_n) \equiv \begin{pmatrix} \epsilon(\boldsymbol{k}) & \Delta_\uparrow(\boldsymbol{k}, i\nu_n) & 0 & 0 \\ \Delta_\uparrow^*(\boldsymbol{k}, i\nu_n) & -\epsilon(\boldsymbol{k}) & 0 & 0 \\ 0 & 0 & -\epsilon(\boldsymbol{k}) & \Delta_\downarrow^*(\boldsymbol{k}, i\nu_n) \\ 0 & 0 & \Delta_\downarrow(\boldsymbol{k}, i\nu_n) & \epsilon(\boldsymbol{k}) \end{pmatrix}. \tag{64}$$

$\boldsymbol{\Psi}(\boldsymbol{k}, i\nu_n)$ is the extended Nambu spinor $\boldsymbol{\Psi}(\boldsymbol{k}, i\nu_n) = (\psi_{\downarrow,L}(\boldsymbol{k}, i\nu_n), \psi_{\downarrow,R}(\boldsymbol{k}, i\nu_n), \psi_{\uparrow,R}(\boldsymbol{k}, i\nu_n), \psi_{\uparrow,L}(\boldsymbol{k}, i\nu_n))^T$. Performing the Gaussian integral over the fermionic fields, we can express the effective action as

$$\begin{aligned} \frac{S_\Delta}{\hbar} &= -\sum_{\boldsymbol{k}} \sum_n \ln\left\{\det\left[\beta(-i\hbar\nu_n \underline{1} + \underline{h}_\Psi(\boldsymbol{k}, i\nu_n))\right]\right\} \\ &\quad + \beta \sum_\sigma \sum_{mn} \sum_{\boldsymbol{kk'}} \Delta_\sigma^*(\boldsymbol{k}, i\nu_m) U_\sigma^{-1}(\boldsymbol{k} - \boldsymbol{k'}, i\nu_m - i\nu_n) \Delta_{-\sigma}(\boldsymbol{k'}, i\nu_n) \\ &= -\sum_\sigma \sum_n \sum_{\boldsymbol{k}} \ln\left\{\beta^2\left[|\Delta_\sigma(\boldsymbol{k}, i\nu_n)|^2 + \epsilon(\boldsymbol{k})^2 + (\hbar\nu_n)^2\right]\right\} \\ &\quad + \beta \sum_\sigma \sum_{mn} \sum_{\boldsymbol{kk'}} \Delta_\sigma^*(\boldsymbol{k}, i\nu_m) U_\sigma^{-1}(\boldsymbol{k} - \boldsymbol{k'}, i\nu_m - i\nu_n) \Delta_{-\sigma}(\boldsymbol{k'}, i\nu_n). \end{aligned} \tag{65}$$

Imposing the saddle-point approximation condition that $\delta S_\Delta / \delta[\Delta_\sigma^{(*)}(\boldsymbol{k}, i\nu_m)] = 0$, we find the gap equation to become

$$\frac{\delta S_\Delta}{\delta\left[\Delta_\sigma^*(\boldsymbol{k}, i\nu_m)\right]} = -\frac{\Delta_\sigma(\boldsymbol{k}, i\nu_m)}{|\Delta_\sigma(\boldsymbol{k}, i\nu_m)|^2 + \epsilon(\boldsymbol{k})^2 + (\hbar\nu_m)^2} + \beta \sum_n \sum_{\boldsymbol{k'}} U_\sigma^{-1}(\boldsymbol{k} - \boldsymbol{k'}, i\nu_m - i\nu_n) \Delta_{-\sigma}(\boldsymbol{k'}, i\nu_n) = 0. \tag{66}$$

Inverting the above gap equation through the identity in Eq. (55), we obtain

$$\Delta_{-\sigma}(\boldsymbol{k'}, i\nu_n) = \sum_m \sum_{\boldsymbol{k}} \beta^{-1} U_\sigma(\boldsymbol{k} - \boldsymbol{k'}, i\nu_m - i\nu_n) \frac{\Delta_\sigma(\boldsymbol{k}, i\nu_m)}{|\Delta_\sigma(\boldsymbol{k}, i\nu_m)|^2 + \epsilon(\boldsymbol{k})^2 + (\hbar\nu_m)^2}. \tag{67}$$

Solving the general case for when the gap depends on momentum and frequency is extremely challenging, as one then has to solve for an infinite set of coupled self-consistent equations. We can reduce the complexity by only considering frequency independent

gaps. This assumption requires that only the frequency independent part of the magnon-mediated potential contributes to the exciton pairing. We can then consider the potential and gaps as constants when performing the Matsubara sum.

Defining $E_\sigma(\boldsymbol{k}) \equiv \sqrt{|\Delta_\sigma(\boldsymbol{k})|^2 + [\epsilon(\boldsymbol{k})]^2}$, we note that

$$\sum_m \frac{1}{E_\sigma(\boldsymbol{k})^2 + (\hbar\nu_m)^2} = \sum_m \sum_\pm \frac{1}{2E_\sigma(\boldsymbol{k})} \frac{\pm 1}{i\hbar\nu_m \pm E_\sigma(\boldsymbol{k})} . \tag{68}$$

Using the Matsubara sum

$$\frac{1}{\hbar\beta} \sum_m \frac{1}{i\nu_m - E/\hbar} = \frac{1}{e^{\beta E} + 1} \equiv n_F(E), \tag{69}$$

we perform the Matsubara sum in the gap equation:

$$\sum_m \frac{1}{E_\sigma(\boldsymbol{k})^2 + (\hbar\nu_m)^2} = \frac{\beta}{2E_\sigma(\boldsymbol{k})} \left[ n_F(-E_\sigma(\boldsymbol{k})) - n_F(E_\sigma(\boldsymbol{k})) \right] = \frac{\beta}{2E_\sigma(\boldsymbol{k})} \tanh\left[ \frac{\beta E_\sigma(\boldsymbol{k})}{2} \right] . \tag{70}$$

The gap equation is then simplified to

$$\Delta_{-\sigma}(\boldsymbol{k}') = \sum_{\boldsymbol{k}} U_\sigma(\boldsymbol{k} - \boldsymbol{k}', 0) \frac{\Delta_\sigma(\boldsymbol{k})}{2E_\sigma(\boldsymbol{k})} \tanh\left[ \frac{\beta E_\sigma(\boldsymbol{k})}{2} \right] . \tag{71}$$

Note that the exciton interaction is attractive when $U_\sigma(\boldsymbol{k} - \boldsymbol{k}', 0) > 0$, which explains the sign difference from the typical form of the normal BCS gap equation.

## X. CRITICAL TEMPERATURE

We now wish to determine an analytical estimate of the critical temperature of the exciton condensation. Finding an analytical self-consistent solution of Eq. (71) is too complicated, so we will focus on the simple limit where both the magnon-mediated potential and the gap functions are independent of both momentum and frequency. Starting from Eq. (67), we then approximate the gap equation as

$$\Delta_{-\sigma} = \beta^{-1} U_\sigma(\boldsymbol{0}, 0) \Delta_\sigma \frac{N_A}{(2\pi/a)^2} \sum_n \int \mathrm{d}^2 k \frac{1}{|\Delta_\sigma|^2 + [\epsilon(\boldsymbol{k})]^2 + (\hbar\nu_n)^2} . \tag{72}$$

Here we have gone to the continuum limit:

$$\frac{1}{N_{L/R}} \sum_{\boldsymbol{k}} \to \frac{1}{A_k} \int \mathrm{d}^2 k , \tag{73}$$

where we assume that $N_{L/R} = N_A$ is the number of sites in one of the fermion reservoirs for an uncompensated mathced interface. $A_k = (2\pi/a)^2$ is the reciprocal area of the Brillouin zone of each fermion reservoir, with $a$ being the lattice constant. We consider atomically thin films such that the Brillouin zone is 2D, and consider a quadratic dispersion of $\epsilon(\boldsymbol{k})$ on the form

$$\epsilon(\boldsymbol{k}) = \frac{\hbar^2 k^2}{2m} - \mu \tag{74}$$

so that the Fermi surface is a circular disk. Here $\mu$ is the chemical potential, which we assume to be the Fermi energy $\epsilon_F$, and $m$ is the effective fermion mass. For our simplified contact interaction (independent of momentum) the magnon potential just becomes a constant and therefore has to lead to an isotropic s-wave pairing. We can then write the momentum integral as an energy integral

$$\int_{\mathrm{BZ}} \mathrm{d}^2 k \to 2\pi \int_0^{k_{\mathrm{BZ}}} \mathrm{d}k\, k \to \frac{2\pi m}{\hbar^2} \int_{-\epsilon_F}^{\epsilon_{\mathrm{BZ}} - \epsilon_F} \mathrm{d}\epsilon \to \frac{2\pi m}{\hbar^2} \epsilon_F \int_{-\infty}^\infty \mathrm{d}x , \tag{75}$$

where $x$ is a dimensionless energy integral, $\epsilon_F = \hbar^2 k_F^2/(2m)$ is the Fermi energy, and $\epsilon_{\mathrm{BZ}} = \epsilon(k_{\mathrm{BZ}})$ is the energy at the Brillouin zone boundary $k = k_{\mathrm{BZ}}$. We extend the integration limits on the integral over $x$ to $\pm\infty$, as the biggest contributions come from

near the Fermi surface ($x = 0$), and we will just add a small error by integrating over all energies. Noting that the energy integral can be determined to be

$$\epsilon_F \int_{-\infty}^{\infty} dx \frac{1}{(\epsilon_F x)^2 + |\Delta_\sigma|^2 + (\hbar \nu_n)^2} = \frac{\pi}{\sqrt{|\Delta_\sigma|^2 + (\hbar \nu_n)^2}}, \tag{76}$$

the gap equation simplifies further to

$$\Delta_{-\sigma} = \beta^{-1} U_\sigma(\mathbf{0}, 0) \Delta_\sigma \frac{N_A}{(2\pi/a)^2} \frac{2\pi^2 m}{\hbar^2} \sum_n \frac{1}{\sqrt{|\Delta_\sigma|^2 + (\hbar \nu_n)^2}}. \tag{77}$$

While the Matsubara sum in the gap equation above in principle runs over all frequencies for the approximations we have made, the sum will be divergent. To ensure that the sum converges, we introduce some upper limit to the sum. Looking at the form of the magnon-mediated potential in Eq. (47), we see that the potential is only attractive in a certain range of frequencies. We assume that the interfaces are defined so that it is attractive for small frequencies, i.e. we have an interface with sublattice $A$ on one side and the other interface is with sublattice $B$. Through an analytic continuation of Eq. (47) one can see that the attractive frequency region is then bounded by $\omega_n = \varepsilon_{\mathbf{q},\mu}/\hbar$ on one side, and by $\omega_n = \varepsilon_{\mathbf{q},\nu}/\hbar$ on the other. As we are only looking at contact interactions ($\mathbf{q} = \mathbf{0}$), the bounds on the attractive frequency region is given by the magnon gaps $\varepsilon_{\mathbf{0},\mu/\nu}$. In the system we consider the magnon gaps are identical, $\varepsilon_{\mathbf{0},\mu} = \varepsilon_{\mathbf{0},\nu} \equiv \varepsilon_{\mathbf{0}}$. We therefore only sum over Matsubara frequencies for $n$ between $-N$ and $N$, where $N$ is defined as $|\hbar \nu_N| = \varepsilon_{\mathbf{0}}$. Assuming $N$ is large, we have $N \approx \beta \varepsilon_{\mathbf{0}}/(2\pi)$.

At the critical temperature the gaps $\Delta_{\pm\sigma}$ vanish. We assume that the gaps have the same critical temperature $T_c$, and that they obey the limit

$$\lim_{T \to T_c} \frac{\Delta_{-\sigma}}{\Delta_\sigma} = 1. \tag{78}$$

If not exactly 1, the ratio still has to be positive for there to be a solution of the gap equation. In the ideal spin-degenerate case, it is however a sensible assumption that the ratio should be 1. With these assumptions, the gap equation simplifies to

$$\frac{2\hbar^2 \beta}{N_A m a^2 U_{\pm\sigma}(\mathbf{0}, 0)} \approx \sum_{n=-N}^{N} \frac{1}{|\hbar \nu_n|} = \frac{\beta}{\pi} \sum_{n=0}^{N} \frac{1}{|n + 1/2|} \tag{79}$$

The sum can be approximated by [2]

$$\sum_{n=0}^{N} \frac{1}{n + 1/2} \approx \ln(N) + 2\ln(2) + \gamma_{\text{EM}}, \tag{80}$$

where $\gamma_{\text{EM}} = 0.577\ldots$ is the Euler–Mascheroni constant. If we consider the scenario where we have an interface with sublattice $A$ on the left side and an interface with sublattice $B$ on the right side, as this yields an attractive potential for the exciton condensation, we obtain

$$\frac{2\pi \varepsilon_{\mathbf{0}}}{S u_0 v_0 m a^2 J_A^L J_B^R} \equiv \frac{1}{\lambda} \approx \ln\left(\frac{\beta \varepsilon_{\mathbf{0}}}{2\pi}\right) + 2\ln(2) + \gamma_{\text{EM}}. \tag{81}$$

Exponentiating the above equation, we find the analytical expression for $T_c$:

$$T_c = \frac{2 e^{\gamma_{\text{EM}}} \varepsilon_{\mathbf{0}}}{\pi k_B} \exp\left(-\frac{2\pi \varepsilon_{\mathbf{0}}}{S u_0 v_0 m a^2 J_A^L J_B^R}\right). \tag{82}$$

If we assume the exchange energy of the antiferromagnetic spins is much larger than the interface coupling ($\hbar \omega_E \gg S m a^2 J_A^L J_B^R$), we find that the $T_c$ is maximized for a given exchange energy by the anisotropy

$$\omega_\parallel^{(\text{opt})} = \frac{S m a^2 J_A^L J_B^R}{16\pi\hbar}. \tag{83}$$

When the anisotropy takes on this optimal value, the critical temperature becomes

$$T_c = \frac{\sqrt{\hbar \omega_E S m a^2 J_A^L J_B^R}}{\sqrt{2} \pi^{3/2} k_B} e^{\gamma_{\text{EM}} - 1/2}. \tag{84}$$

[1] P. Coleman, *Introduction to Many-Body Physics* (Cambridge University Press, 2015).
[2] N. Kopnin, *Theory of Nonequilibrium Superconductivity*, International Series of Monographs on Physics (Clarendon Press, 2001).

# Paper [5]

**Øyvind Johansen, Vetle Risinggård, Asle Sudbø,
Jacob Linder, and Arne Brataas**

*"Current Control of Magnetism in Two-Dimensional $Fe_3GeTe_2$"*

# Current Control of Magnetism in Two-Dimensional Fe$_3$GeTe$_2$

Øyvind Johansen,[*] Vetle Risinggård,[†] Asle Sudbø, Jacob Linder, and Arne Brataas

*Center for Quantum Spintronics, Department of Physics, Norwegian University of Science and Technology,*
*NO-7491 Trondheim, Norway*

The recent discovery of magnetism in two-dimensional van der Waals systems opens the door to discovering exciting physics. We investigate how a current can control the ferromagnetic properties of such materials. Using symmetry arguments, we identify a recently realized system in which the current-induced spin torque is particularly simple and powerful. In Fe$_3$GeTe$_2$, a single parameter determines the strength of the spin-orbit torque for a uniform magnetization. The spin-orbit torque acts as an effective out-of-equilibrium free energy. The contribution of the spin-orbit torque to the effective free energy introduces new in-plane magnetic anisotropies to the system. Therefore, we can tune the system from an easy-axis ferromagnet via an easy-plane ferromagnet to another easy-axis ferromagnet with increasing current density. This finding enables unprecedented control and provides the possibility to study the Berezinskiǐ-Kosterlitz-Thouless phase transition in the 2D $XY$ model and its associated critical exponents.

*Introduction.*—Magnetism in lower dimensions hosts interesting physics that has been studied theoretically for many decades. Examples include the intriguing physics of the exactly solvable 2D Ising model [1] and the Berezinskiǐ-Kosterlitz-Thouless (BKT) phase transition in the 2D $XY$ model [2–4]. However, experimentally realizing the details of these theoretical predictions has proven difficult. One reason for this difficulty is that fabricating atomically thin films is challenging. The isolation of graphene in 2004 provided a path for exploring two-dimensional van der Waals materials [5]. Creating two-dimensional films that have long-range magnetic order at finite temperatures is more challenging because of the Mermin-Wagner theorem [6]. This theorem states that long-range magnetic order does not exist at finite temperatures below three dimensions when the exchange interaction has a finite range and the material has a continuous symmetry in spin space. Consequently, realizing two-dimensional magnetic materials requires breaking the continuous symmetry of the system, e.g., by a uniaxial magnetocrystalline anisotropy. This provides an energy cost (also known as a magnon gap) to suppress long-range fluctuations that can destroy the magnetic order. The recent discovery of magnetic order in two-dimensional van der Waals materials has therefore led to a large number of studies of magnetism in atomically thin films [7]. Magnetic order has been reported in FePS$_3$ [8], Cr$_2$GeTe$_6$ [9], CrI$_3$ [10], VSe$_2$ [11], MSe$_x$ [12], and Fe$_3$GeTe$_2$ [13,14]. In addition, multiferroicity has been identified in CuCrP$_2$S$_6$ [15]. These new two-dimensional magnets are amenable to electrical control [14,16–18] and produce record-high tunnel magnetoresistances [19].

Currents can induce torques in magnetic materials [20]. In ferromagnets with broken inversion symmetry, the spin-orbit interaction leads to spin-orbit torques (SOTs) [21]. These torques can be present even in the bulk of the materials without requiring additional spin-polarizing elements. The effects of SOTs are typically sufficiently large to induce magnetization switching or motion of magnetic textures [22]. With the rich physics that is known to exist in two-dimensional magnetic systems, we explore how currents can provide additional control over the magnetic state via SOTs.

Although many of the newly discovered two-dimensional magnetic systems exhibit SOTs, we find that in one material the torque is particularly simple and powerful. The form of the torque is simple because it is determined by a single parameter. The torque is also influential in determining the magnetic state of the system. In contrast to many other systems, we can describe the current-induced effects via an effective out-of-equilibrium free energy. Therefore, the SOT enables unprecedented control over the magnetic state via the current. We will demonstrate how the current can drive the system from having easy-axis anisotropy along one direction to anisotropy along a different axis by proceeding via an intermediate state with easy-plane anisotropy.

Interestingly, the current-induced easy-plane configuration provides the possibility to study the BKT phase transition in this system. The BKT transition is an example of a so-called conformal phase transition in which the scale invariance of a topologically ordered state, i.e., conformal invariance, is lost at the (topological) phase transition [23]. When driven by a current, we realize a 2D conformal field

theory in the low-temperature phase, with conformality being lost [23] at the transition to the paramagnetic phase. Additionally, it was recently discovered that an ionic gate considerably increases the critical temperature [14]. Consequently, two-dimensional $Fe_3GeTe_2$ forms an ideal and very rich laboratory for studying fundamental problems of broad current interest in condensed matter physics and beyond at elevated temperatures.

*System.*—We consider a monolayer of $Fe_3GeTe_2$. Figure 1 shows the crystal structure of this material. $Fe_3GeTe_2$ crystallizes in the hexagonal system, space group 194, point group $6/m\,2/m\,2/m$, known as $D_{6h}$ in the Schönflies notation [24]. However, the basis reduces the point group symmetry to $\bar{6}m2$ ($D_{3h}$). Placing a $Fe_3GeTe_2$ monolayer on a substrate may reduce the symmetry even further (point group $3m$) if the bottom tellurium layer hybridizes with the surface. Here, we assume that a possible monolayer-substrate interaction is weak. In the case of a strong monolayer-substrate interaction, we can preserve the out-of-plane mirror symmetry by suspending the monolayer between two electrodes [25] or encapsulating it in another van der Waals material, such as hexagonal boron nitride.

The SOT can be written as [26]

$$\boldsymbol{\tau} = -|\gamma|\boldsymbol{m} \times \boldsymbol{H}_{\text{SOT}}, \quad (1)$$

where $\gamma$ is the gyromagnetic ratio and $\boldsymbol{m}$ is the magnetization unit vector. For a spatially uniform magnetization, the effective magnetic field $\boldsymbol{H}_{\text{SOT}}$ due to the SOT in a $Fe_3GeTe_2$ monolayer is [27]

$$\boldsymbol{H}_{\text{SOT}} = \Gamma_0[(m_x J_x - m_y J_y)\boldsymbol{e}_x - (m_y J_x + m_x J_y)\boldsymbol{e}_y] \quad (2)$$

for current densities and magnetizations in any direction. Here, $m_i$ are magnetization components, and $J_i$ are components of the current density. $\Gamma_0$ is a free parameter that is determined by the spin-orbit coupling.

We provide a rigorous derivation of the effective field $\boldsymbol{H}_{\text{SOT}}$ based on Neumann's principle in the Supplemental Material [27]. In $Fe_3GeTe_2$, we can understand the
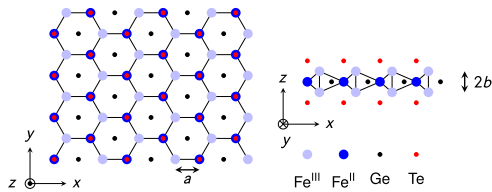


FIG. 1. Crystal structure of a $Fe_3GeTe_2$ monolayer. (Left) View along $\boldsymbol{e}_z$. (Right) View along $\boldsymbol{e}_y$. $a$ is the in-plane bond length between $Fe^{III}$ and $Fe^{II}$. $2b$ is the out-of-plane distance between the two $Fe^{III}$ sublattices. $Fe^{III}$ and $Fe^{II}$ represent the two inequivalent Fe sites in oxidation states $+3$ and $+2$, respectively. Redrawn after Ref. [14].

dependence of the SOT on the magnetization and currents in Eq. (2) as follows. The crystal structure in Fig. 1 is invariant under a threefold rotation about the $z$ axis ($3_z$), an inversion of the $y$ axis ($m_y$), and an inversion of the $z$ axis ($m_z$). These symmetry operations generate the point group $\bar{6}m2$. Since $\boldsymbol{H}_{\text{SOT}}$ only contains terms that are quadratic in $y$, it is invariant under the operation $m_y$. The operation $3_z$ transforms $(m_x, m_y)$ into

$$\frac{1}{2}\begin{pmatrix} -1 & \sqrt{3} \\ -\sqrt{3} & -1 \end{pmatrix}\begin{pmatrix} m_x \\ m_y \end{pmatrix} = \frac{1}{2}\begin{pmatrix} -m_x + \sqrt{3}m_y \\ -\sqrt{3}m_x - m_y \end{pmatrix}, \quad (3)$$

and similarly for $(J_x, J_y)$ and $(\boldsymbol{e}_x, \boldsymbol{e}_y)$. Backsubstitution of the transformation in Eq. (3) into Eq. (2) shows that $\boldsymbol{H}_{\text{SOT}}$ is also invariant under this operation. The effective field $\boldsymbol{H}_{\text{SOT}}$ is invariant under $m_z$ since neither $m_z$ nor $e_z$ appear in Eq. (2).

*Micromagnetics.*—The magnetization dynamics can be described by the semiclassical Landau-Lifshitz-Gilbert equation

$$\dot{\boldsymbol{m}} = -|\gamma|\boldsymbol{m} \times \boldsymbol{H}_{\text{eff}} + \alpha\,\boldsymbol{m} \times \dot{\boldsymbol{m}} + \boldsymbol{\tau}. \quad (4)$$

Here, $\alpha > 0$ is the dimensionless Gilbert damping parameter, $\boldsymbol{H}_{\text{eff}} = -M_s^{-1}\delta f[\boldsymbol{m}]/\delta\boldsymbol{m}$ is an effective magnetic field that describes the magnetization direction $\boldsymbol{m}$ that minimizes the free energy density functional $f[\boldsymbol{m}]$, and $M_s$ is the saturation magnetization. Interestingly, we note that a functional exists that generates the effective SOT field in Eq. (2), which is given by

$$f_{\text{SOT}}[\boldsymbol{m}] = M_s\Gamma_0\left[J_y m_x m_y - \frac{1}{2}J_x(m_x^2 - m_y^2)\right]. \quad (5)$$

The out-of-equilibrium current-induced SOT can therefore be absorbed into an effective field $\tilde{\boldsymbol{H}}_{\text{eff}}$ that minimizes the *effective* free energy density $f_{\text{eff}}[\boldsymbol{m}] = f[\boldsymbol{m}] + f_{\text{SOT}}[\boldsymbol{m}]$.

The 2D ferromagnet $Fe_3GeTe_2$ is a uniaxial ferromagnet with an out-of-plane easy axis [13,14,29]. The contribution of the dipole-dipole interaction to the spin wave spectrum can be neglected for a monolayer system [30–34]. If we consider a spatially uniform magnetization and use a spherical basis, $(m_x, m_y, m_z) = (\sin\theta\cos\phi, \sin\theta\sin\phi, \cos\theta)$, the effective free energy becomes

$$f_{\text{eff}}[\theta, \phi] = -\frac{M_s}{2}[K_z\cos^2\theta + \Gamma_0|J|\sin^2\theta\cos(2\phi + \phi_J)]. \quad (6)$$

Here, $K_z > 0$ is the out-of-plane anisotropy constant, and $|J|$ and $\phi_J = \arctan(J_y/J_x)$ are the magnitude and azimuthal angle of the applied current, respectively. From this, we find that the SOT effectively acts as in-plane magnetocrystalline anisotropies. The anisotropy originating from the SOT always comes in a pair of perpendicular easy and hard axes.

The directions of the anisotropy axes depend on the direction of the applied current. For weak currents ($|\Gamma_0 J| < K_z$), the magnetization of $Fe_3GeTe_2$ remains out of plane ($\theta = 0, \pi$). However, for sufficiently strong currents ($|\Gamma_0 J| > K_z$), an in-plane configuration of the magnetization becomes more energetically favorable. Assuming that $\Gamma_0 > 0$, the effective free energy is then minimized by $\theta = \pi/2$ and $\phi = n\pi - \phi_J/2$ ($n = 0, 1, 2, \ldots$). When $\Gamma_0 < 0$, the easy and hard axes are interchanged, and the minima are $\phi = (n + 1/2)\pi - \phi_J/2$. The easy and hard axes also interchange upon reversal of the applied current.

*Magnon gap.*—Because the SOT can effectively be considered a current-controlled magnetocrystalline anisotropy, we can electrically control the magnon gap in $Fe_3GeTe_2$. The magnon gap is governed by the energy difference between the out-of-plane and in-plane magnetization configurations, i.e., $|K_z - |\Gamma_0 J||$. At the critical current $|J_c| = K_z/|\Gamma_0|$, the magnon gap vanishes as the magnetic easy axis transitions from an out-of-plane axis to an in-plane axis. Exactly at this transition point, we obtain a magnetic easy plane. Below the critical current, the magnon gap decreases monotonically with the applied current, whereas it increases monotonically above the critical current. The ability to electrically tune the magnon gap in a 2D magnetic material opens the door for exploring a wide variety of effects in magnetism in two dimensions.

*Curie temperature.*—The first effect that is characteristic of a two-dimensional system that we will now illustrate is the dependence of the Curie temperature on the magnon gap. Because the Curie temperature in 2D is primarily governed by the magnon gap, unlike in 3D [35], we will study its behavior as we tune the SOT-controlled magnon gap through the transition from an out-of-plane easy axis to an in-plane easy axis. To illustrate the basic aspects of current control of the Curie temperature, we make a few simplifications to reduce the number of free parameters and the complexity of the calculations. $Fe_3GeTe_2$ is an itinerant ferromagnet, and its magnetic interactions are therefore described by the Stoner model [29]. The Stoner model can in our system be transformed into a Ruderman-Kittel-Kasuya-Yosida (RKKY) exchange interaction between the iron atoms [36]. We assume that the exchange interaction in a $Fe_3GeTe_2$ monolayer has a finite range and therefore obeys the Mermin-Wagner theorem. To simplify the calculations, we replace the Stoner or RKKY exchange interaction by a simple nearest-neighbor interaction between the $Fe^{II}$ and $Fe^{III}$ atoms (i.e., there is no exchange interaction within each sublattice or between the two different $Fe^{III}$ sublattices). This will also obey the Mermin-Wagner theorem, and this system will consequently also exhibit the same qualitative dependence on the magnon gap as other finite-range interactions. We also assume that the magnetic anisotropy constants are identical at all sites. Consequently, we consider the model Hamiltonian

$$\mathcal{H} = -\frac{\varepsilon_J}{2\hbar^2} \sum_r \sum_\delta \mathbf{S}_r \cdot \mathbf{S}_{r+\delta} - \frac{\varepsilon_z}{2\hbar^2} \sum_r (S_{r,z})^2$$
$$- \frac{\varepsilon_x}{2\hbar^2} \sum_r [(S_{r,x})^2 - (S_{r,y})^2]. \tag{7}$$

Here, $\varepsilon_J > 0$ is an energy constant that describes the nearest-neighbor exchange interactions of spins separated by $\boldsymbol{\delta}$, $\varepsilon_z > 0$ is an energy constant that describes the out-of-plane anisotropy, and $\varepsilon_x \propto \Gamma_0 J_x > 0$ is an energy constant that describes the effective in-plane anisotropies caused by the SOT. $S_{r,i}$ ($i = x, y, z$) describes the $i$th component of the spin operator located at position $r$. We split the $Fe_3GeTe_2$ monolayer into three distinct sublattices: one for the $Fe^{II}$ atoms, one for the $Fe^{III}$ atoms at $z = +b$, and one for the $Fe^{III}$ atoms at $z = -b$.

We proceed by performing a Holstein-Primakoff transformation of the spin operators around the equilibrium spin direction. This is in the $z$ direction below the critical current $J_c$ and along the $x$ direction above the critical current. Because of the anomalous Hall effect in $Fe_3GeTe_2$ [14,37,38], applying the current exactly along the $x$ direction can be experimentally challenging. However, as can be deduced from Eq. (6), a scenario in which the current is applied in a different direction can be achieved by a rotation of the unit cell or Brillouin zone. Since it is the magnons closest to the $\Gamma$ point that dominate the calculation of the Curie temperature, we expect the results to be very similar for an off-axis current.

In our calculations, we keep terms to the second order in the Holstein-Primakoff magnon operators. We expect this to be a good qualitative approximation, although it will not be a very good quantitative approximation because the magnon population diverges at the critical point. However, keeping terms to, for instance, the fourth order in the magnon operators to include magnon-magnon interactions [9] would be complicated because Eq. (7) does not conserve the magnon number for finite currents.

Following the Holstein-Primakoff transformation, we perform a Fourier transformation of the magnon operators to momentum space. We then diagonalize the Hamiltonian by a Bogoliubov transformation such that it takes the form [27]

$$\mathcal{H} = \sum_{\mathbf{k},\mu} \varepsilon_{\mathbf{k},\mu} \alpha_{\mathbf{k},\mu}^\dagger \alpha_{\mathbf{k},\mu}. \tag{8}$$

Here, the operator $\alpha_{\mathbf{k},\mu}^{(\dagger)}$ annihilates (creates) an eigenmagnon with a momentum $\mathbf{k}$ and energy $\varepsilon_{\mathbf{k},\mu}$. There are three different modes ($\mu = I, II, III$) of the eigenmagnons. We have imposed the constraint on the Bogoliubov transformation that the new operators have to satisfy bosonic commutation relations: $[\alpha_{\mathbf{k},\mu}, \alpha_{\mathbf{k}',\mu'}^\dagger] = \delta_{\mathbf{k}\mathbf{k}'}\delta_{\mu\mu'}$.

From the energy spectrum of the eigenmagnons in $Fe_3GeTe_2$, we can estimate the Curie temperature $T_c$. To determine $T_c$, we use the fact that the magnetization along

the equilibrium direction of the spins vanishes at this temperature. Because we consider a monolayer system, we only have magnons with in-plane momenta. Balancing the magnetic moments, we find the constraint

$$\sum_\nu s_\nu - \sum_\mu \frac{1}{A_{BZ}} \int_{A_{BZ}} d^2k \frac{S_{\boldsymbol{k},\mu}/\hbar}{\exp(\varepsilon_{\boldsymbol{k},\mu}/k_B T_c) - 1} = 0. \quad (9)$$

Here, $s_\nu$ is the dimensionless spin number of the magnetic moments in sublattice $\nu$ (where $\nu = 2$ for the $Fe^{II}$ atoms, and $\nu = 3_\pm$ for the $Fe^{III}$ atoms located at $z = \pm b$), and $A_{BZ} = \sqrt{3}\pi^2/(2a^2)$ is the (reciprocal) area of the first Brillouin zone. $S_{\boldsymbol{k},\mu}$ is the spin of the eigenmagnons, which is *not* an integer for finite SOT because of magnon squeezing [39]. The spin of the eigenmagnons depends on the parameters of the Bogoliubov transformation and is given in the Supplemental Material [27].

We can now calculate the Curie temperature numerically based on Eq. (9). In our calculations, we set the out-of-plane anisotropy constant to be $\varepsilon_z = 0.335$ meV [29]. The value of the nearest-neighbor exchange coupling is set to be $\varepsilon_J = 0.705$ meV to reproduce the experimental $T_c$ of a monolayer of $\sim$130 K [13] (note, however, that a different experiment determined the $T_c$ of a monolayer to be $\sim$68 K [14]). The real value of $\varepsilon_J$ is in all likelihood larger [14] because the linear response method typically overestimates $T_c$. The dimensionless spin numbers $s_\nu$ for the spins in sublattice $\nu$ are $s_2 = 2$ and $s_{3_-}, s_{3_+} = 5/2$ [40]. We plot the Curie temperature as a function of the applied current in Fig. 2.

Because we only kept terms to the second order in the magnon operators, we do not expect that our calculation of $T_c$ will be quantitatively correct. However, the qualitative features of our result appear to be physically reasonable. When we apply a SOT below the critical current $|J_c|$, we
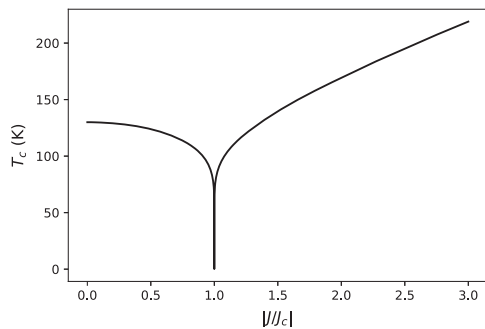


FIG. 2. Numerical calculation of $T_c$ for a spontaneous magnetization based on a simple linear response model of the magnon spectrum. The result is identical for any direction of the applied current $\boldsymbol{J}$. Below $|J_c|$, the magnetization is along the $z$ axis, whereas above $|J_c|$, the magnetization is along an in-plane axis determined by the direction of the applied current.

effectively reduce the magnon gap by creating a pair of easy and hard axes perpendicular to the out-of-plane magnetization. Because the Curie temperature in 2D materials is governed by the magnon gap, this also reduces $T_c$. At the critical current strength, we obtain a continuous symmetry in the form of an easy plane when the in-plane easy axis induced by the SOT becomes equal to the out-of-plane magnetocrystalline anisotropy. Because of the Mermin-Wagner theorem, there can be no long-range magnetic order at finite temperatures in this scenario, and $T_c$ drops to zero. Above the critical current, we now increase the magnon gap for an in-plane magnetization configuration, and $T_c$ increases accordingly. $T_c$ will then saturate at the Curie temperature of the Ising model for large currents, which our model does not capture [41].

In addition to the current affecting the Curie temperature through a SOT, the current will also increase the temperature in the material due to joule heating, which needs to be taken into account when measuring the Curie temperature of the material. The joule heating increases quadratically with the applied current. Conversely, the SOT is linear in the applied current, but its effect on the Curie temperature depends on whether we are above or below the critical current. Consequently, if the critical current is sufficiently small, then the effect of the SOT will dominate that of the joule heating. In this case, the magnetic ordering exhibits reentrant behavior as a function of the applied current. Notably, above the critical current, when the magnetization is in the plane, the easy and hard axes are interchanged upon reversal of the current direction. A reversal of the applied current would therefore lead to a 90° rotation of the magnetization.

*2D XY model.*—Although the spontaneous magnetization vanishes for finite temperatures at the critical current density $|J_c|$, this regime remains an interesting region for studying the magnetic properties. At the critical current density ($|\varepsilon_x| = \varepsilon_z$), the model in Eq. (7) becomes, quite remarkably, a 2D easy-plane ferromagnet, where the easy plane is perpendicular to the plane of the monolayer. Therefore, at this current density, the model features a critical phenomenon in the universality class of the 2D *XY* model. Consequently, the system has a topological phase transition rather than the more conventional phase transition of the 2D Ising model [1]. The 2D Ising universality class falls within the framework of the Landau-Ginzburg-Wilson paradigm of phase transitions of an order-disorder transition monitored by a local order parameter [42,43]. The spin-spin correlation length diverges from above and below $T_c$ as $\xi \sim |T - T_c|^{-\nu}$, where $\nu$ is a universal critical exponent. There is true long-range order in the low-temperature phase, short-range order in the high-temperature phase, and power-law spin-spin correlations precisely at the critical point. In contrast, the 2D *XY* model features a genuine phase transition with no local order parameter. At this phase transition, the spin-spin correlation

length diverges as $\xi \sim \exp(\text{const}/\sqrt{T - T_{\text{BKT}}})$ from the high-temperature side only [4], where $T_{\text{BKT}}$ is the critical temperature of the BKT transition. The high-temperature phase has short-range order, and the entire low-temperature phase is critical with a spin-spin correlation function featuring a nonuniversal temperature-dependent anomalous dimension $\eta$, $\langle \mathbf{S_r} \cdot \mathbf{S_{r'}} \rangle \sim 1/|\mathbf{r} - \mathbf{r'}|^{\eta}$ [4].

In 2D $Fe_3GeTe_2$, we may realize this type of highly nontrivial behavior by tuning the electric current to the critical value and then drive the system through the phase transition by varying the temperature. Moreover, below the BKT transition, the temperature dependence of the non-universal anomalous dimension $\eta$ of the 2D $XY$ model can be mapped by varying the temperature and measuring the spin-spin correlation function by polarized small-angle neutron scattering, which is particularly well suited for ultrathin films [44]. The present system is also amenable to studying the universal anomalous dimension of the 2D Ising model at $T = T_c$, $\eta = 1/4$ [45]. The prediction for the 2D $XY$ model, $\eta = k_B T/4\pi J$ [4], where $J$ is the effective exchange coupling and $k_B$ is Boltzmann's constant, has not been tested in real 2D magnetic systems to our knowledge.

Examples of real physical systems with this level of control over such phenomena are very rare, particularly for systems where the phenomena are accessible at relatively elevated temperatures. The most well-known example is superfluidity in thin films of $^4$He, where the BKT transition occurs below 1.2 K [46]. In that context, the remarkable prediction and experimental verification of a universal jump in the superfluid density of the system [46,47] is also worth noting. We expect the corresponding physics of a universal jump in the spin stiffness of the system to occur at liquid nitrogen or oxygen temperatures in the system studied here. The spin stiffness may be measured in spin wave resonance experiments [48]. Furthermore, and in contrast to our present case, $\eta$ is not experimentally accessible in superfluid thin films of $^4$He.

The parameter $\Gamma_0$ determines the magnitude of the critical current and thus the accessibility of the effects that we discuss. This value cannot be obtained purely from symmetry considerations but rather needs to be determined experimentally or by *ab initio* calculations. In light of the exciting physics that can be realized and the flexibility of the system, determining its value would be very interesting. Based on the strong magnetic anisotropy of the material, we believe that the spin-orbit coupling is sufficiently strong. Paired with the observation that SOTs are typically sufficiently large to induce magnetization switching in other materials [22], we have reason to believe that reentrant magnetism and topological phase transitions can be experimentally observed in $Fe_3GeTe_2$.

Ø. J. and V. R. contributed equally to this work.

* oyvinjoh@ntnu.no

† vetle.k.risinggard@ntnu.no

[1] L. Onsager, Crystal statistics. I. A two-dimensional model with an order-disorder transition, Phys. Rev. **65**, 117 (1944).

[2] V. L. Berezinskiǐ, Destruction of long-range order in one-dimensional and two-dimensional systems having a continuous symmetry group I. Classical systems, Sov. Phys. JETP **32**, 493 (1971).

[3] V. L. Berezinskiǐ, Destruction of long-range order in one-dimensional and two-dimensional systems possessing a continuous symmetry group. II. Quantum systems, Sov. Phys. JETP **34**, 610 (1972).

[4] J. M. Kosterlitz and D. J. Thouless, Ordering, metastability and phase transitions in two-dimensional systems, J. Phys. C **6**, 1181 (1973).

[5] K. S. Novoselov, A. K. Geim, S. V. Morozov, D. Jiang, Y. Zhang, S. V. Dubonos, I. V. Grigorieva, and A. A. Firsov, Electric field effect in atomically thin carbon films, Science **306**, 666 (2004).

[6] N. D. Mermin and H. Wagner, Absence of Ferromagnetism or Antiferromagnetism in One- or Two-Dimensional Isotropic Heisenberg Models, Phys. Rev. Lett. **17**, 1133 (1966).

[7] K. S. Burch, D. Mandrus, and J.-G. Park, Magnetism in two-dimensional van der Waals materials, Nature (London) **563**, 47 (2018).

[8] J. U. Lee, S. Lee, J. H. Ryoo, S. Kang, T. Y. Kim, P. Kim, C.-H. Park, J.-G. Park, and H. Cheong, Ising-type magnetic ordering in atomically thin $FePS_3$, Nano Lett. **16**, 7433 (2016).

[9] C. Gong *et al.*, Discovery of intrinsic ferromagnetism in two-dimensional van der Waals crystals, Nature (London) **546**, 265 (2017).

[10] B. Huang *et al.*, Layer-dependent ferromagnetism in a van der Waals crystal down to the monolayer limit, Nature (London) **546**, 270 (2017).

[11] M. Bonilla, S. Kolekar, Y. Ma, H. C. Diaz, V. Kalappattil, R. Das, T. Eggers, H. R. Gutierrez, M.-H. Phan, and M. Batzill, Strong room-temperature ferromagnetism in $VSe_2$ monolayers on van der Waals substrates, Nat. Nanotechnol. **13**, 289 (2018).

[12] D. J. O'Hara *et al.*, Room temperature intrinsic ferromagnetism in epitaxial manganese selenide films in the monolayer limit, Nano Lett. **18**, 3125 (2018).

[13] Z. Fei *et al.*, Two-dimensional itinerant ferromagnetism in atomically thin $Fe_3GeTe_2$, Nat. Mater. **17**, 778 (2018).

[14] Y. Deng *et al.*, Gate-tunable room-temperature ferromagnetism in two-dimensional $Fe_3GeTe_2$, Nature (London) **563**, 94 (2018).

[15] Y. Lai, Z. Song, Y. Wan, M. Xue, Y. Ye, L. Dai, W. Yang, H. Du, and J. Yang, Discovery of two-dimensional multiferroicity in van der Waals $CuCrP_2S_6$ layers, arXiv:1805.04280.

[16] B. Huang *et al.*, Electrical control of 2D magnetism in bilayer CrI$_3$, Nat. Nanotechnol. **13**, 544 (2018).

[17] S. Jiang, L. Li, Z. Wang, K. F. Mak, and J. Shan, Controlling magnetism in 2D CrI$_3$ by electrostatic doping, Nat. Nanotechnol. **13**, 549 (2018).

[18] Z. Wang *et al.*, Electric-field control of magnetism in a few-layered van der Waals ferromagnetic semiconductor, Nat. Nanotechnol. **13**, 554 (2018).

[19] H. H. Kim, B. Yang, T. Patel, F. Sfigakis, C. Li, S. Tian, H. Lei, and A. W. Tsen, One million percent tunnel magneto-resistance in a magnetic van der Waals heterostructure, Nano Lett. **18**, 4885 (2018).

[20] A. Brataas, A. D. Kent, and H. Ohno, Current-induced torques in magnetic materials, Nat. Mater. **11**, 372 (2012).

[21] A. Manchon and S. Zhang, Theory of nonequilibrium intrinsic spin torque in a single nanomagnet, Phys. Rev. B **78**, 212405 (2008).

[22] A. Manchon, I. M. Miron, T. Jungwirth, J. Sinova, J. Zelenzný, A. Thiaville, K. Garello, and P. Gambardella, Current-induced spin-orbit torques in ferromagnetic and antiferromagnetic systems, arXiv:1801.09636.

[23] D. B. Kaplan, J.-W. Lee, D. T. Son, and M. A. Stephanov, Conformality lost, Phys. Rev. D **80**, 125005 (2009).

[24] H.-J. Deiseroth, K. Aleksandrov, C. Reiner, L. Kienle, and R. K. Kremer, Fe$_3$GeTe$_2$ and Ni$_3$GeTe$_2$ — two new layered transition-metal compounds: Crystal structures, HRTEM investigations, and magnetic and electrical properties, Eur. J. Inorg. Chem. **2006**, 1561 (2006).

[25] J. C. Meyer, A. K. Geim, M. I. Katsnelson, K. S. Novoselov, T. J. Booth, and S. Roth, The structure of suspended graphene sheets, Nature (London) **446**, 60 (2007).

[26] K. M. D. Hals and A. Brataas, Phenomenology of current-induced spin-orbit torques, Phys. Rev. B **88**, 085423 (2013); Spin-motive forces and current-induced torques in ferro-magnets, Phys. Rev. B **91**, 214401 (2015).

[27] See Supplemental Material at http://link.aps.org/supplemental/10.1103/PhysRevLett.122.217203 for a derivation of the spin-orbit torques and the details of the critical-temperature calculation, which includes Ref. [28].

[28] R. R. Birss, in *Symmetry and Magnetism*, edited by E. P. Wohlfarth, Selected Topics in Solid State Physics, Vol. 3, 1st ed. (North-Holland Publishing Company, Amsterdam, 1964).

[29] H. L. Zhuang, P. R. C. Kent, and R. G. Hennig, Strong anisotropy and magnetostriction in the two-dimensional Stoner ferromagnet Fe$_3$GeTe$_2$, Phys. Rev. B **93**, 134407 (2016).

[30] D. N. Chartoryzhskii, B. A. Kalinikos, and O. G. Vendik, Parallel pump spin wave instability in thin ferromagnetic films, Solid State Commun. **20**, 985 (1976).

[31] B. A. Kalinikos, Excitation of propagating spin waves in ferromagnetic films, IEE Proc. H **127**, 4 (1980).

[32] B. A. Kalinikos, Spectrum and linear excitation of spin waves in ferromagnetic films, Sov. Phys. J. **24**, 718 (1981).

[33] B. A. Kalinikos and A. N. Slavin, Theory of dipole-exchange spin wave spectrum for ferromagnetic films with mixed exchange boundary conditions, J. Phys. C **19**, 7013 (1986).

[34] B. A. Kalinikos, M. P. Kostylev, N. V. Kozhus, and A. N. Slavin, The dipole-exchange spin wave spectrum for aniso-tropic ferromagnetic films with mixed exchange boundary conditions, J. Phys. Condens. Matter **2**, 9861 (1990).

[35] A. Auerbach, *Interacting Electrons and Quantum Magnet-ism*, Graduate Texts in Contemporary Physics (Springer-Verlag, Berlin, 1994).

[36] R. E. Prange and V. Korenman, Local-band theory of itinerant ferromagnetism. IV. Equivalent Heisenberg model, Phys. Rev. B **19**, 4691 (1979).

[37] C. Tan, J. Lee, S.-G. Jung, T. Park, S. Albarakati, J. Partridge, M. R. Field, D. G. McCulloch, L. Wang, and C. Lee, Hard magnetic properties in nanoflake van der Waals Fe$_3$GeTe$_2$, Nat. Commun. **9**, 1554 (2018).

[38] N. Nagaosa, J. Sinova, S. Onoda, A. H. MacDonald, and N. P. Ong, Anomalous Hall effect, Rev. Mod. Phys. **82**, 1539 (2010).

[39] A. Kamra, U. Agrawal, and W. Belzig, Noninteger-spin magnonic excitations in untextured magnets, Phys. Rev. B **96**, 020411(R) (2017).

[40] J. H. Rodriguez, H. N. Ok, Y.-M. Xia, P. G. Debrunner, B. E. Hinrichs, T. Meyer, and N. H. Packard, Mössbauer spec-troscopy of the spin-coupled Fe$^{3+}$–Fe$^{2+}$ center of reduced uteroferrin, J. Phys. Chem. **100**, 6849 (1996).

[41] D. Torelli and T. Olsen, Calculating critical temperatures for ferromagnetic order in two-dimensional materials, 2D Mater. **6**, 015028 (2019).

[42] L. D. Landau, E. M. Lifshitz, and E. M. Pitaevskii, *Statistical Physics*, 1st ed. (Butterworth and Heinemann, London, 1999).

[43] K. G. Wilson and J. B Kogut, The renormalization group and the $\varepsilon$ expansion, Phys. Rep. **12**, 75 (1974).

[44] T. Maurer, S. Gautrot, F. Ott, G. Chaboussant, F. Zighem, L. Cagnon, and O. Fruchart, Ordered arrays of magnetic nanowires investigated by polarized small-angle neutron scattering, Phys. Rev. B **89**, 184423 (2014).

[45] C. Itzykson and J.-M. Drouffe, *Statistical Field Theory*, Cambridge Monographs on Mathematical Physics (Cambridge University Press, Cambridge, England, 1989), Vol. 1.

[46] D. J. Bishop and J. D. Reppy, Study of the Superfluid Transition in Two-Dimensional $^4$He Films, Phys. Rev. Lett. **40**, 1727 (1978).

[47] D. R. Nelson and J. M. Kosterlitz, Universal Jump in the Superfluid Density of Two-Dimensional Superfluids, Phys. Rev. Lett. **39**, 1201 (1977).

[48] M. Golosovsky, P. Monod, P. K. Muduli, and R. C. Budhani, Spin-wave resonances in La$_{0.7}$Sr$_{0.3}$MnO$_3$ films: Measure-ment of spin-wave stiffness and anisotropy field, Phys. Rev. B **76**, 184413 (2007).

**Supplementary Material to**
**"Current Control of Magnetism in Two-Dimensional Fe$_3$GeTe$_2$"**

Øyvind Johansen,[*] Vetle Risinggård,[†] Asle Sudbø, Jacob Linder, and Arne Brataas
*Center for Quantum Spintronics, Department of Physics, NTNU,*
*Norwegian University of Science and Technology, N-7491 Trondheim, Norway*
(Dated: December 19, 2018)

## I. DERIVATION OF SPIN–ORBIT TORQUES IN Fe$_3$GeTe$_2$

Ref. [1] has shown that in the linear response regime under the local approximation, the current-induced torques can be written as

$$\boldsymbol{\tau}(\boldsymbol{r},t) = -|\gamma|\boldsymbol{m}(\boldsymbol{r},t) \times \boldsymbol{H}_{\mathrm{SOT}}, \qquad H_{\mathrm{SOT},i} = \eta_{ij} J_j, \qquad (1)$$

where $\boldsymbol{m}$ is the magnetization unit vector, $\boldsymbol{J}$ is the current density applied to the system, and $\eta$ is a second-rank tensor. (Summation over repeated indices is implied.) Which elements of $\eta_{ij}$ that are nonzero is determined by the symmetry of the system. The tensor $\eta$ can be expanded in the magnetization components $m_i$ and their derivatives $\partial_i m_j$. If we only consider a uniform magnetization, one obtains to lowest order

$$\eta_{ij} = \Lambda_{ij} + \Gamma_{ijk} m_k + \dots \qquad (2)$$

where $\Lambda_{ij}$ is an axial second-rank tensor, and $\Gamma_{ijk}$ is a polar third-rank tensor.

To determine which contributions to the tensors $\Lambda_{ij}$ and $\Gamma_{ijk}$ that are allowed by symmetry, Ref. [1] imposes the criterion that these tensors must be invariant under all transformations $R$ in the point group $G$ of the structure. This amounts to demanding that the relations

$$\Lambda_{ij} = |R| R_{ii'} R_{jj'} \Lambda_{i'j'}, \qquad (3)$$
$$\Gamma_{ijk} = R_{ii'} R_{jj'} R_{kk'} \Gamma_{i'j'k'}, \qquad (4)$$

are fulfilled for all $R \in G$.

Monolayer Fe$_3$GeTe$_2$ crystallizes in point group $\bar{\mathbf{6}}\mathbf{m2}$ ($D_{3h}$) [2]. Since this group is generated by the elements $\bar{\mathbf{6}}_z$, $\mathbf{m}_y$, and $\mathbf{2}_x$, it is sufficient to impose that $\eta_{ij}$ should be invariant under these operations [3]. The representing matrices of these symmetry operations are

$$\mathbf{m}_y = \begin{pmatrix} 1 & & \\ & -1 & \\ & & 1 \end{pmatrix}, \ \mathbf{2}_x = \begin{pmatrix} 1 & & \\ & -1 & \\ & & -1 \end{pmatrix}, \ \bar{\mathbf{6}}_z = \frac{1}{2}\begin{pmatrix} -1 & -\sqrt{3} & \\ \sqrt{3} & -1 & \\ & & -2 \end{pmatrix}.$$

Eq. (3) with $R = \mathbf{2}_x$ implies that $\Lambda_{ij}$ vanishes when $x$ appears an odd number of times in the indices $ij$. (That is, $\Lambda_{xj} = \Lambda_{ix} = 0$ for $i,j = y,z$.) Similarly, $R = \mathbf{m}_y$ implies that $\Lambda_{ij}$ vanishes when $y$ appears an even number of times in the indices $ij$. (That is, $\Lambda_{ij} = 0$ for $i,j = x,z$ and $\Lambda_{yy} = 0$.) Consequently, only

$\Lambda_{yz}$ and $\Lambda_{zy}$ are invariant under the symmetry operations $\mathbf{2}_x$ and $\mathbf{m}_y$. The operation $\bar{\mathbf{6}}_z$ gives

$$\Lambda_{yz} = -\tfrac{1}{2}\Lambda_{yz} \quad \text{and} \quad \Lambda_{zy} = -\tfrac{1}{2}\Lambda_{zy}$$

for these elements. These relations can only hold for $\Lambda_{ij} = 0$. Thus we conclude that $\Lambda_{ij} = 0 \ \forall \ i,j$.

Repeating the analysis for $\Gamma_{ijk}$ with Eq. (4), $R = \mathbf{2}_x$ implies that $\Gamma_{ijk}$ vanishes when $x$ appears an even number of times in the indices $ijk$, and $R = \mathbf{m}_y$ implies that $\Gamma_{ijk}$ vanishes when $y$ appears an odd number of times in the indices $ijk$. Consequently, only $\Gamma_{yyx}$, $\Gamma_{xzz}$, $\Gamma_{xxx}$, and the four other elements generated by freely permuting the indices $yyx$ and $xzz$ are invariant under the symmetry operations $\mathbf{2}_x$ and $\mathbf{m}_y$. The operation $\bar{\mathbf{6}}_z$ gives

$$\Gamma_{xzz} = -\tfrac{1}{2}\Gamma_{xzz}, \quad \Gamma_{zxz} = -\tfrac{1}{2}\Gamma_{zxz}, \quad \text{and} \quad \Gamma_{zzx} = -\tfrac{1}{2}\Gamma_{zzx},$$

which implies that $\Gamma_{xzz} = \Gamma_{zxz} = \Gamma_{zzx} = 0$. Furthermore,

$$\Gamma_{yyx} = \tfrac{1}{8}(-\Gamma_{yyx} + 3\Gamma_{yxy} + 3\Gamma_{xyy} - 3\Gamma_{xxx}),$$
$$\Gamma_{yxy} = \tfrac{1}{8}(3\Gamma_{yyx} - \Gamma_{yxy} + 3\Gamma_{xyy} - 3\Gamma_{xxx}),$$
$$\Gamma_{xyy} = \tfrac{1}{8}(3\Gamma_{yyx} + 3\Gamma_{yxy} - \Gamma_{xyy} - 3\Gamma_{xxx}),$$

and

$$\Gamma_{xxx} = -\tfrac{1}{8}[\Gamma_{xxx} + 3(\Gamma_{yyx} + \Gamma_{yxy} + \Gamma_{xyy})].$$

Together these relations imply $\Gamma_{yyx} = \Gamma_{yxy} = \Gamma_{xyy} = -\Gamma_{xxx}$. We conclude that $\Gamma_{ijk}$ has four nonzero components, but only one free parameter, $\Gamma_{xxx} = \Gamma_0$. The effective field corresponding to the spin–orbit torque in Fe$_3$GeTe$_2$ is thus

$$\boldsymbol{H}_{\mathrm{SOT}} = \Gamma_0[(m_x J_x - m_y J_y)\boldsymbol{e}_x - (m_y J_x + m_x J_y)\boldsymbol{e}_y]. \quad (5)$$

## II. MAGNON SPIN AND ENERGY SPECTRUM

Using the result that the spin-orbit torque leads to a set of perpendicular in-plane easy and hard axes, as derived in the manuscript, we can write a model Hamiltonian in zero-external field,

$$\mathcal{H} = -\frac{\varepsilon_J}{2\hbar^2} \sum_{\boldsymbol{r}} \sum_{\boldsymbol{\delta}} \boldsymbol{S}_{\boldsymbol{r}} \cdot \boldsymbol{S}_{\boldsymbol{r}+\boldsymbol{\delta}} - \frac{\varepsilon_z}{2\hbar^2} \sum_{\boldsymbol{r}} (S_{\boldsymbol{r},z})^2$$
$$- \frac{\varepsilon_x}{2\hbar^2} \sum_{\boldsymbol{r}} \left[ (S_{\boldsymbol{r},x})^2 - (S_{\boldsymbol{r},y})^2 \right]. \quad (6)$$

Here we only consider nearest-neighbour exchange interaction between sites separated by $\boldsymbol{\delta}$, and only consider a current in the $x$-direction ($\varepsilon_x \propto \Gamma_0 J_x > 0$), as the anisotropy behaves similarly (just with different axes) if we have a $y$-component of the current.

## A. Below the critical current

Below the critical current, the equilibrium configuration is along the $z$ axis. We do a Holstein–Primakoff transformation of the spin operators, defined by

$$S_{i,\nu,+} = \hbar\sqrt{2s_\nu}\, a_{i,\nu}^\dagger \sqrt{1 - \frac{a_{i,\nu}^\dagger a_{i,\nu}}{2s_\nu}} \approx \hbar\sqrt{2s_\nu}\, a_{i,\nu}^\dagger, \qquad (7)$$

$$S_{i,\nu,-} = \hbar\sqrt{2s_\nu} \sqrt{1 - \frac{a_{i,\nu}^\dagger a_{i,\nu}}{2s_\nu}}\, a_{i,\nu} \approx \hbar\sqrt{2s_\nu}\, a_{i,\nu}, \qquad (8)$$

$$S_{i,\nu,z} = \hbar \left( a_{i,\nu}^\dagger a_{i,\nu} - s_\nu \right), \qquad (9)$$

where $S_\pm = S_x \pm i S_y$, $i$ is the label of the unit cell, and $\nu = 2, 3_\pm$ indicates the sublattice of the $Fe^{II}$ and $Fe^{III}$ atoms, respectively, where sublattice $\nu = 3_+$ ($\nu = 3_-$) consists of the $Fe^{III}$ atoms located at $z = +b$ ($z = -b$). We assume the nearest-neighbor exchange interaction is only between sublattice $\nu = 2$ and $\nu = 3_\pm$, and that there is no exchange interaction between the $Fe^{III}$ atoms. Rewriting the Hamiltonian to the $S_\pm$ basis, we get

$$\mathcal{H} = -\frac{\varepsilon_J}{2\hbar^2}\sum_{r,\delta} \left[ \frac{1}{2}\left( S_{r,+}S_{r+\delta,-} + S_{r,-}S_{r+\delta,+}\right) + S_{r,z}S_{r+\delta,z} \right]$$
$$- \frac{\varepsilon_z}{2\hbar^2}\sum_r \left(S_{r,z}\right)^2 - \frac{\varepsilon_x}{4\hbar^2}\sum_r \sum_{m=\pm}\left(S_{r,m}\right)^2. \qquad (10)$$

Inserting the Holstein–Primakoff transformation, keeping terms to second order in the magnon operators, we get

$$\mathcal{H} = -\varepsilon_J \sum_i \sum_{r_j = r_i + \delta}\sum_{\nu = 3_\pm} \left[ \sqrt{s_2 s_\nu}\left( a_{i,2}^\dagger a_{j,\nu} + a_{j,\nu}^\dagger a_{i,2}\right)\right.$$
$$\left. - s_\nu a_{i,2}^\dagger a_{i,2} - s_2 a_{j,\nu}^\dagger a_{j,\nu} \right] + \varepsilon_z \sum_{i,\nu} s_\nu a_{i,\nu}^\dagger a_{i,\nu}$$
$$- \frac{\varepsilon_x}{2}\sum_{i,\nu} s_\nu (a_{i,\nu}^\dagger a_{i,\nu}^\dagger + a_{i,\nu}a_{i,\nu}), \qquad (11)$$

disregarding any constant terms, where $r_j$ is the position of the nearest-neighbor atom of the atom located in unit cell $i$ and sublattice $\nu = 2$. Next we perform a Fourier transform to momentum space, defined by

$$a_{i,\nu} = \frac{1}{\sqrt{N}}\sum_k a_{k,\nu}\, e^{-ik\cdot r_{i,\nu}}, \quad a_{i,\nu}^\dagger = \frac{1}{\sqrt{N}}\sum_k a_{k,\nu}^\dagger\, e^{ik\cdot r_{i,\nu}}, \qquad (12)$$

with $N$ being the number of unit cells, and $k$ the wave vector running over the first Brillouin zone. The Hamiltonian then becomes (disregarding any constant terms)

$$\mathcal{H} = \sum_k \sum_{z=\pm} \varepsilon_J \left[ 3s_3 a_{k,2}^\dagger a_{k,2} + 3s_2 a_{k,3_z}^\dagger a_{k,3_z} \right.$$
$$\left. - \sqrt{s_2 s_3}\left( \gamma_{-k}^z a_{k,2}^\dagger a_{k,3_z} + \gamma_k^z a_{k,3_z}^\dagger a_{k,2}\right) \right] + \varepsilon_z \sum_{k,\nu} s_\nu a_{k,\nu}^\dagger a_{k,\nu}$$
$$- \frac{\varepsilon_x}{2}\sum_{k,\nu} s_\nu \left( a_{k,\nu}^\dagger a_{-k,\nu}^\dagger + a_{k,\nu}a_{-k,\nu}\right). \qquad (13)$$
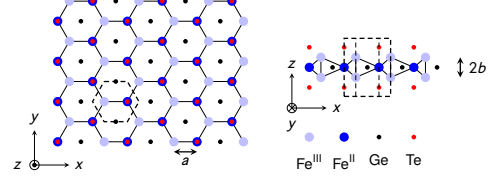


Figure 1. Crystal structure of monolayer $Fe_3GeTe_2$. All the drawn in-plane bindings are at a 120° (in-plane) angle relative the neighboring bindings. Dashed lines denote the unit cell. Left: view along $e_z$; right: view along $e_y$. $Fe^{III}$ and $Fe^{II}$ represent the two inequivalent Fe sites in oxidation states +3 and +2, respectively. Redrawn after Ref. [4].

Here we have introduced the structure factor

$$\gamma_k = \sum_\delta e^{ik\cdot\delta}, \qquad (14)$$

which becomes

$$\gamma_k^\pm = e^{\pm ik_z b}\left[ e^{-ik_x a} + 2e^{ik_x a/2}\cos\left(\frac{\sqrt{3}}{2}k_y a\right)\right] \qquad (15)$$

for $Fe_3GeTe_2$ between the $\nu = 2$ and $\nu = 3_\pm$ sublattices, as can be seen from Fig. 1. Here $a$ is the in-plane lattice constant between the $Fe^{II}$ and $Fe^{III}$ atoms, and $2b$ the separation between two $Fe^{III}$ atoms in the $z$ direction. We have also used that there are three nearest neighbors in each sublattice. We can write the Hamiltonian on the form

$$\mathcal{H} = \sum_k \left( \frac{A}{2}a_{k,2}^\dagger a_{k,2} + \frac{B}{2}a_{k,3_-}^\dagger a_{k,3_-} + \frac{B}{2}a_{k,3_+}^\dagger a_{k,3_+} \right.$$
$$\left. + C_k a_{k,2}^\dagger a_{k,3_-} + D_k a_{k,2}^\dagger a_{k,3_+} + \sum_\nu E_\nu a_{k,\nu}a_{-k,\nu} \right) + \text{H.c.} \qquad (16)$$

The coefficients $A$, $B$, $C_k$, $D_k$, and $E_\nu$ are given in Table I.

We now have to diagonalize the Hamiltonian. This can be done by a six-dimensional Bogoliubov transformation, defined by the matrix $\underline{B}_6$

$$\alpha_\kappa = \begin{pmatrix} \alpha_{\kappa,\mathrm{I}} \\ \alpha_{\kappa,\mathrm{II}} \\ \alpha_{\kappa,\mathrm{III}} \\ \alpha_{-\kappa,\mathrm{I}}^\dagger \\ \alpha_{-\kappa,\mathrm{II}}^\dagger \\ \alpha_{-\kappa,\mathrm{III}}^\dagger \end{pmatrix} = \underline{B}_6 \begin{pmatrix} a_{\kappa,2} \\ a_{\kappa,3_-} \\ a_{\kappa,3_+} \\ a_{-\kappa,2}^\dagger \\ a_{-\kappa,3_-}^\dagger \\ a_{-\kappa,3_+}^\dagger \end{pmatrix} \equiv \underline{B}_6 a_\kappa$$

$$= \sum_\nu \begin{pmatrix} u_{\mathrm{I},\nu} & v_{\mathrm{I},\nu} \\ u_{\mathrm{II},\nu} & v_{\mathrm{II},\nu} \\ u_{\mathrm{III},\nu} & v_{\mathrm{III},\nu} \\ \tilde{v}_{\mathrm{I},\nu}^* & \tilde{u}_{\mathrm{I},\nu}^* \\ \tilde{v}_{\mathrm{II},\nu}^* & \tilde{u}_{\mathrm{II},\nu}^* \\ \tilde{v}_{\mathrm{III},\nu}^* & \tilde{u}_{\mathrm{III},\nu}^* \end{pmatrix} \begin{pmatrix} a_{\kappa,\nu} \\ a_{-\kappa,\nu}^\dagger \end{pmatrix}, \qquad (17)$$

Table I. The coefficients for the Fourier transformed Hamiltonian in Eq. (16) below and above the critical current $|J_c|$.

| Coefficient | $|J| < |J_c|$ | $|J| > |J_c|$ |
|---|---|---|
| $A$ | $6s_3\varepsilon_J + s_2\varepsilon_z$ | $6s_3\varepsilon_J + \frac{1}{2}s_2(3\varepsilon_x - \varepsilon_z)$ |
| $B$ | $3s_2\varepsilon_J + s_3\varepsilon_z$ | $3s_2\varepsilon_J + \frac{1}{2}s_3(3\varepsilon_x - \varepsilon_z)$ |
| $C_{\boldsymbol{k}}$ | $-\sqrt{s_2 s_3}\gamma^{-}_{-\boldsymbol{k}}\varepsilon_J$ | $-\sqrt{s_2 s_3}\gamma^{-}_{-\boldsymbol{k}}\varepsilon_J$ |
| $D_{\boldsymbol{k}}$ | $-\sqrt{s_2 s_3}\gamma^{+}_{-\boldsymbol{k}}\varepsilon_J$ | $-\sqrt{s_2 s_3}\gamma^{+}_{-\boldsymbol{k}}\varepsilon_J$ |
| $E_\nu$ | $-\frac{1}{2}s_\nu\varepsilon_x$ | $-\frac{1}{4}s_\nu(\varepsilon_x + \varepsilon_z)$ |

where $\boldsymbol{\kappa}$ now only runs over half the vector space of $\boldsymbol{k}$, so that the Hamiltonian can be written as

$$\mathcal{H} = \sum_{\boldsymbol{\kappa},\mu}\left(\varepsilon_{\boldsymbol{\kappa},\mu}\alpha^{\dagger}_{\boldsymbol{\kappa},\mu}\alpha_{\boldsymbol{\kappa},\mu} + \varepsilon_{-\boldsymbol{\kappa},\mu}\alpha^{\dagger}_{-\boldsymbol{\kappa},\mu}\alpha_{-\boldsymbol{\kappa},\mu}\right). \quad (18)$$

The Bogoliubov coefficients with a tilde, e.g. $\tilde{v}_{1,2}$, are evaluated at $-\boldsymbol{\kappa}$ while the coefficients without tilde are evaluated at $\boldsymbol{\kappa}$. To diagonalize the Hamiltonian we impose bosonic commutation relations ($[\alpha_{\boldsymbol{\kappa},\mu},\alpha^{\dagger}_{\boldsymbol{\kappa}',\mu'}] = \delta_{\boldsymbol{\kappa},\boldsymbol{\kappa}'}\delta_{\mu,\mu'}$) as well as the relation $\left[\alpha_{\boldsymbol{\kappa},\mu},\mathcal{H}\right] = \varepsilon_{\boldsymbol{\kappa},\mu}\alpha_{\boldsymbol{\kappa},\mu}$. The bosonic commutation relation leads to the constraint

$$\left[\alpha_{\boldsymbol{\kappa}},\alpha^{\dagger}_{\boldsymbol{\kappa}}\right] = \underline{B}_6\left[\boldsymbol{a}_{\boldsymbol{\kappa}},\boldsymbol{a}^{\dagger}_{\boldsymbol{\kappa}}\right]\underline{B}^{\dagger}_6 = \underline{B}_6\underline{Y}\underline{B}^{\dagger}_6 = \underline{Y}, \quad (19)$$

where we have introduced the matrix

$$\underline{Y} = \mathrm{diag}(1,1,1,-1,-1,-1). \quad (20)$$

The relation in Eq. (19) requires the normalization

$$\sum_{\nu}\left(|u_{\mu\nu}|^2 - |v_{\mu\nu}|^2\right) = 1. \quad (21)$$

The relation from the commutation with the Hamiltonian leads to the eigenvalue problem

$$\begin{pmatrix} A & C^*_{\boldsymbol{\kappa}} & D^*_{\boldsymbol{\kappa}} & -2E_2 & & \\ C_{\boldsymbol{\kappa}} & B & & & -2E_{3_-} & \\ D_{\boldsymbol{\kappa}} & & B & & & -2E_{3_+} \\ 2E_2 & & & -A & -C_{-\boldsymbol{\kappa}} & -D_{-\boldsymbol{\kappa}} \\ & 2E_{3_-} & & -C^*_{-\boldsymbol{\kappa}} & -B & \\ & & 2E_{3_+} & -D^*_{-\boldsymbol{\kappa}} & & -B \end{pmatrix}\boldsymbol{e}_\mu = \varepsilon_{\boldsymbol{\kappa},\mu}\boldsymbol{e}_\mu,$$

$$\quad (22)$$

where $\boldsymbol{e}_\mu = (u_{\mu,2},u_{\mu,3_-},u_{\mu,3_+},v_{\mu,2},v_{\mu,3_-},v_{\mu,3_+})^{\mathrm{T}}$. We note that $C_{-\boldsymbol{\kappa}} = C^*_{\boldsymbol{\kappa}}$ and $D_{-\boldsymbol{\kappa}} = D^*_{\boldsymbol{\kappa}}$, and all other elements in the matrix are real and independent of $\boldsymbol{\kappa}$. Consequently, we therefore have that $\tilde{u}_{\mu,\nu} = u^*_{\mu,\nu}$ and $\tilde{v}_{\mu,\nu} = v^*_{\mu,\nu}$. We also have that $\varepsilon^*_{\boldsymbol{\kappa},\mu} = \varepsilon_{-\boldsymbol{\kappa},\mu}$, and as $\varepsilon_{\boldsymbol{\kappa},\mu}$ is a real quantity, we therefore also have $\varepsilon_{-\boldsymbol{\kappa},\mu} = \varepsilon_{\boldsymbol{\kappa},\mu}$.

In addition to finding the energy of the eigenmagnons, we also wish to determine their spin, as these are not integer due to squeezing from the SOT-induced anisotropy [5]. Using Eq. (17) and Eq. (19) we see that $\boldsymbol{a}_{\boldsymbol{\kappa}} = \underline{B}^{-1}_6\alpha_{\boldsymbol{\kappa}} = \underline{Y}\underline{B}^{\dagger}_6\underline{Y}^{-1}$. This can be written explicitly as

$$a_{\boldsymbol{\kappa},\nu} = \sum_{\mu}\left(u_{\mu,\nu}\alpha_{\boldsymbol{\kappa},\mu} - v_{\mu,\nu}\alpha^{\dagger}_{-\boldsymbol{\kappa},\mu}\right), \quad (23)$$

$$a^{\dagger}_{\boldsymbol{\kappa},\nu} = \sum_{\mu}\left(u^*_{\mu,\nu}\alpha^{\dagger}_{\boldsymbol{\kappa},\mu} - v^*_{\mu,\nu}\alpha_{-\boldsymbol{\kappa},\mu}\right). \quad (24)$$

Together with the fact that non-diagonal expectation values of the product of two eigenmagnon operators vanish, we see from Eq. (9) and Eq. (21) that

$$\sum_{i,\nu}\langle S_{i,\nu,z}\rangle = \sum_{\boldsymbol{\kappa},\mu}\hbar\sum_{\nu}\left(|u_{\mu,\nu}|^2 + |v_{\mu,\nu}|^2\right)\sum_{m=\pm}\langle\alpha^{\dagger}_{m\boldsymbol{\kappa},\mu}\alpha_{m\boldsymbol{\kappa},\mu}\rangle$$

$$= \sum_{\boldsymbol{k},\mu}\hbar\left(1 + 2\sum_{\nu}|v_{\mu,\nu}|^2\right)\langle\alpha^{\dagger}_{\boldsymbol{k},\mu}\alpha_{\boldsymbol{k},\mu}\rangle, \quad (25)$$

where we have disregarded all constant terms. We can then see that the eigenmagnon spin contribution is

$$S_{\boldsymbol{k},\mu} = \hbar\left(1 + 2\sum_{\nu}|v_{\mu,\nu}|^2\right). \quad (26)$$

### B. Above the critical current

Above the critical current, the lowest energy configuration of the spins is along the $x$ axis. We therefore have to change the Holstein–Primakoff transformation to reflect this, with the following transformation:

$$\tilde{S}_{i,\nu,+} = \hbar\sqrt{2s_\nu}a^{\dagger}_{i,\nu}\sqrt{1 - \frac{a^{\dagger}_{i,\nu}a_{i,\nu}}{2s_\nu}} \approx \hbar\sqrt{2s_\nu}a^{\dagger}_{i,\nu}, \quad (27)$$

$$\tilde{S}_{i,\nu,-} = \hbar\sqrt{2s_\nu}\sqrt{1 - \frac{a^{\dagger}_{i,\nu}a_{i,\nu}}{2s_\nu}}a_{i,\nu} \approx \hbar\sqrt{2s_\nu}a_{i,\nu}, \quad (28)$$

$$\tilde{S}_{i,\nu,x} = \hbar\left(a^{\dagger}_{i,\nu}a_{i,\nu} - s_\nu\right), \quad (29)$$

with $\tilde{S}_{\pm} = -\tilde{S}_z \pm i\tilde{S}_y$. Using this transformation in the Hamiltonian in Eq. (6), we get

$$\mathcal{H} = -\varepsilon_J\sum_{i}\sum_{\boldsymbol{r}_j=\boldsymbol{r}_i+\boldsymbol{\delta}}\sum_{\nu=3_\pm}\left[\sqrt{s_2 s_\nu}\left(a^{\dagger}_{i,2}a_{j,\nu} + a^{\dagger}_{j,\nu}a_{i,2}\right)\right.$$

$$\left. - s_\nu a^{\dagger}_{i,2}a_{i,2} - s_2 a^{\dagger}_{j,\nu}a_{j,\nu}\right]$$

$$- \frac{\varepsilon_z}{4}\sum_{i,\nu}s_\nu\left(a^{\dagger}_{i,\nu}a^{\dagger}_{i,\nu} + 2a^{\dagger}_{i,\nu}a_{i,\nu} + a_{i,\nu}a_{i,\nu}\right)$$

$$+ \frac{\varepsilon_x}{4}\sum_{i,\nu}s_\nu\left(6a^{\dagger}_{i,\nu}a_{i,\nu} - a^{\dagger}_{i,\nu}a^{\dagger}_{i,\nu} - a_{i,\nu}a_{i,\nu}\right). \quad (30)$$

We again do a Fourier transformation as before, and find the Hamiltonian to be on the form (again disregarding any constant terms)

$$\mathcal{H} = +\sum_{\boldsymbol{k}}\sum_{z=\pm}\varepsilon_J\left[3s_3 a^{\dagger}_{\boldsymbol{k},2}a_{\boldsymbol{k},2} + 3s_2 a^{\dagger}_{\boldsymbol{k},3_z}a_{\boldsymbol{k},3_z}\right.$$

$$\left. - \sqrt{s_2 s_3}\left(\gamma^z_{-\boldsymbol{k}}a^{\dagger}_{\boldsymbol{k},2}a_{\boldsymbol{k},3_z} + \gamma^z_{\boldsymbol{k}}a^{\dagger}_{\boldsymbol{k},3_z}a_{\boldsymbol{k},2}\right)\right]$$

$$- \frac{\varepsilon_z}{4}\sum_{\boldsymbol{k},\nu}s_\nu\left(2a^{\dagger}_{\boldsymbol{k},\nu}a_{\boldsymbol{k},\nu} + a^{\dagger}_{\boldsymbol{k},\nu}a^{\dagger}_{-\boldsymbol{k},\nu} + a_{\boldsymbol{k},\nu}a_{-\boldsymbol{k},\nu}\right)$$

$$+ \frac{\varepsilon_x}{4}\sum_{\boldsymbol{k},\nu}s_\nu\left(6a^{\dagger}_{\boldsymbol{k},\nu}a_{\boldsymbol{k},\nu} - a^{\dagger}_{\boldsymbol{k},\nu}a^{\dagger}_{-\boldsymbol{k},\nu} - a_{\boldsymbol{k},\nu}a_{-\boldsymbol{k},\nu}\right). \quad (31)$$

From this expression we can read off the coefficients in Eq. (16), and use the results in the previous subsection for the case below the critical current to determine the energy and spin of the eigenmagnons. The coefficients in Eq. (16) are given in Table I both above and below the critical current.

[1] K. M. D. Hals and A. Brataas, "Phenomenology of current-induced spin-orbit torques," Phys. Rev. B **88**, 085423 (2013); "Spin-motive forces and current-induced torques in ferromagnets," Phys. Rev. B **91**, 214401 (2015).

[2] H.-J. Deiseroth, K. Aleksandrov, C. Reiner, L. Kienle, and R. K. Kremer, "$Fe_3GeTe_2$ and $Ni_3GeTe_2$ – two new layered transition-metal compounds: Crystal structures, HRTEM investigations, and magnetic and electrical properties," Eur. J. Inorg. Chem. **2006**, 1561–1567 (2006).

[3] R. R. Birss, *Symmetry and Magnetism*, 1st ed., edited by E. P. Wohlfarth, Selected Topics in Solid State Physics, Vol. 3 (North-Holland Publishing Company, 1964).

[4] Y. Deng, Y. Yu, Y. Song, J. Zhang, N. Z. Wang, Z. Sun, Y. Yi, Y. Z. Wu, S. Wu, J. Zhu, J. Wang, X. H. Chen, and Y. Zhang, "Gate-tunable room-temperature ferromagnetism in two-dimensional $Fe_3GeTe_2$," Nature **563**, 94–99 (2018).

[5] A. Kamra, U. Agrawal, and W. Belzig, "Noninteger-spin magnonic excitations in untextured magnets," Phys. Rev. B **96**, 020411 (2017).

# Index